Heat transport by low-energy quasiparticles in $YBa_2Cu_3O_y$: a field and doping dependent study

by

Michael L. Sutherland

A thesis submitted in conformity with the requirements
for the degree of Doctor of Philosophy
Graduate Department of Physics
University of Toronto

ABSTRACT

Heat transport by low-energy quasiparticles in $YBa_2Cu_3O_y$: a field and doping
dependent study

Michael L. Sutherland
Doctor of Philosophy
Graduate Department of Physics
University of Toronto
2005

Measurements of heat and charge transport at very low temperature were used to
investigate the ground state of high-purity single crystals of the cuprate $YBa_2Cu_3O_y$ as a
function of doping. Samples were investigated on either side of the superconducting phase
boundary, in both zero and applied magnetic field. We find that from optimal doping
to a doping near the onset of superconductivity the elementary electronic excitations
are understood to be nodal quasiparticles, whose excitation spectrum is governed by
the energy scale of the pseudogap. In a magnetic field, these quasiparticles behave
unexpectedly in our purest samples - conventional transport theory cannot account for
their field and temperature dependence in either the unitary or Born scattering limits.
At very low dopings, such that the hole concentration in the CuO_2 planes is slightly
less than the critical doping needed for the onset of superconducting order, we observe
delocalized fermionic excitations at zero energy. This reveals that the ground state of
clean underdoped cuprates is metallic, in contrast to the insulating ground state observed
in underdoped $La_{2-x}Sr_xCuO_4$. The ratio of heat to charge transport in this metallic state
violates the Wiedemann-Franz law, the first such observation in underdoped cuprates.

To my friends and family

Acknowledgements

STATEMENT OF ORIGINALITY

The group that I have been fortunate to work with is highly collaborative - we have all contributed in some way or another to each others' research projects. In the interests of originality, I use this section to define my role in each of the projects that I present in this thesis. The key results of this thesis can roughly be broken down into five seperate studies, covered succesively in chapters 7-12. I summarize the major acheivements of these projects, and define my contribution to each in the paragraphs below.

Doping dependence of the residual linear term in cuprate superconductors

One of the major efforts in our group over the past few years is to use thermal conductivity to study low energy quasiparticles from the over-doped to the under-doped regime of the cuprate phase diagram. In the underdoped regime of YBCO, we find that the residual linear term decreases with decreasing doping, in a manner which tracks the energy scale of the pseudogap. In LSCO, we find the same qualitative behaviour, but the linear term in additionally supressed, likely as a result of the insulator to metal phase transition. I grew and measured several of the YBCO samples used in this study, as well as characterizing and measuring the samples that were provided by UBC. All measurements were done with the assistance of members of the group - Robert Hill, Cyril Proust, Fil Ronning, Makariy Tanatar, Shiyan Li, Etienne Boaknin, Dave Hawthorn, Christian Lupien, and Johnpierre Paglione. For the LSCO study I also assisted in some of the fridge measurements. This work was published in Phys. Rev. B. [1] and the manuscript was written by myself and Louis Taillefer, with a preliminary draft prepared by Dave Hawthorn.

We note that similar work on the doping dependence of the residual linear term has been published by the group of Yoichi Ando. Measurements of LSCO were reported prior to our publication [2], although their data does not extend to as low temperature and doping as our study. In YBCO results by Sun *et.al.* were reported after ours [3], and are qualitatively the same. A re-analysis of their data using more advanced fitting techniques in Appendix 3 shows that the values of the residual linear term versus doping agree quite well with ours.

Field dependence of thermal transport in YBCO

Measurements of the thermal conductivity of YBCO at a number of dopings, and in crystals of varying purity were made to test the limits of semi-classical theories of transport in the mixed state. In an ultra pure sample of $YBCO_{6.99}$ in magnetic fields applied perpendicular to the planes, the temperature dependence of the data was found to be poorly described in both the Born and Unitary limits, suggesting that theories incorporating intermediate scattering phase shifts need to be developed. Additionally, the field dependence of the linear term suggested that quasiparticle-vortex scattering can not be negelected in this compound. The results of this study were reported in Phys. Rev. Lett, [4] in a manuscript authored by Rob Hill with inputs from myself, Louis Taillefer, Dave Hawthorn, Cyril Proust and Christian Lupien. Experimentally, I assisted in both the characterization measurements and low temperature dilution fridge measurements.

Thermal transport in the stoichiometric underdoped cuprate $YBa_2Cu_4O_8$

One of the more puzzling results of heat transport measurements was the absence of a residual linear term in the double-chained YBCO-124 compound reported by Hussey *et.al* [5]. In collaboartion with the authors of this work, we have repeated measurements on their samples, and extended the study to include measurements made in a magnetic field. We find that there is in actuality a finite linear term in this compound, and that the field dependence of heat transport displays novel behaviour. All preparation, characterization

and fridge measurements in this sample were performed principally by myself, with the assistance of Johnpierre Paglione, Dave Hawthorn, Shiyan Li and Makariy Tanatar. The resolution of our results and those of Nigel Hussey was made possible by the theory of Mike Smith and Mike Walker, who revealed the effects of electron-phonon decoupling on heat transport measurements in the cuprates. This work is at present unpublished, but at the time of writing I have begun the task of drafting a manuscipt to be submitted to Phys. Rev. B.

Pulsed field measurements of ortho-II ordered YBCO$_{6.50}$

Until now our knowledge of the charge conductivity of the field induced normal state of cuprates has been limited to the LSCO system. We have performed measurements of resitivity in applied fields as high as 55 Tesla, sufficient to supress superconductvitiy in sample of ortho-II ordered YBCO$_{6.50}$. We reveal a metallic ground state, in contrast to LSCO. Measurements were performed by myself in Toulouse, France with the assistance of Cyril Proust and Marc Nardonne of the CNRS.

Wiedemann-Franz law study in highly underdoped curpates

We have measured both thermal and charge conductivity in the normal state of very low doped YBCO. We find metallic behaviour in both channels - a resistivity that is essentially flat down to low temperatures, and a residual linear term in thermal conductivity that reveals the presence of low-energy delocalized quasipartilces. The ratio of the two violate the Wiedemann-Franz law, the first time such an observation has been seen in underdoped cuprates. This violation could be the result of a strange localization mechanism, or the fingerprint of spin charge separation. For this study I performed all of the sample characterization and contact preparation, as well as taking the lead role in the dilution fridge measurements. Shiyan Li, Rob Hill, Dave Hawthorn, Makariy Tanatar and Johnpierre Paglione also provided assitance with the experiments.

Summary

Here I summarize the contributions that I have made to the work presented in this thesis, as well as note any publications which have arisen, or will arise in the near future. In order of involvement, the roles in each study can be catagorized as: 1. principal author (overseeing sample preparation, measurement, data analysis and manuscript authoring). 2. assisting author (actively participating in measurements and data analysis) and 3. contributing author (non-trivial contributions to either measurments or authouring of manuscripts).

Table 1: Summary of the author's contributions to the projects summarized in this Thesis.

Study	Role	Reference
Doping Dependence	Principal Author	PRB [1] Physica C [6]
$\kappa(H)$ in $YBCO_{6.99}$	Assisting Author	PRL [4]
$\kappa(H)$ in $YBCO_{6.50}$,$YBCO_{6.75}$	Principal Author	unpublished
κ in YBCO-124	Principal Author	preprint in preparation
κ in LSCO	Contributing Author	PRL [7]
κ in Tl2201	Contributing Author	preprint in preparation
$\rho(55T)$ in $YBCO_{6.50}$	Principal Author	preprint in preparation
κ in low doped YBCO	Principal Author	preprint (to be submitted to PRL)
WF law violation in YBCO	Principal Author	preprint in preparation
κ in $Sr_3Ru_2O_7$	Assisting Author	preprint (to be submitted to PRB)

CONTENTS

9   Thermal Conductivity in the Vortex State of $YBa_2Cu_3O_y$

104

10 κ in the Stoichiometric Underdoped Cuprate $YBA_2Cu_4O_8$

121

FIGURES AND TABLES

FIGURES

xviii

TABLES

1

HIGH T_c CUPRATES: PROGRESS AND CHALLENGES

1.1 Chapter overview

The discovery of a family of superconducting ceramic oxides was both a major surprise, and a major advance in materials physics. Prior to 1986 most ceramic oxide materials were known to have semiconducting or insulating electronic properties, making them unlikely hosts for superconductivity. Up until this point superconductivity was typically observed in systems with low electrical resistivities, such as the elemental metals Pb or Hg, or intermetallics like $NbSe_2$. The observation by Bednorz and Müller [8] of superconductivity persisting to relatively high temperatures in the La-Ba-Cu-O system came as a shock to the community, and triggered a monumental research effort focussed on understanding the complex physics of these systems.

In the past 20 years there have been many important advances in our knowledge of these systems, however several fundamental questions remain unanswered. In the following sections I attempt to briefly review some of the key established facts about the cuprates, and emphasize the gaps in our understanding[1] In the final section I pose the questions that may be answered by measurements of thermal conductivity at low temperatures, setting the stage for the chapters to follow.

1.2 Cuprate superconductors: basic electronic properties

The cuprate superconductors exhibit a variety of complex crystal structures, however each is composed of the same fundamental building blocks. The common element in these systems is the existence of a planar arrangement of copper and oxygen atoms, sandwiched between layers that act as a charge reservoir for accepting (or donating) electrons, as shown schematically in Figure 1.1. In the copper oxides, the energies of

---

[1]A much more in-depth review of the physics of the cuprates can be found in the excellent articles by Orenstein and Millis[9], Norman and Pepin[10] , and Hussey [11].
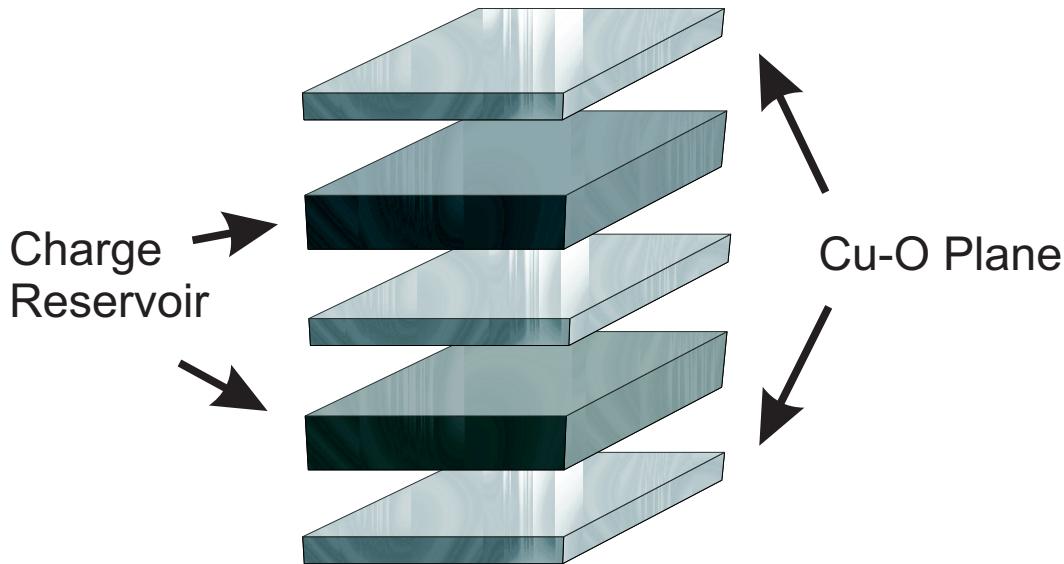
Figure 1.1: The basic building blocks of a cuprate superconductor. Cu-O planes host electronic transport, separated by charge reservoir layers which either serve to dope holes or electrons into the planes.

the copper and oxygen orbitals are very close, meaning that both the copper *and* oxygen electrons contribute to conductivity. This is a very different situation than in the majority of metallic oxides, where the bands are formed primarily by the overlap of the metallic d-orbitals [12].

The electronic configuration of the Cu^{2+} ions that form the basis of these compounds is responsible for the unusual properties of the cuprates. In the undoped parent compounds of the cuprate superconductors, Cu^{2+} has an orbital configuration of $3d^9$, where the tetragonal crystal symmetry requires the one unpaired electron to rest in the $d_{x^2-y^2}$ orbital. This electron carries a spin of 1/2, resulting in a lattice in which spin-spin interactions are large, and influence the behaviour of conduction electrons.

The effect of the oxygen $2p$ orbitals is illustrated schematically in the band diagram in Figure 1.2. The 1/2 filled Cu $x^2 - y^2$ band lies close in energy to the band formed by filled O and Cu orbitals, and one would predict the undoped system should be a metal. This is however not the case, as the undoped parent compounds are observed to be strong electrical insulators.

The insulating behaviour is a direct result of the strong interactions between the electrons, which is greatest for electrons in half filled bands. The energy required to place a second electron into the half filled $d_{x^2-y^2}$ orbital is large, a result of the strong
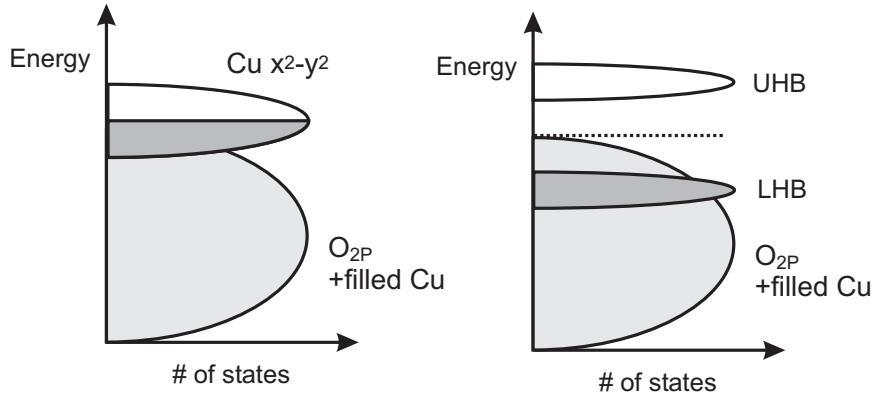
Figure 1.2: Schematic picture of the energy states of the cuprate Mott insulator, adapted from reference [12]. In a non-interacting systems (left) the cuprates are expected to be metallic. When electron interactions are turned on, the $Cu_{x^2-y^2}$ band is split in two - with a sizable energy gap U in between. This splitting results in an insulating material.

Coulomb repulsion between the charges. This additional energy has the effect of splitting the single x^2-y^2 band into two bands, separated by an energy U. These bands are known as the upper and lower Hubbard bands (UHB and LHB) and the energy gap U is typically on the order of about 2 eV [10], effectively preventing electrons from moving through the lattice. Materials that are unable to transport charge in this manner are known as Mott insulators.

The electronic gridlock is broken by adding (or removing) electrons from the copper-oxygen planes, a process known as doping. Theoretical understanding of the evolution of the Mott insulator with doping is still lacking, but is commonly viewed as the starting point for a theoretical understanding of the cuprates [13]. Adding charge carriers to the planes evolves the Mott insulator towards a fully metallic Fermi-liquid state, and we shall now discuss this evolution in the context of the doping phase diagram.

1.3 Cuprate phase diagram

The concentration of doped charge carriers in the CuO planes is denoted by p, with $p=0$ referring to the Mott insulating state discussed above. Carriers can either be electron-like as in $Nd_{2-x}Ce_xCuO_{4-y}$ (NCCO) and $Pr_{2-x}Ce_xCuO_{4-y}$ (PCCO), or hole-like as in $YBa_2Cu_3O_y$ (YBCO). $La_{2-x}Sr_xCuO_{4-y}$ (LSCO), $Bi_2Sr_2CaCu_2O_{8+\delta}$ (BSCCO) and $Tl_2Ba_2CuO_{6+\delta}$ (Tl2201). The phase diagram for both types is similar[2] and the ma-

---

[2]The phase diagram for electron doped superconductors exhibits a lower maximal T_c, and has an insulating phase that persists over a wider range of dopings. See for instance, reference [14].
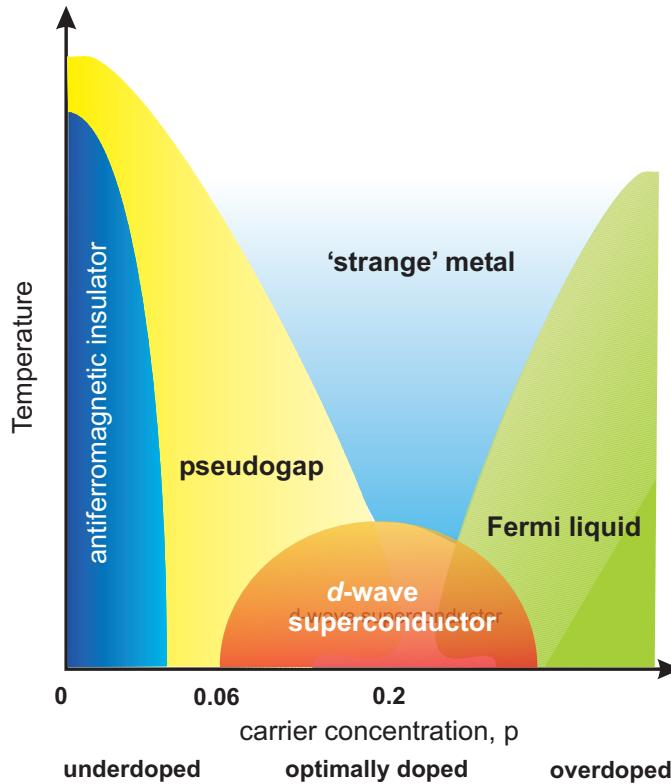
Figure 1.3: The temperature-doping phase diagram of cuprate superconductors.

terials we study in this work are on the hole doping side of the phase diagram shown in figure 1.3.

Understanding the complexity of phases evident in figure 1.3 is one of the outstanding goals in cuprate research. At very low doping $p \lesssim 0.03$ the cuprates are anti-ferromagnetic insulators discussed above, where transport is crippled by strong Coulomb interactions. At low to moderate dopings, the materials are in the "pseudogap phase" where remnants of a gap in the electronic excitation spectrum persist to temperatures above T_c. Close to $p = 0.06$, superconductivity occurs, reaching a maximum T_c at an optimal doping of p=0.16. For YBCO, BSCCO and Tl2201 this T_c is on the order of 90 K, but can reach as high as 138 K in the Hg based compound $Hg_{0.8}Tl_{0.2}Ba_2Ca_2Cu_3O_{8.33}$ [15]. At high temperatures above the superconducting dome, the material is a so-called strange metal, bounded by the pseudogap line at low dopings and the metallic transition line at high dopings and characterized by transport and spectroscopic properties that are inconsistent with conventional metallic theory. Finally, when doping is increased beyond p=0.26 superconductivity is entirely suppressed, resulting in a metal well-described by

Fermi liquid physics.

1.4 The superconducting phase

The distinguishing feature of the superconducting phase that sets it apart form conventional superconductors is the exotic nature of its pairing symmetry. In typical elemental superconductors, the pairing is isotropic in momentum space, electrons form Cooper pairs in zero spin and zero angular momentum states ($S = 0$, L=0) leading to a gap that is constant around the Fermi surface. This s-wave pairing symmetry gaps out excitations at low energies, leading to an activated behaviour in most physical properties.

The cuprates are now known to be unconventional superconductors, pairing in states of non-zero angular momentum like the heavy fermion superconductors [16] and ^3He [17]. Early evidence that the order parameter (equivalent to the gap in BCS theory) had nodes was found in the linear dependence of the penetration depth with temperature [18]. The order parameter was soon shown to undergo a change of sign upon a 90° rotation in the tri-crystal experiments of Kirtley and Tsuei [19], clinching the case for an S=0, L=2 d-wave pairing state[3].

The existence of d-wave symmetry means that the order parameter must vanish at four nodal points on the Fermi surface, where low energy excitations abound. The precise location of these nodes has been identified by Angle-Resolved Photoemission Spectroscopy (ARPES) to lie in the ($\pm \pi, \pm \pi$) direction, which is the $d_{x^2-y^2}$ form of the gap.

What remains unknown at present is the *mechanism* responsible for pairing in high T_c superconductors. The electron-phonon interaction is unlikely to provide the whole story, as it is difficult to reconcile the observed order parameter symmetry with such a pair potential. Many have suggested instead that the pairing is electronic in origin, perhaps mediated by the antiferromagnetic spin fluctuations observed in the underdoped regime. The resemblance of the cuprate phase diagram to that observed in quantum critical systems such as $CePd_2Si_2$ [21] where antiferromagnetic order is suppressed with pressure is intriguing. This parallel suggests that understanding the role of magnetism may be crucial to understanding superconductivity in the high-T_c's.

The superconducting state in cuprates at optimal and over-doping bears much resemblance to its less exotic cousins. Elementary excitations take the form of long lived

---

[3]A very thorough review of the evidence for d-wave pairing can be found in the article by Kirtley and Tsuei [20]

quasiparticles for example, which are well described by a BCS Fermi-liquid theory. In the underdoped regime however ARPES [22] and tunnelling [23, 24] have shown that the superconducting gap continues to increase as the Mott insulator is approached, despite the fact that T_c and the superfluid density [25] is suppressed towards zero. This region of the phase diagram sees the breakdown of conventional BCS theory, and understanding it may is a key step towards unravelling the puzzles of high temperature superconductivity.

1.5 The underdoped regime

There are two major characteristics of underdoped cuprates that distinguish them from those at optimal doping. First, the integrity of the Fermi surface is challenged, and second, a gap like feature in the normal state electronic excitation spectrum is observed. In this section I briefly review these characteristics, and summarize some of the experimental and theoretical progress in this regime of the phase diagram.

1.5.1 Evolution of Fermi surface with p,T

In the past decade sustained progress in the development of the ARPES technique have made it the principal tool for studying the cuprate Fermi surface. At optimal and over-doping, the quasi 2D Fermi surface is observed to consist of cylinders centered at the (π,π) position in k space, with a Fermi vector of $k_F \sim 0.7$ $\mathring{A}$ [26]. The first study to probe the Fermi surface in the underdoped regime was performed by Marshall *et.al.*, who found that in underdoped BSCCO well defined Fermi surface crossings only existed in an arc centered about the nodal points at $(\pi/2, \pi/2)$ [27] at temperatures above T_c. Away from these regions the observed spectra were broad, and lacking the sharp peaks associated with long-lived quasiparticles. Norman *et.al.* [28] traced the temperature dependence of the Fermi surface in the underdoped regime, showing that the full cylindrical shape above T^* fragmented in Fermi arcs upon cooling, eventually shrinking to consist of only the four nodal points at $T < T_c$.

Similarly, in underdoped LSCO with 6% Sr Zhou *et.al.* have found only sharp quasiparticles around the nodal region, with spectral broadening in the antinodal directions [29]. This washing out of the Fermi surface has been attributed to either effects of coupling to strong magnetic fluctuations along the (π,π) direction [30] or quasiparticle scattering between nested portions of the Fermi surface [29].

Although the dependence of the Fermi surface topology on doping and temperature is yet to be settled, it is clear that the behaviour is rather unlike that seen in normal

metals.

1.5.2 The pseudogap regime

For $p < p_{SC}$ nuclear magnetic resonance (NMR) measurements were the first to establish that a peculiar remnant of the low energy excitation gap persists to temperatures above T_c, and is closed in at the characteristic temperature T^*, known as the pseudogap temperature. In 1989 Warren *et.al.* [31] observed a temperature dependent spin susceptibility to high temperatures in underdoped YBCO, and postulated the existence of a spin-gap in the normal state. Subsequent experiments have established that this gap in fact exists in both the charge and spin channels[4]. To date, evidence of the pseudogap has been observed in ARPES [28, 33, 22], optical conductivity [34], tunnelling [23, 24] and Raman spectroscopy [35] among others. Most recently the pseudogap has been observed for the first time using ultra-low temperature thermal conductivity measurements [1] by our own group [5].
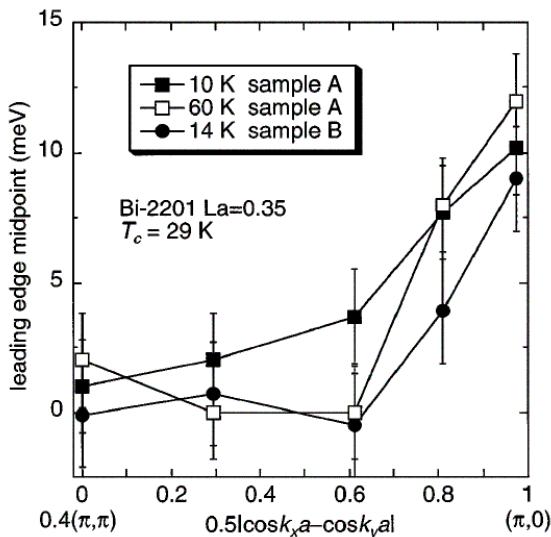
Figure 1.4: The angular dependence of the pseudogap energy in underdoped BSCOO, from Harris *et.al.* [36]. The figure shows ARPES measurements of the gap as the angle around the Fermi surface is varied in both the superconducting and non-superconducting states. The angular dependence is observed to be identical, and to possess *d*-wave symmetry, with nodes in the (π, π) direction.

Using ARPES, Harris *et.al.* have determined that the pseudogap shares the same sym-

---

[4]A very thorough review of the topic can be found in the article by Timusk and Statt [32]

[5]This observation is a major component of this thesis, and is discussed in chapter 8

metry as the superconducting gap in k-space. This observation is reproduced in figure 1.4, which shows the angular dependence of the gap measured in both the superconducting state and above T_c. This intriguing similarity is suggestive of a common origin, although this is the subject of some speculation and debate. Theoretical ideas concerning the pseudogap identity roughly fall into two categories. Either the pseudogap is thought to be an *extrinsic* feature, mainly unrelated to superconductivity, or it is an *intrinsic* feature, derived from the superconductivity itself.

Intrinsic origins of the pseudogap

Emery and Kivelson have pointed out that the role that classical [37] and quantum phase fluctuations [38, 39] of the superconducting order parameter play in determining the scale of T_c. The low superfluid density of the doped insulator implies that superconducting phase fluctuations are unusually large in the cuprates. For a very low phase stiffness, these fluctuation effects can conceivably govern the entire doping phase diagram. Measurements of ρ_S via the microwave penetration depth highlight the role of fluctuations well. The behaviour of the superfluid density versus temperature for $T < T_c$ is observed to be linear, and may in part be described by a quasi-two dimensional fluctuation model [40]. Using such measurements, one can determine the characteristic phase fluctuation temperature T^θ itself, which is the temperature at which long range phase coherence disappears and bulk superconductivity is lost. In the limit where T^θ is much greater than the mean-field BCS transition temperature T_{BCS-MF}, the fluctuations are not expected to suppress T_c noticeably. When $T^\theta \sim T_{BSC-MF}$, the bulk transition temperature can be greatly reduced, as long range phase coherence is lost at relatively low temperatures. Such a scenario is believed to be particularly relevant to underdoped cuprates due to their 2D nature, low carrier density and their proximity to an insulating phase. The picture that emerges is a phase diagram of the type shown in figure 1.5, where the underdoped phase exhibits pairing up to T^* but bulk superconductivity is not realized. The characteristic dome shape of the superconducting region is then defined by the doping dependence of these two energy scales. The magnitude of the pseudogap is then expected to be determined by the energy scale of the pairing, given by BCS theory.

This scenario has found some experimental backing, most noticeably in measurements of the Nernst effect at $T > T_c$. In such experiments a large transverse Nernst voltage has been observed in both underdoped LSCO and high quality ortho-II ordered YBCO [42, 43, 44] at temperatures well above the bulk superconducting transition tempera-
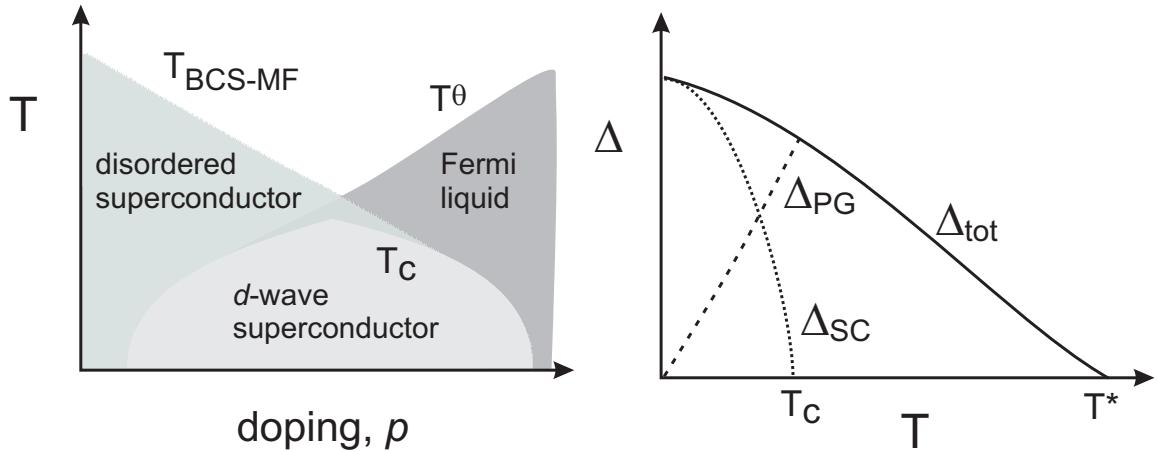
Figure 1.5: **Left** : The doping phase diagram of the cuprates in the intrinsic pseudogap model, where phase fluctuations destroy superconductivity in the underdoped regime, but superconducting pairing persists. T^{θ} is the experimentally determined phase ordering temperature, while T_{BCS-MF} is the transition temperature expected from BCS theory. **Right** : Schematic diagram showing the temperature dependence of the superconducting gap Δ_{SC}, the pseudogap Δ_{PG} and the total gap $\Delta_{tot} = \sqrt{\Delta_{SC}^2 + \Delta_{PG}^2}$ in the underdoped regime, assuming an intrinsic origin for the pseudogap. Adapted from reference [41].

ture. The persistence of this signal has been interpreted as evidence of remnant vortex like excitations above T_c, supporting the idea of preformed pairs below the pseudogap temperature.

Extrinsic origins of the pseudogap

In the picture that the pseudogap is the result of a secondary order that co-exists or competes with superconductivity there are many proposed models. Such an order parameter would posses its own gap Δ_{PG} independent of the superconducting gap Δ_{SC}, resulting in the phase diagram and temperature dependence of the total energy gap Δ seen in figure 1.6.

Among these theories Chakravarty *et.al.* [45] have argued for the existence of a *d*-density wave (DDW) state that gives rise to the pseudogap - which is understood to be a full gap of energy Δ_{PG} that is rounded out by the presence of disorder. Such a state is proposed to break translational, rotational and time-reversal symmetries, resulting in circulating bond currents. Such currents are arranged in plaquettes and give rise to local magnetism, with small but experimentally measurable magnetic fields on the order of a few Gauss. In their model, competition between the DDW state and the *d*-wave superconducting order parameter is what eventually destroys superconductivity in the
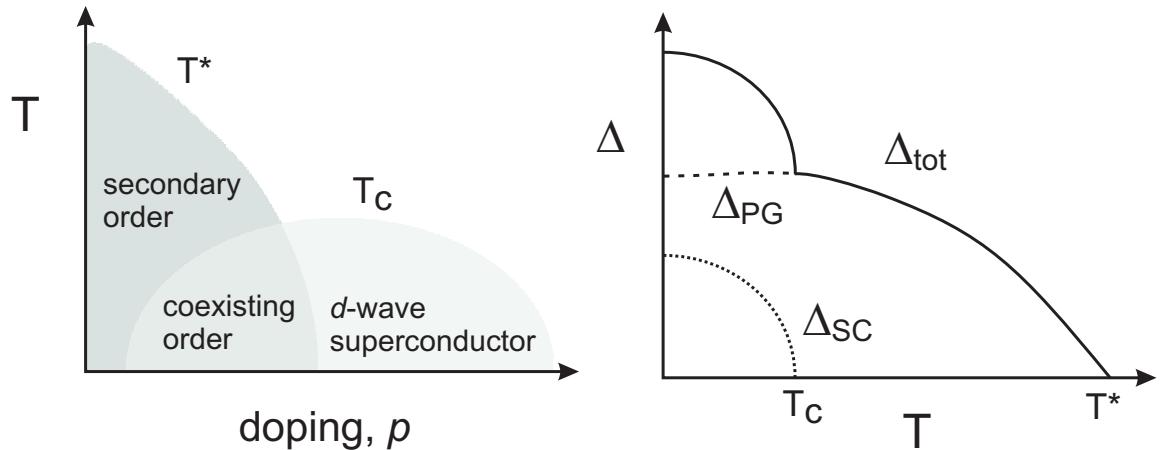
Figure 1.6: **Left** : The doping phase diagram of the cuprates in the extrinsic pseudogap model, where a secondary order competes with superconductivity.   **Right** : Schematic diagram showing the temperature dependence of the superconducting gap Δ_{SC}, the pseudogap Δ_{PG} and the total gap $\Delta_{tot} = \sqrt{\Delta_{SC}^2 + \Delta_{PG}^2}$ in the underdoped regime using the mean field approximation. Adapted from reference [41].

underdoped regime. Similar models incorporating orbital currents have been proposed by Varma [46] and Wen and Lee [47]. Whether these states are realized in cuprates is still the subject of investigation.

Stripe order

A second class of extrinsic pseudogap models is related to the existence of unidirectional density wave states [48]. These can consist of modulations of the charge density (charge stripes) or both the spin and charge density (spin stripes). In these scenarios the spin and charge is inhomogeneously organized within the superconducting phase. In the strong coupling limit it is proposed that a microscopic phase separation occurs, and the charge is restricted to one dimensional conducting rivers, bounded by antiferromagnetically ordered insulating domains. Ample experimental evidence of such order has been observed in the LSCO [49] and Nd-doped LSCO [50, 51, 52] systems, where a characteristic four fold splitting of Bragg peaks observed with neutron scattering is seen. The size of the splitting in reciprocal space is observed to scale inversely with stripe separation, as expected.

In the weak coupling limit both the charge and spin densities exhibit incommensurate modulations, although a strict real-space segregation of phases is not observed. The study and classification of the various types of stripes and their fluctuations is an ongoing
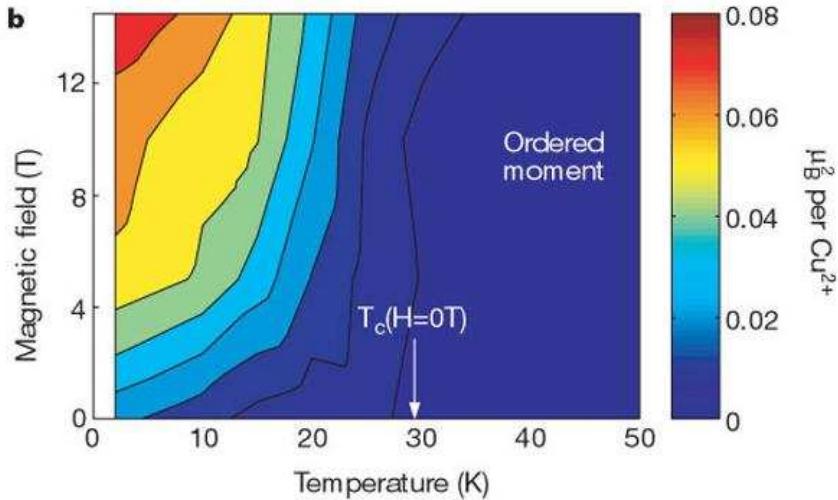
Figure 1.7: The magnitude of the ordered spin moment per Cu ion as a function of temperature and applied field in underdoped LSCO. The large enhancement in the signal at low temperatures and high fields is a signature of the coexistence of superconductivity and SDW order in underdoped LSCO. From reference [55].

task, with neutron and x-ray scattering in LSCO being the most common avenues of investigation. Studies on other systems are hampered by the large sizes and low mosaic spreads needed for neutron scattering measurements, and as a result several key questions remain unanswered at present. Does the existence of stripe order serve to inhibit or aid superconductivity, or are stripes just passive bystanders? [6] Furthermore, to what extent are the results observed in LSCO relevant to other systems such as YBCO, where no evidence of static stripe order has yet been observed [53]?

Recent measurements by Stock, Buyers *et.al.* [53, 54] on very high quality samples of underdoped YBCO have attempted to overcome these limitations. Their results show that the superconducting phase exhibits one-dimensional incommensurate modulations at low energies, consistent with hydrodynamic stripes. There appears to be no evidence for static stripe order of the same type as that observed in LSCO. From a transport perspective, at the low energies accessed in a dilution fridge, it is only static modulations that could conceivably influence κ measurements in the limit $T \to 0$.

In this respect the situation in underdoped LSCO is much more clear. Lake *et.al.* have used magnetic neutron scattering to study the spin order of an underdoped sample

---

[6]In LSCO it seems at present that there is some competition between superconductivity and static stripes as observed through the depression of T_c at 1/8 doping [49]
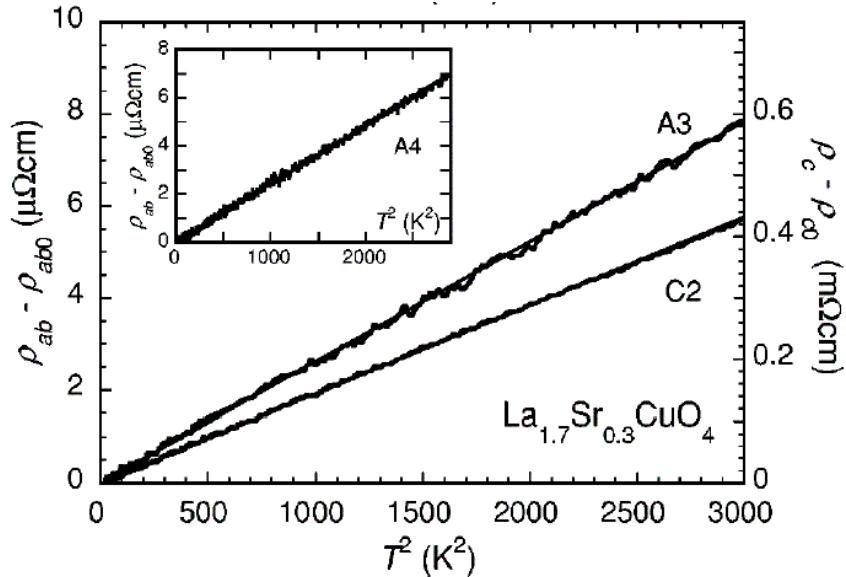
Figure 1.8: Resistivity of LSCO in the extreme overdoped region of the phase diagram, from [56]. Samples with J $\parallel$ *ab*-plane (A3,A4) and J $\parallel$ *c*-axis (C2) show a T^2 dependence of the resistivity - clear evidence of a Fermi-liquid metal.

of $La_{1.9}Sr_{0.1}CuO_4$ subjected to a 14.5 Tesla magnetic field. In such an experiment the applied field is used as a tuning parameter, moving the sample between *d*-wave superconductivity and spin-density wave (SDW) order. They found that the average magnetic moment per Cu ion was greatly enhanced by the application of a field, as reproduced in figure 1.7. The correlation length of this local ordering was large - much larger than the superconducting coherence length or inter-vortex spacing. This point is significant, it implies that the spin ordering is not localized within the vortex cores but permeates throughout the sample. The effects of such a co-existing antiferromagnetic order on transport in low doped LSCO is investigated in chapter 8.

1.6   The overdoped regime

For dopings slightly above optimal doping Tallon and Loram have proposed that the pseudogap is still present in the normal state [57], and that it falls to a zero at a critical doping of *p*=0.19. Such a scenario is still controversial, but supported by a wide variety of experimental data. For dopings much greater than $p = 0.16$ there is mounting evidence that the ground state is metallic in nature, well described by Fermi-liquid physics.

Evidence of this can be found in transport measurements by our group, in which

superconductivity is suppressed by a magnetic field in a sample of strongly overdoped Tl2201 with a T_c of 15 K and estimated doping of $p = 0.26$ [58]. Measurements of both thermal and charge transport reveal that the ground state obeys the Wiedemann-Franz law, a well-known property of Fermi-liquids. In the LSCO system it is possible to increase doping even further, such that $p > 0.27$ and the samples are non-superconducting in zero-field. Studies by Nakamae *et.al.* [56] on crystals with $p = 0.30$ reveal that the region of the phase diagram that lies beyond the superconducting dome is a highly correlated metal with a T^2 resistivity, as observed in Figure 1.8. All of this points towards a phase diagram that is conventional for high dopings, and increasingly unconventional as one approaches the Mott insulator.

1.7   Why study low-temperature heat transport?

Advantages of the technique

In many ways heat transport is a privileged probe of the cuprates. Since it is a bulk technique, it can circumvent many of the materials issues that can complicate interpretation of data from surface sensitive measurements, such as ARPES and tunnelling. Measurements are possible on extremely small samples if one is careful enough, compared to neutron scattering for instance, which often require large mosaics of smaller crystals to obtain a sizable signal. Additionally, thermal conductivity (κ) is a measure of only *mobile* excitations, and thus can very easily distinguish between a metallic or insulating state. These measurements may also be extended to very high magnetic fields, providing information on the evolution of the heat carriers with field or in a superconductor, the nature of the ground state in the absence of superconductivity, provided H $> H_{c2}$.

In a superconductor heat is not carried by Cooper pairs, which exist in a zero-entropy state. Instead electronic heat transport is accomplished via excitations out of the condensate, which carry with them valuable information about the superconducting state itself. It is usually quite easy for instance to distinguish between an order parameter which has nodes, and therefore quasiparticle excitations to $T = 0$, and an order parameter which is fully gapped. In a *d*-wave superconductor the linear in T electronic term caries information about the quasiparticle dispersion, and hence the superconducting gap itself. At low enough energies, the thermal conductivity in such materials has been shown to be universal with respect to impurity concentration, and is impervious to vertex and Fermi-liquid corrections [59, 60]. These facts combine to make interpretation of the date

relatively straight forward.

Applications to cuprate physics

With these considerable advantages there exist many open questions that thermal conductivity may address in the cuprates. Prior to the work reported in this thesis, low temperature κ measurements in the high-T_c compounds had only been attempted at optimal doping on a limited number of materials [61, 60]. By extending our scope to include cuprates in the under and overdoped regimes in YBCO, LSCO and Tl2201 [7] we hope to investigate the evolution of the ground state across the superconducting dome and beyond.

As the above sections highlight, one of the most contentious issues is the nature of the ground state in the underdoped regime. Is the pseudogap the result of some exotic form of competing order, or is it merely a signature of superconductivity that has failed to achieve long range order? Does a BCS theory modified to incorporated a d-wave order parameter accurately describe the superconducting ground state in the underdoped regime, as it does at optimal doping? In the limit of very low dopings does the ground state in the absence of superconductivity bear any resemblance to that at higher dopings? And finally - how universal is the doping dependence between cuprates? Should YBCO exhibit different behaviour than the much more disordered LSCO system?

In the presence of an applied magnetic field much of the details of heat transport by nodal quasiparticles are left to be filled in. An outstanding question is the role that disorder plays in setting the scale of the response of the quasiparticles to a field. At a more fundamental level, how does one treat scattering by impurities in cuprates? Is the scattering process best modelled theoretically by strong (unitary) or weak (Born) scattering?

Our approach

The preceding questions - and others, are the focus of this Thesis. Our approach to answering these queries is two-fold. We study in great detail the doping dependence of heat transport across the phase diagrams of cuprates, at many intervals in both zero and applied magnetic field using state of the art instrumentation and analysis. Secondly, we restrict our investigations to only the best quality single crystal samples available,

---

[7]This broad initiative is the collective work of many members of our group past and present, and is summarized in this Thesis, as well as the Thesis of Dave Hawthorn [62].

thereby reducing any uncertainties associated with materials issues.

THEORETICAL FOUNDATIONS OF TRANSPORT IN SOLIDS

2.1 Introduction

A complete description of transport in solids involves a detailed and sometimes complex accounting of carriers and the processes which scatter them. In this section I offer a brief review of the general theory of transport in a material possessing long range order. I begin with a short discussion of the kinetic theory of transport, then summarize three basic results: the conduction of charge by free electrons in a metal, the conduction of heat by the same electrons, and the conduction of heat by quantized lattice vibrations (phonons). In the final sections I introduce an empirical fitting procedure based on the specular reflection of phonons from crystal boundary that is used extensively throughout this body of work to extract electronic and phononic contributions to thermal conductivity. A rigorous and much more comprehensive treatment of these ideas may be found in references [63], and particularly the book by Ziman [64], where the more formal approach of the Boltzmann theory is developed.

2.2 The kinetic theory of heat transport

The kinetic theory of transport in metals has its roots in the kinetic theory of gases, developed in the latter part of the 19th century. Soon after the discovery of the electron by J.J. Thompson, Drude successfully applied the formalism developed for an ensemble of randomly moving gas molecules to a gas of free electrons inhabiting a crystal lattice. The calculation of the thermal conductivity κ of such a gas is straightforward. Consider a collection of free particles, with an average velocity of v. If the gas is sufficiently rarefied, collisions between particles will happen fairly infrequently. Let us assume that the probability $P(t)$ that a particle will survive unperturbed for a time τ is an exponential function of time t, that is $P(t) = exp^{-(t/\tau)}$. If one applies a temperature gradient ΔT across the gas, then the thermal current per unit area is given by:

$$U = \frac{1}{3}v^2\tau C_v \Delta T = \kappa \Delta T \qquad (2.1)$$

where C_v is the heat capacity of the system at constant volume, and the coefficient of the temperature gradient, κ, is called the thermal conductivity. It is convenient to describe a mean free path ℓ of the particles. We define this as the average distance that a particle may travel before suffering a collision, or $\ell = v\tau$. The thermal conductivity of the gas is then recast as:

$$\kappa = \frac{1}{3}C_v v \ell \qquad (2.2)$$

In many situations this simple result is quite useful in estimating the thermal conductivity of a given system of particles, and can be applied equally well to a gas of phonons.

In a situation were there are many individual scattering mechanisms limiting the mean free path, Matthiessen [65] showed that collision rates will add in a linear manner, provided that the presence of one mechanism does not influence the way in which other mechanisms operate. In other words, the relaxation times add as follows:

$$\frac{1}{\tau} = \frac{1}{\tau_1} + \frac{1}{\tau_2} + \dots \qquad (2.3)$$

2.3 Heat transport by free electrons in metals

The kinetic theory of heat transport 2.2 allows one to calculate the electronic thermal conductivity of a metal in a fairly straightforward manner. In the low temperature limit, the scattering of electrons is primarily through elastic processes involving impurities, which yields a temperature independent mean free path. The temperature dependence of the thermal conductivity is thus set by the electronic heat capacity, which in the Sommerfeld theory of metals takes the well-known form:

$$C_v = \frac{\pi^2}{2}\left(\frac{k_B T}{\epsilon_F}\right)nk_B \qquad (2.4)$$

The use of equation 2.2 combined with the result above yields an estimate for the electronic thermal conductivity in a metallic system:

$$\kappa_{el} = \frac{\pi^2}{6}\left(\frac{k_B T}{\epsilon_F}\right)nk_B v_F \ell \qquad (2.5)$$

The resulting expression is linear in T, and typically dominates the phonon conductivity at low temperatures. The well-defined temperature dependence of κ_{el} at low temperatures is key to separating the electronic and phononic thermal conductivities.

2.4 Charge transport in metals

In a conventional metal, with an applied electric field $\mathbf{E}$, and electrical current density $\mathbf{j}$ the DC electrical conductivity σ is defined by

$$\mathbf{J} = \sigma \mathbf{E} \tag{2.6}$$

For an electron density n, travelling along the direction set by $\mathbf{j}$ the kinetic theory of transport predicts that the magnitude of the conductivity is given by:

$$\sigma = \frac{ne^2\tau}{m} \tag{2.7}$$

Clearly, the electrical conductivity is greatly dependent on the form of τ, which is itself dependent on a myriad of potential scattering processes, but in the low temperature limit is solely determined by impurity scattering, leading to a residual resistivity that is a measure of the purity of the material.

2.5 The Wiedemann-Franz law

In the limit of elastic scattering at low temperatures, one may take the ratio of the coefficients of thermal and charge transport, which results in the famous law of Wiedemann and Franz [66]:

$$\frac{\kappa}{\sigma T} = \frac{\pi^2}{3}\left(\frac{k_B}{e}\right)^2 \equiv L_0 \tag{2.8}$$

This relationship tells us that for an arbitrary band structure, the ability of an electron to transmit heat is closely mirrored by its ability to transport charge, and the ratio of the two is the Lorenz number L_0. This is a fundamental property of conductive materials, observed to be valid in the low temperature limit in virtually all known materials, from metals to semiconductors. In superconductors, the law appears to be violated since the electrical conductivity goes to infinity while the thermal conductivity remains finite. This is however not a rigorous violation, since the charge $2e$ Cooper pairs are not heat carriers,

and transport of heat is accomplished by charge e quasiparticles, which are shorted out electrically by the condensate.

In overdoped cuprate superconductors the destruction of superconductivity by a strong magnetic field was seen to reveal a state that obeys the Wiedemann-Franz law in the $T \rightarrow 0$ limit [58], while in underdoped LSCO the results were inconclusive [7]. Testing the validity of this law in the low doped regime of the YBCO cuprate is the subject of chapter 12.

2.6 Heat transport by the lattice

In many situations the conduction of heat by vibrations of the lattice (phonons) is often quite large, and may in some cases dominate the contribution from electrons. Since the subject of this work is primarily to study the electronic heat conduction in superconductors, our goal is to correctly model the conductivity of the lattice in order to separate out electronic and phononic contributions to thermal conductivity. This task was first accomplished by Debye and cast into a more modern form by Peierls [67]. We can estimate the magnitude of this conductivity at low temperatures in an isotropic crystal using the kinetic theory formulation of Equation 2.2 [1].

$$\kappa_{ph} = \frac{1}{3} C_{ph} v_{ph} \ell_{ph} \tag{2.9}$$

In the low temperature limit the phonon heat capacity (C_{ph}) takes the well known Debye form [63]:

$$C_{ph} = \frac{\partial}{\partial T} \int \frac{d^3k}{(2\pi)^3} \frac{\hbar\omega(\mathbf{k})}{e^{\hbar\omega(\mathbf{k})/k_B T} - 1} \sim \frac{2\pi^2}{5} k_B \left(\frac{k_B T}{\hbar c} \right)^3 \tag{2.10}$$

Equation 2.10 tells us that at sufficiently low temperatures, where $T \ll \Theta_D$, the heat capacity is a cubic function of the temperature. The resulting temperature dependence of the phonon thermal conductivity is then the product of the cubic in temperature heat capacity and the temperature dependence of the various scattering mechanisms summed used Matthiessen's rule. Table 2.1 summarizes some of the physically important scattering mechanisms that contribute to the phonon relaxation time in the low temperature limit. In the regime typically accessed by our experiments ($T \ll 1K$) most of these are frozen out except the first, which sets the magnitude of κ_{phonon}.

---

[1]A more detailed treatment can be found in the books by Klemens and Berman [67, 68]

Table 2.1: Temperature dependences of τ and κ_{ph} in the low temperature limit ($T \ll \Theta_D$). Adapted from P.G. Klemens [67]

Scattering Mechanism	τ	κ_{ph}
External crystal boundaries	T^0	T^3
Grain boundaries	T^0	T^3
Stacking faults	T^2	T
Conduction electrons in metals	T^1	T^2
Dislocations (strain field)	T^1	T^2
Dislocations (core)	T^3	T^0
Point defects	T^4	T^{-1}
Umklapp processes	T^1	$T^3 e^{\theta/\alpha T}$

2.6.1 The phonon boundary scattering regime

As the temperature of a sample is cooled 1 K, many of the usual processes which scatter phonons freeze out, and thus cease to contribute significantly to the relaxation time τ. As τ increases, so to does the phonon mean free path $\ell_{ph} = v_{ph} \times \tau$. Eventually, when the temperature is lowered far enough, ℓ_{ph} grows to be limited by the physical dimensions of the crystal itself. The phonon thermal conductivity in this instance is then given by:

$$\kappa_{ph} = 1/3 C_{ph} \ell_{boundaries} \tag{2.11}$$

where $\ell_{boundaries}$ is a suitable geometric average of the crystal dimensions. For a rectangular slab of width w and thickness t we define

$$\ell_{boundaries} = 2 \times \sqrt{wt/\pi} \tag{2.12}$$

In this temperature regime, the mean free path is to first approximation temperature independent, so that the phonon thermal conductivity is determined solely by the temperature dependence of C_{ph}. For studies of samples with mobile electronic excitations one typically models the low temperature thermal conductivity as having a T linear contribution from the electrons, as discussed in section 2.3, and a T^3 contribution from the phonons:

$$\kappa = \kappa_{el} + \kappa_{ph} = AT + BT^3 \tag{2.13}$$

where A and B are constants set by the properties of the electronic and phononic excitations respectively. By plotting κ/T versus T^2 the T = 0 linear electronic term simply shows up as the y-intercept, with the slope given by the coefficient of the phonon term, B.

Clearly, if one is interested in an accurate determination of A, the linear electronic term, then one must be confident that the model describing the temperature dependence of the phonons is correct. During the course of this study we have developed an empirical model which appears to improve upon the considerations discussed above. In especially pure crystals, with exceptionally smooth surfaces, one may find a slight temperature dependence to the phonon mean free path arising from specular reflection of the phonons at the crystal boundaries.

2.6.2 Powerlaw fitting: beyond the T^3 approximation

The extension of our measurements into the highly underdoped region of the cuprate phase diagram, where the linear electronic term κ_0/T becomes very small, has led us to refine the form of equation 2.13. To motivate why this may be necessary, consider the possible scattering mechanisms available to a phonon impinging upon the surface of a crystal. The phonon may either be absorbed and re-emitted with an energy distribution given by the local temperature (diffuse scattering) or it may be reflected elastically (specular reflection). In the case of diffuse scattering, the phonon is re-radiated in a random direction resulting in a temperature independent value of ℓ_{ph} and a T^3 dependence of κ_{ph} as recognized by Casimir. [69] In studies of low temperature heat transport in diamond [68], Berman *et.al.* demonstrated that the effect of phonon specular reflections occurring with probability $1 - f$ caused the mean free path to deviate from the geometrical limit by:

$$\ell_{ph} = \ell_{geo}(2 - f)/f \tag{2.14}$$

where ℓ_{geo} is set by the dimensions of the sample itself. In the limit where no specular reflections occur, $f = 1$ and the usual mean free path is recovered, as defined in equation 2.12.

The probability of specular reflection occurring is itself dependent on the characteristic wavelength of the phonon. As the temperature of a crystal is reduced and the average phonon wavelength increases, a surface of a given roughness appears smoother, which may increase the occurrence of specular reflection. This in turn leads to a temperature
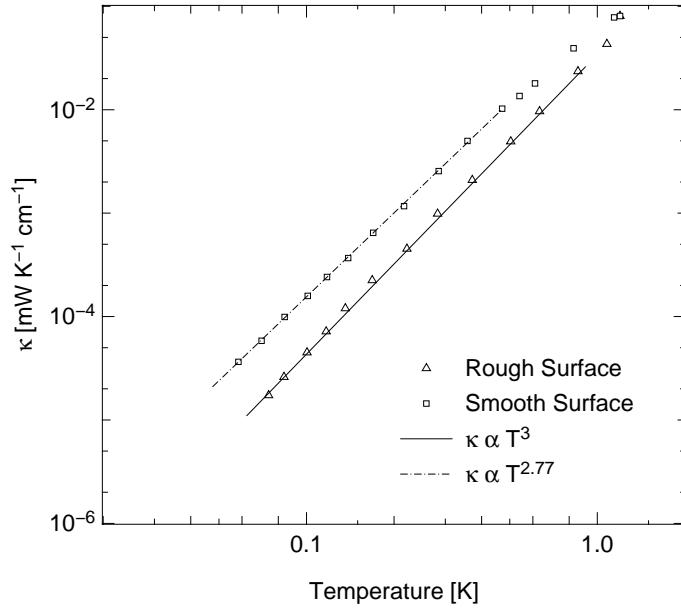
Figure 2.1: Low temperature thermal conductivity of the insulator Al_2O_3. Triangles are for a sample with a roughened surface, squares are for a sample with a flame polished smooth surface. The data is plotted as κ vs. T on a logarithmic plot. Specular reflection from sufficiently smooth surfaces may cause a deviation from the usual T^3 phonon thermal conductivity in the boundary scattering regime. Data adapted from reference [70].

dependent ℓ_{ph}. Early studies of dielectric crystals have indeed lent support to this idea. Figure 2.1 shows the effects of surface quality on the low temperature phonon conductivity in samples of sapphire (Al_2O_3) [70]. A rough surface produces the expected T^3 temperature dependence while a smooth surface results in a slightly lower power law owing to the temperature dependence of ℓ_{ph}.

Such an effect has also been observed in high-quality crystals of Si, [71] KCl and KBr, [72] LiF [73] and diamond. [74]. We indeed see evidence of this behaviour in many of our cuprate samples, manifesting itself as a gradual curvature in the low temperature part of our data when plotted as κ/T vs. T^2.

In light of this, we propose that the thermal conductivity in the boundary scattering regime is more correctly modelled as:

$$\kappa = \kappa_{el} + \kappa_{ph} = AT + BT^{\alpha} \tag{2.15}$$

with $\alpha < 3$.

Here A is the coefficient of the electronic linear term, and B the temperature-independent coefficient of the phonon term, where α is some power of temperature, typically between 2 and 3. Note that there is no fundamental reason for a single power law - it is simply
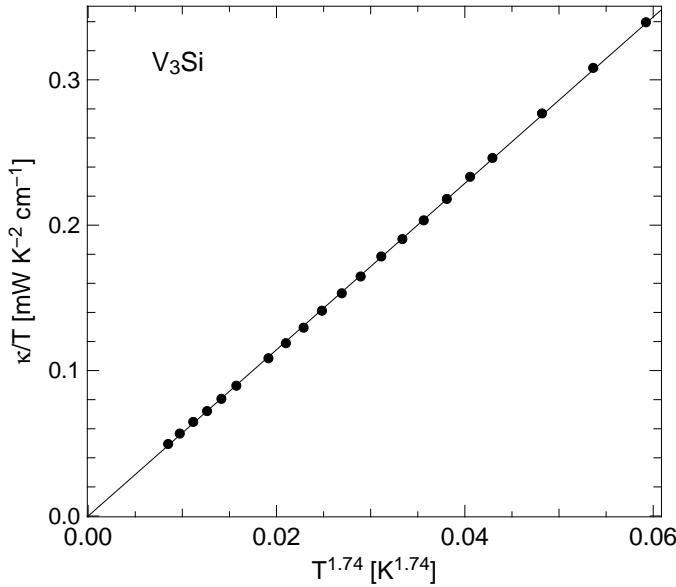
Figure 2.2: Thermal conductivity of the *s*-wave superconductor V$_3$Si. The data is plotted as $\frac{\kappa}{T}$ vs $T^{1.74}$, and the line represents a free fit to the data of the form of Eq. 9. The resulting linear term is zero: $0 \pm 1~\mu$W K^{-2} cm^{-1}, consistent with that expected for a nodeless superconductor.

an empirical result that is well supported experimentally.

In superconductors possessing an isotropic or *s*-wave gap, the absence of an electronic linear term at low temperatures reveals this effect well [2]. Plotted in figure 2.2 is thermal conductivity data for the *s*-wave superconductor V$_3$Si, [75] where the line is the result of a free fit to a simple power law as in equation 2.15. Such a procedure yields a linear term A = -0.04 $\pm$ 1 μW/K^{-2}cm^{-1}, a phonon coefficient B = 5.73 $\pm$ 0.07 mW/K$^{-(\alpha+1)}$cm^{-1}, and an exponent α = 2.74 $\pm$ 0.01. The validity of such a fitting procedure is best seen by plotting the data as in figure 2.2, with the x-axis in units of $T^{\alpha-1}$. The striking linearity of the data on this plot, and the fact that it extrapolates to zero, is good evidence for the appropriateness of this model.

It is worth stressing that the single power-law fitting procedure described here is simply an empirical approach to extrapolate the most reliable value of κ/T at $T = 0$. As a three-parameter *free* fit to the data over a temperature range typically of a decade (50 - 500 mK), it is far better than the old two-parameter *forced* fit to a $\kappa/T = a + bT^2$ form, which invariably must be limited to the very lowest temperatures (usually below 150 mK or so) and typically overestimates the value of κ_0/T. That such considerations must be applied to our samples of cuprate superconductors is a testament to the purity

---

[2]A theoretical treatment of heat transport in *s* and *d*-wave superconductors is given in chapter 3

and quality of our crystals.

3

LOW-ENERGY EXCITATIONS OF A d-WAVE SUPERCONDUCTOR

3.1 Chapter overview

The d-wave nature of the superconducting order parameter in cuprates governs all of their low temperature properties. Since the energy gap vanishes along the four nodal directions, quasiparticle excitations exist to zero energy. This is dramatically different than the s-wave case, where the fully gapped Fermi surface yields activated behaviour in low temperature experiments. In this section I review the underlying physics behind the d-wave nodal excitation spectrum, and discuss its relevance to several important physical quantities. I summarize the results in both the clean and dirty limits, and discuss the effects of applying a magnetic field. The results of this chapter are used as the foundation for interpreting much of the data discussed in later chapters.

3.2 The nodal excitation spectrum of a d-wave superconductor

There is no longer any reasonable doubt that the superconducting gap in cuprate superconductors is of the $d_{x^2-y^2}$ form [76, 20], which may be expressed as:

$$\Delta(k) = \Delta_0(cosk_xa - cosk_ya) \tag{3.1}$$

Here k_x and k_y are reciprocal lattice vectors in the x and y directions, a is the (tetragonal) lattice parameter, and Δ_0 is the maximum of the order parameter. Defining ϕ as the in-plane angle in reciprocal space that is equal to zero along the k_x direction allows us to simplify this expression. Equation 3.1 becomes $\Delta(\phi) = \Delta_0 cos2\phi$, which is plotted in the left hand panel of figure 3.1. The gap vanishes completely along the $\phi = (2n + 1)\,\pi/4$ directions, and reaches a maximum at $\phi = n\pi/2$, where $n =$0,1,2.... In the LSCO and YBCO superconductors the lobes of the d-wave order parameter are situated along the
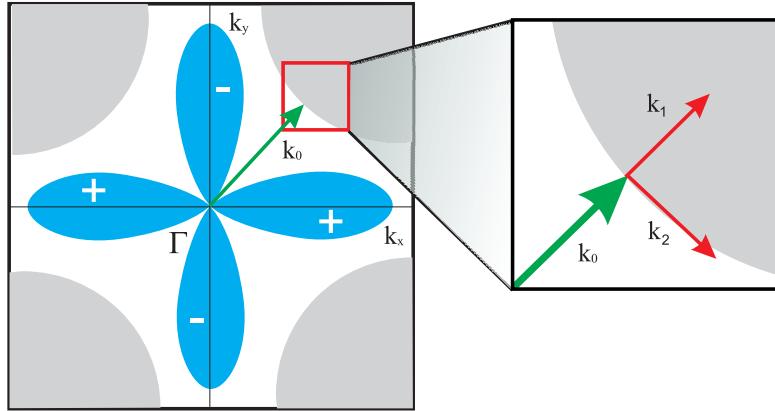
Figure 3.1: **Left** : The *d*-wave order parameter and cylindrical Fermi surface of the cuprate superconductor. **Right** : Change of basic vectors from k_x and k_y to those centered around the nodal point, a useful basis for describing the low energy quasiparticle excitations.

Cu-O bond directions, while the nodes are along the diagonal.

In a simple tight-binding approximation the Fermi surface of a tetragonal high temperature superconductor may be expressed as:

$$\epsilon_k = -2t(cosk_xa + cosk_ya) - \mu \tag{3.2}$$

where $2t$ is the in-plane hopping integral and μ us the chemical potential. The energy spectrum of quasiparticle excitations is then calculated from the sum of the gap and the Fermi surface energies added in quadrature - $E(k) = \sqrt{\epsilon_k^2 + \Delta_k^2}$. If we restrict ourselves to very low energies we may linearize this spectrum about the nodes. It is convenient in this respect to switch basis vectors from those collinear with the reciprocal lattice vectors k_x and k_y to those whose origin is centered at the node:

$$k_1 = \frac{(k_x + k_y)}{\sqrt{2}} - |k_0| \tag{3.3}$$

$$k_2 = \frac{(k_x - k_y)}{\sqrt{2}} \tag{3.4}$$

with k_1 perpendicular and k_2 tangential to the Fermi surface respectively. Linearizing equations 3.1 and 3.2 about the nodal points $k_1 = k_2 = 0$ gives:

$$\epsilon(k) \simeq k_1\frac{\delta\epsilon}{\delta\mathbf{k}} = \hbar k_1 v_F; \quad v_F = \hbar\sqrt{2}ta\ sin(k_0a/\sqrt{2}) \tag{3.5}$$

$$\Delta(k) \simeq k_2\frac{\delta\Delta}{\delta\mathbf{k}} = \hbar k_2 v_2; \quad v_2 = \hbar 2\sqrt{2}a\Delta_0\ sin(k_0a) \tag{3.6}$$
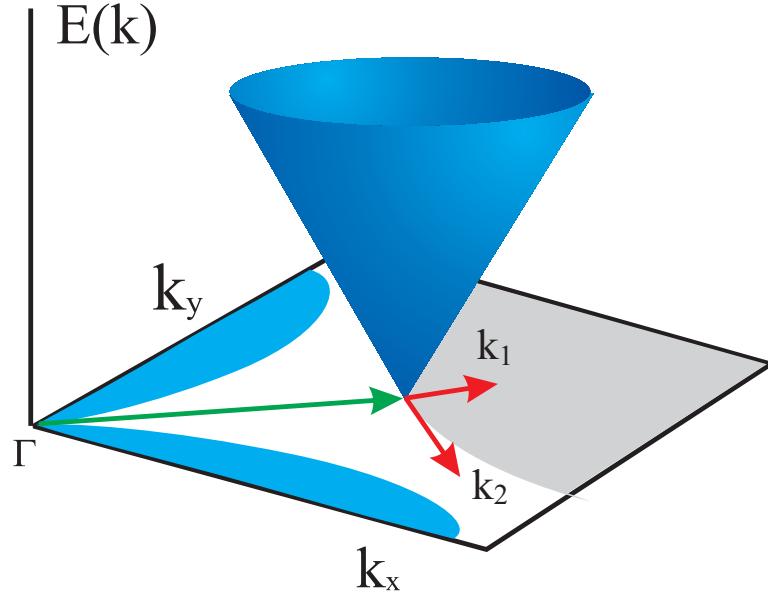
Figure 3.2: Dirac like excitation spectrum of nodal quasiparticles in a *d*-wave superconductor.

The parameters v_F and v_2 refer here to quasiparticle velocities perpendicular and parallel to the Fermi surface respectively. The excitation spectrum near the node can then be written in the following form:

$$E(k) = \sqrt{(v_F k_1)^2 + (v_2 k_2)^2} \tag{3.7}$$

The excitation spectrum is colloquially known as a Dirac spectrum, or Dirac cone when it is plotted as $E(k)$ along the axis perpendicular to the plane. The relative sizes of the of the two velocities determine the anisotropy of the cone, plotted in figure 3.2

The persistence of excitations having the spectrum of 3.7 governs the low temperature physical properties of *d*-wave superconductors. The density of states from such a spectrum is linear in energy, and is determined by the fundamental quasiparticle parameters v_F and v_2:

$$N(E) = \left(\frac{2}{\pi \hbar^2} \right) \left(\frac{1}{v_F v_2} \right) E \tag{3.8}$$

In theory $N(E)$ from equation 3.8 can be used as the basis for calculating most physical properties, it leads for instance to an electronic specific heat $C_{el} \propto T^2$. We have however at this point neglected to incorporate the effects of elastic scattering from impurities, which modifies the energy dependence of the density of states significantly. We can view equation 3.8 as the clean limit expression for $N(E)$, valid when the effects of impurity
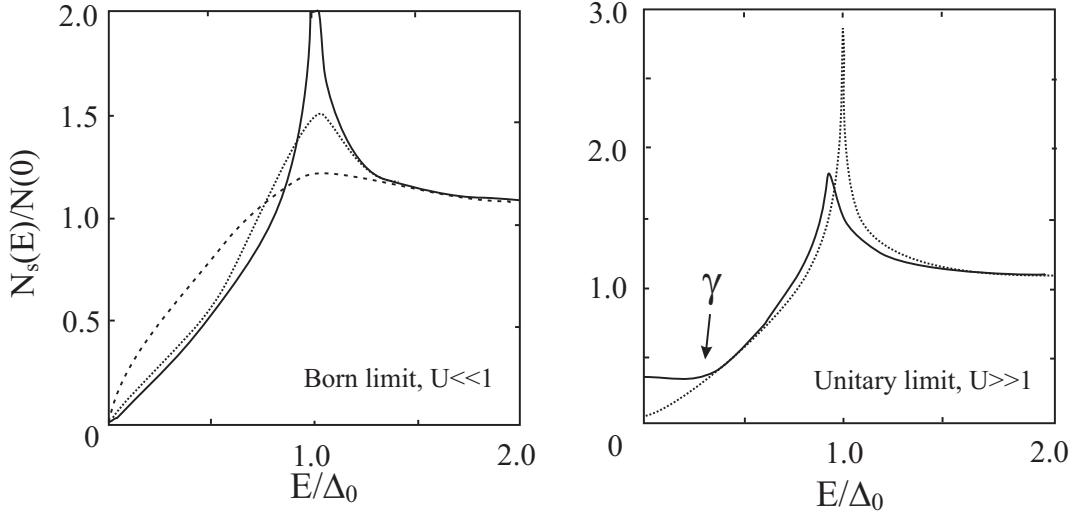
Figure 3.3: **Left** : The density of states normalized by N_s as a function of energy in the Born scattering limit. Curves are for scattering rate $\Gamma/\Delta = 0$ (solid line), 0.05 (dotted line) 0.2 (dashed line) [77]. **Right** : The unitary limit density of states, with Γ/Δ=0.001 (dotted line) and 0.1 (solid line). γ denotes the energy scale at which the density of states becomes constant in energy [78].

scattering are negligible.

3.3 Impurities effects in unconventional superconductors

In standard scattering theory the quasiparticle scattering rate Γ is calculated through the use of Fermi's golden rule:

$$\Gamma = \frac{2}{\pi\hbar} n_{imp} |<k|U|k'>|^2 N_n(0) \tag{3.9}$$

where n_{imp} is the impurity concentration and $N_n(0)$ is the density of states at the Fermi level. U is the scattering strength, in the weak (Born) limit $U \ll 1$ and in the strong (unitary) limit $U \gg 1$. The effects of scattering in metals, semiconductors and superconductors are usually considered within the framework of the self consistent T-matrix approximation (SCTMA), a perturbative method [11]. The modification of the density of states is strongly dependent on the scattering strength, as shown in figure 3.3 adapted from Puchkaryov and Maki [77] and Preosti *et.al.* [78].

In the Born limit, the slope of the density of states is modified at low energies as the scattering rate is increased, but $N(E)$ retains some energy dependence even to very low energies. In the unitary limit, below an energy scale γ that is determined by the scattering rate Γ, the density of states becomes constant in energy. For experiments that

probe energies lower than γ, also called the impurity bandwidth, the modified density of states is seen to dramatically influence quasiparticle behaviour.

The existence of a regime of constant $N(E)$ is understood to arise from the breaking of Cooper pairs by impurity scattering, and the resulting formation of bound states [79]. The strength of the scattering potential U governs the formation of these bound states into bands, and determines the scale of γ [80]:

$$\gamma = 4\Delta_0 exp(-\pi\Delta_0/2\Gamma_n) \quad U \ll 1, (Born) \tag{3.10}$$

$$\gamma = 0.63\sqrt{\Delta_0\Gamma_N} \quad U \gg 1, (unitary) \tag{3.11}$$

where Γ_N is the normal state scattering rate. Of these scenarios, the general consensus has been that in the cuprate superconductors scattering is best described as being close to the unitary limit, evidenced by a strong suppression of T_c with Zn impurity doping and finite residual density of states density of states [81, 82, 80, 83, 84, 85]. The same has been found to be true in unconventional superconductors with more complicated gap topologies, such as UPt$_3$ [86]. Much of the discussion of the results in this work will focus on low and zero temperature results where $k_B T \ll \gamma$, and γ is the dominant energy scale. We define this as the "dirty" limit, and the case where $k_B T \gg \gamma$ as the corresponding "clean" limit.

3.3.1   Universal conductivity

One of the most remarkable consequences of the dirty limit is the existence of universal transport. In 1993 Patrick Lee [87] noted that the nodal quasiparticles induced by impurity scattering were scattered in such a way that the decrease in the quasiparticle lifetime, τ, was exactly compensated for by the growth in the low energy density of states as impurity concentration was increased. The conductivity in the zero frequency limit in this "universal" regime displays no dependence on scattering rate:

$$\sigma_{00} = \frac{e^2}{2\pi\hbar}\frac{2}{\pi}\left(\frac{n}{d}\right)\left(\frac{v_F}{v_2}\right) \tag{3.12}$$

where n/d is the number of CuO$_2$ planes per unit cell, and v_F and v_2 are the quasiparticle parameters introduced in equations 3.5 and 3.15.

Durst and Lee [59] later considered the effects of vertex and Fermi liquid corrections to the universal form of 3.12. Fermi liquid corrections arise from the intrinsic interactions

between the quasiparticles excited from the condensate, while vertex corrections reflect the fact that back scattering is more effective at degrading a charge current than forward scattering. With these additions 3.12 becomes:

$$\sigma_{00} = \frac{e^2}{2\pi\hbar} \frac{2}{\pi} \left(\frac{n}{d}\right) \left(\frac{v_F}{v_2}\right) \beta_{VC} \alpha_{FL}^2 \tag{3.13}$$

Thermal transport in the universal limit was studied originally by Graf *et.al.* [88] and later by Durst and Lee [59]. For transport as $T \to 0$ in the dirty limit, the thermal conductivity has a term linear in temperature governed by v_F and v_2:

$$\frac{\kappa_0}{T} = \frac{k_B^2}{3\hbar} \left(\frac{n}{d}\right) \left(\frac{v_F}{v_2} + \frac{v_2}{v_F}\right) \tag{3.14}$$

The parameter v_2 is simply the slope of the gap at the node, showing that the residual linear term can be used to provide information about the superconducting gap itself:

$$\mathbf{v_2} = \frac{1}{\hbar} \frac{d\Delta}{d\mathbf{k}}\Big|_{node} = \frac{1}{\hbar k_F} \frac{d\Delta}{d\phi}\Big|_{node} = v_2 \hat{\mathbf{k}}_2 \tag{3.15}$$

where k_F is the Fermi wavevector at the nodal position.

These are remarkably simple formulae, which provide a direct access to the parameters that govern low-energy phenomena in a *d*-wave superconductor. Not only is the thermal conductivity universal with respect to impurity concentration, but is robust to vertex and Fermi-liquid corrections, unlike σ. These features make thermal conductivity an extremely useful probe of a *d*-wave superconductor. The universal limit in thermal conductivity was first established in YBCO by Taillefer *et.al.* [60], which serves as a confirmation that the basic formalism derived by Graf, Durst, Lee and others is valid. The formalism was shown to work remarkably well in optimally doped BSCCO by Chiao *et.al.* [89]. Using the residual linear term in thermal conductivity, they estimated the quasiparticle anisotropy ratio to be 19, which is in perfect agreement with a v_F/v_2 of 20 from ARPES measurements by Mesot *et.al.* [90].

3.3.2 Microwave penetration depth

Measurements of the microwave penetration depth have been used from early on to study the quasiparticle excitations in superconductors. At low T, the temperature dependence of the penetration depth reveals the temperature dependence of the normal fluid density, as the superfluid is depleted by thermal activation of quasiparticles:

$$\rho_S(T) = \rho_S(0) - \rho_N(T) = \frac{mc^2}{\pi e^2 \lambda^2(T)} \tag{3.16}$$

In *s*-wave superconductors the normal fluid density is expected to grow in an activated manner, but in a nodal superconductor it is expected to grow linearly with temperature [59]:

$$\frac{\rho_N(T)}{m} = \frac{2ln2}{\pi} \frac{k_B}{\hbar^2} \frac{n}{d} \alpha^2 \left(\frac{v_F}{v_2}\right) T \tag{3.17}$$

Used in conjunction with thermal conductivity measurements, which directly probe v_F/v_2 the value of the Fermi-liquid factor α_2 may be revealed, as demonstrated in chapter 8.

3.3.3 Beyond the universal limit

For a sufficiently large scattering rate Equation 3.14 is expected to break down, as the superconducting order parameter is suppressed to zero by the pair breaking effects of impurity scattering. Sun and Maki [91] have shown that outside of the universal regime the thermal conductivity should vary as in figure 3.4 where κ is shown normalized to the zero disorder limit and plotted as a function of Γ/Γ_C (where Γ_C is the critical scattering rate needed to suppress superconductivity altogether).
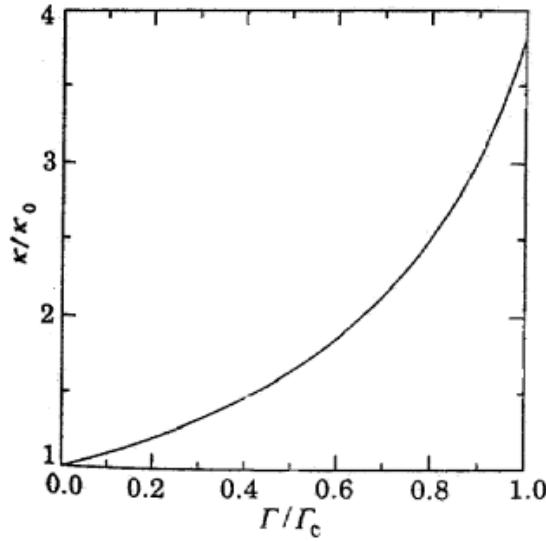
Figure 3.4: Low-temperature quasiparticle thermal conductivity in the high disorder limit, adapted from Sun and Maki. The data is plotted normalized to the normal state limit of κ, versus the scattering rate Γ [91].

Additional corrections to the universal limit are obtained at finite temperatures. Graf *et.al.* [88] have shown that the leading order correction to κ/T is:

$$\frac{\kappa_0}{T} = \frac{k_B^2}{3\hbar}\left(\frac{n}{d}\right)\left(\frac{v_F}{v_2} + \frac{v_2}{v_F}\right)\left(1 + \frac{7\pi^2}{15}\frac{a^2 k_B^2 T^2}{\gamma_0^2}\right) \qquad (3.18)$$

where the constant a is highly dependent on the phase shift (strength) of the impurity scattering. In the unitary limit a is 1/2, while in the Born limit $a = (\pi v_2/4\Gamma_N)$ where Γ_N is the normal state scattering rate. Such finite temperature corrections have been observed in our work, as we shall see in chapter 9.

3.4 Thermal transport in a magnetic field

In an extreme type-II superconductor like the cuprates, $\kappa = \lambda_0/\epsilon_0 \sim 100$ and a magnetic field penetrates the material in the form of long tubes of flux. The vortices typically have core radii of $\epsilon \sim 15$ Å and circulating currents that decay over length scales on the order of $\lambda_0 \sim 1500$ Å. The quasiparticle excitations in the mixed state are typically of two origins - those arising from bound states within the normal vortex cores, and those arising from bulk excitations with the superconductor coupled to the swirling supercurrents.

3.4.1 $\kappa(H,T)$: s-wave case

The suppression of the order parameter in the vortex cores of a type-II superconductor creates a localization potential that can create bound states. Known as Caroli-de Gennes bound states, the energy spacing of this spectrum is determined by vortex radius $E_{spacing} \sim \hbar/m\epsilon^2$, in analogy to the particle in a box scenario of elementary quantum mechanics. Such states were first observed directly with STM [92, 93], and the contribution to specific heat in the range where $k_B T \gg E_{spacing}$ is [94]:

$$C_{cores}(T,H) = \gamma_N T(H/H_{c2}) \qquad (3.19)$$

where γ_N is the normal state electronic specific heat. If the separation between the vortex cores is sufficiently large, these states remain localized and are thus unable to contribute to heat transport. When the field is increased the intervortex separation is reduced, and tunnelling between adjacent vortices causes some delocalization. This contribution is expected to grow exponentially with ratio of the vortex spacing to the vortex core size, such that $\kappa/T \propto exp(-\alpha\sqrt{H_{c2}/H})$ where α is a constant [75]. In order to contrast this behaviour with the *d*-wave case in this next section, the field dependence of the electronic
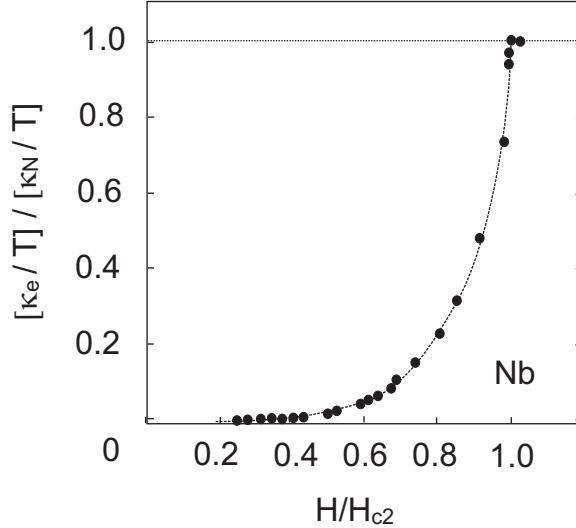
Figure 3.5: Low-temperature electronic thermal conductivity as a function of field in the elemental type II superconductor Nb, adapted from [95]. κ is normalized by the normal state value, reached when $H > H_c$.

thermal conductivity at low temperatures ($T=0.2T_c$) is shown for the elemental type-II s-wave superconductor Nb in figure 3.5 [95].

3.4.2 $\kappa(H,T)$: d-wave case

The nodal structure of the order parameter in a d-wave superconductor makes the effects of a magnetic field markedly different than that of the s-wave case. Volovik found that in these materials the contribution from overlapping bound states associated with the cores in an s-wave superconductor are dominated by extended states from the superconducting bulk [96]. Volovik's model considered the effects of swirling supercurrents on the quasiparticle excitation spectrum, and predicted the excitation energy would be take the form $E(k, A) = E(k)$ - $ev_k \cdot$ **A** where v_k is the normal state velocity and **A** is the vector potential. The effect of the supercurrents can thus be thought of as a Doppler shift of energies, and in the case of nodal quasiparticles the basic Dirac form is preserved, shifted in energy by an amount $ev_k \cdot$ **A**. This energy shift is calculated by integrating over a vortex lattice unit cell of lattice parameter a:

$$E_H = e < v_k \cdot \mathbf{A} >= \frac{1}{R^2} \int r v_F \cdot \mathbf{A} dr = a\hbar \left(\frac{2}{\pi}\right) v_F \sqrt{\frac{H}{\phi_0}} \tag{3.20}$$

where a is 0.5(0.465) for a square (triangular) vortex lattice respectively [11]. In fully gapped superconductors, this energy is typically very small compared to Δ_0 but close to

the vortex cores in nodal superconductors the Doppler shift energy is comparable to the gap, and population of extended states by field is expected.

How these newly populated states contribute to transport is highly dependent on the magnitudes of three competing energy scales: the Doppler shift energy (E_H) the impurity bandwidth γ and the thermal energy $k_B T$. In the "clean" regime, where the Doppler shift energy dominates both $k_B T$ and the impurity bandwidth such that $E_H \gg k_B T \gg \gamma$ the contribution to thermal conductivity is expected to be linearly dependent on temperature, and dependent on $\sqrt{H}$. When the thermal energy dominates such that $k_B T \gg E_H \gg \gamma$ the thermal conductivity is expected to be the same as the zero field clean limit case, $\kappa \propto T^2$ with a field dependent correction factor. In between these two regimes scaling laws are expected in the specific heat [97], with $C_{el} \propto F(x)T$ with $x = \sqrt{\frac{H_{c2}}{H}}\frac{T}{T_c}$. Experimental verification for the Volovik model was found in studies of the specific heat [98, 99, 100, 101], where a $\sqrt{H}$ dependence of the linear electronic term on field was observed.

Kübert and Hirschfeld [102] calculated the behaviour of the thermal conductivity in the "dirty" limit, where impurity scattering is the principal energy scale and $\gamma \gg E_H, k_B T$. In the geometry where $\mathbf{J} \perp c$ and $H \parallel c$ at low temperatures:

$$\frac{\kappa(0, H)}{T} = \frac{\kappa_0}{T}\frac{\rho^2}{\rho\sqrt{1 + \rho^2} - sinh^{-1}(\rho)} \tag{3.21}$$

where the effects of vortex scattering have been neglected. The parameter ρ is essentially the ratio of the two relevant energies - the Doppler shift E_H, and γ and the form it takes is dependent on which energy scale dominates. In the regime where $E_H < \gamma$ and assuming unitary scattering, ρ is calculated to be [102]:

$$\rho = \sqrt{6/\pi}\gamma/E_H \tag{3.22}$$

If the Doppler shift energy is instead the dominant scale, such that $E_H > \gamma$, then ρ becomes:

$$\rho = \frac{8\Gamma H_{c2}}{(\pi^2 a^2 \Delta_0 H)^{0.5}} \tag{3.23}$$

where Γ is the normal state scattering rate, a is the vortex lattice constant and Δ_0 is the superconducting gap maximum. This model was found to give a good quantitative description of the evolution of the residual linear term with field in the dirty limit, in both pure and Zn-doped YBCO as seen by Chiao *et.al.* [61].

4

EXPERIMENTAL TECHNIQUES

4.1 Chapter overview

The measurement of thermal conductivity at temperatures as low as 40 mK and in applied fields as large as 13 Tesla requires a significant amount of expertise in cryogenic infrastructure. A great deal of careful planning was necessary to design reliable probes and mounts to operate in this challenging environment, work that has been shared by the numerous postdocs and graduate students that have passed through our group. The following sections describe our two principal measurement systems: a ^4He dip probe capable of temperatures as low as 1.5 K, and a Kelvinox 300 dilution refrigerator capable of continuous operation at temperatures down to 40 mK. In this chapter I provide a comprehensive overview of our technique and our thermal conductivity mounts, with emphasis on the analysis of possible sources of heat losses and experimental errors. Further information on low temperature techniques in general may be found in reference [103].

In the last section of this chapter the experimental setup and techniques for measurements of resistivity in pulsed fields is discussed. A series of such high field measurements was performed at the Laboratoire National des Champs Magnétiques Pulsés, Toulouse, France.

4.2 Cryogenic inserts

4.2.1 ^4He dip probe

For temperatures above 1 K, resistivity and thermal conductivity measurements were performed on a custom built ^4He dip probe capable of operating in the 1.5 K - 150 K temperature range. The samples were mounted on a sample stage affixed to the bottom of a 1 K pot, and were enclosed in a vacuum can typically pumped to p $\sim 1 \times 10^{-6}$ Torr by a turbo pump. The pot was cooled by continual pumping with a rotary pump. Leads

to the mount were made mainly of resistive alloys such as manganin and constantan and are thermalized around posts at various points in the system to minimize the heat conducted through the leads from room temperature. Resistivity curves were typically obtained by pumping out the vacuum can and immersing the probe in Helium, taking measurements as the sample slowly cooled from room temperature. The key assumption is that the sample and principal thermometer are isothermal during cool down.

Thermal conductivity measurements as a function of temperature were made by sweeping the base temperature upwards and allowing sufficient time for the sample temperature to stabilize at each point. By controlling the flow of helium through the 1K pot, it was possible to obtain temperatures as low as 1.4 K in our apparatus, with a stability of $\pm$ 10 mK. A detailed description of the construction of this probe can be found in the thesis of Etienne Boaknin [104].

4.2.2   Dilution refrigerator

To access temperatures below 1 K we use a commercially built Oxford Kelvinox 300 dilution refrigerator, The fridge was inserted into a custom built 13/15 Tesla superconducting magnet from Oxford instruments, which had a field compensated zone around the mixing chamber to eliminate any effects of magnetoresistance on our primary thermometry.

In a dilution fridge, cooling is achieved by using the unique properties of mixtures of two isotopes of Helium, ^4He and ^3He [105]. For concentrations of less than about 60% ^3He, cooling below the so-called "lambda line" brings the system into a phase characterized by a dilute Fermi liquid of ^3He in a superfluid of ^4He. Further cooling sees the system phase separate, with the lighter ^3He forming a layer on top of the more dense ^4He, akin to a mixture of oil and water. From a technological standpoint, dilution refrigerator technology exploits the fact that there exists a finite solubility of ^3He in ^4He as $T \rightarrow 0$.

Operation of the fridge unit is achieved by submersing it in a ^4He bath, and cooling the 1 K pot by pumping. $^3He/^4He$ mixture is allowed to condense inside the unit, and when it is sufficiently cold it phase separates, with the phase boundary lying within the mixing chamber. Pumps are then connected to the still pumping line, which preferentially removes ^3He from the still since it has a vapour pressure some two orders of magnitude greater than ^4He at the same temperature. This sets up a concentration gradient in the mixing chamber, causing ^3He from the upper part of the mixing chamber to cross the phase boundary and enter the dilute phase of ^3He dissolved in ^4He. The ^3He that has
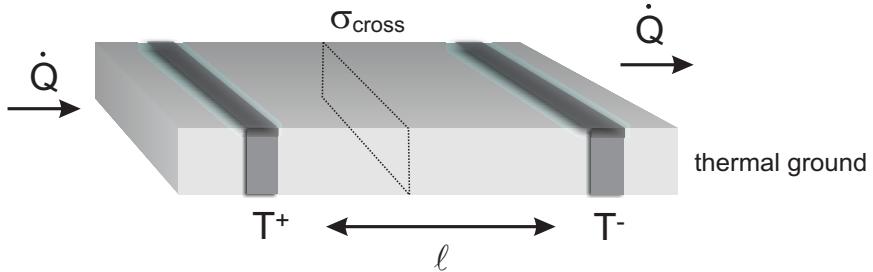
Figure 4.1: Schematic diagram depicting the one heater two thermometer method of thermal conductivity measurement. The heat flows in through one face of the crystal to thermal ground, and the resulting thermal gradient is measure at two thermometers denoted by T^+ and T^-.

been pumped out is then allowed to cool and re-enter the mixing chamber through the high impedance condenser line. The process is continuous, and the fridge can stay cold for durations on the order of several weeks or months.

The cooling power of this process can be estimated by noting that the heat absorbed from the surroundings by n moles per second of ^3He crossing the phase boundary is simply:

$$\frac{dQ}{dt} = \frac{dn}{dt}T(S_{dilute}(T) - S_{concentrated}(T)) \tag{4.1}$$

where S refers to the molar enthalpies of the ^3He in the dilute and concentrated phases. Treating the ^3He as a simple Fermi gas and calculating the enthalpies of the phases [33]

yields $dQ/dt = 84dn/dtT^2$ Watts for T < 100 mK. In the Kelvinox 300 used in our laboratory, this cooling power is as large as 250 μW at 50 mK. This is sufficiently great so that the heat load from the 50 leads that run from the experiment to room temperature does not affect the temperature of the fridge. While circulating, stability of the unit is typically on the order of $\pm$ 0.1mK at 50 mK.

4.3 Measurement of thermal conductivity

4.3.1 Basic theory

All of our thermal conductivity measurements were performed with a two heater steady state technique. The basic principle of the measurement is very similar to a standard four wire resistivity measurement, and is shown schematically in figure 4.1. The sample is affixed on one end with conductive paste to thermal ground, and heat ($\dot{Q}$) is introduced into the opposite end of the crystal, setting up a thermal gradient ΔT. The temperature of the crystal is sampled at two locations on the crystal, separated by a length ℓ. The

temperature difference $\Delta T = T_{hot}$ - T_{cold} and the input heat current are used to calculate the thermal conductivity κ of the sample:

$$\kappa = \frac{\dot{Q}}{\Delta T} \frac{\ell}{\sigma_{cross}} \tag{4.2}$$

Here σ_{cross} is the cross sectional area of the crystal, which for a uniform platelet is just the width (w) × thickness (t). The error in our measurement is typically dominated by the error in determining the geometric factor, on the order of 10 % - 20 %. This error is usually set by the difficulty in defining the separation of the voltage pads, as measured under an optical microscope.

4.3.2 *Thermal conductivity mounts*

The mounts used in our measurement are of slightly different designs depending on the temperature range of use. Our high temperature thermal conductivity mounts for use in the ^4He probe are described in detail elsewhere [104]. Here we will concentrate on the design of the mounts used in low temperature dilution fridge measurements, with which the majority of the κ data presented in this Thesis was taken. The high temperature mounts are similar in design, but slightly different geometries and materials are used in construction.

A schematic diagram of one of these mounts is shown in Figure 4.2. Two uncalibrated RuO_2 chip resistors are affixed to the sample with conductive silver wires, and the sample is mounted on a large Copper block firmly bolted to the Copper tail, which is isothermal with the mixing chamber. Heat is provided by passing a small current (I) through a strain gauge, which has a temperature independent resistance R of approximately 10 $k\Omega$. By measuring the current to the heater, one may estimate the amount of heat provided to the sample via Joule heating; $Q = I^2 R$.

In order to obtain as accurate data as possible, we recalibrate the RuO_2 sensors during *each* run. The basic methodology of our measurement is as follows. The dilution fridge is set to the desired temperature, then allowed to sit for a period of time until the thermometers on the sample no longer change with time. A measurement of the resistances of the thermometers is then made with no heat applied, and is compared to the principal Germanium thermometer on the mixing chamber, which is in a field compensated zone in the magnet. The Ge resistor itself (model GR-200A-30), was manufactured and independently calibrated by Lakeshore instruments down to 50 mK. Heat is then applied to the sample, the thermometers are allowed to stabilize again, and a measurement of
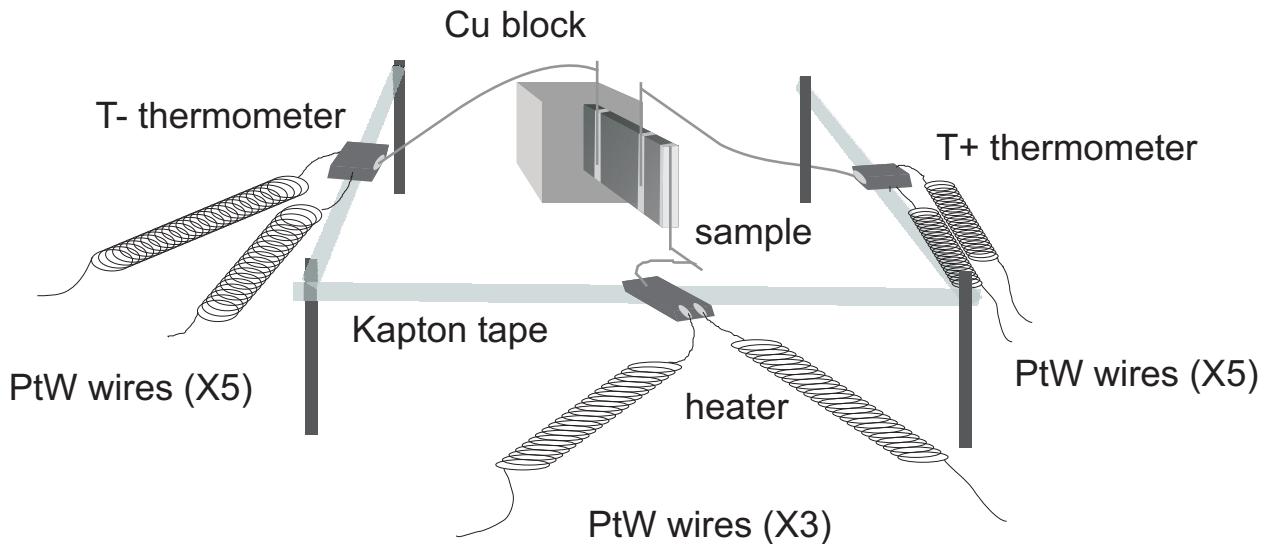
Figure 4.2: A Schematic diagram of a mount used in our measurements of thermal conductivity. The geometry is dubbed "the washing line configuration" since the thermometers and heater are suspended by $7\mu m$ thick Kapton tape strung up between Vespel posts. Heat is provided by passing current through a resistive strain gauge, and temperature is recorded by measuring the resistance of RuO_2 chips.

their resistance is made. By repeating this many times, we then have a calibration for the thermometer resistance versus temperature from the heat off points, which we can use to estimate the thermometer temperatures with the heat on. This method minimizes uncertainties due to thermometer calibrations, and introduces at most a 1% error into our measurements.

4.3.3 Electronics

The measurement of the resistivity of the RuO_2 sensors is accomplished using a Linear Research LR-700 resistance bridge operating at 16 Hz. The measurement current was chosen to be as small as possible to eliminate any self-heating of the thermometers. Typical currents were in the 1 - 3 nA range, which had negligible impact on the thermometer temperature at 40 mK. Prior to June 2002 thermometer resistances were measured using an Stanford research SR-830 series lockin amplifier, which was later abandoned due to the multiplexing capabilities of the LR-700. All sample resistivity measurements were made using either the LR700 or SR830 devices.

Heat was provided to the strain gauge with ultra high stability, low noise Keithley 220 and 224 current sources, which allowed incremental changes in the heater current as small as 5 nA. The overall fridge temperature control was maintained with a Lakeshore

model 370 AC temperature controller, with very high long term stability.

All leads to the tail were passed through a home made filter box consisting of low pass filters to eliminate any heating from rF frequency radiation. The entire system is automated to run under Labview$^{\text{TM}}$, and the computer is optically isolated from the measurement system with fibre optic cables to eliminate electrical coupling to the experiment. In addition, the entire magnet cryostat and electronics are enclosed in a Faraday cage to further screen the measurement.

4.3.4 Analysis of heat losses

One of essential design requirements of a thermal conductivity mount is to ensure that all of the heat which is generated by the heater travels through the sample to thermal ground, and is not lost through other routes. Heat losses in the thermal circuit are generally of three types. If the heater temperature is much higher than the base temperature, heat may be lost via radiation. If there is residual exchange gas within the sample chamber, heat may be conducted away from the heater through the gas itself. Finally, if the thermal impedance of the sample plus contacts is too high, heat may travel down the resistive electrical leads of the thermometers, or along the Kapton support structure. We briefly look at each of these mechanisms, and obtain estimates for the amount of heat lost by each. This exercise gives added confidence in the reliability of our technique, and the robustness of the design of our thermal conductivity mounts.

Radiative heat losses

Heat transfer between two parallel plates by radiation in a near vacuum is treated by the Planck law. Heat losses could occur via this mechanism if heat from the heater is radiated away to the base of the tail. For two plates of surface area A at temperatures T_2 and T_1 the rate of heat transfer is [106]:

$$\dot{Q}[Watt] \sim \sigma A(T_2^4 - T_1^4)\frac{\epsilon_1 \epsilon_2}{\epsilon_1 + \epsilon_2 \epsilon_1 \epsilon_2} \tag{4.3}$$

where σ is the Stefan-Boltzmann constant $\sigma = 5.67 \times 10^{-8} Wm^{-2}K^{-4}$, ϵ_1 and ϵ_2 are the emmissivity of the plates, and are equal to one for a black body. A typical heater temperature would be approximately 55 mK when the fridge is at 50 mK. For a heater surface are of 1 cm^2 then $\dot{Q} \sim = 1.6 \times 10^{-15}$ W per square cm of tail, where we have assumed $\epsilon_1 = \epsilon_2 = 1$. Thus the heat transfer from this mechanism is negligible. In

the ^4He probe this effect is much larger due to larger thermal gradients, but has been calculated to have a small impact on our measurements [104].

Heat Losses through exchange gas

At the low temperatures and pressures typically found in the sample space of our cryostats the mean free path of a residual gas molecule is much larger than the dimensions of the cryostat itself (the Knudsen condition). In this extreme environment Corruccini [107, 33] showed that the heat transfer rate between two parallel plates of surface area A with a temperature gradient ΔT between them is given by:

$$\dot{Q}[Watt] \sim 0.02aA[cm^2]p[mbar]\Delta T[K] \tag{4.4}$$

where a is a coefficient dependent on the adhesiveness of gas on the walls of the IVC, a = 1 for a very rough surface and 0.025 for a smooth metallic surface. For IVC walls at 4K with a vacuum of 1×10^{-7} mbar and a sample surface area of 1 mm^2 this works out to be on the order of 10^{-12} W per mm^2 of IVC can. It is clear that these considerations do not affect us much in the fridge. In the ^4He probe however, higher IVC pressures and larger ΔT ($\sim$ 100K) can begin to affect the measurement at high temperatures. For this reason, we truncate our dipper measurements at 150 K, the point at which we can still be relatively sure that our measurement is unaffected [1].

Heat Losses through the mount

Heat losses through conduction via the mount structure are potentially from two paths: the leads to the thermometers and the Kapton supporting strips. The leads to the heater and thermometers are made of coiled PtW wires (model 479 from Sigmund Cohn Corporation) with resistances of approximately 150 Ω each. For later experiments on highly underdoped cuprates some of the leads were replaced with 12 μm PtW wires with resistances of 500 Ω or greater.

The resistance of the RuO_2 thermometers are measured using a four point technique, so there are two current and two voltage leads for each. There are also two leads to the heater, and an additional three leads for electrical resistivity measurements, for a total of 13 electrical leads in the thermal circuit. Each of these leads contains a coiled segment of resistive PtW wire which has a residual resistance of approximately 150 Ω, acting to

---

[1]For a detailed treatment of heat losses in the ^4He probe see Appendix A of the thesis of Etienne Boaknin [104]
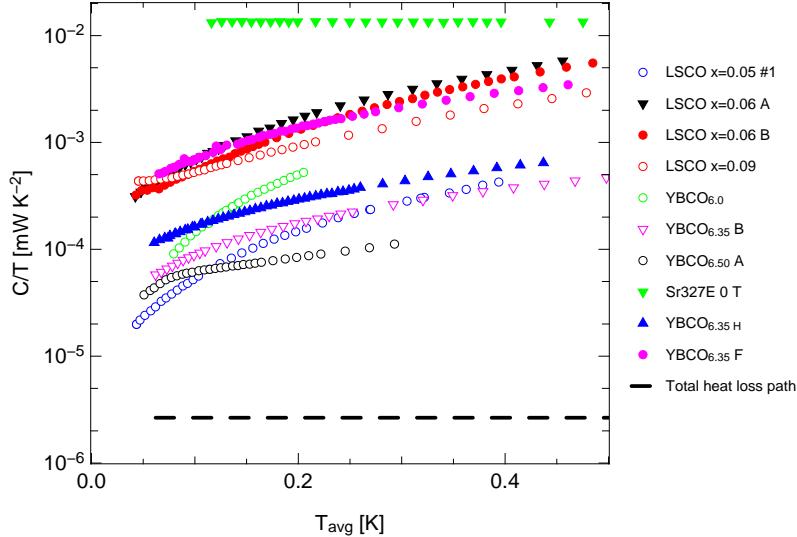
Figure 4.3: Conductance of selected samples divided by temperature, shown over the range in which the dilution fridge experiments are typically performed. The conductance of the Kapton strips and PtW wires used in the mount construction is plotted using the estimates of Kapton conductance from Radebaugh [108]. In each of these cases shown, the conductance of the heat loss path is much lower than that of the sample, meaning heat losses are negligible.

prevent the flow of heat from the sample to thermal ground. Using the Wiedemann-Franz law with $L_0 = 2.45 \times 10^{-8} W\Omega/K^2$ we find that the thermal conductance of each coil is $\kappa = L_0 T/\rho = 1.6 \times 10^{-7} mW/K$ T, provided T < 1 K.

The "washing line" supports for the thermometers are made of 7 μm thick strips of a resistive polyamide film (Kapton HN30 from Dupont), which are anchored to the mount on Vespel posts with Ge varnish. The Kapton was cut into 3 strips of length $\sim$2 cm and width $\sim$0.1 mm, with the thermometers and heater lying in the middle. The thermal conductivity of the Kapton films has been investigated at cryogenic temperature by a number of authors [109, 110, 111, 108].

Using the average of Barucci and Radebaugh's values for Kapton, we may estimate the total conductance of the heat loss path through the wires and supports to be $13 \times 1.6 \times 10^{-7} + 6 \times 3.85 \times 10^{-2}$ mW cm$^{-1} \times 7 \times 10^{-6} = 3.7 \times 10^{-6}mW/K\times$ T. In this calculation we have completely ignored any added phonon Kapitza resistance at the various junctions in the system, which may be considerable at low temperatures. Experimentally the Kapitza resistance is observed to grow as $T^{-(2-4)}$ for many materials in the low temperature limit [112]. Although it is difficult to know the size of the thermal boundary resistances in our setup exactly, we may view the preceding estimate as a very conservative lower bound on the heat loss conductance.

A plot of the conductance of the heat loss path alongside the conductance of many of the samples measured with our setup is shown in figure 4.3. In the majority of the cases the conductance of the samples is much greater than that of the heat loss paths, but for highly resistive samples we are careful to check that heat losses are not occurring with additional tests.

4.4 Test of mount accuracy: the Wiedemann-Franz law in metallic systems
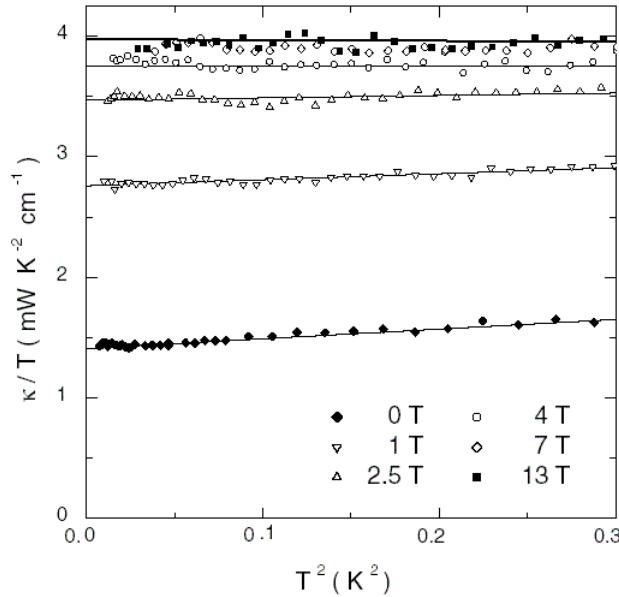
Figure 4.4: The recovery of the Wiedemann-Franz law in the field induced normal state of the overdoped cuprate Tl2201. The thermal conductivity data is plotted as κ/T versus T^2, and the thick line is the value of L_0/ρ at 13 Tesla, where superconductivity is suppressed. Adapted from reference [58].

Over the past 5 years our low temperature thermal conductivity mounts have been continually upgraded and refined to improve their thermalization time, and minimize heat losses. The most accurate test of our design is to measure both heat and charge conductivity on a metallic sample, and recover the Wiedemann-Franz law. This was achieved with silver wire, $LuNi_2B_2$ [75], $NbSe_2$ [113], $Sr_3Ru_2Ru_7$ [114] and $CeCoIn_5$ [115]. Perhaps the finest example of this is shown in figure 4.4 which shows measurements of heat and charge on the cuprate superconductor Tl2201 in the strongly overdoped region of the phase diagram [58]. At sufficiently high fields superconductivity is suppressed revealing
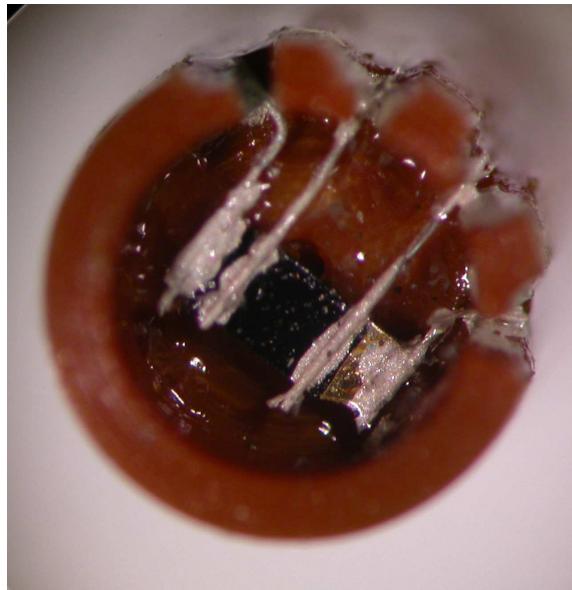
Figure 4.5: Resistivity mount for measurements in pulsed magnetic fields. The probe inserted such that the magnetic field is ⊥ to the face of the crystal.

a metallic state that conducts heat precisely as predicted through measurements of the electrical resistivity and the Wiedemann-Franz law. Given the high magnetic fields and extremely tiny samples used, this can be seen as an excellent validation of the performance of our experimental setup.

4.5 Measurements of resistivity in pulsed magnetic fields

In YBCO crystals with intermediate dopings, the static magnetic fields available in our laboratory are unable to suppress superconductivity entirely, since H_{c2} is too large. In order to study transport in the normal state of a sample with y=0.5 we performed measurements at the Laboratoire National des Champs Magnétiques Pulsés in Toulouse, France with the assistance of Cyril Proust and Marc Nardonne of the CNRS [2].

Pulsed magnetic field strengths of up to 60 Tesla are available at this facility for brief periods of time. The magnets are made of reinforced Copper, and connected to a large central capacitor bank which is charged to 20 kV. When the bank discharges, currents on the order of 40,000 Amps flow through the magnet, for a typical pulse length of 0.3 seconds. The main drawback of such a technique is that the surge of current produces large Joule heating. After a pulse it requires on the order of an hour to cool the magnet

[2]The data is presented and discussed in section 11.4

back down to operational temperatures, making a ρ vs. T curve painstakingly slow to accumulate.

Two YBCO$_{6.50}$ samples were mounted in a simple sample holder as shown in figure 4.5. The crystals were held in place with grease with H $\parallel$ c to minimize the vibrations associated with the large field gradient. Data was collected on two probes - a ^3He probe spanning the temperature range from 0.3 K to 1 K, and a ^4He probe spanning the range from 1K - 50 K. For each data point, the sample was allowed to stabilize and the temperature was recorded before and after the pulse to ensure there were no heating effects from the field. The field strength was measured by recording the voltage induced through a small pickup loop of area S aligned perpendicular to the field such that V_{pickup} = -S dB/dt.

Resistivity measurements were performed with a Stanford Research lock-in amplifier operating at 20-40 kHz, with a measurement current of $\sim 400\mu$A. The data acquisition card operated with an 80 kHz sampling rate, sufficiently fast to ensure a large density of points for the brief window when the pulse was at maximum amplitude. In general we use the data points on the downward sweep of the pulse, but check to make sure the overall hysteresis is small.

5

Physical characteristics of Y-based superconductors

5.1   Chapter overview

In this chapter I review the basic chemistry and structure of several relevant high-T_c compounds, focusing primarily on the Yttrium based superconductor YBa$_2$Cu$_3$O$_y$ (YBCO). The availability of ultra-pure single crystals of YBCO from the group of Hardy, Bonn and Liang at the University of British Columbia has made much of the work in this Thesis possible. In such pure samples complex meta stable arrangements of oxygen are possible, and I review work in this area. I also discuss the intriguing phenomena of room temperature oxygen annealing in low doped YBCO, where the carrier concentration evolves as a function of time spent annealing at 300 K. Such a phenomena is the basis for much of the work presented in chapter 12 of this Thesis.

5.2   Motivations for studying YBa$_2$Cu$_3$O$_y$

There are to date about 44 known families of structurally and chemically distinct copper oxide superconductors [12], with the discovery rate trailing off to near zero in the past few years. These materials have widely varying structures, with different chemical compositions for the charge reservoir layers, and different numbers of adjacent stacked CuO planes. At one extreme is the so-called "infinite layer phase" Sr$_{1-x}$Ca$_x$CuO$_2$ which has CuO$_2$ planes with no intermediate insulating layers. At the other extreme are the single plane cuprates such as Tl$_2$Ba$_2$CuO$_6$ which have only one CuO$_2$ plane separated by intermediary layers. Amongst this chemical zoo we choose to focus our experimental work on one particular group of compounds, the Yttrium based Y-Ba-Cu-O family. We investigate the fully oxygenated YBa$_2$Cu$_4$O$_8$ (Y124) compound which has a T_c of 81 K, and the YBa$_2$Cu$_3$O$_y$ (YBCO) compound at a variety of oxygen concentrations y.

Our reasons for studying this family are threefold. First, and most importantly, these crystals can be made with the highest quality of any of the cuprates. Evidence for

this comes in the form of extremely high chemical purity (99.99 - 99.995%), very weak magnetic flux pinning due to a low defect concentration, and exceptionally sharp x-ray rocking curves [116]. There is also strong evidence for exceedingly long electronic mean-free paths, on the order of 1μm [117, 118]. Second, it is possible to control the doping (by controlling the oxygen concentration) to produce samples which cover the doping range from Mott Insulator (y=0) to slightly past optimal doping ($y = 7.00$). This allows us to investigate the evolution of the ground state of the electronic system as it evolves from a correlated insulator to a high temperature superconductor. Finally, highly underdoped YBCO of sufficient purity has a carrier concentration which slowly evolves as a function of time spent at room temperature. We exploit this remarkable property to allow us to tune the hole concentration over a small range within the same crystal, allowing us to scan the phase diagram through the onset of superconductivity at low dopings.

5.3   YBCO crystal structure

$YBa_2Cu_3O_y$ formally belongs to a class of structures known as Perovskites and the unit cell can be seen in figure 5.1. The polyhedra are drawn to show the configuration of the planar copper atoms and their immediate oxygen neighbours. At each vertex there is an oxygen atom. The crystal structure is orthorhombic near optimal dopings, slightly elongated along the b-axis. There is an orthorhombic-tetragonal structural transition which occurs as oxygen is depleted, at around a concentration of $y = 6.4$ [119]. One of the key features of the Y123 compound, which is not present in the LSCO or BSCCO systems, are the existence of Copper-Oxygen chains which run along the b-axis in between the insulating Ba-O layer and the CuO_2 plane. These chains contribute their own electronic states to the overall conductivity of the crystal, as evidenced by the a-b resistivity anisotropy [120]. It is the addition and removal of these chain oxygen atoms that controls the concentration of holes doped into CuO_2 basal planes.

5.4   Oxygen ordered phases

For fully oxygenated YBCO crystals ($y = 7.00$) the CuO chains running along the crystallographic b-axis are completely full: there are no vacant oxygen chain sites. During crystal growth domains in which the chains are aligned in a parallel fashion are formed, and this structure is known as ortho-I ordering. These domains are essentially 3-dimensional in nature, and may measure anywhere from a few hundred Å   to many microns in length
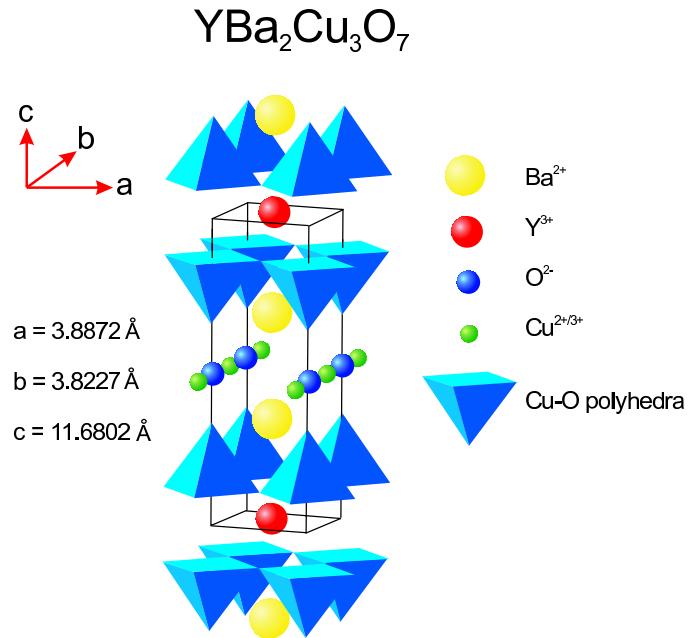
YBa$_2$Cu$_3$O$_7$

Figure 5.1: Schematic representation of the unit cell of the cuprate superconductor YBa$_2$Cu$_3$O$_y$. The essential structural element is the CuO$_2$ planes, as realized from very early on by Anderson [13]. The planes are separated by insulating layers, making the overall structure highly 2 dimensional.

[121]. In typically prepared crystals however true long range order is prevented by the formation of twin boundaries, where neighbouring ortho-I ordered domains meet in such a way that their chain orientations are perpendicular. This phenomena is known as twinning, and may be easily observed using a polarized light microscope.

Away from optimal doping, the removal of oxygen from the YBCO structure introduces vacancies into the chain sites. Early on it was noticed that underdoped crystals that were cooled rapidly after growth had a lower T_c than those of an identical oxygen concentration that had been allowed to age at room temperature [122, 123]. For example, a crystal with $y = 6.45$ with an initial T_c of 39 K was observed to increase to $T_c = 46$ K after one month of annealing at 300 K [124]. This was interpreted as an enhancement in the charge transfer between the chains and planes that is dependent not only on the overall oxygen concentration, but the degree of local oxygen order [124, 125]. In crystals rapidly quenched from high temperatures the oxygen is distributed more or less randomly throughout the lattice, but may form domains of local order over time if the oxygen mobility is large enough and the samples are allowed to anneal for long periods of time. In high purity crystals with few defects, this effect is particularly pronounced.
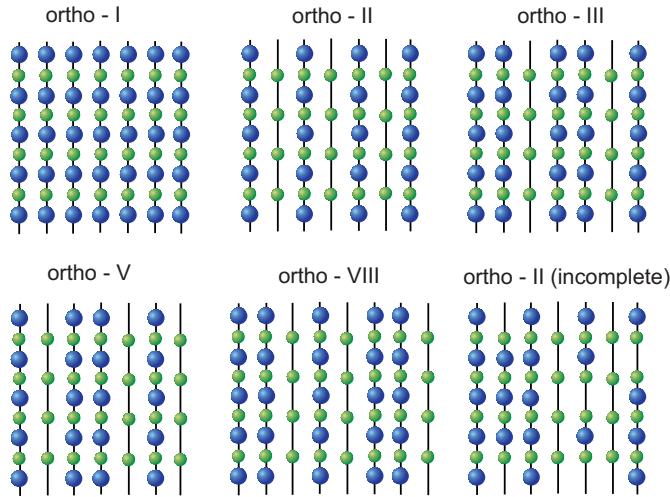
Figure 5.2: Schematic representation of the observed oxygen ordered phases in YBCO. The blue circles represent the larger oxygen atoms and the green the copper atoms. The chains run along the crystallographic *b*-axis. Incomplete ordering is observed when the mobility of the oxygen vacancies is impaired by defects in the crystal structure, or when insufficient annealing time has elapsed [124].

The variety of local oxygen ordered phases is rich, and considerable effort has been made towards identifying and classifying these oxygen superstructures. The fingerprints of these phases may be found in diffraction experiments, where superstructure reflections with periodicity ma along the a-axis are found at the reciprocal lattice vectors $\mathbf{Q} = (n/m, 0, 0)$ where n and m are integers and m denotes the superstructure periodicity. To date, ordered phases with $m = $ 2,3,4,5 and 8 have been observed experimentally [121] and are colloquially named ortho-II, ortho-III, ortho-IV, ortho-V and ortho-VIII ordering respectively. The corresponding periodicity in real space is observed in sequences of alternating full and empty Cu-O chains, meaning the unit cell is increased by a factor of m along the a-axis correspondingly. Figure 5.2 shows a schematic representation of the organization of the chains for these phases.

The only true equilibrium states are the ortho-I state and the tetragonal phase (observed for $y < 6.35$). The oxygen order phase diagram as a function of temperature and doping has been the subject of careful study using hard x-ray diffraction, which is a bulk probe because of the large penetration depth of high energy x-rays (on the order of a 1 mm). Using data on samples grown by the UBC group [121, 126], the phase diagram shown in figure 5.3 can be constructed. In the doping range $6.32 < y < 6.60$ only the ortho-II superstructure is observed to be stable, while for $y > 6.82$ only the ortho-I phase
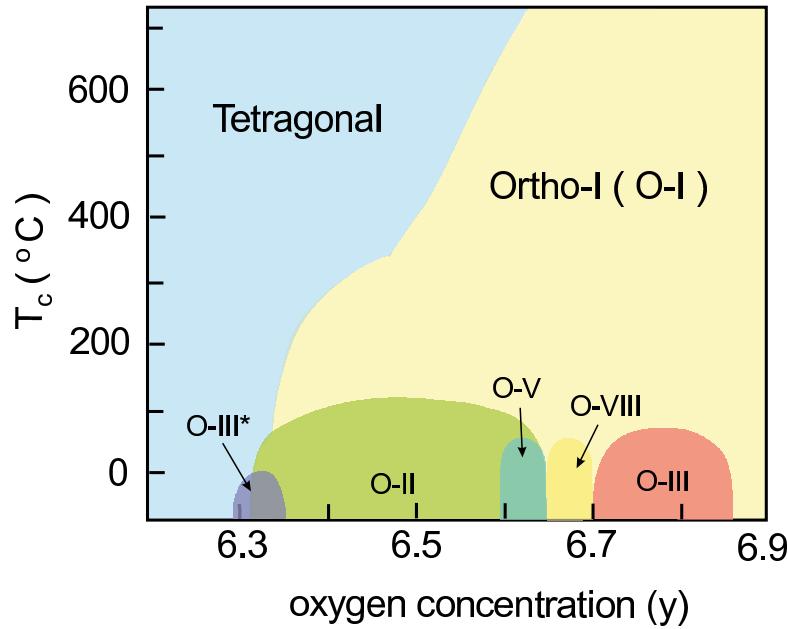
Figure 5.3: Temperature-Doping phase diagram for oxygen ordered phases in YBCO. The data is compiled from x-ray studies on high quality single crystals [121, 126, 127, 128]. The correlation length of the phases depends strongly on the crystal quality, the procedure used for cooling the samples from growth temperatures, and the post-growth annealing time and temperature.

is seen. There are small islands of stability for the ortho-III and ortho-VIII phases for $6.6 < y < 6.8$ and the ortho-V phase is observed to co-exist in the same doping range as ortho-II order. Close to the SC-AFM boundary , where $6.28 < y < 6.32$, the ortho-III inverse phase (two empty and one full chain) is observed along with both ortho-I and ortho-II order, making preparation of homogenous crystals in this regime particularly challenging. All ordered orthorhombic phases for $m \geq 2$ are destroyed when heating above about 180 °C, where only ortho-I ordering is observed.

In addition to enhancing the number of holes transferred from the chains, the existence of long range oxygen order has important secondary effects on electronic properties since disordered vacancies can act as vortex pinning and electronic scattering centres. Evidence for the role of oxygen order in vortex pinning was found in measurements of magnetization [129, 130] of YBCO crystals. Watahiki and co-workers for instance found that changing the oxygen concentration in a sample from y=7.0 (all chains full) to y=6.95 greatly increased the magnetization hysteresis, consistent with an enhanced pinning of vortices by oxygen vacancies. The ability to prepare samples free of oxygen disorder is thus extremely advantageous in investigating the intrinsic properties of YBCO, allowing one

to mostly ignore effects associated with scattering from disordered oxygen vacancies.

5.4.1   The influence of oxygen ordered phases on hole doping and T_c

Veal and Paulikas have proposed a simple microscopic model [131] based on the chemical valences of the atoms in the YBCO structure which demonstrates the unique dependence of hole doping upon local ordering of oxygen vacancies. They take the generally accepted view that Cu atoms that are surrounded by two neighbouring oxygen atoms (2 coordinated) are monovalent. Cu atoms that are 3 or 4 coordinated are divalent, and all oxygen are O^{2-} unless charge balance requires O^{1-} (and consequently Cu^{3+}). The number of Cu atoms with a formal valence of 3 is then taken to be equal to the concentration of holes, since charge balance requires them to accept a hole from the Cu-O plane.

The effects of increasing oxygen order results in decreasing the average co-ordination number of each copper atom. This is turn alters the valence from Cu^{2+} to Cu^{1+}, drawing an electron from elsewhere in the structure, and creating a charge vacancy (hole). To see how this works in practice we consider the effects of perturbing the fully ordered ortho-II structure in figure 5.4. In the ordered phase, all of the copper atoms in the chains are 4-fold coordinated - two oxygen atoms on either side along the *b*-axis, and two oxygen atoms in the apical sites above and below. Their valence is thus +2. The copper atoms in the empty chains are only two coordinated with the apical oxygen, and have a valence of +1. Disordering the structure by moving an oxygen from a full chain to an empty chain site has two effects. First, the Cu atoms at the old site move from a 4-fold to a 3-fold coordination - with no resulting change in valence. The two copper atoms adjacent to the oxygen at the new site however change from 2-fold to 3-fold coordination, and each see their valence change from +1 to +2 as they give up an electron to form the usual oxygen bonding condition of O^{2-}. This means that they can no longer serve as electron acceptor sites, causing the hole concentration in the planes below to *decrease* by 2. In addition to providing a microscopic mechanism for order induced doping, this model works quite well in describing the evolution of T_c with doping in the YBCO system, reproducing the 60K plateau observed around $y = 6.6$.

5.4.2   Oxygen annealing rates

The rate at which local oxygen order is increased is strongly dependent on the annealing temperature, the elapsed time, and the overall oxygen concentration. Of particular interest to our work is an accurate knowledge of the rate at which the superconducting
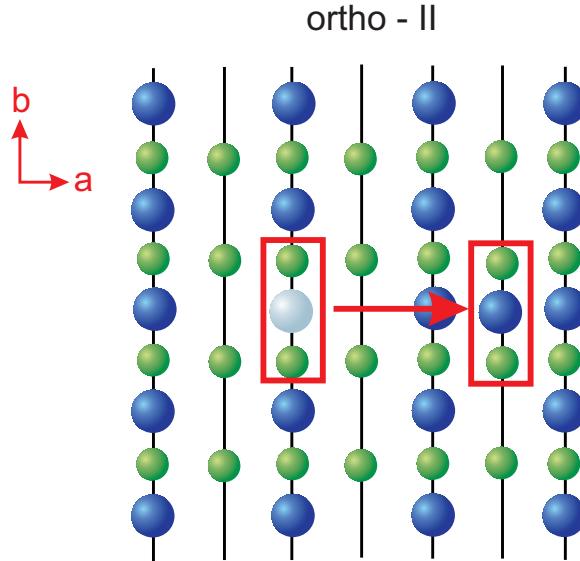
Figure 5.4: The microscopic model of Veal and Paulikas [131] describing the dependence of hole concentration on oxygen coordination. Disordering the ortho-II structure by moving an oxygen atom from a full chain site to an empty one changes the valence of the copper atoms adjacent to the new site from +1 to +2, thus removing two holes from the plane.

critical temperature increases with time spent at room temperature. In extremely low doped samples, it is possible to use this effect to tune between the non-superconducting and superconducting states simply by allowing a sufficiently long annealing time to elapse.

Detailed investigations of the dependence of T_c on annealing time have been performed in $Tl_2Ba_2CuO_y$ and $YBa_2Cu_3O_y$ at ambient [122, 124, 132, 133, 123] and high pressures [134, 135, 136]. Such dependence has been analysed in terms of a simple model by Veal and Paulikas discussed above, and found to give the following dependence of T_c on time [123]:

$$T_c(t) = T_c(\infty) - [T_c(\infty) - T_c(0)]exp[-(t/\tau)^{1/2}] \tag{5.1}$$

Here $T_c(\infty)$ and $T_c(0)$ are the final and initial transition temperatures respectively, t is the elapsed time since crystal growth was stopped, and τ (which is doping dependent) is a characteristic time constant of the oxygen annealing process.

Using measurements of magnetization Jorgensen *et.al.* [123] have studied the evolution of T_c in a highly underdoped sample of $YBa_2Cu_3O_{6.41}$, and found excellent agreement to the expected form of equation 5.1, with a time constant $\tau = 386$ minutes.

5.5 $YBa_2Cu_4O_8$: structure and properties

The cuprate superconductor $YBa_2Cu_4O_8$ is closely related to the YBCO-123 compound with one important distinction. The unit cell of this material is shown in figure 5.5 and is seen to be orthorhombic in character[137], with a *double* layer of CuO chains between the CuO_2 planes. These chains are completely full, having two interesting consequences. First, the double chains exclude the possibility of forming twinned domains in the grown crystals, and secondly the absence of any oxygen vacancies in the chains means that samples are grown essentially disorder free.
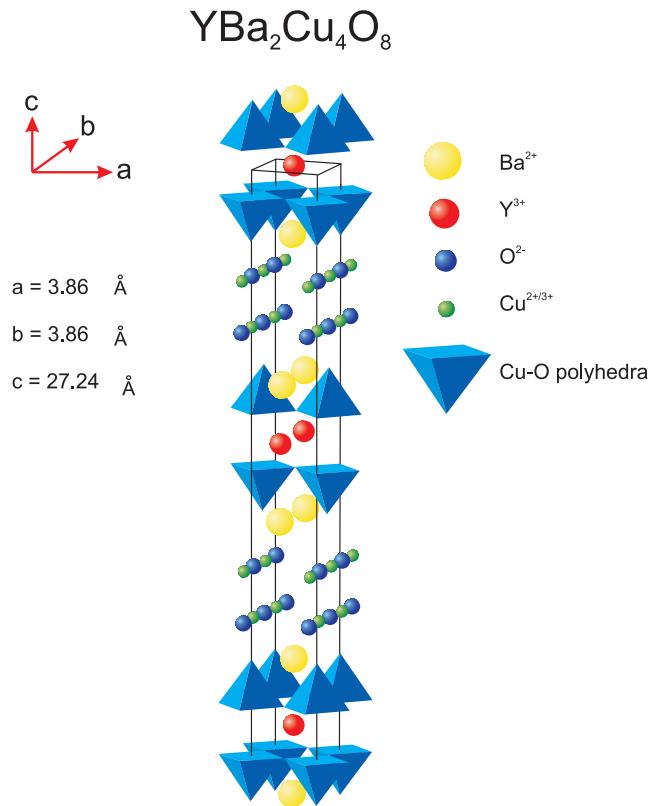
Figure 5.5: The crystal structure of the double chain cuprate superconductor $YBa_2Cu_4O_8$, or YBCO-124. The compound is naturally underdoped, with a T_c of 81 K, and can be prepared with extremely low levels of disorder.

The T_c of this material is measured to be about 80 K [138], and doping by the removal of oxygen destabilizes the crystal structure. This 15 % reduction of T_c with respect to the optimally doped YBCO-123 compound is believed to signify that the material is in fact in a naturally underdoped state. Proof of this has been provided by many authors who observe a pseudogap in the normal state, akin to that observed in underdoped YBCO-

123. Studies of spin-lattice-relaxation rate [139], Knight shift [140], resistivity [141] and thermopower [142] have put the characteristic crossover temperature T^* of this gap at 160 - 250 K.

5.6 $La_{1-x}Sr_xCuO_4$: growth and structure

Much of the thermal and charge transport data on YBCO presented in later sections is best understood by placing it in the context of results on the $La_{1-x}Sr_xCuO_4$ (LSCO) system[1]. LSCO is a double layer cuprate with two structural phases, orthorhombic and tetragonal. The lattice constants in the tetragonal phase are a = 3.812 Å and c = 13.15 Å and a = 5.35 Å, b = 5.40 Å in the orthorhombic phase, where the orthorhombic planar unit vectors are shifted 45 ° from the tetragonal ones. Doping may be achieved by either intercalation of oxygen, but is more usually accomplished by cation substitution of Ba^{2+} or Sr^{2+} for La^{3+}. This cation substitution creates much larger in plane disorder than in YBCO, although the chemical and crystal perfection of the two systems may be comparable. The enhanced disorder over YBCO is a theme we shall revisit many times in comparing the data on the two systems.

---

[1]The study of transport in LSCO is the primary component of the Thesis of Dave Hawthorn, and is discussed fully in that work [62].

6

SAMPLE PREPARATION AND CHARACTERIZATION

6.1   Chapter overview

In the following chapter I detail the physical characteristics and preparation of the samples used in this study. The YBCO crystals were obtained from three separate sources. Good quality single crystals of $YBa_2Cu_3O_y$ in the doping range $y = 6.6$ to $y = 6.95$ were grown in Yttria stabilized Zirconia (YSZ) crucibles by Robert Gagnon at McGill University and Harry Zhang at the University of Toronto. Ultra high purity samples of $y=6.33$, 6.35, 6.5 and 6.99 grown in $BaZrO_3$ (BZO) crucibles were obtained from Ruixing Liang, Walter Hardy and Doug Bonn at the University of British Columbia. Our $YBa_2Cu_4O_8$ samples were provided by Nigel Hussey at the University of Bristol.

The exact procedure for Oxygen annealing and sample detwinning are discussed, and the development of a new technique for obtaining good quality low resistance contacts on YBCO using thin films of evaporated gold is presented. Our samples were characterized by measuring resistivity, and in some cases AC susceptibility. This data is then used to establish the superconducting critical temperature, and to estimate the relative amounts of disorder in our samples. From our measurements of T_c, we then obtain an estimate of the planar hole concentration, p, using an empirical relation from the literature.

6.2   Preparation and growth of YBCO samples

6.2.1   Preparation of ultra high purity $BaZrO_3$ grown YBCO samples

Flux grown YBCO single crystals are prepared at high temperatures, and the Y_2O_3-BaO-CuO melt is known to be very reactive. Contamination from the growth crucible itself is typically the principal source of impurities in these materials. Y_2O_3 stabilized with ZrO_2 (YSZ) is usually used to minimize this contamination since Zr^{4+} has little solubility in the melt and YBCO lattice [116]. Commercially available YSZ crucibles however are

only 99 % pure, which limits the final crystal purity to only 99.9 % despite using starting materials that are considerably more pure. To overcome this limit Erb. *et.al.* [143, 144] developed the use of homemade $BaZrO_3$ crucibles which are much less reactive with the melt, and can be prepared to higher levels of purity.

These superior crucibles were adopted by the group at UBC [116] and have resulted in the growth of some of the most pure samples of the YBCO compound in existence. Chemical analysis on their samples have shown only trace levels of Zr,La,Sm,Al and Mg, with the overall purity of the crystals being limited by the starting materials themselves, typically 99.995 %. This dramatically improved quality has resulted in narrow superconducting transitions, smaller magnetization hysteresis and incredibly sharp x-ray rocking curves compared to previous generations of YBCO samples [116]. The crystals provided by this group are widely considered to be the best in the world.

$\mathbf{YBa_2Cu_3O_{6.33-6.35}}$

The preparation of homogenous YBCO samples with carrier doping near the AFM-SC boundary is a difficult task due to the extreme sensitivity of the materials to annealing conditions and the coexistence of multiple phases in that region of the phase diagram. Recently, Liang *et.al.* [126] have succeeded in producing samples that have sharp superconducting transitions, and exhibit no signs of the tetragonal or ortho-III* phase. We were provided with 6 of these crystals, prepared with y in the range of 6.33-6.35, very close to the onset of superconductivity. The actual Oxygen content of the samples varied slightly from batch to batch and is reflected in their T_cs. In this region of the phase diagram a change in the Oxygen content by 0.001 results in a change of T_c by 0.8 K.

The samples were grown by a self-flux method in $BaZrO_3$ crucibles and the oxygen was set to $y \sim 6.35$ by annealing at 900-930 °C for one week in flowing Oxygen. Annealing took place in a small quartz ampoule which contained an appropriately doped ceramic pellet of $YBCO_y$, and the samples were rapidly quenched to room temperature after words. Further annealing at 500 °C was required to eliminate the Oxygen inhomogeneity, which was followed with a quench into ice water. Samples prepared in this manner are initially disordered, and had either very low T_cs or were non-superconducting altogether. Further annealing at room temperature or above sees the T_c rise with time, as described in section

5.4.2. We obtained 3 samples of YBCO$_{6.35}$ (B,H,F)[1] which were designed to have a final T_c in the 10 K range, and 3 samples of YBCO$_{6.33}$ (J,K,L) which were designed to have a final T_c of approximately 5 K. All of these samples were quenched to 0° C immediately after annealing then shipped to Toronto or Sherbrooke on dry ice to preserve Oxygen disorder.

Oxygen ordered ortho-II YBa$_2$Cu$_3$O$_{6.50}$

In total we obtained 3 high quality, detwinned single crystals of YBa$_3$Cu$_3$O$_{6.50}$ from the group at UBC [145] (samples A,B,C). The samples were grown in BaZrO$_3$ crucibles, then detwinned at 300°C by applying 100 *atm* of uniaxial pressure along the *a*-direction. To set the Oxygen content to y=6.50 the samples were sealed in a quartz ampoule with large, previously prepared ceramic YBCO$_{6.5}$ pellets. The crystals and pellet were then annealed at 390 °C for 2 weeks. Ortho-II order was maximized by low temperature annealing at 84 °C for 2 days followed by 60 °C for 5 days. Crystals prepared in this manner were found to posses sharp superconducting transitions, and three dimensional ordering with very long correlations lengths, on the order of hundreds of Å [145].

Oxygen ordered ortho-I YBa$_2$Cu$_3$O$_{6.99}$

A single sample of BaZrO$_3$ grown overdoped YBCO was also obtained from the UBC group. As in the previous batches the starting material was of the highest commercially available purity [116]- 99.999% (Y$_2$O$_3$) 99.995% (CuO) and 99.997 % (BaCO$_3$). The compounds were mixed in powder form, then placed in the crucible, which was heated to 1020 °C, held there for 15 hours then slowly cooled to 960 °C over the period of a few days. The Oxygen content was set by annealing in ultra-pure Oxygen and the sample was detwinned using the procedure mentioned above.

6.2.2 *YSZ grown YBCO samples with $y = 6.6$ - 6.95*

Underdoped YBCO crystals were prepared in our own labs under the guidance of Harry Zhang. Optimally doped YSZ grown samples were placed in a quartz tube that had been cleaned in a weak HCl solution. The samples were set atop a few cc's of YBCO powder, previously prepared to have an Oxygen concentration in the range that we desired. Following the temperature-pressure phase diagram reported by Schleger *et.al.* [146] we set

---

[1]A brief note on sample nomenclature: The samples were assigned names based on when they arrived - A first, B second etc. Samples which are not discussed in this thesis were either damaged, broken, or did not posses electrical and thermal contacts of sufficient quality for low temperature measurements

the Oxygen partial pressure within the tube to be between 100 mTorr and 450 mTorr after pumping and flushing the tube repeatedly with high purity dry Oxygen. The samples were then allowed to anneal for 7-10 days at 450 °C, followed by a quench into liquid nitrogen. This procedure yielded crystals with sharp superconducting transitions as seen in susceptibility measurements, but several had "double-step" resistive transitions indicating some surface Oxygen inhomogeneity. Lower partial pressures of Oxygen seemed to result in sharper transitions. Sample O and K were prepared with a partial pressure of 350 mTorr Oxygen and samples Q and S with 100 mTorr. The later pair did not posses the "double-step" transition which plagued the first set.

6.2.3 Preparation of $YBa_2Cu_4O_8$

The growth of the $YBa_2Cu_4O_8$ cuprate can only be achieved under extremely high pressures, making these crystals quite rare. We were fortunate enough to receive four of such samples (A,B,C,D) from Nigel Hussey at the University of Bristol for transport measurements. The samples were grown by a flux method in Y_2O_3 crucibles in an Ar/O_2 mixture at 2000 bar [147] at the Superconducting Research Laboratory in Tokyo. The samples were exceeding small platelets requiring the utmost care in handling. Two were aligned along with the long dimension along the *a*-axis and two along the *b*-axis.

6.3 *Physical dimensions of YBCO samples used in the study*

The determination of the physical dimensions of each of our crystals was done with great care, as uncertainty in the size of the sample is the chief source of error in our absolute determination of κ. This was accomplished either by using a calibrated light microscope or, when samples were smaller, a scanning electron microscope (SEM). The greatest contribution to geometric factor error is typically found in measuring the contact separation between the voltage wires, which is sometimes complicated if large amounts of silver paint are used to bond the wire to the sample. The typical resistance of a silver wired bonded to a bare YBCO surface with silver paint was however measured to be on the order of 1 MΩ, so we take the true contact separation to be the distance between the low resistance diffused pads and not the actual wires themselves. For especially large contacts, there exists the possibility that the contact separation for electrical current (determined via the pad separation) is different than the contact separation for thermal current. This is due to the fact that the latter is determined in part by the path of least resistance for the phonons, which is in some way related the size of the patch that the
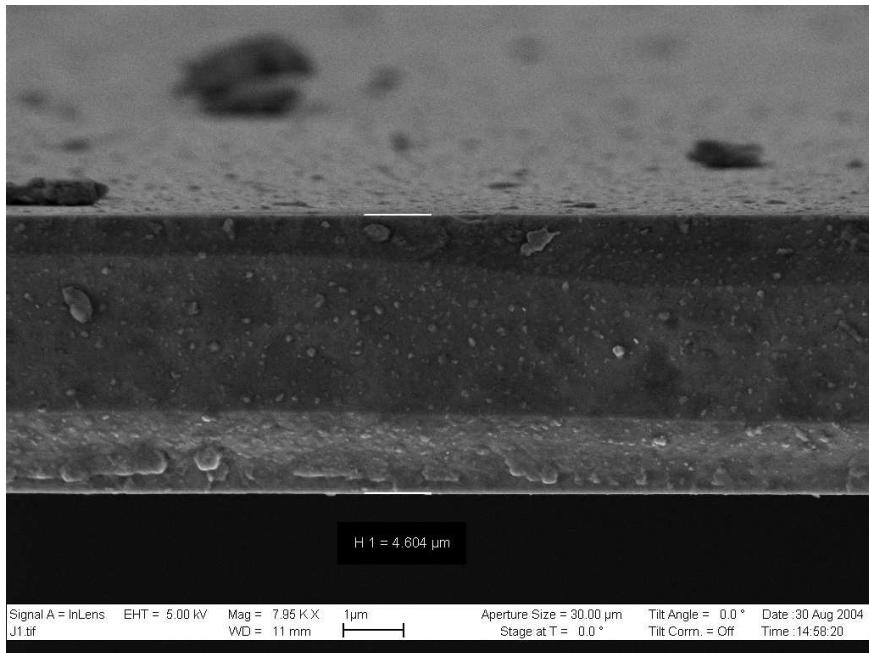
Figure 6.1: SEM image of YBCO$_{6.33}$ sample J, showing a measurement of the thickness. The image was taken at the university of Sherbrooke by Ronan Larger and Shiyan Li.

silver paint makes on the face of the crystal. For the most part we ignore this effect, which is small in samples with well defined contacts. Figure 6.1 shows an SEM image of one of our samples, demonstrating how the thickness is determined.

The measured dimensions and geometric factor for all samples studied during this work are summarized in Appendix 1. The error in the width and the thickness of the sample is given by the resolution of the measurement apparatus when the samples were perfect platelets. For unevenly shaped samples the average thickness or width was used, with the error given by the maximum and minimum variation of these values. The error in the contact separation was taken to be the width of the diffused pads where possible, or else the width of the silver paint used to bond the wire to the crystal. The geometric factor is the calculated as $\alpha = thickness \times width \ / \ length$ and the error is the geometric mean of the errors in the three measured dimensions. Only samples that yielded usable data are included in the table. Those that were omitted were samples that were damaged, broken or had poor contacts.

6.4 Preparation of low-resistance contacts

The application of good quality, low resistance contacts to cuprate materials is somewhat of a black art. The basic idea is to lay down a conductive material in the desired contact configuration, then bake these pads in order to let the material diffuse through the top few insulating layers of the crystal and make electrical contact with the conductive layers beneath. Typically, silver wires are attached to these pads with a small amount of Dupont 4929N silver paint diluted with 1-Acetoxy-2-butoxyethane.

In the process of this study many attempts were made to develop a rigorous and reproducible method for preparing low resistance pads. Our early work focused on preparing the sample surface and then applying strips of Epoxy Technology H81E silver epoxy that were baked in an oven at high temperatures. In order to get the best quality contacts possible, attempts to were made to mechanically abrade the crystal surfaces, or to etch them with a weak Bromine solution of 0.5 % Br in methanol or a strong acid solution of $20CH_3OH:4HCl:1HNO_3$. Such attempts resulted in marginally improved contact resistance. The principal factors that appeared to most strongly influence the contact quality were determined to be the annealing environment, and the annealing temperature. For annealing temperatures less than 400 °C with test pieces of YBCO, contacts with resistances of less than 100 Ω were rare even when annealing was performed for several hours. To obtain low resistance contacts with these low temperatures, annealing times of several days or weeks were necessary. Contacts annealed at temperatures close to 500 °C for one hour yielded much lower electrical resistances, usually with R < 1 Ω. It should also be noted that annealing samples in a very clean environment is essential, and a steady flow of ultra pure Oxygen helps improve contact quality, although this is not practical with underdoped samples.

A more advanced method was developed with Jennifer DeBenedictis from the University of British Columbia which involved masking off the crystal with Kapton ®film, then applying a thin coating ($\sim$1000 Å) of evaporated gold. The contacts were then annealed at around 400 °C for long periods of time in a sealed quartz crucible resting on a large volume of ceramic prepared to the correct Oxygen content. This procedure was found to result in reproducible contacts with R $\sim$ 1 Ω, even in highly underdoped YBCO.
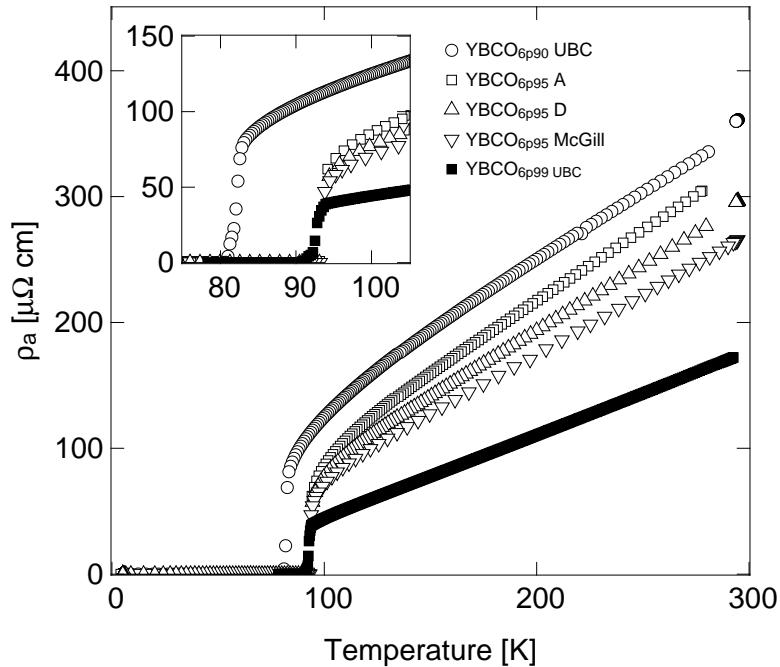
Figure 6.2: The *a*-axis resistivity for the single crystal YBCO samples near optimal doping. The inset shows a zoom of the superconducting transition, and we define T_c to be where $\rho \sim 0$.

6.5   Sample characterization: determination of T_c.

Measurements of electrical resistivity were the primary tool for establishing the superconducting critical temperature of our samples, and were performed using the methods and apparatus described in chapter 4. In some cases additional measurements of the AC magnetic susceptibility were taken with a PPMS susceptometer by Patrick Fournier at the University of Sherbrooke. The characterization data is grouped into sections of crystals with similar Oxygen concentrations below.

6.5.1 $YBa_2Cu_3O_y$, y=6.90-6.99

a-axis resistivity for the single crystal YBCO samples with y near optimum doping is shown in figure 6.2. The samples with y=6.95 have a room temperature resistivity of 300 ± 30 $\mu\Omega$ cm, which agrees favourably with typical values reported previously in the literature [148]. We define the resistive T_c as the temperature where ρ=0, with the transition width being determined as the temperature difference between the onset of the resistive downturn and where ρ=0. For the samples A and D, grown at the university of Toronto, $T_c = 92.8$ K and 93.2 K respectively, with $\Delta T_c = 0.5$ K for each. For the McGill grown sample, $T_c = 93.5$ K with ΔT_c also 0.5 K. The overdoped sample, grown in
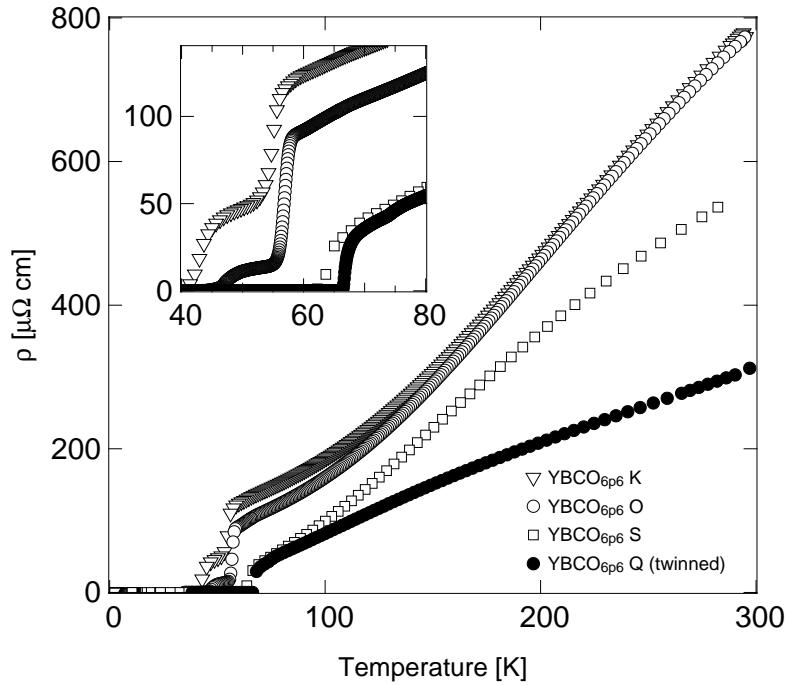
Figure 6.3: Resistivity for the 4 four underdoped YBCO samples prepared at the university of Toronto with the assistance of Harry Zhang. The Oxygen concentrations were determined by comparing their T_cs and room temperature resistivity as outlined in the text.

a BZO crucible, had a T_c of 90.4 K, with a transition of width 3 K. Finally, the slightly underdoped sample had a T_c of 81 K with a 2 K transition width. We estimate the Oxygen concentration of this sample to be $y = 6.9$, based on comparing the value of ρ_{300K} and T_c with that found for samples with directly measured Oxygen concentrations in the literature [148] see section 6.7.

6.5.2 $YBa_2Cu_3O_y$, $y=6.6$-6.7

The resistivity of samples prepared by annealing fully doped crystals in partial pressures of Oxygen (as outlined in section is shown in figure 6.3. We estimate the Oxygen concentration y based on the values of room temperature resistivity found in the literature. The samples with a slightly higher doping level have sharp transitions: T_c where $\rho=0$ is 61.7 K and 66.4 K for samples S and Q respectively, with transition widths of 3.6 and 1.4 K. The lower doped samples have "double-step" transitions, which likely arise from doping inhomogeneity at the surface of the crystals. From resistivity the T_cs defined by the criteria $\rho=0$ are 40 K and 44 K for samples K and O respectively, although the total transition width is very large - 17 and 14 K respectively. In order to determine the true
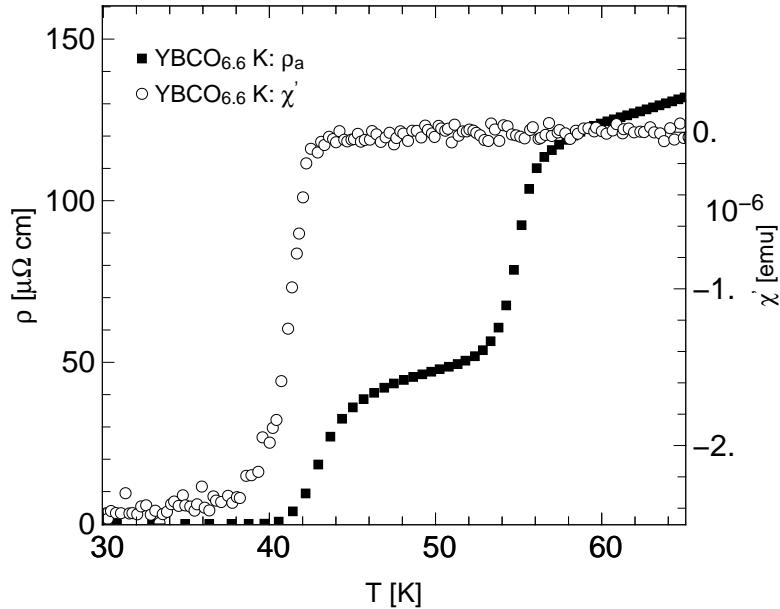
Figure 6.4: ρ_a (left axis) and χ'_{AC} (right axis) measured on the same sample. The transition in χ'_{AC} is quite narrow, while that in resistivity is broad. T_c can be estimated from the susceptibility data, since it is a probe of the bulk state of the crystal and is not affected by small impurity phases occurring at the surface of the sample. We note that this is equivalent to the point where ρ=0.

bulk T_c of the samples measurements of AC-Susceptibility were performed on sample K, and the result is displayed in figure 6.4. The transition observed by susceptibility is rather sharp, meaning there is a homogenous Oxygen distribution in the bulk of the crystal. The T_c observed as the midpoint of χ'_{AC} is 41.2 K, which coincides very well with the temperature at which resistivity goes to zero. Since thermal conductivity is a bulk measurement we thus ignore the large transition widths arising from the double-step transition, and retain the ρ =0 criteria for estimating T_c from these crystals.

6.5.3 $YBa_2Cu_3O_y$, y=6.5

Of the three samples of ortho-II ordered YBCO$_{6.5}$ prepared to y=6.5 and in the ortho II ordered state, only two (B and C) yielded electrical contacts good enough to perform resistivity measurements, although all three had acceptable thermal contacts for κ measurements. The resistivity for samples B and C, which were prepared with evaporated gold pads, is shown in figure 6.5 alongside samples with y=6.5 and 6.6 from the literature [148]. Using the criteria ρ=0 we see that ortho-II B (C) had a T_c of 54.9 K (55.0 K) and each had a transition width of 5 K. The T_c for these samples are considerably
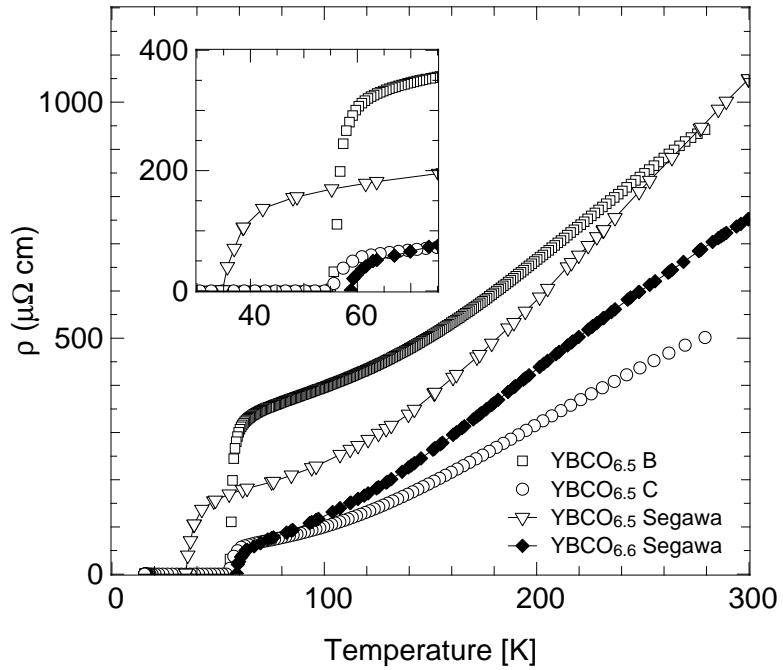
Figure 6.5: ρ_a for two of the ortho-II ordered YBCO$_{6.5}$ samples provided by UBC, compared to samples of comparable doping from the literature [148]. The magnitudes of the resistivities seem to be quite different, even allowing for geometric factor errors. This indicates that one of the samples may have suffered from current inhomogeneity.

higher than that for a y=6.5 sample from Segawa, [148], which had a T_c of 35 K. This considerable difference likely arises from the long range Oxygen ordering present in our samples, which enhances hole doping into the planes and thus increases the transition temperature. Independent magnetization measurements on similar crystals provided by UBC have yielded T_cs as high as 62 K [145], which coincides with the onset of the super-conducting transition in our samples.

Judging by the values of the T_c, the expected resistivity curve should appear closer to that observed by Segawa and Ando for y=6.6, where they measure $\mathrm{T}_c = 66\mathrm{K}$. Sample C is much closer in this respect than sample B, whose resistivity appears anomalously large. This could be explained by the presence of c-axis contamination in the resistivity measurement, caused by either poor electrical contacts or intrinsic faults within the crystal. The fact that sample B is some 3 times thicker than sample C lends weight to that scenario, since c-axis effects are expected to be more severe in thicker samples. In either case, the thermal conductivity is not affected by such problems, since thermalization of the electrons by the phonons (who have negligible anisotropy) ensure an even spatial

distribution of heat current.

6.5.4 $YBa_2Cu_3O_y$, y=6.33-6.35

The low doped samples of $YBa_2Cu_3O_{6.33}$ and $YBa_2Cu_3O_{6.35}$ yielded resistivity curves that were dependent on the time spent annealing at room temperature, as a result of the microscopic process outlined in section 5.4.1. We use the resistivity, or where possible the magnetic susceptibility, to define and track T_c as a function of annealing (doping).

$YBa_2Cu_3O_{6.35}$ Sample B: ρ, χ'_{AC}

The 0 field resistivity of $YBa_2Cu_3O_{6.35}$ Sample B is shown in figure 6.6 as measured over the course of a year. The annealing time is taken to be the number of days spent at room temperature, starting from the time the sample was removed from cold storage. The most noticeable feature of the curve is the partial transition and plateau like feature occurring around 50 K. This can be explained by a small concentration of regions of ortho-II ordering with a large correlation length, a result of imperfect Oxygen homogeneity (similar in principle to the $YBCO_{6.6}$ discussed above). Microscopically, Oxygen is clustering in areas of the crystal and forming a one chain full, one chain empty ordering that leaves other regions of the sample Oxygen deficient. These regions have a larger effective hole concentration, and hence a much higher T_c than the rest of the sample. Since electrical current will take the path of least resistance in the sample, resistivity is extremely sensitive to small superconducting impurities, causing the resulting resistivity measurement to display step like features.

The degree that this inhomogeneity affects thermal conductivity entirely depends on what percentage of the total sample volume these regions occupy, since measurements of κ are a bulk probe. We tested this by measuring the bulk AC susceptibility (χ'_{AC}) on this sample to T 60 K, and the results can be seen in the left hand panel of Figure 6.7. In cooling from 60 K to 20 K, χ'_{AC} was observed to decrease by 2×10^{-7} emu, compared to a drop of 6×10^{-5} emu in cooling below the bulk T_c of the sample seen in figure 6.7. Demagnetization effects can be extreme in thin rectangular platelets, but the width of the superconducting transition appeared insensitive to an order of magnitude reduction of the excitation, indicating that the probe field of 0.5 Oe was well below H_{c1} even accounting for geometric effects.

Judging by the large difference in the relative size of the drops in χ'_{AC} we estimate that the overall concentration of ortho-II regions in the sample can be no greater than
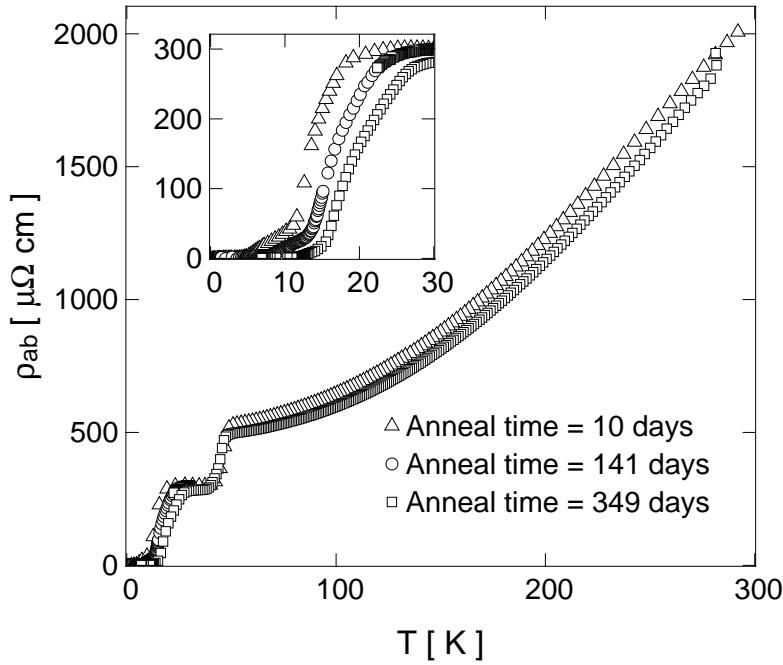
Figure 6.6: **Main** : ρ_{AB} for YBCO$_{6.35}$ sample B. A distinct double transition is observed, presumably caused by regions of ortho-II ordered material with a higher T_c. **Inset** : Zoom on the data showing where ρ goes to zero.

1% of the total volume. This means they will have no measurable effect on thermal conductivity measurements, but unfortunately complicate a direct comparison of heat and charge.

How one correctly defines a representative T_c is for this sample is complicated by the broad transition, so we turn to susceptibility in an attempt to correlate the features in resistivity with those in the bulk measurement of χ'_{AC}. Figure 6.7 shows the susceptibility versus temperature of YBa$_2$Cu$_3$O$_{6.35}$ Sample B after 127 days of annealing, alongside the resistivity taken at approximately the same time.

What is evident from this figure is that the onset in the drop in susceptibility occurs at a much lower temperature than the onset of the drop in resistivity, confirming that the domains that are shorting the resistivity do not comprise a significant volume fraction of the sample. We note that the temperature where the transition in χ'_{AC} is 50 % complete again corresponds to where the foot of the resistivity curve falls to zero, and we take these two definitions of T_c to be equivalent. Thus from figure 6.7 we have $T_c \sim 7.0$ for
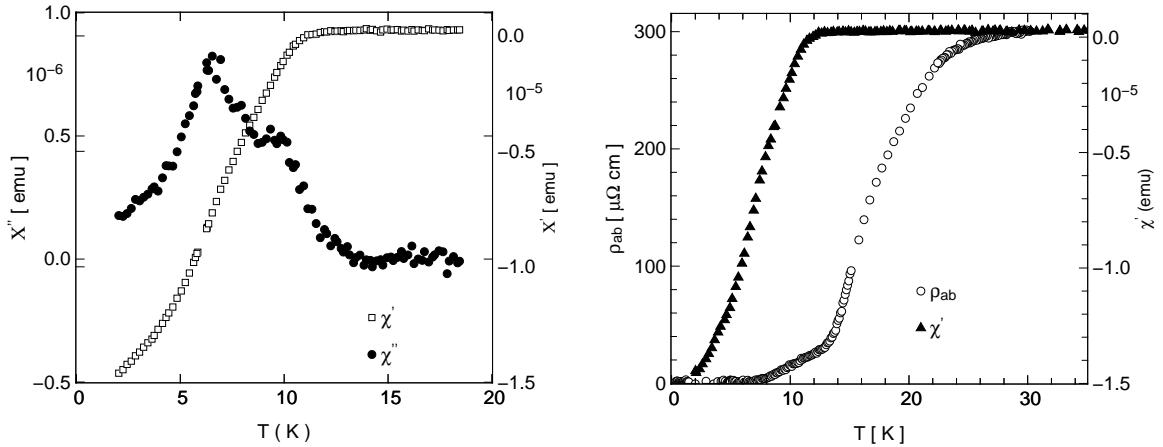
Figure 6.7: **Left**, **main** : AC susceptibility (χ'_{AC}) and derivative (χ''_{AC}) of YBCO$_{6.35}$ sample B. **Left** : A small drop is seen in (χ'_{AC}) due to the partial superconductivity from ortho-II ordered domains. We estimate them to account for no more than 1% of the sample by volume. **Right** : AC susceptibility and resistivity for the same sample. The midpoint of the transition in χ'_{AC} is seen to coincide with $\rho=0$, where we define T_c to be.

this anneal[2].

$YBa_2Cu_3O_{6.35}$ Sample F,H: χ'_{AC}

The quality of the electrical contacts on YBa$_2$Cu$_3$O$_{6.35}$ Sample F became extremely poor at low temperatures, resulting in a large out of phase component in the measurement of resistivity. At room T, ρ was observed to be 2700 $\mu\Omega$cm, which is comparable to sample H. Measurements at lower temperatures were however inconclusive. AC susceptibility measurements for the sample show T_c to be 6.0 K using the criteria of 50 % drop after 25 days of annealing, which is comparable to the results for sample H , which had T_c = 4.2 at the same point in time. In the absence of any further data we then take the two samples to have identical values of T_c at all times. This is further justified given that the crystals were grown together and had their Oxygen levels set to nominally the same concentration. Additionally, the fact that their pre-annealing room temperature resistivities are very close (2700 vs. 2600 $\mu\Omega$cm for samples F and H respectively) is suggestive of their doping similarity.

The electrical contacts on YBa$_2$Cu$_3$O$_{6.35}$ sample H were excellent, and good quality thermal conductivity, electrical resistivity and AC susceptibility data was obtained. The

---

[2]We collect the values for all annealing times and all samples in the table at the end of this chapter. Although there is some error in the determination of T_c due to finite transition width, we take this to be insignificant for the conclusions that we later draw from the data.
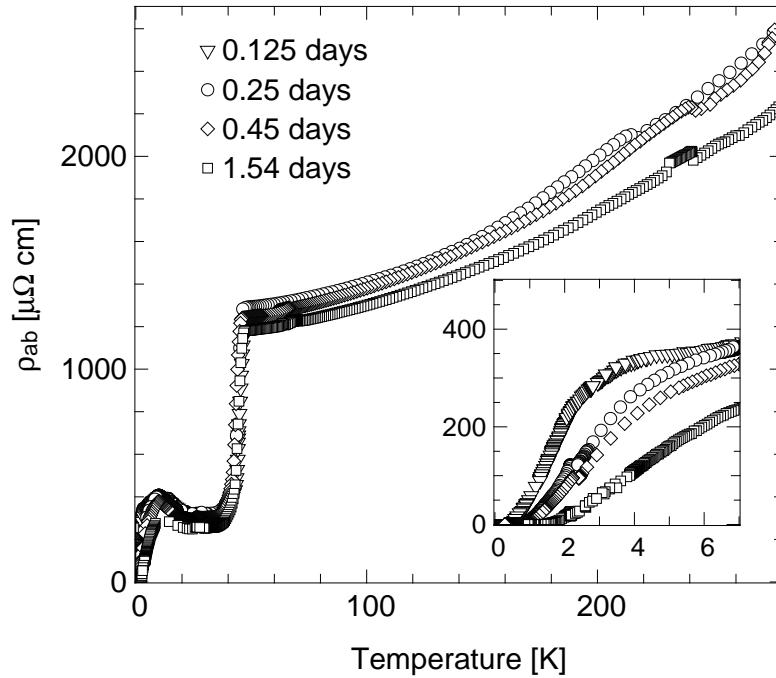
Figure 6.8: Resistivity for YBCO$_{6.35}$ sample H versus temperature, shown after various elapsed times annealing at room temperature. A double step transition is evidence of Oxygen homogeneity problems. The inset shows the T_c, defined as where ρ=0 increases with annealing time.

high temperature resistivity for sample H is shown alongside the low temperature resistivity as a function of annealing time in figure 6.8. It is immediately evident that this sample possessed the same Oxygen homogeneity problems as sample B, although to a slightly lesser degree judging by the relative size of the partial transition at 50 K.

The susceptibility of this sample, measured after a total of 25 days annealing at room temperature, is shown in figure 6.9. At high temperatures a small reduction in signal is seen near the 50 K transition, although it is at least 20 times smaller than the drop at low temperatures. Again we conclude this poses no problems for thermal conductivity measurements. Using the midpoint of the transition in χ'_{AC} we define T_c to be 4.2 K at this time (25 days of annealing), although the transition is quite broad, extending over $\pm$ 2 K. The transition temperature during the fridge measurements was established by resistivity (where ρ=0), since it is not possible to measure susceptibility insituu. These low temperature resistivity curves are shown in the inset of figure 6.8 for the various annealing times. The evolution of T_c with annealing is seen to be logarithmic in time in the right panel of figure 6.9, very similar in behaviour to a YBCO sample with $y = 6.41$ measured by Veal *et.al.* [124].
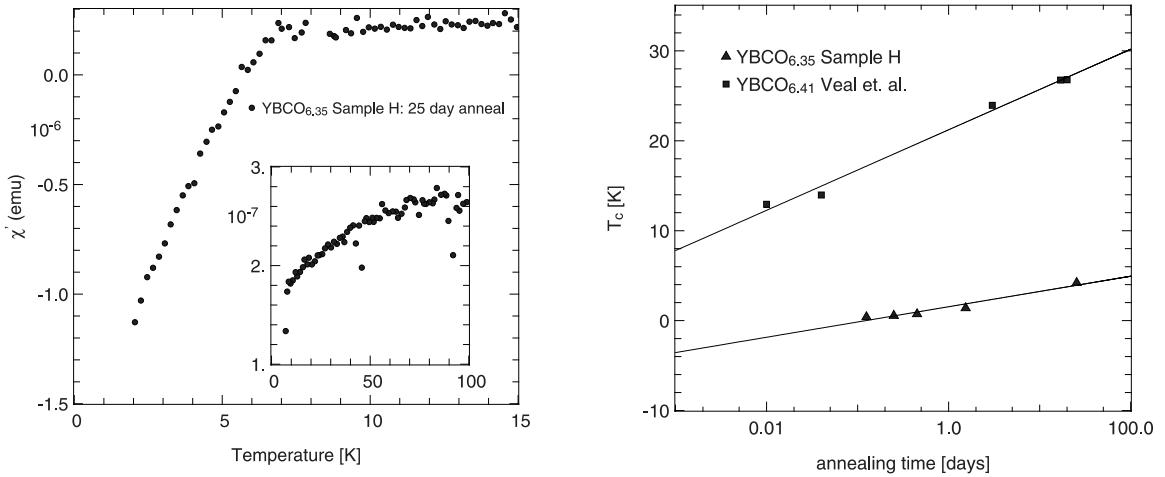
Figure 6.9: **Left** : χ'_{AC} versus temperature for YBCO$_{6.35}$ sample H, after 25 days of annealing. **Right** : T_c versus annealing time for YBCO$_{6.35}$ sample H and a sample of YBCO$_{6.41}$ from the literature [124]. Both sets of data show a logarithmic evolution of T_c.

YBa$_2$Cu$_3$O$_{6.35}$ Sample J,K,L: ρ

The task of identifying T_c for samples YBa$_2$Cu$_3$O$_{6.33}$ J,K and L was made considerably easier by the fact that no large ortho-II downturns were observed in resistivity[3]. The three panels of figure 6.10 show resistivity at low temperatures for these samples for their various anneal times[4]. T_c is again taken to be the temperature where $\rho = 0$ as before, and each of these samples is seen move from a completely insulating state (no superconducting downturn to the lowest experimentally accessible temperature of T = 80 mK) to a fully superconducting state after 3 weeks of annealing ($T_c = 6$ K).

6.5.5 YBa$_2$Cu$_4$O$_8$

Both the a and b axis resistivity of YBa$_2$Cu$_4$O$_8$ has been studied extensively by Hussey *et.al.* [138]. We present their data, along with the data for three of our samples in the left panel of figure 6.11. Calculating the resistivity of our samples using the measured values of the geometric factor yields curves that are considerably different in magnitude than those appearing in the literature. Scaling our data by a factor ranging from 1.5-2.1 however shifts our curves to lie precisely on top of those reported by Hussey *et.al*. This large scaling factor is outside the margins of error estimated from the calibration of the SEM, but not completely unexpected due to the exceedingly small size and irregular

---

[3]A very small downturn was seen for sample K

[4]The full resistivity curves are displayed in chapter 11
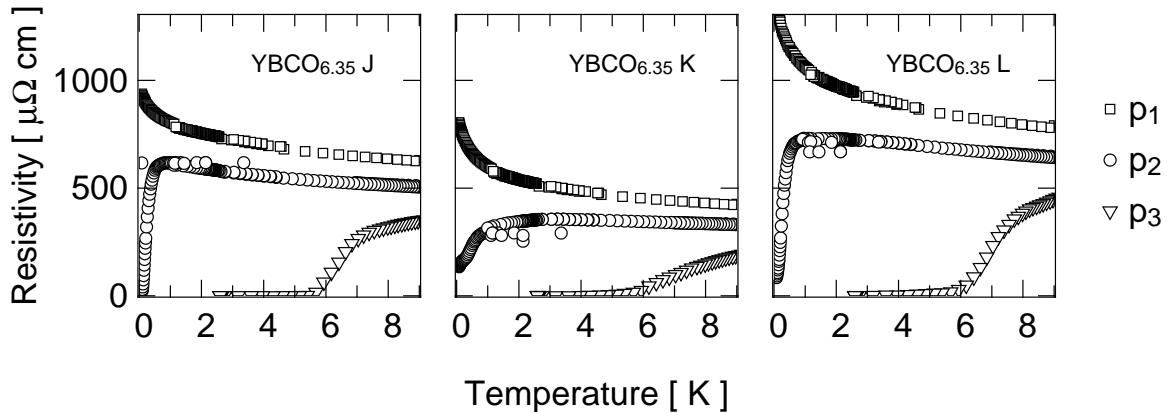
Figure 6.10: The low temperature resistivity of $YBa_2Cu_3O_{6.33}$ samples J,K and L, for different anneals. State p_1 corresponds to freshly quenched samples ($\sim$ 5 hours annealing). State p_2 corresponds to 2 days of annealing, while p_3 is after 3 weeks (essentially fully annealed).

shape of the crystals. Given that Hussey *et.al.* have studied many samples, and cite an overall error of only 25 % in their measurements [138] of ρ_a and ρ_b, we choose to define our geometric factors by this normalization method. Thus α_{geo} changes from 2.3 $\times 10^{-3}$, 3.2 $\times 10^{-4}$ and 8.1 $\times 10^{-5}$ cm to 3.4×10^{-3}, 8.2×10^{-4} and 1.6×10^{-4} cm for samples A, B and D respectively. From the shapes of the temperature dependence of the resistivity it is clear that samples A and B are oriented along the a-axis while D is a b-axis oriented sample.

The resistive T_c for our samples, which is unaffected by issues of geometric factor uncertainty, is observed to be 78 $\pm$ 1 K for all 3 crystals, essentially the same as that quoted in the literature [137, 138]. The large anisotropy between a and b axis transport is the result of the crystal structure - the double-full chains provide an additional channel of conduction over the planes alone. This anisotropy is significantly larger than in the $YBa_2Cu_3O_y$ compound, $\rho_A/\rho_B = 3$ for $YBa_2Cu_4O_8$ versus 2.2 for $YBa_2Cu_3O_{6.95}$ [120, 149]. The change in slope of ρ_a at around 180 K has been proposed to correlate with the suppression of spin scattering [141] that occurs at the pseudogap temperature (T^*), although recent work [138] has suggested that the this suppression of the in-plane scattering rate occurs over a much wider temperature range above T^*.
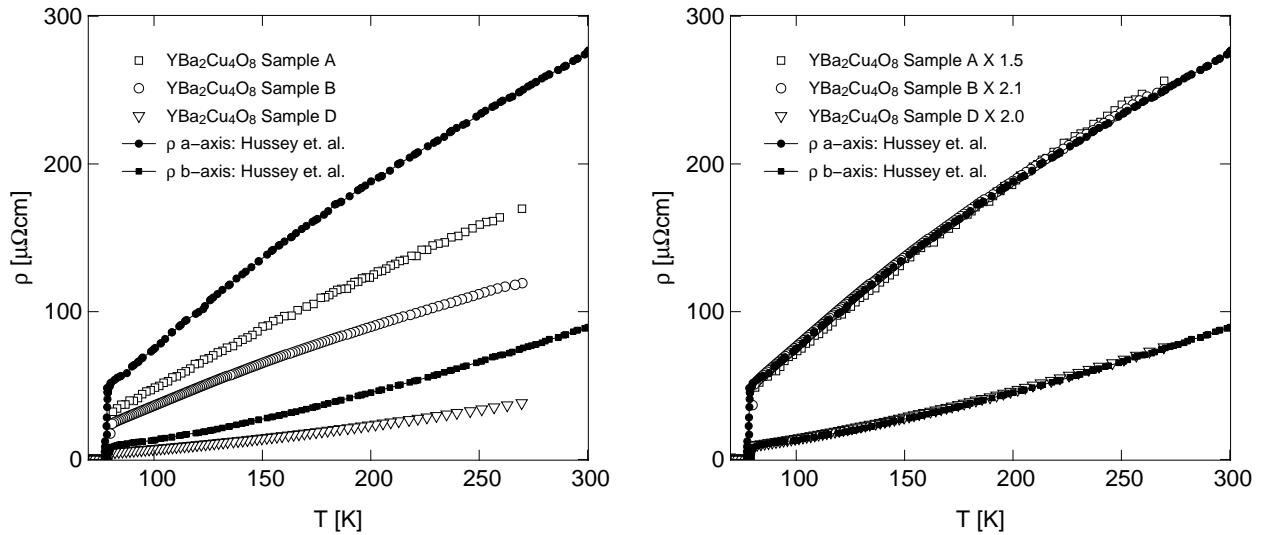
Figure 6.11: Resistivity for $YBa_2Cu_4O_8$ samples A,B and D. The left hand figure shows the raw data using the measured values of geometric factors listed in appendix 1, alongside data on a and b-axis aligned samples from the literature [138]. The right hand figure shows the data for samples A,B and D scaled by a factor to match the data of Hussey *et.al.*

6.6 Doping dependence of ρ: trends, analysis and comparison to the literature.

In figure 6.12 the resistivity of a selection of our samples spanning a large portion of the superconducting region of the phase diagram is shown alongside resistivity on similar samples found in the literature [150]. In this study, Ando *et.al.* carefully controlled the Oxygen content in a series of detwinned samples, using iodometry [151] to measure y. For low doped samples, their approach is to quench the samples directly after growth [148] and ignore the physics of the long range ordered state. This is evident in the resistivity curves for our highly ordered ortho-II phase $YBCO_{6.5}$, compared to their disordered samples. The T_c measured by Ando *et.al.* is some 15 K lower than ours, and the room temperature resistivity is almost twice as large.

The overall phenomenology of our resistivity versus doping data seems to follow that of the literature results: the magnitude of the resistivity decreases with increasing doping, as one would expect for an increased carrier concentration. It is near linear with T at y=6.95, and crosses over to an s-shaped curve for moderately underdoped materials before possessing an upturn at low T for the $y = 6.35$ sample. Attempts have been made to assign a "characteristic temperature" or T^* to the point at which the resistivity devi-

ates from linearity in the underdoped regime, believed to be associated with the opening of the pseudogap [152, 153]. This quantitative analysis is however rather subjective for two primary reasons. First, paraconductivity arising from superconducting fluctuations well above T_c may result in a negative curvature [150, 154] and second, data to high temperatures is often not available to determine whether a true inflection point is present, or merely an extended roll-off [138]. Recently, work by Ando and others [150] has focused on using the second derivative of ρ_{ab} in YBCO, LSCO and $Bi_2Sr_{2-x}La_xCuO_{6+\delta}$ (BSLCO) as a criteria for determining the correct value of T^*, and found a generic doping dependence that suggests that the pseudogap closes near optimal doping.

The role that the pseudogap plays in influencing the shape of the resistivity curves in the underdoped regime is still the subject of some debate. The underlying physics almost certainly lies in the partial destruction of the Fermi surface below T^* as observed by ARPES [155], but precisely how this determines the temperature dependence of ρ_{ab} is not yet fully understood. The s-shaped curvature of the data has been proposed by some authors to be the result of a rapid suppression of the inelastic scattering rate of the electrons upon entering the pseudogap phase [152]. Others have linked the feature to thermally induced $(\pi, 0)$ quasiparticles which play an increasingly important role in transport at high temperatures [156].

At very low dopings, the upturn at low T has been interpreted as a signature of an insulating ground state [157]. In our own data on very pure YBCO at low dopings, the magnitude of the upturn is however greatly reduced, and we discuss this data in detail in chapter 11.

6.6.1 Determination of y from ρ

For our YSZ grown samples with y in the range 6.55-6.85 we use curves from the literature to estimate the Oxygen content. Since long range Oxygen order was not present in samples in this doping range we expect our resistivity curves to match those reported by Ando [148, 150]. Using literature values of ρ_{300K} and T_c versus y we establish the Oxygen concentration for underdoped, detwinned samples K,O,S and T as shown in figure 6.13. In the left panel, we choose a value of y which matches the observed T_c onto the trend from the literature. This yields $y = 6.52, 6.54, 6.75, 6.85$ for samples K,O,S and T respectively. In the right panel, we fit the values of ρ_{300K} versus y and find reasonable agreement to the form of $\rho_{300K} = -380 + 466 \times (y - 6.208)^{-1}$. Adjusting y for our crystals to match the resistivity onto this empirical fit, we get $y = 6.59, 6.60, 6.85$ and 6.83 for
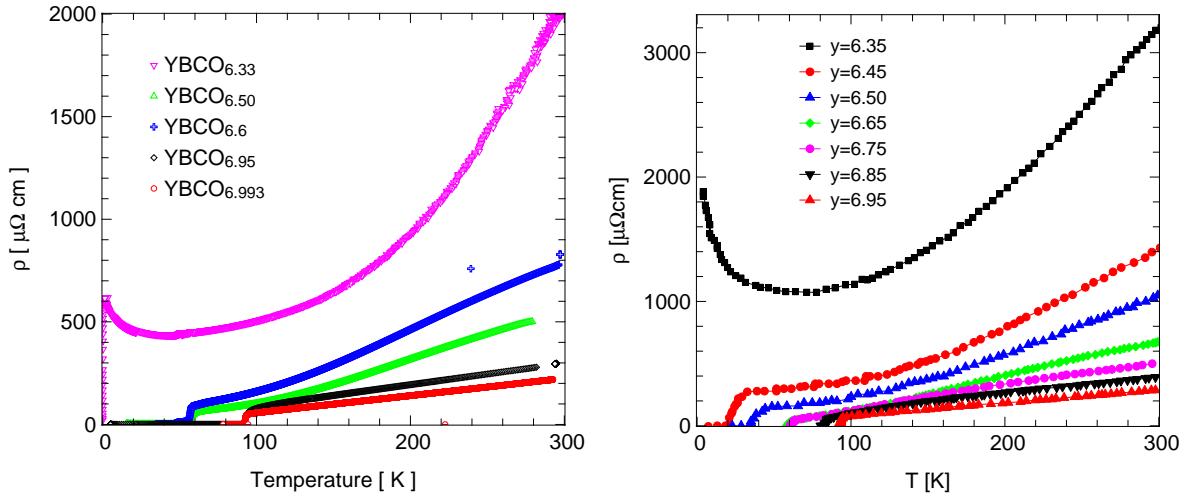
Figure 6.12: **Left** :The resistivity versus temperature for a selection of YBCO samples discussed which span the doping phase diagram. The current is along the a-axis in all cases, except for the YBCO$_{6.35}$ sample, where it was in the plane, and contained contributions from ρ_a and ρ_b. **Right** : Resistivity curves selected from the literature for comparison.

K,O,S and T. Both methods yield very similar values of y, and we take the average of the two fits to set the Oxygen concentration. We thus take the final values of y to be $6.55 \pm 0.03, 6.57 \pm 0.03, 6.79 \pm 0.04$ and 6.85 ± 0.02 for K,O,S and T respectively. This exercise is mainly for nomenclature purposes, as the hole concentration p was estimated independently of y, as discussed in the next section.

6.7   Determination of hole concentration

The determination of the planar hole concentration in the YBCO family is challenging for a number of reasons. First, unlike the LSCO family where cation substitution of Sr^{2+} for La^{3+} directly introduces 1 hole per Sr atom, there is no analogous correlation between Oxygen concentration and p. Secondly, as has been demonstrated conclusively in the preceding chapter, the co-ordination of the Oxygen plays a role in determining the hole concentration. Two structures with identical y can have different p and consequently T_c. We take the view that rather than determine p from y, we should instead try to infer p from T_c, which is an easy experimental quantity to access.

A systematic study of the evolution of T_c with hole concentration was performed by Presland *et.al.* [158] in the $Tl_m(Ba,Sr)_2Ca_{n-1}Cu_nO_{2n+m+2+\delta}$ compounds, where n=1,2,3 m= 1,2 and δ is the adjustable Oxygen concentration. Using their results, and the earlier studies [159, 160] of T_c vs. p in the LSCO system Presland *et.al.* proposed the well-known
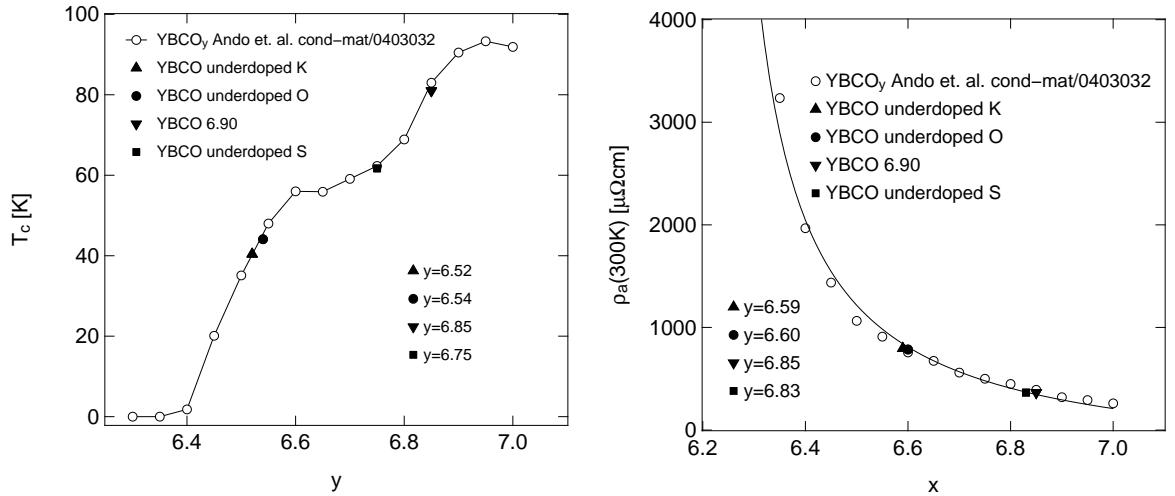
Figure 6.13: **Left**:The superconducting transition temperatures versus iodiometric Oxygen concentration as determined by metric titration in the literature [150]. For samples where we do not know the Oxygen concentration directly, we assign a value of y that scales the T_c onto the curve. **Right**: a-axis resistivity at 300 K versus y reported by Ando *et.al.* [150]. We scale the values for our unknown samples onto the curve by choosing an Oxygen concentration to match the fit.

relation:

$$T_c/T_c(max) = 1 - 82.6(p - 0.16)^2 \tag{6.1}$$

We note that this is in essence an *empirical* result, but one that is widely accepted within the community.

Using equation 6.1 we now estimate the planar hole concentration for each of our samples. For the $YBa_2Cu_3O_y$ system we take T_c^{max} to be 93.5 K. For the $YBa_2Cu_4O_8$ system we take T_c^{max} to be the same, with the understanding that the system exists at only one doping, which is naturally underdoped. Tables 6.1 and 6.2 summarize the values of T_c inferred from ρ and χ in the sections above, as well as the calculated p. For samples that were annealed at room temperature, the p value is given at each anneal. The doping for the initial annealed state of $YBCO_{6.33}$ J,K and L, which were non-superconducting was estimated by extrapolating backwards on a logarithmic plot of hole doping versus time, since p is known to evolve in a logarithmic manner. This procedure estimates p=0.048 for each sample, although the error bars due to the extrapolation process are likely on the order of $\pm$ 0.005.

Table 6.1: T_c and p values for YBCO samples in the doping range $y = 6.50$ - 6.99. T_c was determined by ρ and χ'_{AC}, and p was estimated from 6.1.

Sample	$T_c\rho{=}0$ (K)	p - holes/Cu
YBCO$_{6.99}$ UBC	90.4	0.178
YBCO$_{6.95}$ A	92.8	0.151
YBCO$_{6.95}$ D	93.2	0.154
YBCO$_{6.95}$ McGill	93.5	0.16
YBCO$_{6.85}$ T	81	0.120
YBCO$_{6.55}$ K	40	0.077
YBCO$_{6.57}$ O	44	0.080
YBCO$_{6.79}$ S	62	0.096
YBCO$_{6.7}$ Q	66	0.101
YBCO$_{6.50}$ B	55	0.089
YBCO$_{6.50}$ C	55	0.089
YBCO$_{6.0}$ (A,C,D,E)	-	0
YBa$_2$Cu$_4$O$_8$ (all samples)	78	0.115

6.8 Chapter summary

Using measurements of resistivity and susceptibility, we have established the superconducting transition temperatures for each of our samples of YBCO. We use the criteria $\rho{=}0$ to establish T_c, and in samples with broad resistive transitions we confirm this by measuring χ'_{AC}, which is insensitive to surface superconductivity. Using the empirical relation of Presland *et.al.* [158] we estimate the planar hole concentration as summarized in tables 6.1 and 6.2. From these tables, it is apparent that the many samples we have grown or acquired from collaborators cover a wide swath of the cuprate phase diagram - from slightly overdoped superconductor to Mott insulator.

Table 6.2: T_c and p values for highly underdoped YBCO samples with $y = 6.33\text{-}6.35$. T_c was determined by ρ and χ'_{AC}, and p was estimated from 6.1. The anneal time is counted from when the samples were first warmed to room temperature after storage on dry ice.

Sample	$T_c\rho{=}0$ (K)	p - holes/Cu	Anneal time (days)
YBCO$_{6.35}$ B	4	0.0523	10
YBCO$_{6.35}$ B	11	0.0566	350
YBCO$_{6.35}$ H	0.5	0.0502	0.13
YBCO$_{6.35}$ H	0.8	0.0504	0.25
YBCO$_{6.35}$ H	0.9	0.0505	0.46
YBCO$_{6.35}$ H	1.4	0.0508	1.5
YBCO$_{6.33}$ J	-	0.048	0.17
YBCO$_{6.33}$ J	0.1	0.0503	2
YBCO$_{6.33}$ J	5.5	0.0533	29
YBCO$_{6.33}$ K	-	0.048	0.21
YBCO$_{6.33}$ K	-	0.0500	2
YBCO$_{6.33}$ K	5	0.0529	29
YBCO$_{6.33}$ L	-	0.048	0.25
YBCO$_{6.33}$ L	0.1	0.0500	2
YBCO$_{6.33}$ L	6.0	0.0536	29

7

THERMAL CONDUCTIVITY OF YBCO, $T > 1$K

7.1 Chapter overview

To further characterize our samples we performed a series of high temperature thermal conductivity measurements using the techniques and instrumentation described in chapter 4. In this chapter I present these results, and discuss the conclusions that one may draw from the data. This is the first time such a study has been reported on a series of high quality, detwinned YBCO single crystals as a function of doping. In particular I show how high temperature κ measurements provide us with an independent bulk measurement of T_c, and allow us to estimate the relative impurity scattering rate between samples of similar dopings. The level of intrinsic disorder in optimally doped samples of YBCO from different crystal growers is established and compared to other members of the high-T_c cuprate family. We confirm that YBCO samples grown in $BaZrO_3$ crucibles are of superior purity than those grown using other methods.

7.2 Measurements of κ at $T > 1K$ in $YBa_2Cu_3O_y$

The high temperature ($T > 1$ K) thermal conductivity of our crystals was measured in the ^4He dip probe described in section 4.2.1. The data for a selection of mostly detwinned single crystals at various dopings is shown as a function of temperature in figure 7.1. The samples were oriented such that $\mathbf{J} \parallel \mathbf{a}$[1], in order to eliminate the contributions from the oxygen chains. For moderately underdoped ($y = 6.5$) to overdoped ($y = 6.99$) samples the distinguishing feature of the curves is the large peak centered between 20 and 40 K, which crosses over to a T independent plateau at higher temperatures. The peak position is seen to be sensitive to doping, and falls to lower temperature as carrier concentration is reduced. The peak height also decreases as doping is lowered, although samples that

---

[1]Samples with y=6.33,6.35 are near the orthorhombic-tetragonal transition and are twinned, so $\mathbf{J} \parallel \mathbf{ab}$
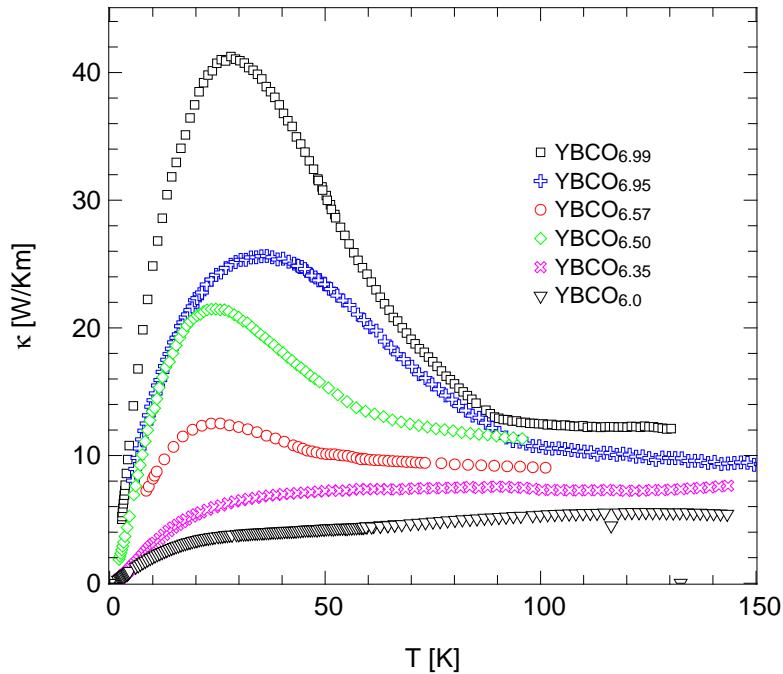
Figure 7.1: The high temperature thermal conductivity for samples of $YBa_2Cu_3O_y$ of various dopings. The current was along the *a*-axis for all samples except *y*=6.35 and 6.0, in which current flowed in the *ab*-plane.

are quite close in y often display significantly different values of κ_{peak}. For very low doped ($y = 6.35$) to undoped ($y = 6.0$) the peak vanishes, and the thermal conductivity monotonically increases from low T to a plateau at higher temperatures.

As discussed in chapter 2 the two dominant heat transport mechanisms in metals are phonons and electrons. We can use the Wieddeman-Franz law introduced in section 2.3 to obtain a rough estimate as to the magnitude of κ_{el} and κ_{ph} in YBCO. Since the Sommerfeld value of the Lorenz number is only realized at very high and very low temperatures, we use the resistivity at 300 K from figure 6.12 and the thermal conductivity of the samples in the plateau region ($T > 100$ K) of figure 7.1[2]. Taking the optimally doped sample with y= 6.95 as an example, we see that $\kappa_{300K} = 10$ W/Km and $\rho_{300K} = 270\ \mu\Omega$. Using the WF law with $L_0 = 2.45 \times 10^{-8}$ W/Km, the electrical resistivity yields a thermal conductivity of 2.8 W/Km, or 30 % of the total conductivity at 300K.

This rough calculation illustrates the difficulty in distinguishing between the electronic and phononic carriers over a wide range of temperatures, when inelastic scattering

---

[2]Previous studies to higher temperatures have indeed shown that the thermal conductivity remains more or less constant for $T > 100$K [161]

processes cause the Lorenz number to vary with T. It is for this reason that the origin of the peak in the thermal conductivity has been the subject of some controversy. Some authors [162, 163, 164] have proposed that its origin lies in an enhancement in the phononic mean free path when Cooper pair formation reduces electron-phonon scattering. Others have proposed[165] that the peak is in fact electronic in origin, arising from an enhanced quasiparticle lifetime due to reduced quasiparticle-quasiparticle scattering in the superconducting state.

In recent years considerable evidence has amassed to support the latter scenario, which we take to be correct. A key piece of evidence is the observation of the collapse of the quasiparticle relaxation rate just below T_c, as observed through microwave measurements [166]. The field dependence of κ in YBCO single crystals also allows a separation of the phononic contribution, and the resulting electronic contribution has a strong peak at intermediate temperatures [167]. In contrast, the temperature dependence of κ_{ph} is found to be featureless in the vicinity of T_c. The most convincing evidence to support the quasiparticle peak scenario is found in thermal Hall measurements, where the Hall thermal conductivity κ_{xy} is measured in a magnetic field. Zhang *et.al.* [168] observed a 1000 fold increase in κ_{xy}/B between T_c and 30 K in a YBCO$_{7.0}$ sample, which must be a direct result of rapidly increasing quasiparticle lifetimes below the superconducting transition since the phonon conductivity is not affected by field.

Drawing from these measurements, the interpretation of the T dependence of the thermal conductivity is as follows. At high T, the temperature dependence is roughly flat, and comprised of phonon and electron contributions of comparable magnitude. As one cools to near T_c, a slight rise is seen in some samples, which has been attributed as a T^{-1} contribution arising from a phonon-phonon Umklapp process [169]. Below T_c inelastic quasiparticle scattering is drastically reduced as electrons form Cooper pairs and disappear into the condensate. As the superfluid density increases, the conductivity of the uncondensed electrons also increases, until elastic scattering associated with crystal impurities and defects becomes dominant. The conductivity of both electronic and phononic channels decreases at the temperature is lowered further, as thermal activation of both quasiparticles and phonons is reduced.

7.3 Evolution with doping: analysis and comparison to the literature

Although a study of κ versus doping in this temperature regime has not been attempted on detwinned samples, we may compare our results to available data on twinned crystals [161, 169, 162]. For the most part the thermal $a - b$ anisotropy is quite small in this temperature range, and observed to be on the order of 10 % [169]. In the normal state, for $T > T_c$ the conductivity in our data seems to be the largest for the two near stoichiometric samples - $YBCO_{6.99}$ and the ortho-II ordered $YBCO_{6.50}$. Since the normal state conductivity is dominated by phonons, this observation is well described by the model of Takenaka *et.al.* [169], who propose that at high temperature $\kappa_{ph} = (W_0^{ph} + \alpha T)^{-1}$ where W_0^{ph} and αT are the phonon thermal resistivities due to phonon defect and phonon-phonon scattering respectively. In this scenario the y dependence of κ_{ph} is determined by oxygen disorder in the chains, which is minimized in the two stoichiometric samples as originally suggested by Popoviciu and Cohn [161]. This also provides an explanation of why the normal state thermal conductivity in our detwinned samples is greater than that of twinned crystals for all dopings [162], since phonon scattering from microscopic twin boundaries almost certainly contributes to W_0^{ph}.

In the superconducting state, the position of the peak is seen to shift downwards with doping. Inyushkin *et.al.* [162] have reported a similar trend, observing a peak at 27 K for a sample with $y = 0.48$. The position of the peak in temperature is expected to vary strongly with disorder [165], so it is possible that the oxygen chain order plays a role in influencing this trend. The overall peak height itself is seen to be reduced at lower dopings in our data, and in the literature for twinned [162, 169] and detwinned[167] single crystals, as well as polycrystalline samples [161] .

For the insulating $y = 6.0$ sample the data we observe seems to differ significantly from that reported in the literature. Takenaka *et.al.* [169] have reported that in a sample of $YBCO_{6.06}$ κ at 100 K is some 3 times greater than that of a sample with $y=6.35$. The temperature dependence for the $y=6.06$ sample is also complex, possessing a double peak structure that is attributed to either heat conduction by magnons, or an anomalous phonon damping mechanism due to tilt distortions of the CuO polyhedra [170]. Our $y=0$ however sample shows a flat, featureless curve with a low conductivity. Further work is needed to clarify this discrepancy.

7.4   Determination of T_c from κ

The dramatic increase in the quasiparticle lifetime below T_c is reflected by a sharp kink in the thermal conductivity at T_c, which we use as a bulk measurement of the transition temperature in samples where it is evident. As doping is decreased, and the overall quasiparticle contribution to the heat current is reduced, this kink is less and less pronounced. At the same time superconducting fluctuations may have a rounding effect near T_c [171, 172] which is likely more pronounced in the underdoped regime where the phase stiffness is lowered. Figure 7.4 shows a close up of the transition region for selected samples in the doping range y=6.5 - 6.99. We determine the T_c from these plots by drawing straight line fits to the data above and below the kink, and taking the intersection of these lines as the transition temperature. The error in this value is determined by the point at which the straight line fit departs from the data, as indicated in the figure. The zero field T_c determined from κ for several dopings is listed alongside the values determined from resistivity[3] in table 7.1.

Table 7.1: Superconducting transition temperatures estimated from the rise in κ at T_c, from figure 7.4.

Sample	T_c, ρ=0 (K)	T_c, κ (K)
YBCO$_{6.99}$ UBC	90.4	89.2 $\pm$ 2
YBCO$_{6.95}$ A	92.8	94 $\pm$ 2
YBCO$_{6.57}$ O	44	51 $\pm$ 4
YBCO$_{6.50}$ B	55	60 $\pm$ 3

This exercise serves as a check of the quality and homogeneity of our samples, since the T_c determined in this manner is a bulk property of the sample. From this data it can be seen that for the most part the transition temperatures determined via the two methods agree fairly well. The lower doped samples each give T_c's slightly higher than those measured by ρ, but the transitions are somewhat smeared in the κ data and thus have larger errors associated with them.

---

[3]Define previous sections as where ρ=0.
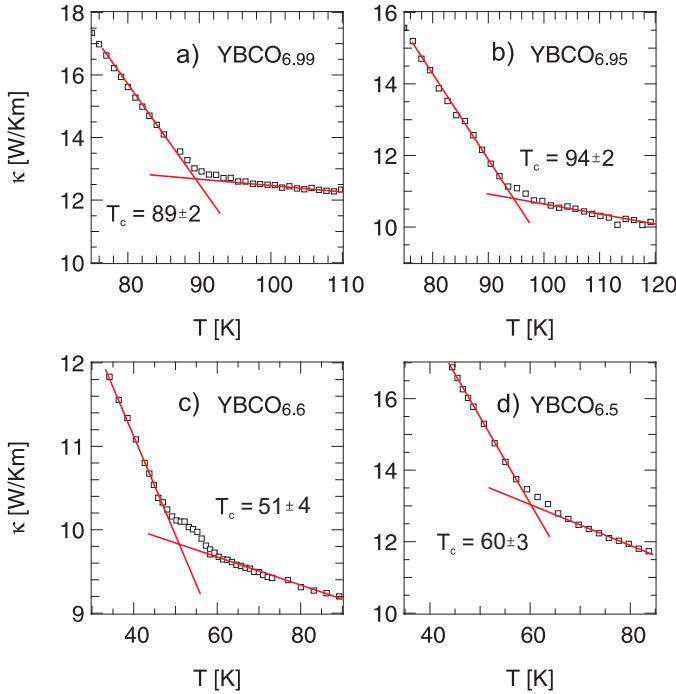
Figure 7.2: The kink observed in high temperature thermal conductivity data near the superconducting transition. We use this feature to identify a bulk T_c by fitting straight lines to the data above and below the kink and defining T_c by their intersection.

7.5   Purity dependence: YSZ vs. BaZrO$_3$ grown samples

The dramatic difference in the superconducting state peak height between the YSZ grown YBCO$_{6.95}$ and the BaZrO$_3$ grown YBCO$_{6.99}$ cannot be accounted for by the small change in doping level. For optimally doped YSZ grown crystals, several measurements of the peak height and normal state plateau values of κ_a have been made [167, 169, 162] and our values compare quite well. The average literature value for the peak is around 22 W/mK with a peak-to-plateau ratio of approximately 2. In all cases the thermal conductivity of our samples is much greater than pressed polycrystalline samples [161], as expected since scattering from grain boundaries may significantly degrade a heat current.

Measurements of κ_a on BaZrO$_3$ grown samples of YBCO$_{6.99}$ have previously been reported [168], and the data is quantitatively consistent with ours. Our peak height is slightly larger than 40 W/mK and the peak-to-plateau ratio is roughly 3 in both sets of data. The clear trend from both the literature and our own measurements is that the higher quality BaZrO$_3$ grown samples have much larger peaks, suggesting a close relationship between peak height and sample purity.
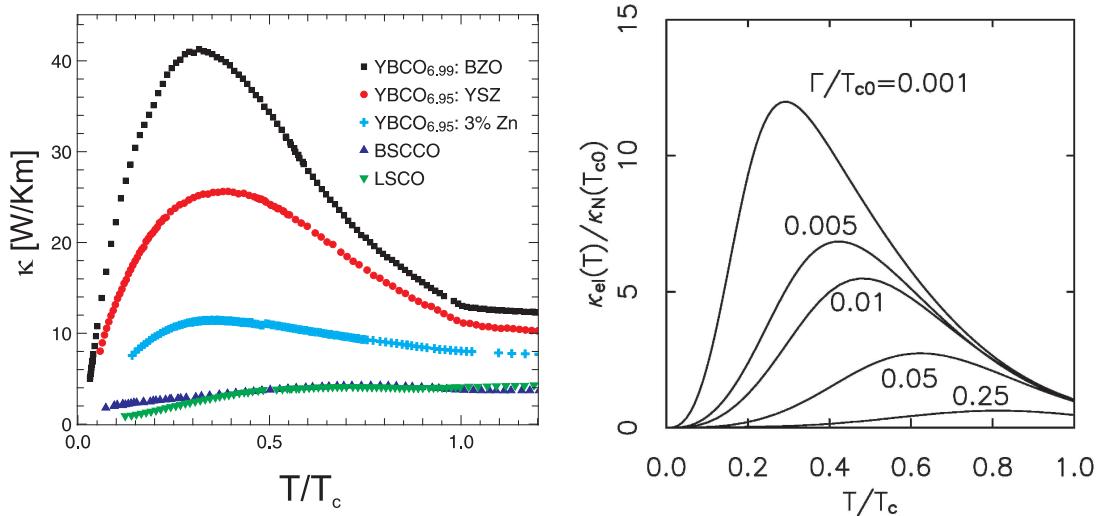
Figure 7.3: **Left** : Thermal conductivity at high temperatures shown for several optimally doped cuprates. The data is plotted versus T/T_c to facilitate comparison with the theory of Hirschfeld and Puttika [165]. **Right** : The ratio of the peak height to plateau value above T_c is a direct consequence of the impurity scattering rate within a crystal, allowing one to estimate the relative amount of impurities. From the theory of Hirschfeld and Puttika[165].

This observation is well described by the theory of Hirschfeld and Puttika [165], who have studied in detail the dependence of the peak in κ on the elastic scattering rate Γ. Assuming unitary scattering, the normal state scattering rate is given by $\Gamma = n_i n/\pi N_0$ where n is the electron density, N_0 is the density of states at the Fermi level, and n_i is the impurity concentration. The authors evaluate the thermal conductivity of a d-wave superconductor, assuming unitary elastic scattering by impurities and inelastic scattering by spin fluctuations. The calculated electronic contribution to thermal conductivity normalized by the value of κ at T_c is plotted as a function of T/T_c in the right side of figure 7.3. The authors predict a monotonic dependence of peak height and position as Γ is varied. The peak position itself is pushed to higher temperatures for large Γ, resulting from the fact that the rapid growth in quasiparticle mean free path is cut off at higher and higher energy scales. The peak height is also seen to be strongly dependent on scattering rate, with the rough relation that a factor of ten increase in Γ results in a factor of 2 decrease in peak height. These results were verified in data supplied by Taillefer *et.al.* on a set of YBCO crystals [165] with controlled Zinc impurity levels. Data for a sample with 3% Zn impurities (determined from T_c suppression) is shown in figure

7.3, alongside our optimally doped YSZ and $BaZrO_3$ grown YBCO. Data from optimally doped LSCO measured in our lab [62], and $Bi_2Sr_2CaCu_2O_8$ from the literature [173] is also plotted.

In the 3 % Zn-doped YBCO sample the addition of this level of impurities causes the peak to nearly vanish. The corresponding residual resistivity extrapolated from the linear temperature dependence of $\rho_a(T)$ goes from being negative in the nominally pure crystal to $\rho_0 = 30$ $\mu\Omega$ cm in the Zn-doped crystal. In the optimally-doped LSCO sample, ρ_0 is estimated to be 33 $\mu\Omega$ cm [62], and the peak is suppressed even further. This is true despite the high chemical purity of the crystal, and is likely a result of the Sr atoms acting as scattering centres.

By comparing to the peak heights to the curves of Hirschfeld and Puttika, we then estimate that the *relative* scattering rates between the crystals are 1:10:100 for the $BaZrO_3$ grown YBCO, the YSZ grown YBCO and the BSCCO and LSCO respectively. In other words, the highest purity YBCO has a relative level of disorder some 100 times smaller than in LSCO and BSCCO. In YBCO this estimate is directly supported by microwave spectroscopy measurements of thermally-excited quasiparticles in the elastic scattering limit. These experiments reveal that the scattering rate in the superconducting state is some 12 times greater for optimally-doped YBCO grown in YSZ crucibles [174] compared to the slightly overdoped $y = 6.99$ samples grown in BZO crucibles [117].

7.6   High temperature thermal conductivity of $YBa_2Cu_4O_8$

Several attempts to measure the thermal conductivity of the $YBa_2Cu_4O_8$ samples to high temperature were made, however due to their small size and large thermal resistances we were unfortunately not able at the time of writing to obtain definitive results on these crystals.

Data on samples similar to ours is available in the literature however, and from this we are able to compare this compound with $YBa_2Cu_3O_y$. Figure 7.4 shows the high T a-axis κ data from Kohn and Karpinski [175] compared to samples of optimally doped $YBa_2Cu_3O_y$ measured in our own lab. The dramatically enhanced peak is the highest yet observed for the cuprates, some 3 times larger than that in the most pure $YBa_2Cu_3O_y$. This is certainly a result of the extremely low levels of oxygen chain disorder present in the stoichiometric Y-124 compound. Using the theory of Hirschfeld and Puttika discussed above, we estimate that these compounds have an impurity scattering rate some 10
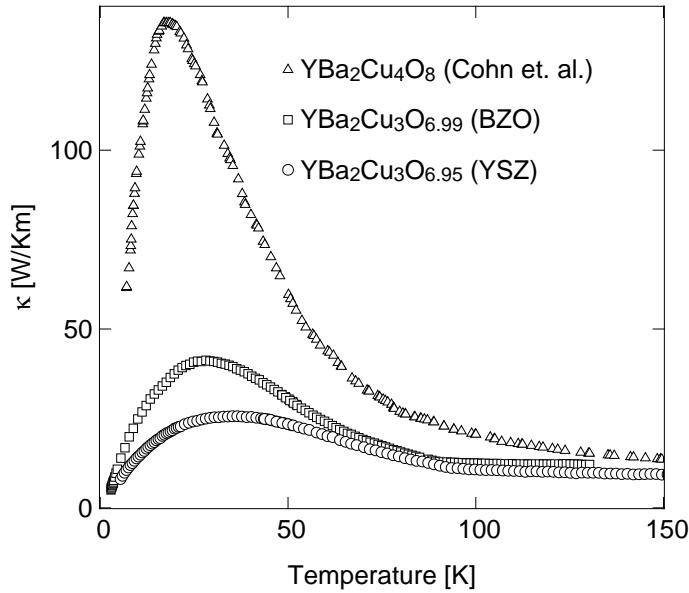
Figure 7.4: Thermal conductivity at high temperatures along the *a*-axis for YBa$_2$Cu$_4$O$_8$ samples from the literature [175] alongside YBa$_2$Cu$_3$O$_y$ samples measured in our own laboratory. The dramatic difference in peak height is likely due to the absence of oxygen chain disorder in the YBa$_2$Cu$_4$O$_8$ system.

times and 100 times lower than the BaZrO$_3$ and YSZ grown samples of YBa$_2$Cu$_3$O$_y$, respectively. These are the lowest-disorder cuprates yet produced, by a wide margin.

7.7   Chapter summary

Measurements of thermal conductivity at temperatures greater than 1 K have yielded important characterization information on our YBCO crystals. The bulk T_c of a selection of samples was checked by observing at what temperature the rise in the thermal conductivity began, and was found to agree with estimates from measurements of ρ. By noting the ratio of the peak heights to plateau values in κ between various samples and systems, we were also able to establish an estimate of the relative elastic scattering rates and thus the intrinsic disorder within.

8

The doping dependence of κ_0/T in $\mathrm{YBa_2Cu_3O_y}$

8.1 Chapter overview

In a d-wave superconductor, the presence of nodes in the gap structure leads to quasiparticle excitations down to zero energy in the presence of even small amounts of disorder [176, 177]. These delocalized excitations carry both charge and heat, and provide a direct measure of the low-energy quasiparticle spectrum [59]. In this chapter, I present work which uses the well-established and robust connection between low-temperature heat transport and the energy spectrum of a d-wave superconductor to probe the evolution of low-energy quasiparticles and the superconducting gap as a function of doping in both YBCO and LSCO. These results appear in reference [1] and in the conference proceeding of the 2003 M2S conference [6].

8.2 Samples

In addition to the YBCO samples described in detail in chapter 6, we make use of single crystal samples of $\mathrm{La_{2-x}Sr_xCuO_4}$ for comparison purposes. The LSCO samples were all grown in an image furnace using the travelling-solvent floating-zone technique and have Sr dopings of $x = 0.06$ (samples A and B), 0.07, 0.09, 0.17 and 0.20. In addition, a non-superconducting LSCO sample with $x = 0.05$ was also measured. With the exception of $x = 0.06$ B, all samples were measured as grown. This may result in off-stoichiometric oxygen content in the samples. The $x = 0.06$ B sample was annealed in flowing argon overnight at 800°C in an attempt to fix the oxygen content. The argon annealing, however, had little effect on our results as both $x = 0.06$ samples gave the same electronic contribution to the thermal conductivity. A detailed description of the growth and characterization of this series of crystals is available elsewhere [62].

In LSCO, the hole concentration per Cu in the $\mathrm{CuO_2}$ planes, p, is taken to be the Sr concentration, x. In YBCO, we use the values of p determined in chapter 6 using

the empirical relationship of Presland and Tallon [158], equation 6.1. Although different criteria may be used for determining the value of the hole doping level in both the LSCO and YBCO systems, we note that small errors in our estimation of hole concentration do not noticeably affect the trends observed in our thermal conductivity data.

8.3   Low temperature measurements of κ

8.3.1   YBCO
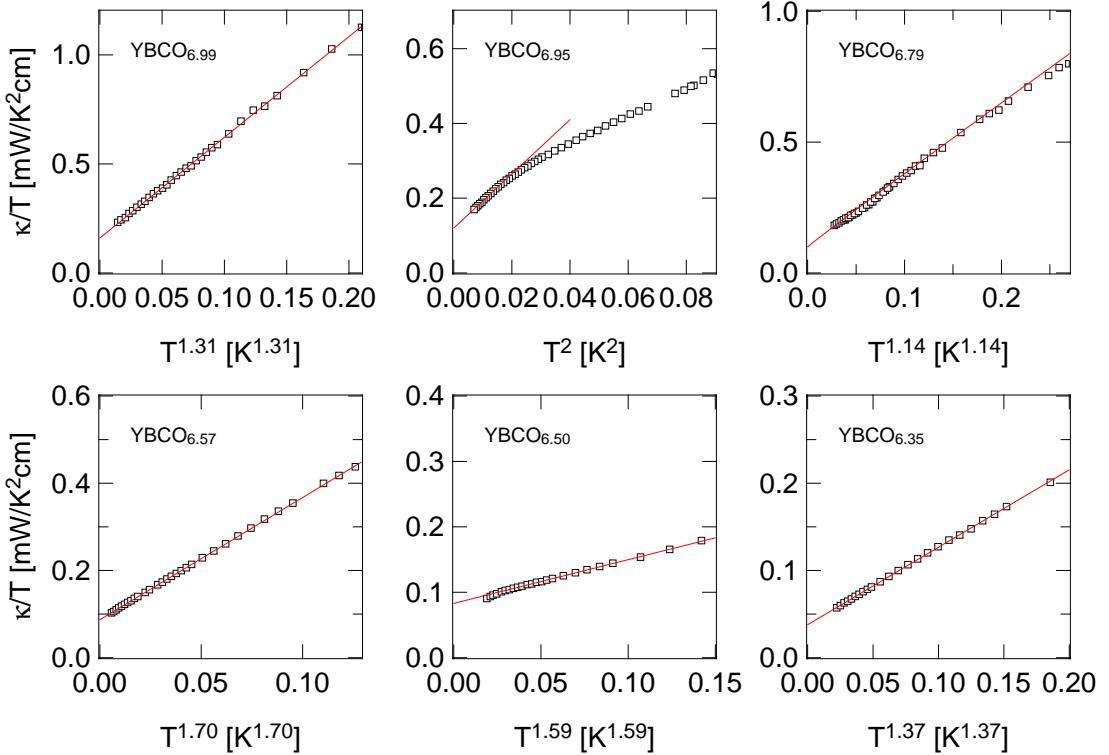
Figure 8.1: The thermal conductivity divided by temperature for samples of $YBa_2Cu_3O_y$ of various dopings. The x-axis is plotted as T^α, where α is the powerlaw fitting exponent introduced in section 2.6.2, and is scaled such that the range of temperature displayed is 0-300mK. For the y=6.95 data we plot versus T^2 since the data is limited in range. The thermal current was along the a-axis for all samples except y=6.35 and, in which current flowed in the ab-plane, as the sample was twinned.

The low-temperature thermal conductivity of the YBCO samples is shown in the panels of figure 8.1. For samples where data to $T > 600mK$ is available, we use the powerlaw extrapolation procedure discussed in section 2.6.2 to determine the value of the residual linear term, κ_0/T. For the optimally doped y=6.95 sample, where data is only available to 300 mK, we use the older method of extracting the linear term involving an

extrapolation of κ/T on a T^2 plot to be consistent with previously published data [1]. The overall trend with doping is immediately evident from figure 8.1: κ_0/T decreases steadily with underdoping, all the way from the slightly overdoped to the highly underdoped regime. The exponent and temperature coefficient of the powerlaw fits do not appear to follow any clear trend with doping, although in general the value of α is much lower then the simple boundary scattering limit of $\alpha+1=3$. A summary of the values for the YBCO samples, as well as the LSCO samples discussed in section 8.3.2 are given in Table 8.2. Finally, we note that a measurement on a fully deoxygenated YBCO sample with $y=6.0$ correctly yields a zero intercept: $\kappa_0/T = 0 \pm 1$ μW K^{-2} cm^{-1}.

8.3.2   LSCO

The low temperature thermal conductivity for the LSCO samples is shown in the two panels of figure 8.2, and details on the analysis and powerlaw fits can be found elsewhere [62]. The values for our LSCO agree with those published in a previous study [154], with the exception of their $x = 0.17$ sample which has been measured to give a value of κ_0/T which is approximately twice the value we observe. We attribute this difference to the fact that the crystal studied by Takeya $et.al.$ had a T_c of 40.2 K compared to our T_c of 34.2 K, pointing to a slightly higher hole concentration (likely due to different oxygen levels within the crystals). The trend with doping of the residual linear term is identical that for LSCO, although the rate at which κ_0/T is suppressed with underdoping is much faster in LSCO.

8.4   Doping dependence of κ_o/T

Let us analyse these results within the framework of the standard d-wave BCS theory discussed in chapter 3. In the dirty limit at low temperature, when $k_BT \ll \gamma \ll k_BT_c$, where γ is the impurity bandwidth, the quasiparticle thermal conductivity can be written in the form of equation 3.14 [59] which relates the residual linear term to values of v_F and v_2, the quasiparticle velocities normal and tangential to the Fermi surface at the nodes respectively. These are the only two parameters that enter the low-energy spectrum, given by $E = \hbar\sqrt{v_F^2 k_1^2 + v_2^2 k_2^2}$, where v_2 is a direct measure of the slope of the gap at the node, as discussed in section 3.4. Figure 8.3 plots the raw values of the linear term as a function of p for both YBCO and LSCO in the left panel, while the right panel shows the calculated value of the anisotropy ratio v_F/v_2 obtained from equation 3.14 using n/d = 5.85 Å and $v_F \simeq 2.5 \times 10^7$ cm/s [29]. Also included is the published value
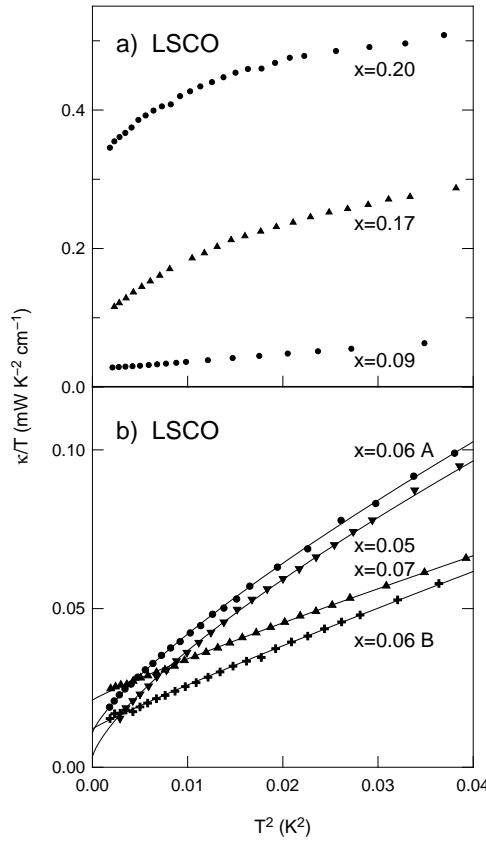
Figure 8.2: Thermal conductivity of $La_{2-x}Sr_xCuO_4$ plotted as κ/T vs T^2, for a) $x = 0.09$, 0.17 and 0.20, and b) $x = 0.05$, 0.06 and 0.07. The lines through the data are power law fits, discussed in the thesis of Dave Hawthorn [62].

for Bi-2212 at optimal doping [89]. All three cuprates have a comparable anisotropy ratio at optimal doping: $v_F/v_2 = 10$, 12 and 19, for LSCO, YBCO, and Bi-2212, respectively. It has already been noted [89] that the value of 19 for Bi-2212 is in excellent agreement with the ratio of 20 coming from values of $v_F = 2.5 \times 10^7 cm/s$ and $v_2 = 1.25 \times 10^6 cm/s$ obtained directly from ARPES [90] [1].

8.5   Nature of the superconducting order parameter

Several authors have proposed the existence of a quantum critical point within the super-conducting dome in the phase diagram of cuprates, either as a theoretical prediction to explain the diagram itself or as suggested in various experiments. Its location is usually taken to be near (or slightly above) optimal doping, in the neighbourhood of $p = 0.2$. If

---

[1]Note the value of 12 for the optimally-doped YBCO crystal differs slightly – albeit within error bars – from our previously published result of 14, which was an average of several samples. [89]
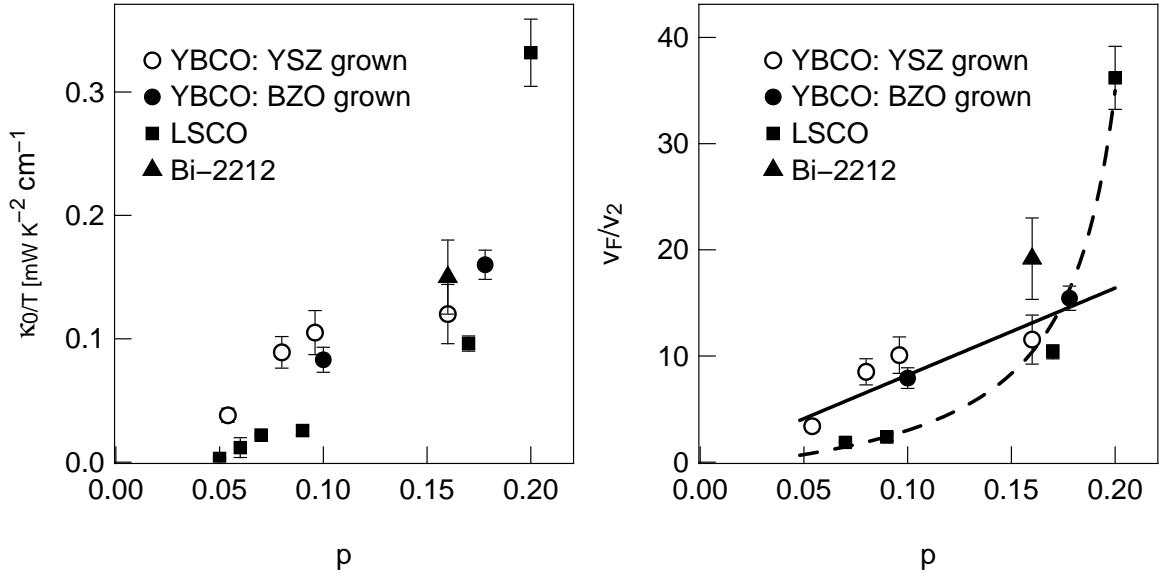
Figure 8.3: **Left**: The doping dependence of κ_0/T vs. hole doping per CuO$_2$ plane, p. **Right**: Anisotropy ratio v_F/v_2, calculated from thermal conductivity data via Equation 3.14, vs. p. The data for Bi-2212 is from Chiao *et.al.* [89]. Lines are guides to the eye (solid for YBCO, dashed for LSCO)

it is associated with a change in the symmetry of the superconducting order parameter, Vojta *et.al.* have argued that the most likely scenario is a transition from a pure $d_{x^2-y^2}$ state to a complex order parameter of the form $d_{x^2-y^2} + ix$, where x can have either s or d_{xy} symmetry [178]. Sharoni *et.al.* have recently reported a split zero-bias anomaly in their tunnelling experiments on Y-123 thin films as soon as the material is doped beyond optimal doping, a feature which they attribute to the appearance of a complex component to the order parameter in the bulk [179]. The presence of a subdominant component ix in the order parameter causes the nodes to be removed, as the gap can no longer go to zero in any direction. Our observation of a residual linear term in the thermal conductivity of both YBCO and LSCO, as well as previous results on optimally-doped Bi-2212 [89] and strongly-overdoped Tl-2201 [58], is a direct consequence of nodes in the gap. It therefore excludes the possibility of any such subdominant order parameter in the bulk throughout the doping phase diagram. In other words, if there truly is a quantum critical point inside the superconducting dome, it does not appear to be associated with the onset of a complex component in the order parameter.

In view of the ubiquitous nature of the residual linear term in superconducting cuprates, observed in four different hole-doped materials from strongly-overdoped Tl-2201 to strongly-underdoped LSCO, two previous results stand out as puzzling anomalies: the absence of

a detectable linear term in electron-doped $Pr_{2-x}Ce_xCuO_4$ (PCCO) [4] and in hole-doped $YBa_2Cu_4O_8$ [5]. In particular, we note that the upper bound of 0.02 mW K^{-2} cm^{-1} quoted for κ_0/T in $YBa_2Cu_4O_8$ is 4 to 5 times lower than the value obtained here for $YBa_2Cu_3O_y$ at a comparable hole concentration ($y = 6.54$ or 6.6) - as assessed by the very similar resistivity curves above T_c[2]. This extremely low value is akin to that found in non-superconducting strongly-underdoped LSCO ($x = 0.05$).

8.6   Effects of disorder

One of the most remarkable results of transport theory in d-wave superconductors is the universal nature of heat conduction, which appears due to a cancellation between the increase in normal fluid density and the decrease in mean free path observed as the concentration of impurities is increased [59]. This universal behaviour is only found in the limit where $\hbar\Gamma \ll \Delta_0$. In situations where Γ is large, (or Δ_0 is small), the behaviour is no longer universal, and the measured linear term may be closer to the normal state value κ_N/T than the universal limit. In the extreme case where $\hbar\Gamma \sim \Delta_0$, superconductivity is destroyed and the normal state value of κ_N/T is recovered, as in figure 3.4. Therefore the validity of using Equation 3.14 to extract values of v_F/v_2 from measurements of the residual linear term is ensured only when samples are in the universal limit, $\hbar\Gamma \ll \Delta_0$. Universal behaviour in YBCO at optimal doping is already well established, [60] and inspection of Fig. 8.3 shows that this is confirmed at other dopings. Indeed, we observe that both BZO and YSZ grown crystals yield values of v_F/v_2 that lie on the same curve despite having an order of magnitude difference in purity level[3], which is strong evidence that the universal limit is reached in our YBCO samples. In particular, the YSZ grown sample with y=0.79 has nominally the same value p as the ortho-II ordered BZO grown sample, and yields the same value of κ_0/T to within error. This is the first confirmation of the universal nature of thermal transport in the underdoped regime, and demonstrates unequivocally the versatility of the BCS theory of nodal quasiparticles across a large region of the phase diagram.

In LSCO, the extremely small values of κ_0/T measured in highly underdoped samples point to a different conclusion. Indeed, for $x = 0.06$, $\kappa_0/T \simeq 12$ μW K^{-2} cm^{-1}, while the minimum value for LSCO allowed by equation 3.14 is $\frac{k_B^2}{3\hbar}\frac{n}{d}(1 + 1) = 18.3$ μW K^{-2} cm^{-1}.

---

[2]Our own investigations in this compound have revealed a robust and sizable linear term. These measurements are presented in chapter 10

[3]See section 7.5
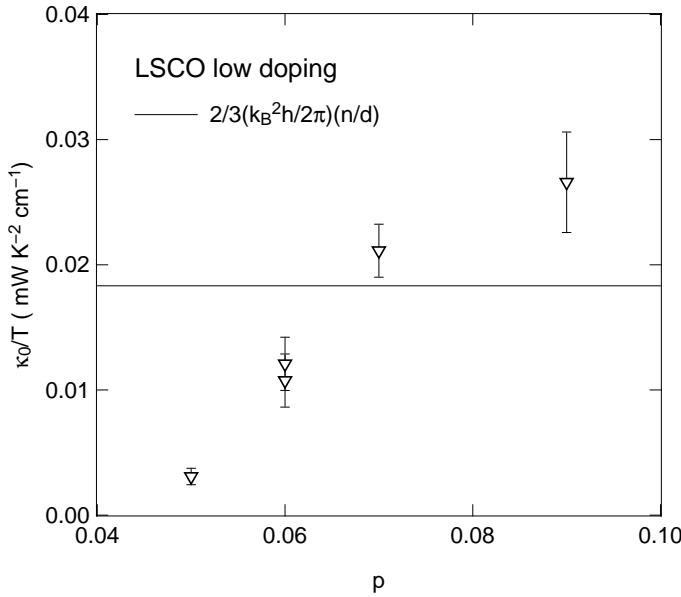
Figure 8.4:   Measured value of κ_0/T for highly underdoped LSCO. The solid line represents the minimum possible value allowed by Equation 3.14, namely when $v_F/v_2 = 1$ [5]

The data for the LSCO samples with the lowest dopings are plotted in Figure 8.4, which shows that the use of the formalism developed by Durst and Lee is invalid for these samples. This breakdown suggests that our underdoped LSCO samples are not in the limit where $\hbar\Gamma \ll \Delta_0$, and hence we cannot extract quantitative information by using equation 3.14, as we do for YBCO in the following sections. The same conclusion would apply to previous LSCO data [154].

In order to understand the LSCO data within a d-wave BCS theory of low temperature heat transport, it will be necessary to incorporate the effects of impurity scattering in the underdoped regime outside of the universal limit. The effect of impurity scattering on a d-wave superconductor has been worked out in the standard case of a normal state that is *metallic*, and conducts heat *better* than the superconducting state [91]. When the concentration of impurities is increased in such a case, T_c is gradually suppressed to zero and the residual linear term *rises* monotonically to meet its normal state value. However, our LSCO samples with $x \leq 0.09$ exhibit the well-known insulating upturns in the normal state resistivity associated with the ground state metal-insulator transition observed near $x \sim 0.16$. [157] In fact the resistivity in a strong magnetic field appears to diverge as $T \to 0$ [7]. Thus, for the LSCO samples where $x < 0.16$, the effect of increasing the impurity concentration would be to evolve the system towards an *insulating* state, or at least one that conducts heat *less well*. In this scenario, we expect the measured

residual linear term κ_0/T to be *smaller* than the universal value, which would explain how in Figure 8.4 we measure a linear term smaller than that allowed by Equation 3.14 This observation underlines the need for further theoretical work in the area.

8.7 Comparison to the work of Sun et.al.

Very recently [6], additional data on low temperature thermal conductivity in YBCO has been published in the literature [3]. The work of Sun *et.al.* finds a different dependence of the residual linear term on doping than we do, however it appears that this difference arises primarily from the way in which the data is extrapolated to $T = 0$. Although the overall trend observed by both groups is the same, it is important to establish the validity of the absolute value of κ_0/T for the analysis that follows in the next few sections.

Figure 8.5 shows the data from Sun *et.al.* plotted in the left panel as κ/T vs. T^2 alongside our own [1], and in the right panel as κ_0/T vs. p. Two important observations immediately follow from the left panel of the figure. First, the lowest temperature point in the curves of Sun *et.al.* is higher than ours - the base temperature is typically 80 mK where we reach 50 mK. Secondly, in all cases the slope of the phonon term is considerably larger for their data than ours, which in turn complicates extrapolation to T=0. This is likely a result of larger sample sizes - the typical dimensions of the crystals of Sun *et.al.* are $1.5mm \times 0.5mm \times 0.15mm$. As was discussed in section 2.6 in the boundary scattering regime it is the physical dimensions of the sample that determine the phonon thermal conductivity. Our samples on the other hand are typically less than a millimeter in length and roughly 1/2 - 1/3 the thickness, consistent with a factor of two or so difference in the slopes.

Using a naive linear extrapolation on a T^2 plot it is apparent that all of their intercepts are higher than ours, and the doping dependence of the residual linear differs from our own. Powerlaw fits of the form $\kappa/T = \kappa_0/T + BT^\alpha$ were performed for all of Sun *et.al.*'s data sets, in hopes of reconciling our measurements of the residual linear term. The error in these extrapolations is slightly higher than is usual for powerlaw fits - Sun *et.al.* only present data up to about 300 mK, so the fit range is smaller than ours. Our powerlaw fits typically extend up to 550 mK, giving lower errors and more confidence in our extrapolations.

The linear terms that emerge from the powerlaw fits to their data sets are much closer

---

[6]The work was published in PRL during the course of writing this manuscript
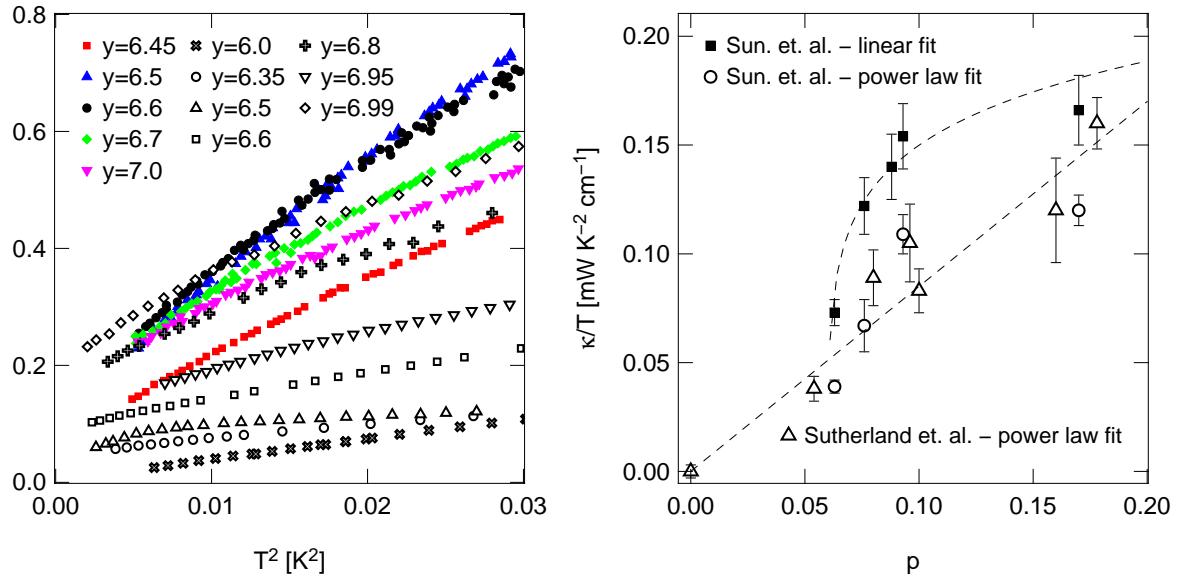
Figure 8.5: **Left** : Thermal conductivity of YBCO samples as function of doping. The data is plotted in the standard way, κ/T vs. T^2 and includes the recent work of Sun *et.al.*[3] (filled symbols) as well as our own [1] (empty symbols). **Right** : The linear term vs. doping in YBCO. The solid squares represent the values of κ_0/T obtained from the data of Sun *et.al.* using a linear extrapolation of κ/T on a T^2 plot, while the open circles represent the values obtained through a power law fit to the same data. Our own data is shown for comparison (open triangles), and the dotted lines are guides to the eye. The error bars are determined by the fitting errors for Sun *et.al.*'s data, and a combination of fitting error and geometric factor error for our own.

in size to ours. The right panel of figure 8.5 plots the values of the linear terms versus p from Sun. *et.al.* obtained both through using a linear extrapolation of κ/T on a T^2 plot, and using our power law fitting method. We feel that the method of using a floating fit with 3 free parameters is superior to a forced fit with one free parameter, and thus view the values obtained from the power law fits as correct, and in agreement with our own data.

8.8   Doping dependence of the superconducting gap

The remarkable success of the *d*-wave BCS theory in describing quasiparticle heat transport is highlighted by the observation of universal behaviour in Zn doped YBCO [60] at optimal doping, and in this work in the underdoped regime by comparing BZO and YSZ grown samples. We may further interpret our measurements of the anisotropy ratio v_F/v_2 in such a theory by using the fact that v_F, the Fermi velocity at the node, is essentially independent of doping. This useful fact was shown by ARPES in both Bi-2212 [90] and in LSCO, [29] where the slope of the E vs k dispersion at the Fermi energy
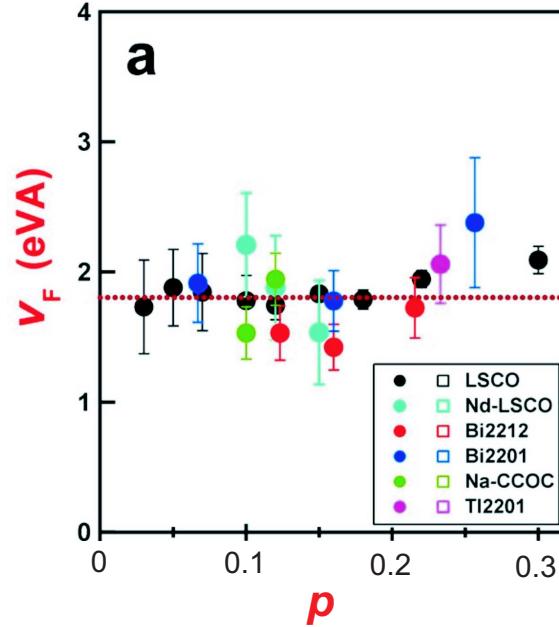
Figure 8.6:   The doping dependence of the Fermi velocity in a host of high-T_c cuprate super-conductors. Adapted from reference [29]. This insensitivity to doping implies that the doping dependence of κ_0/T directly reveals the doping dependence of v_2, the slope of the supercon-ducting gap at the nodes.

is seen to vary by no more than 10% over the range $0.03 < x < 0.3$, with an average value of $v_F \simeq 2.5 \times 10^7$ cm/s in both materials. This key result is shown in figure 8.6, reproduced from reference [29]. The position of the node in k-space is also independent of doping [90], with $k_F \simeq 0.7$ Å $^{-1}$ as measured from (π,π) to the Fermi surface. As a result, a study of κ_0/T vs p yields the doping dependence of $v_2 = v_2(p)$. Assuming a pure d-wave order parameter, this then provides the doping dependence of the corresponding gap maximum, Δ_0 via Equation 3.15:

$$\Delta_0 = \hbar k_F v_2/2 \tag{8.1}$$

In Figure 8.7, we plot the value of Δ_0 calculated for our YBCO samples in this manner, versus hole doping p. The values of Δ_0 are also listed in Table 8.2. Again, here we have confined our analysis to YBCO only, given that LSCO was seen to lie outside the clean limit. Plotted alongside this data is a conventional BCS d-wave gap (dashed curve), where we have assumed $\Delta_0 = 2.14k_BT_c$ (weak-coupling approximation). The p dependence of the gap is estimated using Equation 6.1, with a maximum T_c at optimal doping of 93 K. In the overdoped regime, we have also plotted the value of the gap maximum for

a Tl-2201 compound measured in our laboratory [58] where again we have used T_c to estimate p.

Let us examine the implications of these results by starting on the overdoped side of the phase diagram. We use published data in the strongly-overdoped regime on Tl-2201, [58] a single-plane cuprate with optimal $T_c \simeq 90$ K. For an overdoped crystal with $T_c = 15$ K, the measured residual linear term is $\kappa_0/T = 1.4$ mW K^{-2} cm^{-1}, which yields $v_F/v_2 = 270$ via Equation 3.14. In comparison, the weak-coupling BCS prediction based on the value of $T_c = 15$ K is $v_F/v_2 = 210$, using the values of v_F and k_F given above [58]. The good quantitative agreement shows that in this strongly-overdoped regime BCS theory works quite well, and the much larger anisotropy ratio is a consequence of the much smaller T_c. As one moves towards optimal doping, the linear term decreases significantly, leading to values of Delta that track the weak coupling BSC theory rather well. This observation adds to the mounting evidence that the physics of the overdoped region of the phase diagram is conventional - a metallic ground state well-described by Fermi liquid theory [58, 56] and a superconducting state that is understood within the context of BCS theory[7].

We now turn our attention to the underdoped region of the phase diagram. In the case of YBCO the decrease in κ_0/T by a factor 2 between $y = 6.99$ and $y = 6.50$ provides one of the main results of this chapter: the velocity ratio decreases with underdoping; it drops from 16 to 8 in going from a sample with $T_c = 89$ K to an underdoped sample with $T_c = 62$ K. *This reflects an underlying steepening of the gap at the node while T_c drops, with underdoping.* This is in contradiction with the results of Mesot *et.al.* who extracted a slope of the gap from their ARPES measurements on Bi-2212 near optimal doping that seemed to decrease slightly with underdoping, [90] and with the analysis of Panagopoulos *et.al.* who extract a gap maximum from their penetration depth measurements that remains approximately constant in the underdoped regime [180]. In this context the value for the highly underdoped y=6.35 sample seems anomalously high, which will be discussed in greater detail in chapter 12.

Taken by itself, the trend could be attributed either to a gradual departure from weak-coupling towards strong-coupling BCS superconductivity, with a growing ratio Δ_0/T_c. It

---

[7]A doping dependent study of the residual linear term from p=0.16 to p=0.26 in Tl2201 has recently been completed by our group. The findings essentially show that to within reasonable error the value of Δ_0 extracted from thermal conductivity agrees with what would be expected from strong-coupling BCS theory with μ=4. This work is written up in the thesis of Dave Hawthorn [62] and exists in preprint form at the time of writing.
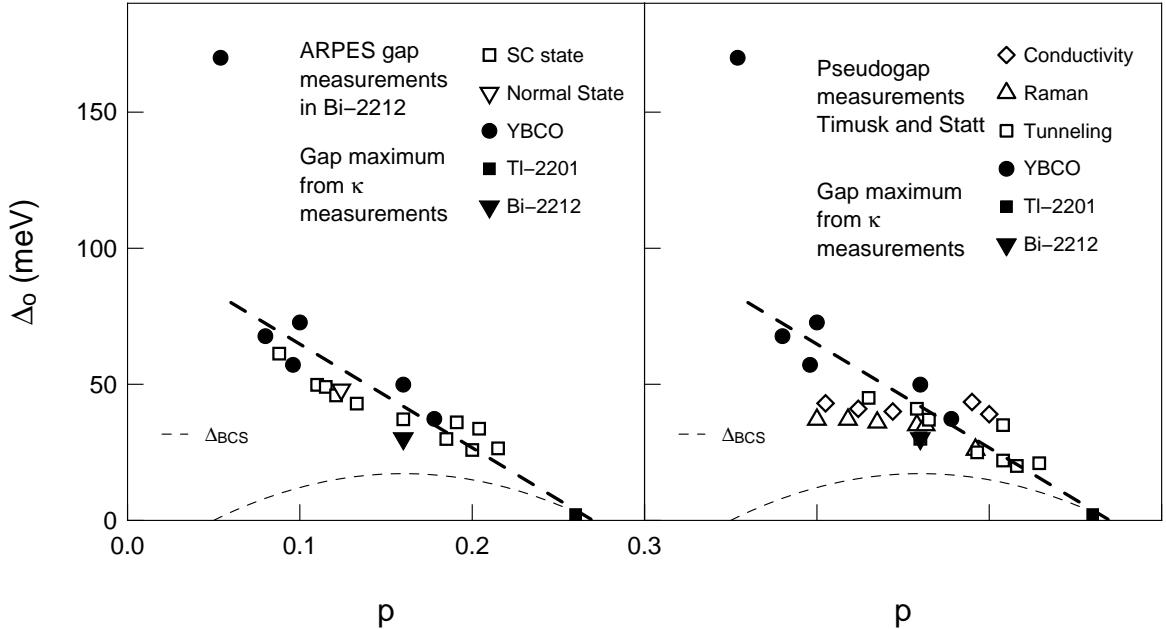
Figure 8.7: **Left**: Doping dependence of the superconducting gap Δ_0 obtained from the quasiparticle velocity v_2 (filled symbols). Here we assume $\Delta = \Delta_0\cos2\phi$, so that $\Delta_0 = \hbar k_F v_2/2$, and we plot data for YBCO alongside Bi-2212 [89] and Tl-2201 [58]. The error bars are left off for clarity, but are set by the geometric factor uncertainty, 10 - 15 %. For comparison, a BCS gap of the form $\Delta_{\mathrm{BCS}} = 2.14k_B T_c$ is also plotted, with T_c taken from Eq. 1 (and $T_c^{max} = 90$ K). The value of the pseudogap in Bi-2212, as measured ARPES is also shown. **Right**: Δ_0 vs. p as in the right panel, compared to pseudogap measurements using various complementary techniques [32]. The thick dashed line in both figures is a guide to the eye.

could also be interpreted as a gradual deformation of the gap shape, from a simple $\cos2\phi$ angular dependence to a much steeper function with a decreasing average gap that scales with T_c. In fact a rounding of the slope of the gap at the nodes was observed [90] in underdoped BSCCO, however this could have simply been a result of a broadening of the ARPES spectra due to impurities.

In view of the known behaviour of the pseudogap, these explanations are unlikely to be the main story. Indeed, the growth of the low-energy gap observed through κ_0/T is highly reminiscent of the similar trend observed in the high energy gap (or pseudogap) with underdoping.

In fact the growth of Δ_0 derived from v_2 is in quantitative agreement with the pseudogap maximum determined by ARPES [181, 28, 33, 22]. In the superconducting state, we use the data of Campuzano *et.al.* [181] and White *et.al.* [33] to define the gap as the energy separating the peak in the ARPES spectral function measured in the $(0, \pi)$ direction and the Fermi energy E_F, as measured in thin films of BSCCO at 15 K. Above

T_c, in the normal state, we use the data of Norman *et.al.* [28], Loeser *et.al.* [22] and define the pseudogap as the energy separating the plateau in the ARPES spectral function measured from E_F also in the $(0, \pi)$ direction. In the right hand side of figure 8.7 we further compare our data to measurements of the pseudogap compiled by Timusk and Statt [32] including tunnelling [23, 24] $a - b$ plane optical conductivity [34] and Raman scattering, [182, 35].

This striking similarity in scaling points to a common origin, which allows us to say the following things on the nature of the pseudogap. First, due to the very existence of a residual linear term, the (total) gap seen in thermal conductivity at $T \to 0$ is one that must have nodes. Any gap larger than a few μeV would serve to lift the nodes off of the Fermi surface, resulting in a κ_0/T of zero. Secondly, the fact that the values of Δ_0 we extract from our thermal conductivity measurements agree so well with ARPES data indicates that the formalism of Durst and Lee applies equally well in the pseudogap regime as it does the case of overdoped Tl2201. From this we conclude that the pseudogap itself must have a linear dispersion as in a d-wave gap (*i.e.* it has a Dirac-like spectrum). Thirdly, the gap that we see is a true quasiparticle gap and not just a spin gap.

A fundamental question is whether the pseudogap is related to or independent of superconductivity. The first and most natural possibility is that it is due to some form of precursor pairing. A second possibility is that it may come from a distinct non-superconducting state. Indeed, a universal thermal conductivity is also possible in a non-superconducting state as long as the energy spectrum is Dirac-like (*i.e.* linear dispersion). For example, a universal (charge) conductivity was derived for a degenerate semiconductor in 2D [183]. Interestingly, the d-density-wave (DDW) state proposed as an explanation for the pseudogap phenomena seen in underdoped cuprates [45] also exhibits a universal conductivity provided that the chemical potential $\mu = 0$. In the region where both orders coexist – DDW and d-wave superconductivity (DSC) – Equation 3.14 is then predicted to hold, [184] with v_2 replaced by $\sqrt{(v_\Delta^{DDW})^2 + (v_\Delta^{SC})^2}$, where v_Δ^{DDW} and v_Δ^{SC} are the gap velocities for the two types of order, respectively. The main unanswered question then is how does the chemical potential evolve as a function of doping?

In summary, our measurements of κ/T throughout the phase diagram allow us to make the following statements about the evolution of Δ_0 with doping. First, the extrapolated value of the gap maximum from thermal conductivity in the overdoped regime is in excellent quantitative agreement with that expected from BCS theory. Secondly, Δ_0 continues to grow with underdoping while T_c rises and then falls, in contradiction to

what one would expect from BCS theory. The divergence of these two energy scales in the underdoped regime is a manifestation of the pseudogap, whose presence is now revealed at very low energies in a bulk measurement on crystals of the utmost quality and purity. The fact that the gap preserves its pure *d*-wave form (with nodes on the Fermi surface) throughout suggests that the pseudogap is superconducting in origin.

8.9   Comparison of κ_0/T to superfluid density

A direct comparison of our measurements of the residual linear term and measurements of the superfluid density from the literature provides useful insight into the doping dependence of nodal quasiparticles. The superfluid density can be accessed by studying the magnetic penetration depth, since $\rho_S e^2/m^* = 1/(\mu_0\lambda^2)$. The temperature dependence of $1/\lambda^2$ is linear in the low temperature regime, a direct consequence of the existence of thermally excited nodal quasiparticles [18]. The slope of the temperature dependence is governed by the quasiparticle anisotropy ratio in much the same way as the linear term in thermal conductivity, as in equation 3.17

Table 8.1: Summary of microwave penetration depth values as a function of doping in YBCO, from the literature [185, 118, 186].

Sample	λ_0 (Å)	$\frac{d\lambda^{-2}}{dT}$ (Å^{-2}K^{-1})	p	$\alpha^2 v_F/v_2$
YBCO$_{6.50}$	2600	$-1.25e^{-9}$	0.089	4.1
YBCO$_{6.60}$	2100 (λ_{AB})	$-1.57e^{-9}$	0.093	5.2
YBCO$_{6.95}$	1600	$-1.90e^{-9}$	0.16	6.3
YBCO$_{6.99}$	1600	$-1.74e^{-9}$	0.169	5.8

The factor α^2_{FL} which enters Equation 3.13 is a Fermi-liquid correction which arises because of quasiparticle-quasiparticle interactions, which renormalize the electrical current. This relationship implies that from the penetration depth measurements we may directly access information about the term $\alpha^2_F v_F/v_2$. Using the formalism of Durst and Lee, we may then obtain an estimate of α^2_F by using our independently determined values of the anisotropy ratio from thermal conductivity.

Microwave penetration depth measurements have been performed on high-quality de-twinned single crystals of YBCO at a number of dopings by the UBC group [187, 188, 117, 118]. Using a cavity perturbation method, they obtain information about the temperature dependence of the penetration depth, i.e. $\Delta\lambda = \lambda(T) - \lambda(1K)$. This data is plotted versus
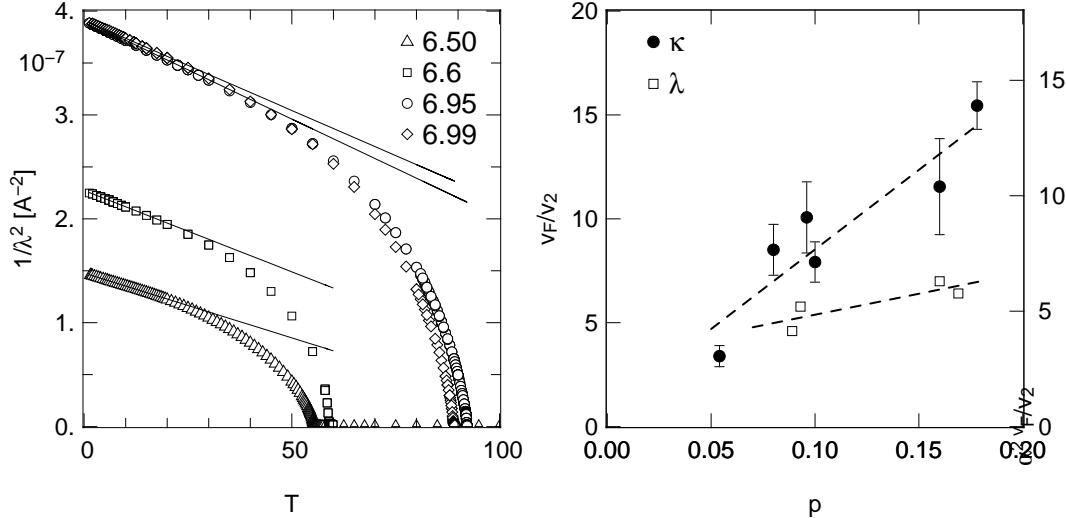
Figure 8.8: **Left**: Microwave penetration depth data plotted as $1/\lambda^2$ vs. T. The data shows a flattening of the slope as one underdopes, consistent with a v_F/v_2 that is reduced. **Right**: Quasiparticle velocity ratio in YBCO obtained from universal heat transport, as v_F/v_2 (circles), and from superfluid density data, as $\alpha_{FL}^2 \frac{v_F}{v_2}$ (triangles). Lines are guides to the eye.

temperature in the left panel of figure 8.8. The absolute value of the penetration depth at $T = 0$ must be inferred from other techniques, which is the main source of error in such a comparison. Until very recently, the most detailed knowledge of $\lambda(0)$ came from infrared spectroscopy [185], or μSR [36, 189]. The values of $\lambda(0)$ from the literature [185, 118, 186], as well as the slopes of the temperature dependencies of the superfluid density are summarized in table 8.1.

In the right panel of figure 8.8 we combine the two data sets and plot the value of α_F^2 as a function of doping. This yields:

$$\alpha_{FL}^2 \simeq 0.4 - 0.5 \;, \qquad \text{at } p \simeq 0.16 \tag{8.2}$$

$$\alpha_{FL}^2 \simeq 0.6 - 0.7 \;, \qquad \text{at } p \simeq 0.09 \tag{8.3}$$

A similar value was previously derived for optimally-doped Bi-2212 [89]. We conclude that this FL parameter is near unity and, more importantly, is only weakly dependent on doping in the range studied.

To improve the accuracy of this comparison, estimates of λ_0 with greater certainty than those provided by the infrared and μSR techniques is required. Very recently, a new method for obtaining this quantity with unprecedented accuracy has emerged. Pereg-Barnea *et.al.* have developed a technique [190] which uses ESR on Gd-doped YBCO

to extract λ_0. For an overdoped sample of $YBCO_{6.99}$ with a T_c of 89 K they find λ_0 = 1030 Å, while for an ortho-II ordered sample of $YBCO_{6.50}$ they find λ_0 = 2020 Å. Both values are some 30 % smaller than those reported previously, which will affect the temperature dependence of $\Delta\lambda$ to some degree. Preliminary estimates [191] of the temperature dependence of the superfluid density suggest that $d/dT 1/\lambda(T)^2 = 4.95 \times 10^{17}$ $(\Omega msK)^{-1}$ and 2.16×10^17 $(\Omega msK)^{-1}$ for $YBCO_{6.99}$ and $YBCO_{6.50}$ respectively. Using these new numbers, we get $\alpha_{FL}^2 \simeq 1.3$ for $p=0.17$ and $\alpha_{FL}^2 \simeq 1.1$ for $p = 0.1$. In other words, for both dopings the values of α_{FL}^2 are essentially unity.

In a recent paper, Ioffe and Millis [192] argue that a doping independent α_{FL}^2, which they interpret as Z^e, the quasiparticle effective charge, severely constrains theories of a doped Mott insulator. A spin-charge separation scenario for instance leads to a Z^e that vanishes as $p \to 0$. The Brinkman-Rice mean field theory approach to the Mott physics does in fact predict a doping independent α_{FL}^2, but a v_F that decreases with decreased doping, which is inconsistent with ARPES data. A slave boson treatment of the doped Mott insulator predicts a Z^e that scales linearly with p. Indeed the combination of a doping independent α_{FL}^2 and v_F, along with a v_2 that increases with decreasing doping provides a significant challenge to microscopic theories of d-wave superconductivity in cuprates [192]. It is clear more experimental data, particularly in the extreme underdoped limit is needed.

8.10 *Comparison of thermal and microwave conductivity*

One way to shed further light on the nature of the low-energy electron state in underdoped YBCO is to compare heat transport and charge dynamics. For a d-wave BCS superconductor, Durst and Lee have shown that the two conductivities are affected differently by scattering anisotropy and quasiparticle interactions [59]. The charge conductivity in the $\omega \to 0$ and $T \to 0$ limit is given by 3.13:

$$\lim_{T \to 0} \sigma_1(T) = \sigma_0 = \frac{e^2}{\hbar} \frac{1}{\pi^2} \frac{n}{d} \; \beta_{VC} \; \alpha_{FL}^2 \; \frac{v_F}{v_2}, \qquad (8.4)$$

where e is the electron charge. The factor β_{VC} is due to vertex corrections and is greater than 1.0 when impurity scattering is anisotropic. This simply reflects the fact that intra-node scattering (scattering with the initial and final k vector at the same node) will degrade a charge current less than inter-node (opposite- or side-node) scattering that involves a larger change in momentum. This is the discrete version of the $(1 - \cos\theta)$ term

that enters normal state conductivity and reflects the predominance of back-scattering over small-angle scattering. Numerical calculations suggest that β_{VC} can be large (*e.g.* in excess of 10) in high-purity samples as long as impurity scattering is in the unitary limit [59]. For Born limit scattering the corrections are independent of impurity concentration, but still lead to a β_{VC} greater than 1. For heat transport on the other hand, vertex corrections have been shown by Durst and Lee to have a negligible effect for all scattering strengths.

The microwave conductivity $\sigma_1(\omega, T)$ of YBCO was recently measured in crystals nominally identical to ours with $y = 6.50$ [118] and $y = 6.99$ [117]. Even though the measurements go down to 1 GHz and 1.3 K, it turns out to be unclear how to reliably extrapolate this data to the $\omega = 0$ and $T = 0$ limit, so that a meaningful comparison of κ_0/T and σ_0 is not quite possible at this stage. The shape and temperature dependence of the microwave spectrum for the $y = 6.50$ sample for example is suggestive of non-unitary scattering close to the Born limit, implying that the low-temperature universal limit regime may not be reached by 1.3 K. Further work is needed to ascertain whether this is indeed the correct scenario.

8.11   Chapter summary

We have studied the evolution of thermal transport as $T \to 0$ in the cuprate superconductors YBCO and LSCO over a wide range of the doping phase diagram. The residual linear term, κ_0/T, is observed to be finite throughout the superconducting region. This proves that the gap always has nodes on the Fermi surface, a fact that has two implications: 1) it rules out the possibility of a multicomponent order parameter of the type $d + ix$ in the bulk, appearing at a putative quantum phase transition, and 2) it argues in favour of a superconducting origin to the pseudogap (*e.g.* precursor pairing). As the Mott insulator is approached, κ_0/T is observed to decrease, leading to a decreasing value of the quasiparticle velocity anisotropy ratio, v_F/v_2. This result offers some of the first insights into the doping dependence of several important quasiparticle parameters. First, the slope of the d-wave superconducting gap at the nodes, v_2, is seen to increase steadily as doping is decreased, consistent with a growth of the gap in the underdoped regime. This is in contradiction to what one naively expects from BCS theory, where the gap scales with T_c. The gap we extract at very low energies follows closely the pseudogap measured mostly at much higher energies by other techniques. This close tracking of

the pseudogap shows that the gap remains roughly of the pure *d*-wave form throughout the phase diagram. Secondly, a comparison with superfluid density reveals that the quasiparticle effective charge is weakly dependent on doping and close to unity.

The considerable difference between the magnitude of the change in κ_0/T with underdoping for the LSCO and YBCO samples provides clues as to the role of disorder in the underdoped regime. In particular, the small value of the residual linear term of the most highly underdoped LSCO samples is incompatible with the standard theory of transport for *d*-wave superconductors, motivating theoretical work which would incorporate the effects of impurities in a superconductor whose normal state is insulating rather than metallic in nature. We summarize the results of this section in Table 8.2.

Table 8.2: Compilation of T_c, doping and residual linear term in the thermal conductivity as well as values of the quasiparticle anisotropy ratio v_F/v_2 and gap maximum Δ_0 from thermal conductivity measurements. Data for optimally doped Bi-2212 [89] and overdoped Tl-2201 [58] from previous studies are provided for completeness.

Sample	T_c [K]	p	κ_0/T $[\frac{\mu W}{K^2 cm}]$	v_F/v_2	Δ_0 [meV]
YBCO$_{6.0}$	—	0.0	0±3	—	—
YBCO$_{6.35}$	4	0.054	38±6	3.4	170
YBCO$_{6.50}$	62	0.10	83±18	7.9	71
YBCO$_{6.6}$	44	0.08	89±13	8.7	66
YBCO$_{6.8}$	61	0.096	105±13	8.7	66
YBCO$_{6.95}$	93.5	0.16	120±24	11.5	50
YBCO$_{6.99}$	90	0.18	160±12	15.5	37
LSCO 0.05	—	0.05	3±1	—	—
LSCO 0.06 A	5.5	0.06	11±2	—	—
LSCO 0.06 B	8.5	0.06	12±2	—	—
LSCO 0.07	19	0.07	22±2	1.9	—
LSCO 0.09	16	0.09	26±10	2.4	—
LSCO 0.17	34	0.17	96 ± 7	10.4	—
LSCO 0.20	33.5	0.20	330 ± 40	36	—
Bi-2212	89	0.16	150 ± 30	19	30
Tl-2201	15	0.26	1400 ± 70	270	2

THERMAL CONDUCTIVITY IN THE VORTEX STATE OF $YBa_2Cu_3O_y$

9.1 Chapter overview

In a d-wave superconductor, the field dependence of the residual linear term in thermal conductivity is typically understood in the context of Volovik physics. As summarized in section 3.4.2, the presence of superfluid vortices serves to Doppler shift the energy spectrum of nodal quasiparticles, resulting in a $\sqrt{H}$ dependence of κ_0/T on field. Away from the universal limit, standard transport theory assumes that quasiparticle scattering is close to the strong (unitary), and the scattering of quasiparticles from vortices is neglected. In this chapter I mainly summarize measurements of thermal conductivity in an ultra pure sample of $YBa_2Cu_3O_{6.99}$ in the presence of a magnetic field, although some data on the in-field conductivity of other samples is presented. Our results force a re-examination of the basic assumptions of mixed state transport - we find evidence that the scattering of quasiparticles from vortices is present in our samples, and that the scattering phase shift is not in the unitary limit. The field dependence of additional samples in the underdoped regime are also presented, and I examine the implications of this work on interpreting other data in the literature. The results on the $YBa_2Cu_3O_{6.99}$ sample appear in Physical Review Letters [4], while the remainder of the data in this section is unpublished at present.

9.2 $\kappa(H)$ in Ultra-pure $YBa_2Cu_3O_{6.99}$

For the past 20 years the central assumption underlying theoretical treatments of electronic transport in unconventional superconductors in that scattering from randomly distributed impurities should be treated in the unitary limit ($\pi/2$ phase shift) [193]. In thermal transport, the nature of the impurity scattering is manifested in the temperature and field dependence of the electronic thermal conductivity. At sufficiently low temperatures, such that $T \ll \Gamma$ the universal limit is reached and the ability of qua-
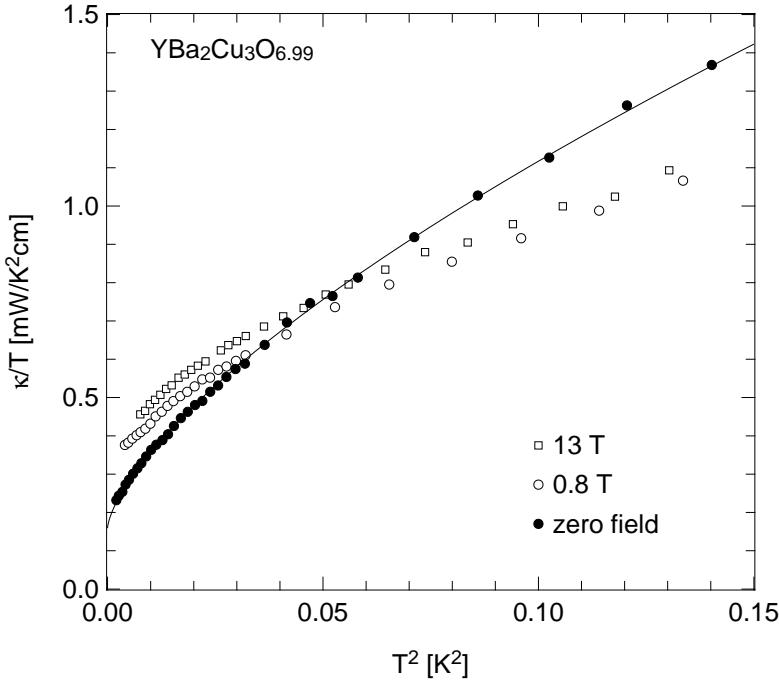
Figure 9.1: Thermal conductivity divided by temperature versus T^2 for a high-purity YBCO sample for magnetic fields applied perpendicular to the *ab* plane. The solid line represents the results of a power law fit to the 0 Tesla data.

siparticles to conduct heat is insensitive to either impurity concentration, or scattering phase shift [88]. Experimental observation of the universal limit has been confirmed in the cuprate superconductors YBCO and BSCCO as well as the *p*-wave superconductor Sr_2RuO_4. Thus far we have confined our analysis in the previous chapter to transport within this limit, but now we look towards testing the assumption of unitary scattering by the application of a magnetic field and extending analysis of the data to $T > 0$. This task is greatly complicated by the necessity of subtracting out any phonon contribution to the temperature dependence of $\kappa(T, H)$, however under certain conditions this may be attempted using a few simple assumptions.

The thermal conductivity of the ultra pure sample of $BaZrO_3$ grown $YBa_2Cu_3O_{6.99}$ was measured in both zero and applied magnetic fields using the standard methods outlined in chapter 4. The heat current was along the *a*-axis while the field was applied perpendicular to the $a - b$ plane. To ensure a spatially homogenous vortex lattice, the sample was field-cooled by cycling to $T > 100$ K before changing the field. The error in the absolute value of the conductivity is estimated to be approximately 10%. The relative error between temperature sweeps at different fields is of order 1%.
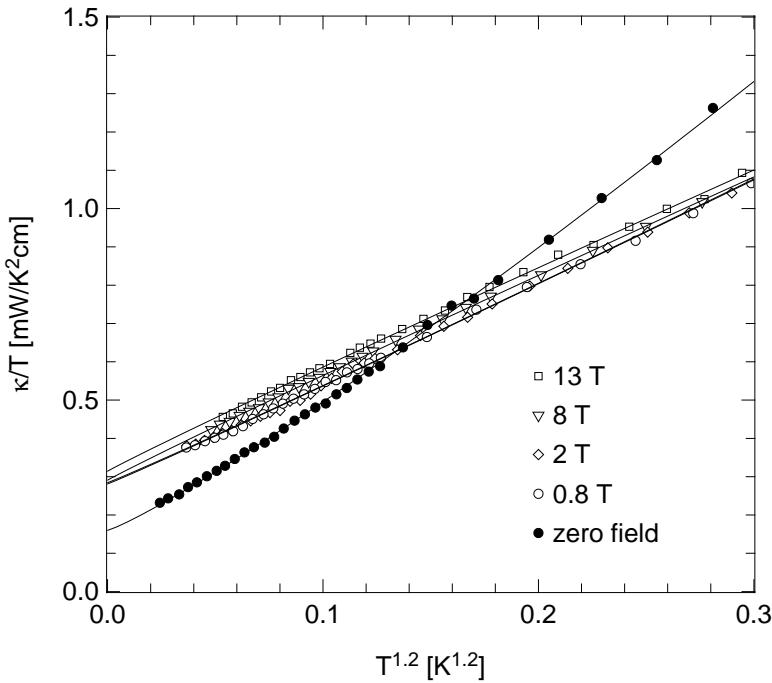
Figure 9.2: Powerlaw fits to the thermal conductivity data for YBa$_2$Cu$_3$O$_{6.99}$ in 0 and applied fields. The data is plotted versus $T^{1.2}$, which is close to the average value of α for each data set.

The data is plotted in Figure 9.1 for zero field, a modest field of 0.8 Tesla and at the maximum experimentally accessible field of 13 Tesla. What is immediately obvious from this plot is that the majority of the evolution of $\kappa(T)$ with field occurs by 0.8 Tesla - the effect of going to a field 16 times stronger is to simply offset the data by a small amount. The solid line shows the result of a powerlaw fit to the zero field data. As we have seen already in Chapter 8, this fit yields a residual linear term which is purely electronic in origin and has a magnitude of 0.16 mW/cmK^2. In Figure 9.2 we plot the raw data and powerlaw fits for all fields versus $T^{1.2}$. The x-scale is chosen to represent the average of the power law exponents, so the data will appear more or less linear in such a graph. The value of the zero-field linear term is essentially in agreement with the value for the YSZ grown optimally doped YBCO, which as argued in chapter 7 is an order of magnitude *less* pure than this crystal. This agreement is further evidence for universal behaviour - in this case we have measured a sample in the more difficult regime of increased purity.

To extract any T-dependence of κ_e/T, we make use of a magnetic field as follows. We first assume that the phonon transport at very low temperatures is limited by scattering from the boundaries of the sample, and is unaffected by scattering from vortices. This

assumption is justified by noting that the phonon mean free paths at very low temperatures are many orders of magnitude greater than the intervortex spacing. Noting that the zero-field curve in Figure 9.1 shows a more rapid increase with temperature than the two in-field curves (which are approximately parallel), we must conclude that this difference arises entirely from electrons since κ_{ph} is assumed to be field independent. Furthermore, since all subsequent in-field curves lie parallel we assume that this additional electronic conduction is completely suppressed when a magnetic field is applied (see inset of Figure 9.3, and the remaining temperature dependence of κ/T is due entirely to phonons. In other words κ_{ph} is the T-dependent part of the 13 T data: $\kappa_{ph}/T = \kappa(13 \text{ T})/T - \kappa_0(13$ T$)/T$, where $\kappa_0(13 \text{ T})/T = 0.31$ mW/K^{2}cm. The electronic conductivity, κ_e/T, is then given by subtracting this from the total conductivity: $\kappa_e(H,T)/T = \kappa(H,T)/T - \kappa_{ph}/T$. This is shown in Figure 9.3 for applied magnetic fields from 0-13 T.

The zero-field electronic conductivity shows a rapid growth with temperature, increasing by a factor of five within 0.5 K. The temperature dependence of this additional electronic term is well described by a T^3 fit. The inset of Figure 9.3 shows this nicely - the electronic conductivity has a finite linear term and a linear slope when plotted on a T^2 graph. A fit to the zero-field electronic conductivity yields $\kappa_e/T = 0.16 + 3.0T^2$. As soon as a magnetic field is applied this temperature dependence is completely suppressed. The temperature dependence of the 0.8 Tesla electronic term is completely flat, as seen in the inset of Figure 9.3. The most reasonable explanation for such a dramatic effect is that the quasiparticles are scattered by vortices, and that the additional temperature dependent part of κ_e/T is extremely sensitive to scattering rate.

We may rule out the possibility that the change in temperature dependence between zero and applied field is due to scattering of phonons by vortices by noting the lack of field dependence above 0.8 T. By increasing the field to 13 T, an order of magnitude more vortices have been introduced to the system, yet the total conductivity remains essentially unchanged.

9.2.1   Zero magnetic field (H=0)

In chapter 3 we saw that using a quasiclassical theory formulated at low temperatures where heat transport is limited by electron scattering, thermal conductivity was universal in the zero temperature limit. Extending this calculation to finite temperatures Graf *et.al.* [88] find:
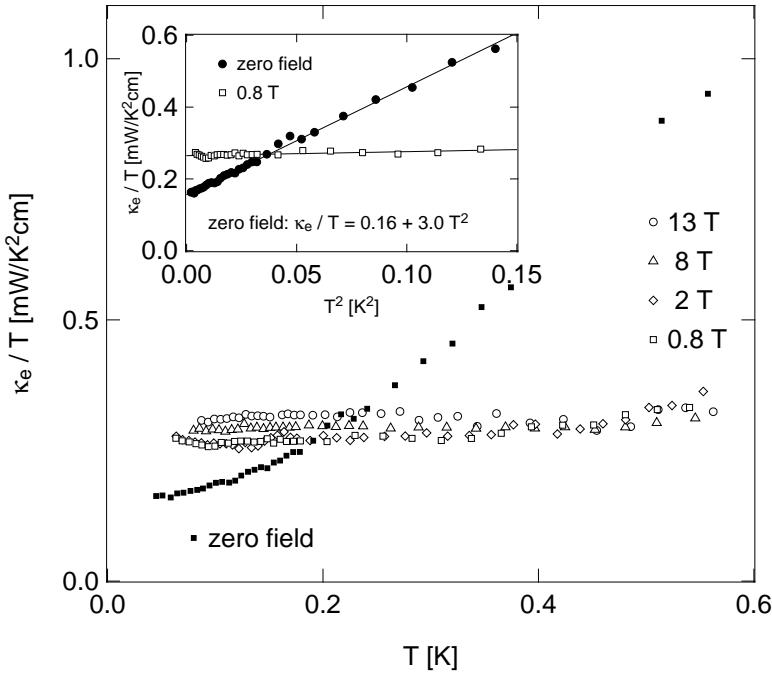
Figure 9.3: Electronic thermal conductivity, plotted as κ_e/T vs T, for magnetic fields from zero to 13 T. The electronic contribution is extracted as discussed in the main text. Inset: The low field curves plotted against T^2.

$$\frac{\kappa_e}{T}(T) = \frac{\kappa_{00}}{T} \left[1 + \frac{7\pi^2}{15} \left(\frac{a^2 T}{\gamma} \right)^2 \right] \tag{9.1}$$

where κ_{00}/T is the universal conductivity limit, γ is the impurity bandwidth and the coefficient a is strongly dependent on the scattering phase shift (Equation 3.18, restated here for clarity). This expression is valid in the dirty limit where $k_B T < \gamma$. Recalling the fit to the zero field data from Figure 9.1 we see that the temperature dependence of our extracted electronic conductivity is well described by this form. From this fit we find that the coefficient of T^3 term in equation 9.1 is equal to 19.2. Remarkably, this corresponds to a huge 20-fold increase in κ_e/T by 1 K.

9.2.2 $H = 0$: Finite temperature

From the temperature dependent part of our fitted data we can estimate the impurity bandwidth and scattering rate. In a d-wave superconductor with a cylindrical Fermi surface Hirschfeld and Goldenfeld [80] have examined the dependence of the impurity band width γ on the scattering rate Γ in the limit of both weak and strong scattering. For scattering in the unitary limit $a = 1/2$ and the impurity bandwidth γ is related

to the normal-state scattering rate Γ_n by the relation $\gamma = 0.63\sqrt{\Delta_0\Gamma_n}$ [80]. Using the value from the fitted zero-field data (inset of Figure 9.3), we obtain $\gamma \sim 0.25$ K and using $\Delta_0 = 2.14 \, k_BT_c$, we get $\Gamma_n/T_c \sim 10^{-5}$, therefore $\Gamma_n \sim 1 \times 10^8$ s^{-1}. Such a small scattering rate is unrealistic. Using $v_F = 2.5 \times 10^7$ cm/s [1], it would imply a normal-state mean free path as long as the longest dimension of the sample: $l \sim 1$ mm! This enormous mean free path would be some 10 times greater than that in the purest GaAs [194] grown by molecular beam epitaxy, which is certainly incorrect.

In the weak scattering Born approximation, the impurity bandwidth is exponentially dependent upon the normal state scattering rate, so that $\gamma = 4\Delta_0 \exp(-\pi\Delta_0/2\Gamma_n)$. The coefficient a is then given by the slope of the gap at the nodes and the scattering lifetime, $a = (\pi v_2\tau_0)/2$. Assuming a pure d-wave gap gives the result $v_2 = 2\Delta_0/\hbar k_F$, which we have used previously to extract a gap maximum from measurements of κ_0/T in chapter 8. Using the fact that $\tau_0 = 1/2\Gamma_n$, and $k_F \sim 0.7$ Å leads to $\gamma \sim 3$ K and $\Gamma_n \sim 0.6\Delta_0 \sim 2.5 \times 10^{12}$ s^{-1}. Again we estimate a scattering rate that is unrealistic, in this case much too large. If the scattering rate were truly this magnitude it would lead to a substantial suppression of T_c, as noted previously [80], which is not observed experimentally.

We are then forced to conclude that either the quasiclassical calculation of Hirschfeld does not capture the physics of quasiparticle impurity scattering in its entirety, or that in this ultra pure sample of YBCO it is incorrect to treat impurity scattering with a single isotropic phase shift of either 0 (Born) or $\pi/2$ (unitary).

In a broader context, thermal conductivity measurements on other unconventional superconductors such UPt$_3$ [86] and Sr$_2$RuO$_4$ [195] reveal conductivities that are most easily, but not completely, understood within the unitary limit. In UPt$_3$ for instance Suderow and co-workers find that an estimate of γ based on normal state data is some 3 times larger than that obtained from low T κ measurements. The implication of this, as was seen in our work, is that the scattering rate estimated in the unitary limit from low temperature data is too small. This in turn leads to mean free paths that are unexpectedly large, suggesting that the standard theoretical approach to transport in unconventional superconductors is generally inadequate.

Microwave conductivity measurements [117, 118] on samples of identical quality to that used in this study have also been compared to current theories of transport in unconventional superconductors [196]. These measurements reflect *some* but not all of the characteristics of weak scattering (Born limit) and point to either inadequacies in the
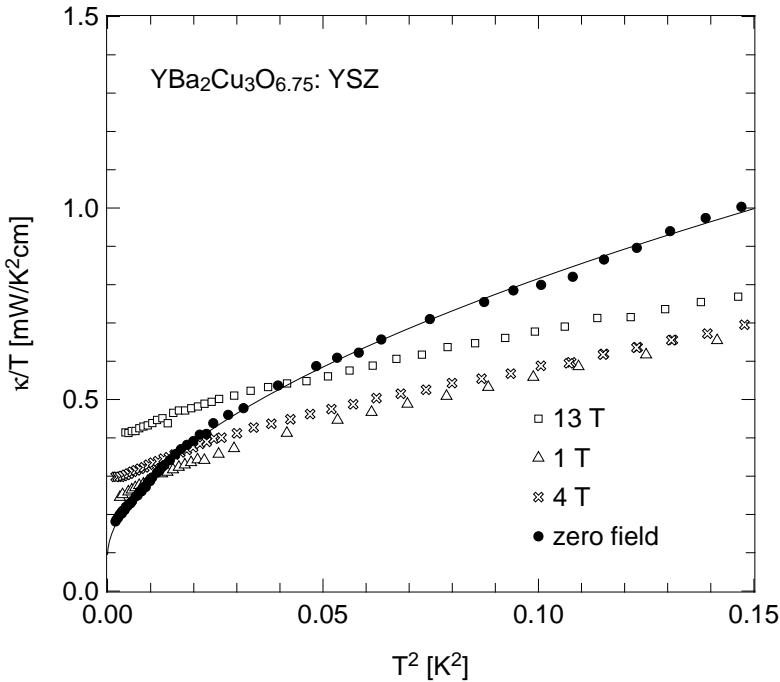
Figure 9.4: Thermal conductivity of the underdoped $YBa_2Cu_3O_{6.75}$ sample as a function of field. The zero field power law fit yields $\kappa/T = 0.1mW/K^2cm + 2.6T^{1.1}$.

conventional theories, or the need to consider intermediate phase shifts, or both.

9.3 $\kappa(H)$ in $YBa_2Cu_3O_{6.75}$

9.3.1 $H = 0$

To extend our investigation of thermal transport in the non-universal regime we performed measurements of $\kappa(H)$ on our underdoped sample of $YBa_2Cu_3O_{6.75}$. This sample was grown in Toronto in a YSZ crucible, was detwinned, and had a resistive T_c of ~ 61 K (see chapter 6). For this series of experiments, the heat current was again along the a-axis to avoid chain contributions, with the field applied perpendicular to the ab plane. The thermal conductivity for this sample at a number of fields is shown in Figure 9.4. The effect of the field is immediately seen to be analogous to what was observed for the ultra-pure $YBa_2Cu_3O_{6.99}$ sample is section 9.5.2: an additional temperature dependence to the 0 field data is dramatically suppressed by the application of a modest field of 1 Tesla. Further evolution of the data with field is also seen to consist of a rigid shift in κ/T. A powerlaw fit to the data yields a linear term of 0.1 mW/K^2cm, consistent with the general trend of reduced κ_0/T with doping.
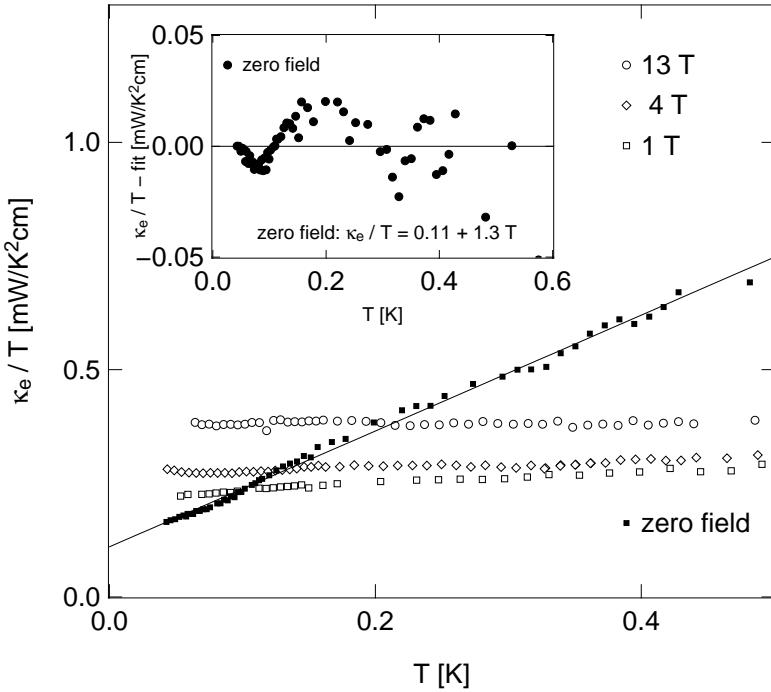
Figure 9.5: **Main**: κ_e/T vs. T for $YBa_2Cu_3O_{6.75}$. The electronic contribution is estimated by subtracting off $\kappa_{ph}(T)$ estimated from the 13 Tesla as described in the text. The solid line is a linear fit to the 0 Tesla κ_{el}/T. **Inset**: Residuals of the of the linear fit to κ_{el}/T in zero field.

9.3.2 T dependence of κ_e, $H = 0$

Using the arguments outlined in the previous section we take the additional temperature dependence of the zero field data to be in the electronic channel, and note that the application of a field destroys it entirely. We may thus take the temperature dependence of the phonons from a power law fit to the 13 Tesla data as before, with the electronic contribution at high fields being given by only by the linear term. The power law fit to the 13 Tesla data reveals that $\kappa_{ph}(T) = 1.6 \times T^{2.4}$ mW/K^{2}cm, and subtracting this away from the data at other fields gives the curves seen in Figure 9.5. From the flat T dependence of the 1 and 4 Tesla data we can see that this treatment works well - the in-field κ_{el}/T is temperature independent up to 500 mK. The temperature dependence of the remaining electronic component of the zero field data reveals a temperature dependence that is *linear* in T, marking a puzzling departure from the $YBa_2Cu_3O_{6.99}$ case.

Such a linear dependence of κ_{el}/T on T is expected in the *clean* limit: where $k_BT > \gamma$. In this regime the density of states of a *d*-wave superconductor is known to be linear in energy [11], which leads to an electronic specific heat (in zero field) of the form:

$$C_{el} = \alpha T^2 = \frac{18\zeta(3)}{\pi} \left(\frac{k_B^3}{\hbar^2} \right) \left(\frac{n}{d} \right) \alpha_{FL}^2 \left(\frac{1}{v_F v_2} \right) T^2 \tag{9.2}$$

where $\zeta(3) = 1.2$. The thermal conductivity of these excitations may be estimated using the kinetic transport theory introduced in section 2.2: $\kappa_{el} = 1/3 C_{el} v_F^2 \tau_e$. Combining this result with equation 9.2 above yields:

$$\kappa_e = \frac{6\zeta(3)}{\pi} \left(\frac{k_B^3}{\hbar^2} \right) \left(\frac{n}{d} \right) \alpha_{FL}^2 \tau_e \left(\frac{v_F}{v_2} \right) T^2 \tag{9.3}$$

We can estimate the electronic scattering time τ_e by using $\alpha_{FL}^2 \sim 1$ and the value of $v_F/v_2 = 10$ calculated from the universal linear term. With a T^2 coefficient in κ_e of 1.3 mW/K^3cm, τ_e is calculated to be 1.40 nS. For a characteristic Fermi velocity of 2.5×10^7 cm/s this works out to give a mean free path of 350 μm, which seems too large to be realistic.

A similar quadratic dependence of κ_e was also reported by Nakamae *et.al.* [197] in samples of optimally-doped Bi-2212. In their experiment, electron irradiation was used to move the sample from the clean limit $k_B T > \gamma$ to the dirty limit $k_B T < \gamma$. The phonon contribution in this case was subtracted by comparing measurements before and after the irradiation. Using similar analysis to ours, they obtained $\tau_e = 1.2$ *p*S, an order of magnitude shorter lifetime than we find. Interestingly, this is roughly consistent with the estimate of an order of magnitude higher impurity concentration in the best quality Bi-2212 compared to YSZ grown YBCO coming from the peak in κ below T_c.

What is difficult to understand in both the underdoped YBCO and optimally doped Bi-2212 study is why the clean limit should be reached at all. From Figure 9.3 we saw that the T dependence of κ_e in the ultra-pure overdoped sample was clearly cubic to at least 500 mK, which places that sample in the dirty limit $k_B T < \gamma$. Since Bi-2212 and YSZ grown YBCO are known to be less pure, these samples should be even deeper in the dirty limit, since γ scales with Γ. Indeed for the underdoped YBCO sample, in the unitary limit $\gamma \propto \sqrt{\Delta_0}$ so one would expect γ to grow as the pseudogap energy scale also increases. At present, this puzzle remains unresolved.

9.4 $\kappa(H)$ in $YBa_2Cu_3O_{6.50}$

$\kappa(H)$ was also measured our ultra-pure BZO grown sample of $YBCO_{6.50}$ with the same field and current alignment. The result, shown in the left hand panel of Figure 9.6 has similar features to the previous curves - an additional T-dependence of the zero field
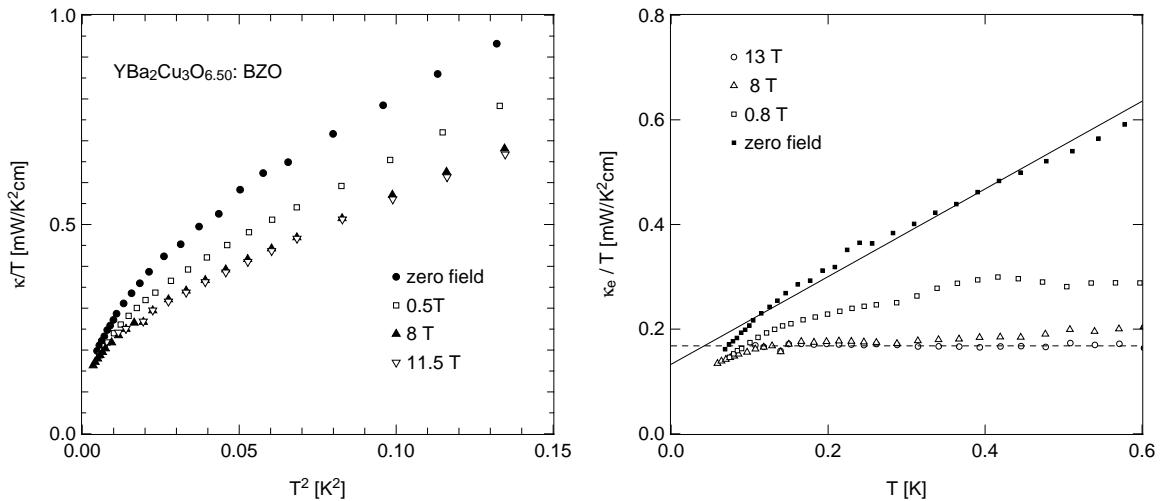
Figure 9.6: **Left** : Temperature and field dependence of the thermal conductivity in ultra-pure samples of YBa$_2$Cu$_3$O$_{6.50}$, with **J** $\parallel$ a, $H \parallel c$. **Right** : The estimated electronic component of the thermal conductivity of $YBCO_{6.50}$ as a function of field. The analysis used for previous samples appears to fail here.

data is suppressed by the application of a strong magnetic parallel to the c-axis. This additional T-dependence partially remains as H=0.5 T, but when one changes the field from 8 to 11 Tesla the data does not shift noticeably.

Using this fact we apply analysis similar to that for the previous samples, where κ_e/T is assumed to be T-independent at high field, and any additional T-dependence is attributed to phonons. Extracting the zero field data of $\kappa(T)/T$ in this manner results in the curve shown in the right hand panel of Figure 9.6. It is certainly clear that the additional T-dependence of κ_e/T is not T^2, nor is it completely described by a linear fit. The data actually seems to vary in a sub linear manner, close to $\sqrt{T}$. This is almost certainly wrong, since extending the curve to zero temperature results in a linear term that is negative. The most likely explanation is that in subtracting away the phonon term too much was taken off of the zero-field κ_e/T, which implies that there must still be some electronic temperature dependence of κ_e/T even at 11 Tesla. This correct interpretation of this observation is for the moment unclear, and further work is needed. Measurements on thinner samples for instance may reduce the magnitude of the phonon term, thus making an extraction of κ_e/T an easier task.

9.5   H Dependence of κ_0/T

In unconventional superconductors, the effect of applying a magnetic field was argued by Volovik [96] to result in a Doppler shift of extended quasiparticle states. In a nodal superconductor, this shift induces a finite residual density of states which is expected to vary as $\sqrt{H/H_{c2}}$. Experimental verification of this scenario was found for localized states by the observation of a $\sqrt{H}$ dependence of electronic heat capacity on field [98, 99, 101]. For thermal transport, which is sensitive to delocalized states, a similar scaling is expected. In the theory of Kübert and Hirschfeld [102] the evolution of the residual linear term with field was stated in chapter 3 to be:

$$\frac{\kappa(0,H)}{T} = \frac{\kappa_0}{T}\frac{\rho^2}{\rho\sqrt{1+\rho^2}-sinh^{-1}(\rho)} \tag{9.4}$$

This expression is valid (to within logarithmic corrections) in the clean limit, where the energy scale associated with the Doppler shift E_H is much larger than impurity bandwidth γ, neglecting any scattering of the quasiparticles by vortices [102]:

$$E_H \sim a\hbar\sqrt{2/\pi}v_F\sqrt{H/\Phi_0} \tag{9.5}$$

where a is a constant determined by the vortex lattice geometry. The parameter ρ is essentially the ratio of the two relevant energies - the Doppler shift (E_H), and the impurity bandwidth γ (see section 3.4.2 for details). In the dirty limit regime, where $E_H < \gamma$, ρ is calculated to be $\sqrt{6/\pi}\gamma/E_H$, assuming unitary scattering [102].

In Figure 9.7 we show the extrapolated linear term in thermal conductivity at $T \to 0$, plotted as a function of magnetic field for previous results on optimally doped YSZ-grown YBCO [61], alongside our new data for YBCO$_{6.99}$ and YBCO$_{6.75}$. The values are normalised by the zero-field value κ_0/T. In contrast to the two other YSZ grown samples, the much purer BZO-grown YBCO$_{6.99}$ shows a rapid increase at fields below $H = 0.4$ T followed by a sudden change to a regime where the field dependence plateaus. We now turn to a quantitative treatment of these results.

9.5.1 κ_0/T vs. H: YBCO$_{6.95}$

The earlier thermal conductivity measurements [61] in optimally doped YBCO shown in Figure 9.7 were found to be in good agreement to theory of Kübert and Hirschfeld. The dotted line through the open circles gives the best fit to equation 9.4 and yields a value of $\rho\sqrt{H} = 2.61$. Evaluating this fit at 8 Tesla, Chiao *et.al.* found that $\gamma/E_H = 0.67$ at
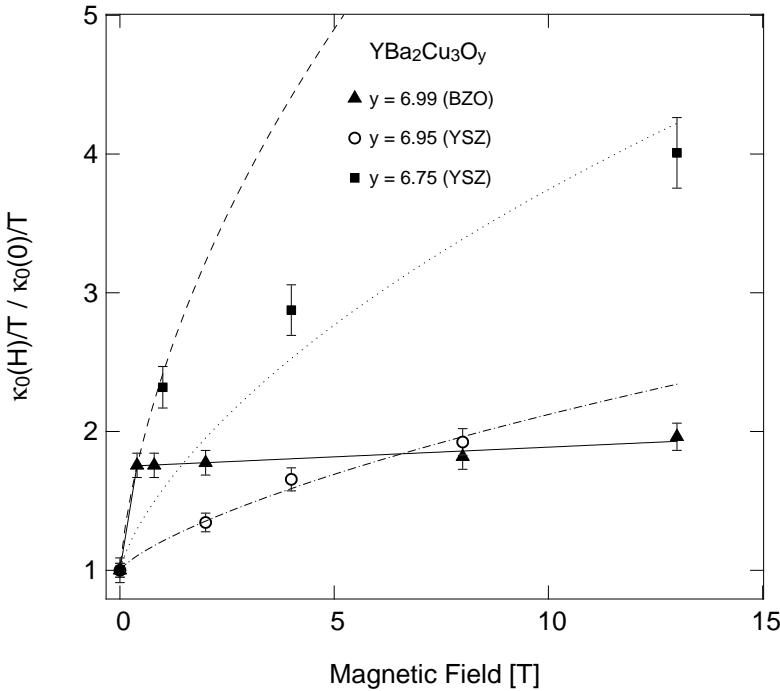
Figure 9.7: Normalized residual electronic conductivity as a function of magnetic field for the slightly overdoped ($y = 6.99$) YBCO, the optimally doped ($y = 6.95$) YBCO, and the underdoped ($y = 6.75$) YBCO. The lines are attempts to fit the data to the semiclassical theory of quasiparticle transport of Kübert and Hirschfeld [102].

8 Tesla, indicating that the sample was still close to the dirty limit. Measurements on Zn doped samples served to further confirm the theory, with estimates of the mean free path from the fits to equation 9.4 yielding results that are in good agreement to those obtained from other methods [61]. All of this serves to prove the following - in ordinary quality, optimally doped YBCO thermal transport is well understood theoretically with a model that assumes unitary scattering of quasiparticles, and neglects any contribution from scattering off of vortices.

9.5.2 κ_0/T *vs. H:* $YBCO_{6.99}$

Clearly the field dependence of the linear term in the BZO-grown sample is of a completely different character than the YSZ-grown sample. The sharp, initial rise of the conductivity is expected given the greatly enhanced purity of the crystal, but the abrupt plateau above 0.5 T is not. This occurs at the same low field that the additional T dependence in κ_e/T is suppressed, as seen in Figure 9.7. We interpret this as an additional scattering mechanism that kicks in at low fields, almost certainly an indication

that quasiparticle-vortex scattering is strongly influencing the transport in this very clean material. An obvious question is why this behaviour is manifest in this sample and not others. Assuming the impurity and vortex-quasparticle scattering mechanisms add in a Matthiessen-like manner, at zero field the conductivity will be in the impurity dominated regime, while in the very high field limit vortices will dominate the scattering. The crossover between these two limits will depend on the relative amount of impurity scattering and the cross-section for vortex scattering. In this model the fact that both the YBCO$_{6.95}$ and the YBCO$_{6.99}$ crystal have similar values of $\kappa_0(H)/\kappa_0(0)$ is perhaps not surprising - at high enough fields the impurity scattering is dwarfed by the vortex scattering.

The dotted line through the black triangles in Figure 9.7 is the best fit for the theory of Kübert and Hirschfeld [102] to the initial rise of the conductivity, which yields $\rho\sqrt{H}$ = 0.7. To get a feel for the magnitude of this rise we may assume unitary scattering, although strictly speaking we know this does not adequately account for the temperature dependence of κ_e in section 9.5.2. Given the high purity of the sample, and resulting small γ, one question is whether the crystal is still in the dirty limit $E_H < \gamma$ even at low fields. Assuming this is the case, and using the fit to the data from Figure 9.7 leads to γ/E_H= 0.8 (at 0.4 Tesla) suggesting the sample is still reasonably close to the dirty limit at low fields. An estimate of E_H for H = 0.4 T may be reached by using equation 9.5 with $a \sim 0.5$ [61] (for a square vortex lattice) and $v_F = 2.5 \times 10^7$ cm/s. This works out to give $E_H \sim 10$ K, which results in $\gamma \sim 8$ K. The unitary limit normal state scattering rate is then $\Gamma_N = \gamma^2/0.40\Delta_0 = 1.1 \times 10^{11} s^{-1}$ (assuming $\Delta_0 = 2.14 k_B T_c$). Intriguingly, if one performs a similar calculation for the YSZ grown sample at 0.4 Tesla, the scattering rate deduced from the fit is $\Gamma_N = 1.5 \times 10^{12} s^{-1}$, an order of larger [1]. This difference in scattering rates is in agreement with the relative difference in magnitude inferred from the rise in thermal conductivity below T_c seen in chapter 7.

For fields greater than 0.4 T, a complete theoretical understanding of the plateau region is still lacking. One approach, formulated at finite temperatures, is to treat the scattering of quasiparticles off of a disordered vortex lattice [198]. In the regime that the mean-free path associated with vortex scattering (ℓ_H) is *smaller* than that imposed by impurity scattering (ℓ_{imp}), the total mean free path is expected to scale like the intervortex distance, $a_v = \epsilon\sqrt{H_{c2}/H}$. Since the Volovik effect produces a heat capacity

---

[1]This value is somewhat larger than that originally derived by Chiao *et.al.*, since I have used updated measurements of $v_F = 2.5 \times 10^7$ cm/s as opposed to 1.0×10^7 cm/s as was used in the original work

that varies as $k_0 N_F T \sqrt{H/H_{c2}}$, the kinetic theory of thermal conductivity requires that $\kappa = 1/3 c_V \ell$ be *universal* with field.

Although this treatment has not been extended to the $T = 0$ limit, the phenomenology is essentially agrees with our observations, and provides a natural explanation for why a plateau should be observed in $YBCO_{6.99}$ and not $YBCO_{6.95}$ - the sample with the enhanced purity would be more likely to be in a regime where ℓ_{imp} remains shorter than ℓ_H. What remains surprising is the sharpness with which this regime is entered.

9.5.3 κ_0/T vs. H: $YBCO_{6.75}$

We now turn to the field dependence of the residual linear term in the underdoped sample of YSZ grown YBCO with y=6.75. It is not at all straightforward to anticipate the behaviour of the in-field low temperature thermal transport as doping is decreased. What is understood is that as p is lowered the effects of quantum fluctuations of the superconducting order parameter should grow as the superconducting critical point is reached [199]. This, coupled with the fact that hidden order may manifest itself in the vortex cores of underdoped cuprates makes transport calculations in this regime difficult.

The data in Figure 9.7 suggests a behaviour that is closer to that expected from the semiclassical theory of Kübert and Hirschfeld [102] than that observed in the $YBCO_{6.99}$ sample. There appears to be a fairly sharp initial rise, followed by a crossover into a regime where the field dependence is reduced, but certainly not absent. The dotted line shows the best attempt to fit to the semiclassical theory, with the result that $\rho\sqrt{H} = 1.3$. At 13 Tesla, E_H is 60 K with a and v_F as before. From the fit this suggests that $\gamma/E_H = 0.26$, using the dirty limit expression for ρ (Equation 3.22). This result places the sample towards the clean regime, where the Doppler shift energy scale is the dominant energy scale in the problem. In this limit, assuming unitary scattering, the parameter ρ is related to the normal state scattering rate Γ in Equation 3.23 Using $E_H = 60$ K and $\Delta_0 = 50$ meV (from the zero field value of the linear term) gives $\Gamma = 1.3 \times 10^{11} s^{-1}$.

For an optimally doped sample of YSZ grown YBCO, $\hbar\Gamma/k_B T_{c0}$ was estimated to be 0.014 from a combination of resistivity, microwave and infrared measurements [60]. In this case, $\hbar\Gamma/k_B T_{c0}$ gives 0.016, which is in remarkable agreement with these values. What this suggests is that even in the underdoped regime a semi-classical treatment of transport does a reasonable job at describing $\kappa(H)$ in crystals of ordinary purity, although additional data points at low fields would help to strengthen this assertion.

9.5.4 κ_0/T vs. H: YBCO$_{6.50}$

Extracting the linear term from powerlaw fits to the BZO-grown sample of YBCO$_{6.50}$ is a difficult task. The curvature of the data is large, and the powerlaw fits often yield results that vary depending on the range of fitting. In order to account for this uncertainty, the data was fit from 0 - 550 mK for all fields, but the error bars were determined by noting how much the extrapolated value of κ_0/T varied when one changed the temperature range the fit was performed over. This is usually not a concern for most samples since κ_0/T is often robust to changes in the fit range. The results can be seen in Figure 9.8, plotted as both κ_0/T vs. H and normalized to the zero field value.

Due to the large error bars on the values of κ_0/T it is not possible at this stage to fit the data to theory. The large uncertainty in the values could possibly be due low temperature downturns resulting from poor contacts (see section 10.2.1), although it is difficult to see why this would be the case. Electrically the contacts were excellent at room temperature and thermally they behaved well down to 50 mK. A more likely explanation is that a simple power law fit does not adequately capture the physics of low-T transport in this sample.

A simple and informative test of the role that disorder plays in setting the field dependence of the thermal conductivity would be to measure an ordered and disordered version of the same sample. Tuning the order may be achieved simply by heating the ortho-II sample, thereby randomly distributing the oxygen atoms in the chain layer and enhance the scattering rate Γ.

9.6 $\kappa/T : H > 0, T > 0$

One of the outstanding unresolved puzzles in the cuprate transport literature is the experimental observation by Krishana, Ong and co-workers [173] of a high field plateau in the value of κ at finite temperatures. They reported that the evolution of κ with field at $T < 20$K consisted of a sharp rise followed by a plateau above some $H^* \propto H_{c2} \left(T/T_c\right)^2$. This observation was initially held up as a possible example of a field-induced transition to a state where the Fermi surface is fully gapped - ie. $d \rightarrow d + id'$. Experimental confirmation of this interpretation with other techniques remains weak, compelling a search for alternative explanations.

Given our assertion that vortex scattering plays a non-neglible role in setting the mean free path for low T transport in the ultra-pure sample of YBCO$_{6.99}$, we plot the
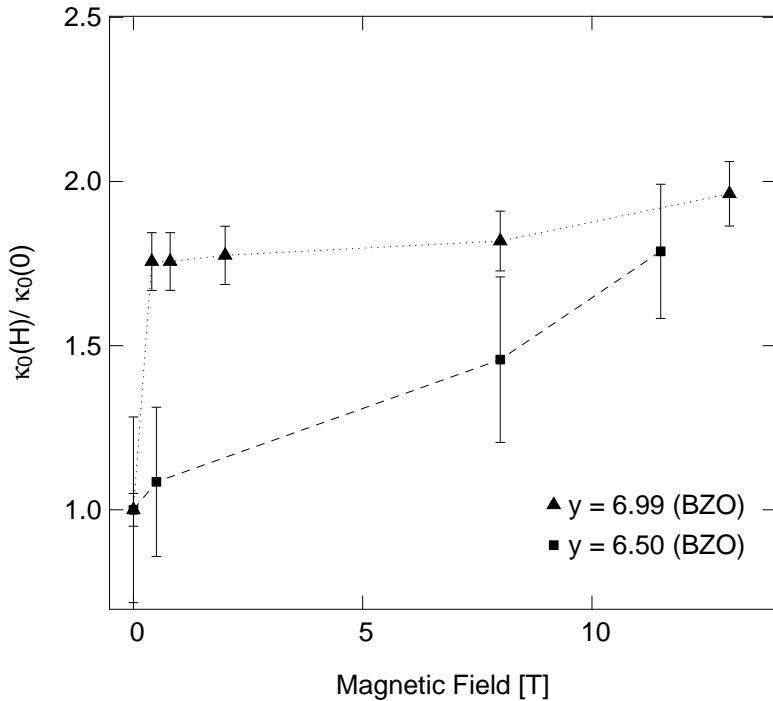
Figure 9.8: Residual linear term versus field for the YBCO$_{6.50}$ and YBCO$_{6.99}$ BZO grown crystals. The dotted lines are guides to the eye.

field dependence of an isotherm at 0.5 K in Figure 9.9 using the data of Krishana *et.al* [173] alongside our own. This remarkable similarity, measured here for the first time in YBCO, is suggestive of a common origin. Since the present work is on a sample of the highest purity and in field-cooled measurements, this phenomena cannot simply be dismissed as material dependent extrinsic behaviour. The hysteresis seen in other Bi-2212 measurements [200] is also naturally explained by the dominance of vortex scattering. The dramatic difference in magnitude between these two measurements is likely a consequence of the small electronic conductivity relative to the phonon contribution (which has not been subtracted) at 6 K in Bi-2212 and the comparatively huge electronic contribution measured in this high-purity YBCO.

An alternative explanation has recently been offered by Franz and Vafek [39]. In their fully quantum-mechanical theory, the Meissner state (at zero field) and the vortex state emerge as two distinct *d*-wave states with different quasiparticle effective velocities. They both exhibit universal conductivity, with different values of the universal limit. This appealingly accounts for the fact that the conductivity of the two different YBCO samples is the same not only at zero field but also at high fields (see Figure 9.7). It is
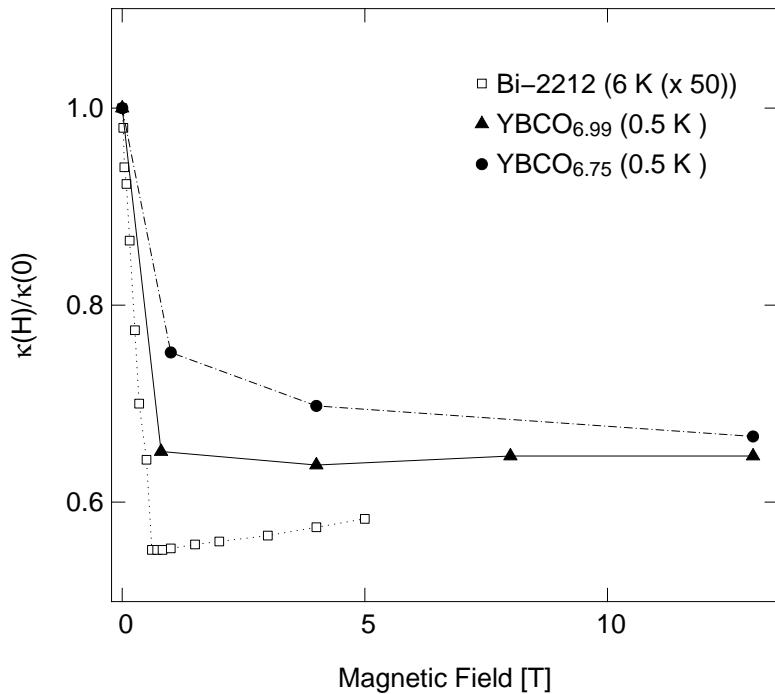
Figure 9.9:   Normalized thermal conductivity at fixed, finite temperature versus field for the ultra-pure YBCO and underdoped YBCO crystals. The data is compared to that for Bi-2212 [173] at 6 K, magnified by a factor of 50.

not clear, however, why the finite temperature correction to this universal limit should be so dramatically different in the two states.

9.7   Chapter summary

The principal conclusions from this chapter are primarily drawn from the study of the ultra-pure YBCO$_{6.99}$ sample. When analysed in terms of the quasiclassical theory of transport for a *d*-wave superconductor, the thermal conductivity of this sample reveals two features: 1) the universal limit as $T \to 0$ is confirmed, 2) the usual assumption that impurity scattering can be treated as single isotropic phase shift in the unitary limit (or the Born limit) is incorrect. Transport theory as it stands must be revised, at least in the clean limit, perhaps by going to intermediate phase shifts and maybe in more profound ways.

Moreover, in the presence of a magnetic field, we find that transport appears to be rapidly dominated by vortex scattering in ultra pure samples of YBCO, which can therefore not be neglected as it usually is.

10

κ IN THE STOICHIOMETRIC UNDERDOPED CUPRATE YBA$_2$CU$_4$O$_8$

10.1   Chapter overview

In Chapter 8 we have seen that reducing the hole concentration p in both YBCO and LSCO leads to a reduction in the residual linear term measured in thermal conductivity. This firmly established trend seems strangely at odds with a report by Hussey *et.al.* [5] that claims the *absence* of any finite κ_0/T in the double chained YBa$_2$Cu$_4$O$_8$ (Y-124) system. This system is a highly desirable candidate to study given that it can be prepared with virtually negligible levels of disorder, and is understood to be naturally underdoped with a T_c of 80 K. In this chapter I summarize the results of our work on low temperature thermal conductivity measurements of the Y-124 system. In contrast to the previous data, a sizable linear term is seen in zero field. With an applied magnetic field along the c-axis, novel dependence of the a-axis thermal conductivity at finite temperatures and at T=0 is observed, likely a manifestation of the extremely low impurity scattering rate.

10.2 κ in YBa$_2$Cu$_4$O$_8$: $H = 0, T = 0$

The thermal conductivity of two samples of Y-124 was measured using the standard techniques and procedures outlined in chapter 4, in both zero and applied magnetic fields with $H \parallel c$ and $\mathbf{J} \parallel a$ or b. The field was swept only when $T > T_c$, to ensure a homogenous vortex lattice. The results for samples B and D are shown in figure 10.1. From the resistivity curves shown in section 6.5.5 we determine that these samples are aligned along the a and b axis for respectively. We have set the magnitude of the geometric factor by normalizing our resistivity curves to those reported in the literature [138] since the extremely small size of the samples made direct determination of dimensions difficult (see section 6.5.5).

The data in figure 10.1 is plotted alongside the previous results of Hussey *et.al.* [5] which purported to show a linear term of zero for transport in both the a and b direc-
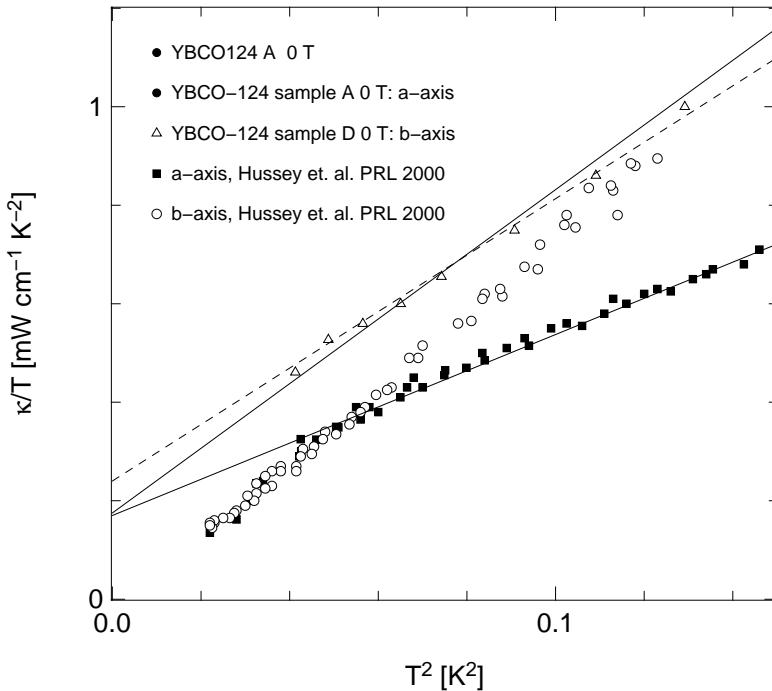
Figure 10.1: κ/T vs. T^2 for Y-124 with heat current along the *a*-axis (sample A) and *b*-axis (sample D). The data from Hussey *et.al.* [5] is shown for comparison, with the dotted lines being guides to the eye.

tions. Using a simple linear extrapolation on our data for both crystals results in a finite and robust linear terms of magnitude of 0.16 and 0.24 mW/K^2cm for sample A and D respectively. It is interesting to note that if one extrapolates the *a*-axis data of Hussey *et.al.* from *above* ~ 250 mK the value of κ_0/T is identical to what we observe, suggesting a mechanism that suppresses the low temperature part of their data. The *b*-axis data for both groups matches at high temperatures, but diverges as T=0 is approached.

10.2.1 Anomalous low temperature downturns in cuprates

In an effort to resolve the discrepancy between these two sets of data, Smith, Paglione, Walker and Taillefer [201] have developed a model which suggests a simple mechanism for the observed "downturns" in thermal conductivity. The basic idea is that below some sufficiently low threshold temperature T_D, the phonon and electron heat baths may become thermally decoupled. If the quality of the electrical contacts to the sample is poor, heat is transferred directly to the phonon bath and is not transferred to the electron bath which implies that the temperature of the sample thermometers are not a true indication of the temperature of the electron bath. The authors have shown that

in the limit where the electrical resistance of the contacts $R_{el(c)}$ is comparable to the electrical resistance of the sample R_{el} then the low T limit of the electronic thermal conductivity in the universal regime takes the following form:

$$\kappa_e/T = \alpha \frac{1}{1 + \frac{r}{1+r(T/T_D)^{n-1}}} \qquad (10.1)$$

where $r=R_{el(c)}/R_{el}$, n is between 4 and 5 and T_D is determined by the dimensions of the samples and the electron-phonon matrix element. In the limit that the sample electrical contacts are very good, $r \to 0$ and the thermal conductivity recovers the usual form $\kappa_e/T \sim \alpha$.

If the contacts are electrically poor ($r \gg 1$, equation 10.1 produces a downturn in κ_e/T which would give an erroneously small linear term. This model was found to work very well to describe similar observations on the LSCO and PCCO systems [201] and is most likely the cause of the different results observed in figure 10.1. The contacts to our samples were made from evaporated gold and annealed for sufficiently long that their resistances were sub-Ohmic. All contacts on sample A had $R_{el(c)} < 100m\Omega$ at 4 K. This is at least an order of magnitude improvement over the silver epoxy contacts of Hussey *et.al.* [202]

10.2.2 Ruling out experimental errors

To give added confidence that the observation of a finite linear term in Y-124 is correct, we rule out two possible sources of contamination in our data. Heat losses through the leads and supports of the thermometers could in theory shift the data upwards and yield a false residual linear term. Provided that the conductance of the sample plus contacts is much greater than the conductance of this path, the effect should be negligible. The left hand panel of Figure 10.2 shows the calculated conductance based on the estimates of the Kapton supports and PtW wires provided in chapter 4 alongside the measured conductance of the sample plus contacts. Even for the extremely small Y-124 sample D the conductance of the sample is at least on order of magnitude greater than that of the heat loss paths, ruling out any chance that the finite κ_0/T is an artifact of heat losses.

As we shall see in section 10.5 the value of the residual linear term in this compound is remarkably sensitive to field. If any sizable stray fields existed within the cryostat this could presumably lead to an inflated value of κ_0/T. The magnet was "zeroed" before the 0 Tesla run by sweeping the field between positive and negative values of successively
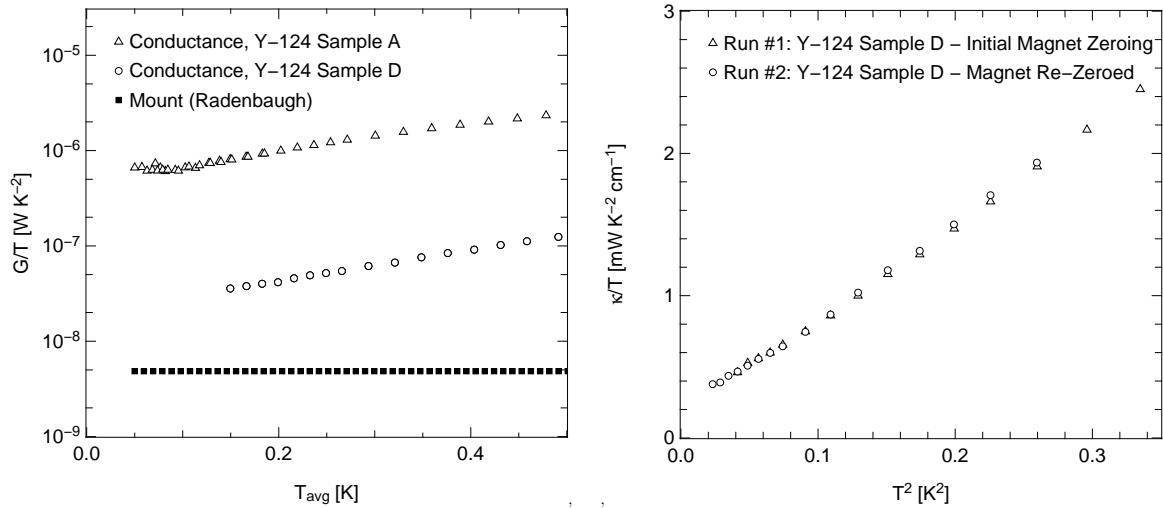
Figure 10.2: **Left**: Conductance of the two Y-124 samples and their contacts, plotted alongside the estimate of the conductance of the heat loss paths in our mount using the data of Radebaugh [108] (see section 4.4 for details). **Right**: Two separate zero field runs on sample D. The magnet was initially zeroed for the first run, then ramped to 13 Tesla and re-zeroed for the second run.

smaller fields until $H=0$ was reached. This procedure should eliminate any sizable stray fields, but in order to double check the magnet was "re-zeroed" with the sample at $T > T_c$ after the 13 Tesla run. The samples were remeasured at $H = 0\ T$ and the data for sample D for both runs is shown side by side in the right hand panel of figure 10.2. If there was a shift caused by stray fields it is difficult to see how applying the zeroing procedure twice should yield precisely the same residual field, and precisely the same linear term. We view this as conclusive evidence that the value of the H=0 term is robust.

10.2.3   Magnitude of the linear term

The precise value of the residual linear term in Y-124 samples A and D is determined by applying the powerlaw fitting procedure to equation 2.15. Figure 10.3 shows the results for each crystal plotted as a function of T^α, and the fitting parameters are summarized in table 10.1.

The overall error in the linear term is assessed from 3 sources - the error associated with fitting, the sensitivity of κ_0/T to fit range, and the overall uncertainty in the absolute value of the resistivity, which we use to define our geometric factors and is estimated to be on the order of 20% [203]. For heat current in either planar direction the value of κ_0/T seems rather large, even making generous allowances for error. For optimally doped $YBCO_{6.95}$ the magnitude of the linear term is for instance only 0.12-0.14 mW/K^2cm.
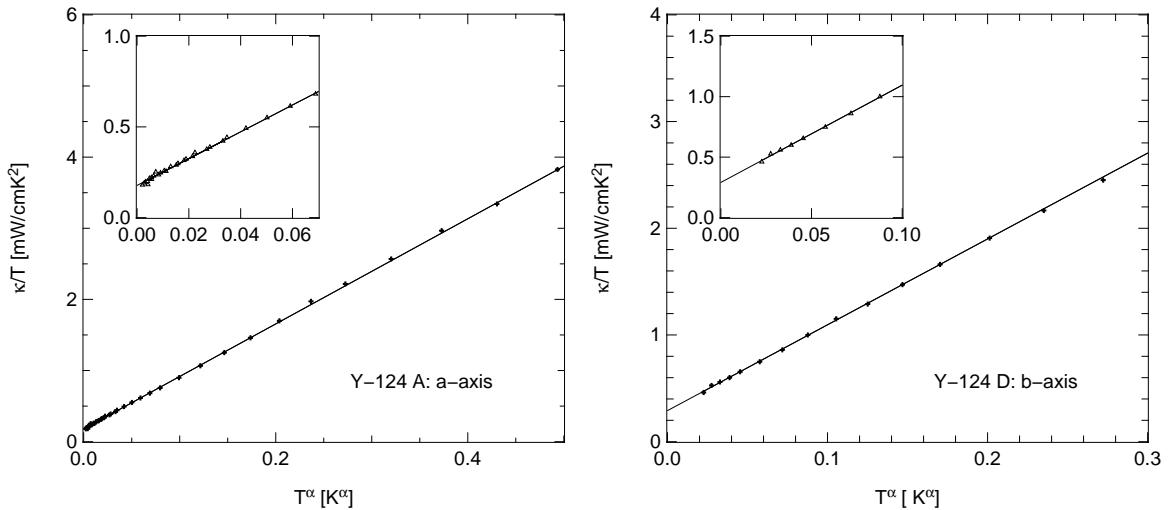
Figure 10.3: **Left**: Powerlaw fit to the thermal conductivity data of the Y-124 sample with **J** $\parallel$ a-axis. The values of α are given in Table 10.1. **Right**: Powerlaw fit to the thermal conductivity data of the Y-124 sample with **J** $\parallel$ b-axis. The small size of this sample caused it to be susceptible to vibrations of the sample mount, which limited the usable data $T > 150mK$.

There is also a marked anisotropy in the value of κ_0/T, which may arise due to contributions to the zero energy density of states from the double chains. Comparing the values from table 10.1 the b/a anisotropy ratio is 1.7 ± 0.5, with the large error bars arising from uncertainties in the geometric factor determination. Interestingly, in the single chained YBCO system at optimal doping, a slightly smaller $T = 0$ anisotropy is observed [204] - $\kappa_{0,b}/\kappa_{0,b} = 1.3 \pm0.3$, although the two agree within errors. In YBCO$_{6.9}$ the authors argue that the small value of the anisotropy (much smaller than that from resistivity in the normal state) suggests that the chain states are either fully gapped or localized. In the double chain system the converse is true, the chain states are delocalized and have no energy gap. This difference could arise from the fact that these samples of Y-124 posses at least 100 times lower levels of disorder than their single chain counterparts.

We may put this into perspective by computing the values of v_F/v_2 and Δ_0 for this compound as we did in chapter 8. Using Equation 3.14 with $d/n = 6.81$ Å[137] and taking the a-axis value of $\kappa_0/T = 0.18$ mW/K^2cm gives $v_F/v_2 = 20$. Band structure estimates suggest that v_F is the same in both the Y-123 and Y-124 systems [205], so we may take v_F to be 2.5×10^7 cm/s as before. Assuming a pure d-wave gap this gives us $\Delta_0 = 29$ meV, which is surprisingly small. If we define $p \sim 0.12$ by T_c and formula 6.1 (taking T_c^{max} to be 93 K) then this value of the gap falls well below what one would expect from the doping evolution in the single chained system, as seen in figure 10.4.
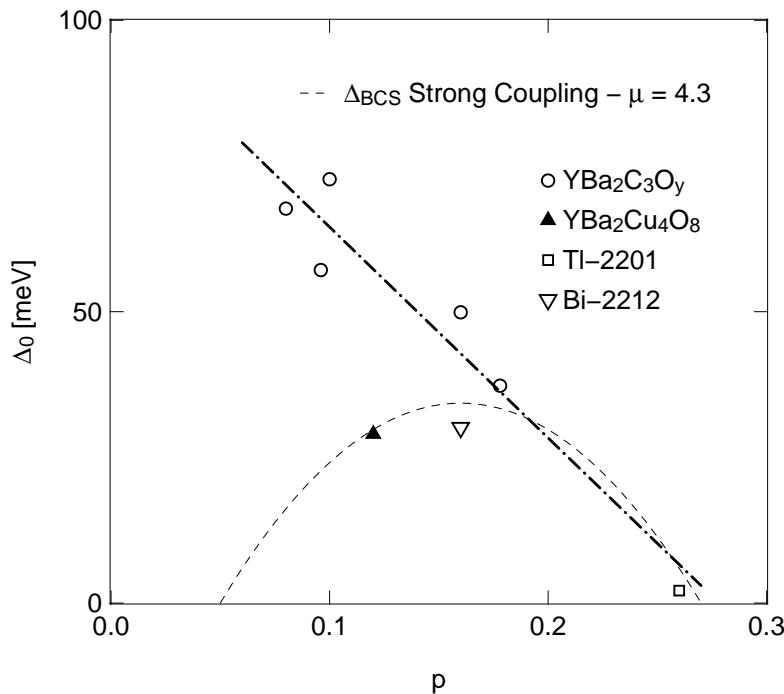
Figure 10.4: The value of the superconducting gap maximum derived from the residual linear term in Y-124 compared with other cuprates from chapter 8. The dotted line is a fit to strong coupling BCS theory, with a coupling constant of 4.2.

How does one account for this? It is tempting from the value of Δ_0 in figure 10.4 to claim that the superconducting state in Y-124 is fully accounted for by strong coupling BCS theory, with μ=4.2. The assertion however is difficult to reconcile with the observation that normal state properties in the system show clear evidence of a pseudogap, and that the low energy quasiparticles in Y-123 are governed by the energy scale of this gap. It is much more likely that either the assumption of a perfect d-wave order parameter used in deriving Δ_0 in incorrect, or that states from the chains may contribute to transport *even with* $\mathbf{J} \perp b$.

10.2.4 Analysis of the $a - b$ anisotropy

Wu, Branch and Carbotte have studied the universal conductivity of a superconductor with an order parameter than is largely d-wave in nature, but contains a subdominant s-wave component [206]. Such a scenario is not unexpected in some cuprates due to the orthorhombicity of the crystal structure, and has been reported in some tunnelling measurements [207, 208, 209]. Note that such an order parameter in no way affects the observation of a linear term, since only an order parameter with a complex or extremely

Table 10.1: Table summarizing the results of powerlaw fits to the 0 field thermal conductivity data on two samples of $YBa_2Cu_4O_8$.

Sample	κ_0/T (mW/K^2cm)	B	α
$YBa_2Cu_4O_8$ A (a-axis)	0.177 ± 0.015	7.4 ± 0.2	2.09 ± 0.02
$YBa_2Cu_4O_8$ D (b-axis)	0.29 ± 0.05	8.05 ± 0.3	2.38 ± 0.07

large, positive s-wave component would serve to lift the nodes off of the Fermi surface.

In their model Wu $et.al.$ treat a gap of the form $\Delta_k = \Delta_0(k_x^2 + k_y^2 + s)$ where s is the s-wave gap component, which may be positive or negative. In the polar representation, with ϕ representing the angle around the Fermi surface, the angular dependence of the gap becomes:

$$f(\phi) = \frac{cos(2\phi) + \alpha}{1 + \alpha cos(2\phi)} + s \qquad (10.2)$$

where α is given by the quasiparticle mass anisotropy

$$\alpha \equiv \frac{m_a - m_b}{m_a + m_b}. \qquad (10.3)$$

In the dirty limit, where $k_B T \ll \gamma$ the anisotropic ratio of the residual linear terms is governed by the parameters s and α as well as the zero temperature values of the penetration depth λ_0.

$$\kappa_{0,a}/\kappa_{0,b} = \frac{\lambda_{0,b}^2}{\lambda_{0,a}^2} \frac{(1 - \alpha)(1 - s)}{(1 + \alpha)(1 + s)} \qquad (10.4)$$

The zero temperature values of the penetration depth along both axes have been measured independently by microwave [180] and infrared techniques [185], and are in good agreement. Wu $et.al.$ find the anisotropy in λ_0 is a direct measure of the parameter α [206]:

$$\frac{\lambda_a(0)}{\lambda_b(0)} = \frac{m_a}{m_b} = \frac{1 - \alpha}{1 + \alpha} \qquad (10.5)$$

With $\lambda_{0,a} = 1880$ Å and $\lambda_{0,b} = 860$ Å from reference [180] we get $\alpha = 0.65$. Utilizing Equation 10.4 with the observed thermal conductivity anisotropy of 1.7 then yields $s = $ -0.86. These numbers are remarkably large, and produce a gap that is grossly deformed from the pure d-wave case, with the nodes shifted well away from the diagonals. This

topology is plotted is figure 10.5, and is likely too distended to be physical. Given the very high anisotropy of the penetration depth measurements, we would need to see a much larger anisotropy in the thermal channel in order to extract a sensibly small value of s and α.
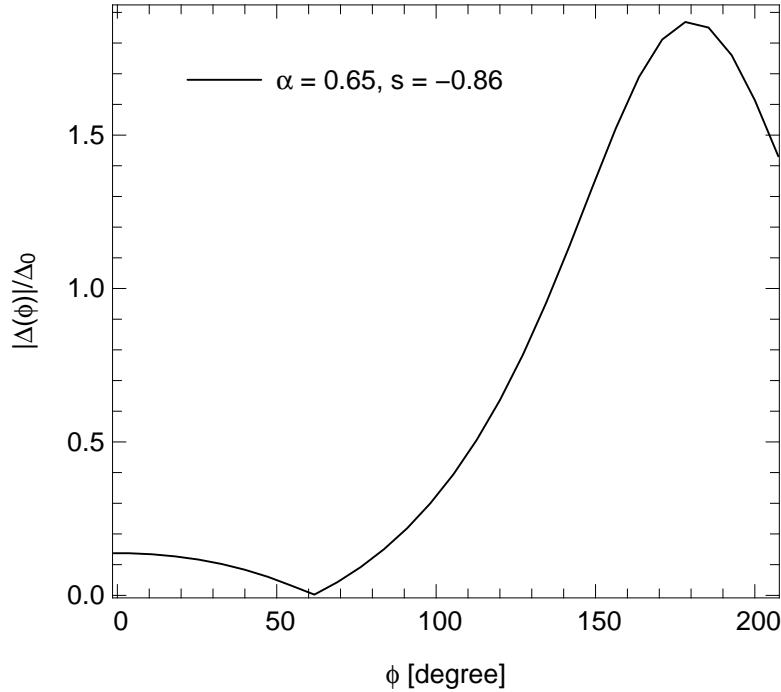
Figure 10.5: The value of the angular dependent part of the superconducting order parameter in the $d + s$ wave scenario of Wu *et.al.* [206]. The gap structure is calculated with the parameters α=0.65 and s=-0.86 extracted from thermal conductivity and penetration depth measurements [180].

It is peculiar that the anisotropy observed previously in Y-123 and now Y-124 is much smaller than that observed in normal state conductivity and penetration depth measurements. In a separate work, Wu and Carbotte [210] have proposed that in the case where the gap is $d_{x^2-y^2}$ the chain Fermi surface may be gapped due to its quasi one dimensional nature. At sufficiently low energies this would lift any observed $a - b$ anisotropy.

10.3 κ in YBa$_2$Cu$_4$O$_8$: $H = 0$, $T > 0$

The temperature dependence for the thermal conductivity of the a-axis sample is shown in figure 10.5 for several fields. It is immediately obvious that the field dependence of the data bears no qualitative resemblance to any Y-123 sample yet measured. The 0 field
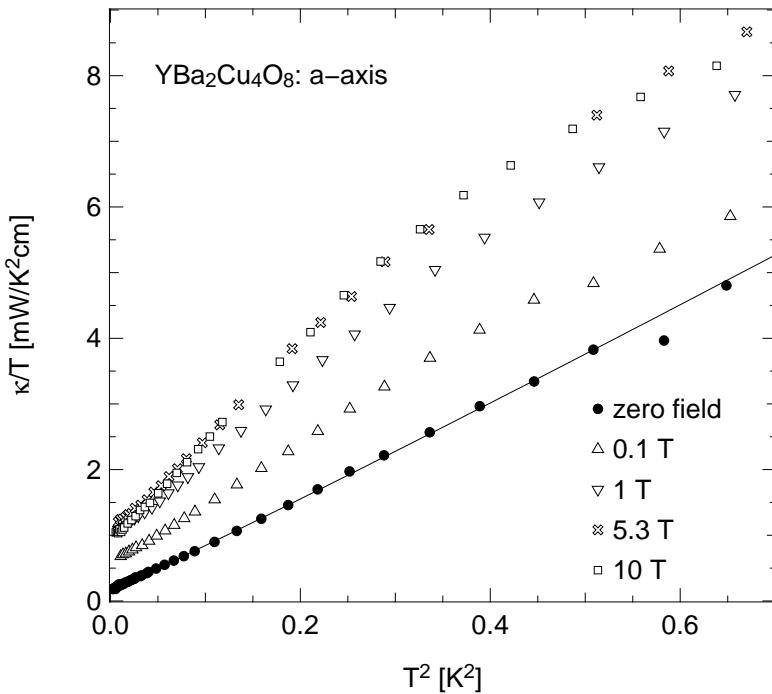
Figure 10.6: Thermal conductivity data for YBa$_2$Cu$_4$O$_8$ with **j** $\parallel$ a and $H \parallel c$ for various fields plotted to high temperatures. The line through the zero field data is the result of a power law fit to Equation 6.1.

data for instance shows *less* of a temperature dependence that does the in-field data, suggesting that there is a temperature dependent electronic term that is *enhanced* by the application of a field. This excludes the use of the analytical techniques of chapter 9, where the infield data was used to estimate the lattice thermal conductivity.

Hussey *et.al.* have estimated that even in these remarkably pure samples the impurity band width γ estimated for **J** $\parallel$ b is still sizable - on the order of 14 K [5]. This estimate assumes unitary scattering, but the scattering phase shift in this material may be closer to the Born limit as we have seen in the ultra pure Y-123 samples in chapter 9. Clear evidence to distinguish between these two scenarios can be found in the temperature dependence of the electronic part of κ_{el}. However with no accurate way to subtract off the phonons from the 0 Tesla data we will have to be satisfied with a crude estimate based on geometrical considerations.

In the boundary scattering regime, $\kappa = \kappa_{el} + 1/3\beta v_{ph}\ell_0 T^3$ (Equation 2.13) where the coefficient β is from the lattice heat capacity, ℓ_0 is the phononic mean free path and v_{ph} is the average acoustic sound velocity. The mean free path in this regime is determined from the dimensions of the sample, $2 \times \pi \sqrt{w\ell}$ where w and l are the width and length

of the sample respectively. Taking suitable values for β (0.5 $\pm$ 0.1 mT/molK^4) [5] and v_{ph} (5 $\pm$ 1 $\times$ 10$^5 cm/s$) [211] with $\ell_0 = 0.17 \pm 0.02$ mm gives $\kappa_{ph} \sim 9.9$ mW/K^{4}cm $\pm$ 3. The 0 field data fits very well to a simple boundary scattering picture, even in a free fit the powerlaw exponent comes out to be ~ 3. This fit yields a T^3 coefficient of 6.9 +/- 0.1 mW/K^{4}cm, which is in good agreement with our crude estimate of κ_{ph}. Using a similar analysis, Hussey *et.al.* find agreement with 3 of their samples [5], with a slightly larger measured T^3 coefficient that arises from fitting to below T_D defined in section 10.2.1.

From this we can conclude the following: any additional temperature dependence of the electronic coefficient in zero field must be relatively small. For comparison, in YBCO$_{6.99}$ we estimated an electronic T^3 term of 3.1 mW/K^{4}cm. The second order correction to the electronic thermal conductivity in the universal regime goes as $a^2/\gamma T^3$ [88], so one may expect for the ultra clean Y-124 system an *enhanced* electronic T^3 should be observed. Although the error bars on our estimate of κ_{ph} are large, it would be hard to attribute a majority of the measured T^3 in Y-124 to electrons. The size of the electronic T^3 term in Y-124 must then be on the order of that observed in YBCO$_{6.99}$.

10.4 κ in $YBa_2Cu_4O_8$: $H > 0$, $T > 0$

The evolution of the finite temperature data with field is an increase in slope as H is increased, as seen in figure 10.5. To quantify this trend we may assume that the phonons are field independent, and subtract the zero field curve from the in field data. Although this may subtract away some of the T dependence of κ_{el}, we can view the subtracted data as a *lower bound* on $\kappa_{el}(H, T)$. The result of this subtraction is displayed in figure 10.7, plotted as κ/T vs. T^2, and summarized in Table 10.2. Below 500 mK the growth of κ_{el} with temperature is observed to be cubic in T, and the coefficient of this term increases with increasing H. In the universal regime, this additional T dependence could be attributed to the second order correction of κ_{el}/T as in the YBCO$_{6.99}$ case. The outstanding question then is the size of the impurity band γ in this material. Using the *b*-axis residual resistivity and plasma frequency, Hussey *et.al.* [5] estimate that $\gamma \sim 14$ K, well above the temperatures accessed in our experiment.

The persistence of the T^3 term to high fields is still somewhat surprising given the strong role that vortex-quasiparticle scattering was shown to play in ultra-pure Y-123. The stoichiometric nature of the compound suggests a plausible explanation - extremely low disorder results in very low vortex pinning, and thus a vortex lattice that is almost
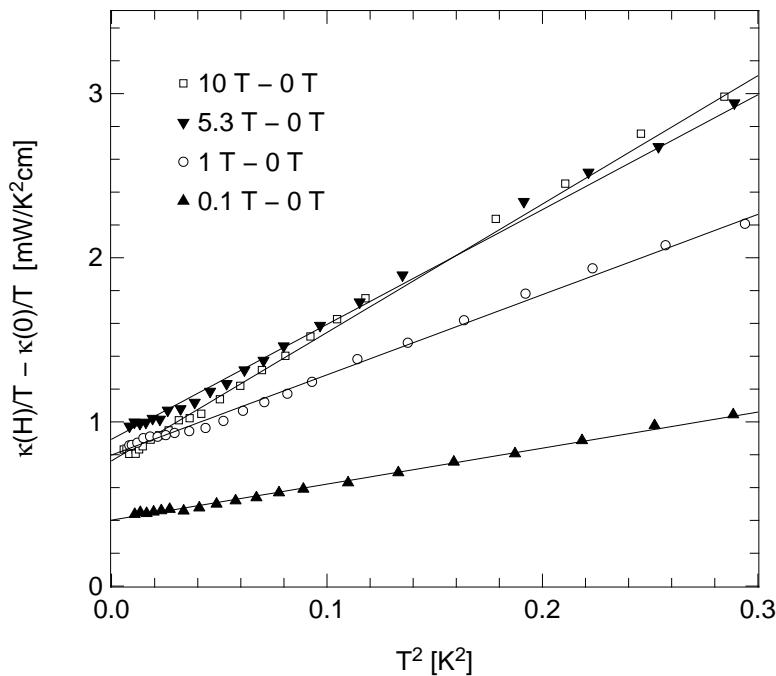
Figure 10.7: In field thermal conductivity data for YBa$_2$Cu$_4$O$_8$ with **j** $\parallel$ a, with the zero field data subtracted.

perfectly ordered. Such a distribution of vortices would have a negligible impact of quasiparticles, a direct consequence of Bloch's theorem. In this respect a comparative study of the vortex lattice in Y-123 and Y-124 by scanning probe microscopy would be useful.

A second possibility is that the T^3 term cannot be analysed within the framework of a semi-classical theory of mixed-state transport, but needs a full quantum mechanical treatment to understand

10.5 κ in YBa$_2$Cu$_4$O$_8$: $H > 0$, $T = 0$

Using a floating power law fit we extract the residual linear term as a function of field. The growth of κ_0/T with H is truly remarkable, eclipsing the already rapid growth in the ultra-pure YBCO$_{6.99}$ sample by a factor of 3. Figure 10.7 shows this growth expressed as κ_0/T vs. H, and as the linear term normalized by the zero field value, compared to previous results in Y-123.

Qualitatively the H dependence of the data is similar to the YBCO$_{6.99}$ case, a rapid initial rise that is cut-off by some mechanism at low fields, resulting in a nearly flat H

Table 10.2: Table summarizing the T^3 coefficient of $\kappa(H)/T - \kappa(0)/T$ in YBa$_2$Cu$_4$O$_8$.

H $\parallel$ c [T]	T^3 Coefficient of $\kappa(H)/T - \kappa(0)/T$ [mW/K^4cm]
0.1	2.2
1	4.9
5.3	7.0
10	7.9

dependence above 1 Tesla. In the ultra-pure Y-123 case, it was argued that the cutoff arose from a sizable vortex scattering term. If this is indeed the cause of the plateau in Y-124 then the hypothesis that the field dependence of the T^3 arises from the electronic channel is very surprising, given its sensitivity to scattering. If one accepts that the plateau is a result of vortex effects, then the H dependence of the finite temperature data cannot be accounted for in the standard theory of Graf. *et.al.* [88].

The initial rise in the data was fit to the semi-classical theory of Kübert and Hirschfeld [102] (Equation 9.4), with the result that $\rho\sqrt{H} = 0.25 \pm 0.04$. We can consider the two limiting cases for the interpretation of ρ: the clean limit where $\gamma < E_H$ and the dirty limit where $\gamma > E_H$. In the dirty limit case, we evaluate the situation at the upper range of the fit - 1 Tesla. At this field the Doppler shift energy E_H is 17 K, using the same values for a and v_F for the Y-124 compound as for the Y-123 compound in chapter 9. Using the dirty limit expression for ρ, Equation 3.22, yields a γ of 3.1 K - placing the sample solidly in the clean limit even at low fields.

In the clean regime, we have seen previously that $\rho = [8\Gamma H_{c2}/(\pi^2 a^2 \Delta_0 H)^{0.5}]$ where Γ is the normal state scattering rate, a is the vortex lattice constant and Δ_0 is the super-conducting gap maximum (Equation 3.23. Using $a=1/2$ and $\Delta_0 = 30$ meV from the zero field value of the linear term yields $\Gamma = 1.7 \times 10^{10}s^{-1}$. Remarkably, this value is exactly an order of magnitude less than that estimate using a similar analysis on YBCO$_{6.99}$ and two orders of magnitude less than that estimated for YBCO$_{6.95}$. This scaling is precisely what was predicted from the relative peak heights in the high temperature thermal conductivity in chapter 6.
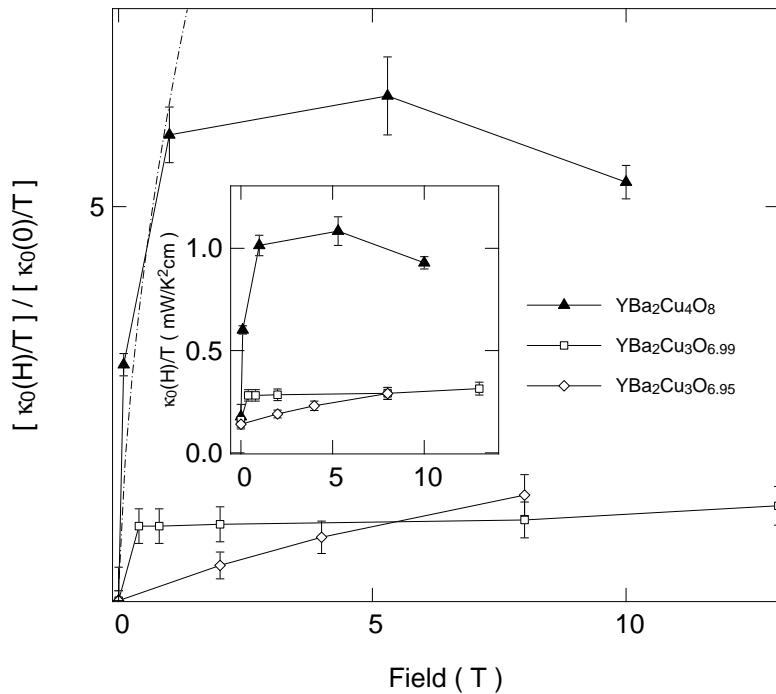
Figure 10.8: **Main** : Normalized value of the residual linear term in YBa$_2$Cu$_4$O$_8$ as a function of field. The results are compared to the Y-123 samples from chapter 8. For each crystal, **J** $\parallel a$, B $\parallel c$. The dotted line is a fit of the initial rise of the data to the semiclassical theory of quasiparticle transport of Kübert and Hirschfeld [102]. **Inset** : Residual linear versus field, as in the main panel but un-normalized.

10.6   Chapter summary

We have used measurements of thermal conductivity to resolve a long standing issue in the cuprate thermal transport literature. Contrary to previous results [5] we see a robust and sizable residual linear term in YBa$_2$Cu$_4$O$_8$. The magnitude of this term is however larger than expected, leading to an estimate of the low-energy gap that does not follow the trend with doping observed in YBCO$_y$. With the application of a magnetic field, the residual linear term is seen to grow more rapidly than in any previous measurement, likely due to the low disorder within the crystal. The in-field finite temperature data is observed to increase in slope as the field is increased, contrary to all previous measurements in the YBa$_2$Cu$_3$O$_y$ system.

11

NORMAL STATE CHARGE TRANSPORT IN ULTRA-PURE YBCO

11.1   Chapter overview

Up to this point, the majority of information on transport properties in the normal, non-superconducting state of underdoped cuprates has been limited to the LSCO family of compounds. To study the normal state in the absence of superconductivity, one typically suppresses the superconducting order by the application of very strong magnetic fields. This is difficult to achieve in cuprates, since the upper critical field in YBCO is on the order of ~ 200 Tesla[1]. The consensus from studies of the LSCO family is that upon application of a strong magnetic field, the resistivity is insulator like ($d\rho/dT < 1$). The resistivity shows a $\log(1/T)$ like behaviour for moderately underdoped materials, and diverges much more strongly for $p < p_{SC}$, where p_{SC} is the critical doping needed for the onset of superconductivity.

In YBCO, information on the normal state is mostly limited to samples where Zn doping has been used to suppress T_c and H_{c2}. Both of these systems however have large amounts of in plane disorder, whether from Zn impurities in doped YBCO or from Sr substitution in LSCO. In this section we ask the question: what is the nature of transport in the normal state of underdoped cuprates where disorder is minimized? To answer this we take two approaches. The first is to perform resistivity measurements in high quality, homogenous single crystals of YBCO samples prepared so that the hole doping p is slightly less than p_{SC} and the samples are non-superconducting in zero field. The second is to suppress superconductivity with a strong magnetic field - around 10 Tesla in YBCO$_{6.33}$ and with very high pulsed magnetic fields ($H > 50$ Tesla) in ultra pure ortho-II ordered YBCO$_{6.50}$, with $T_c = 55$K. This is the first time the field-induced normal state of a YBCO sample at such a high doping has been studied. Here I summarize the results of

---

[1]In the LSCO system, the T_c and H_{c2} at optimal doping are lower, on the order of 60 Tesla. This is why the largest volume of experimental data exists for this compound.
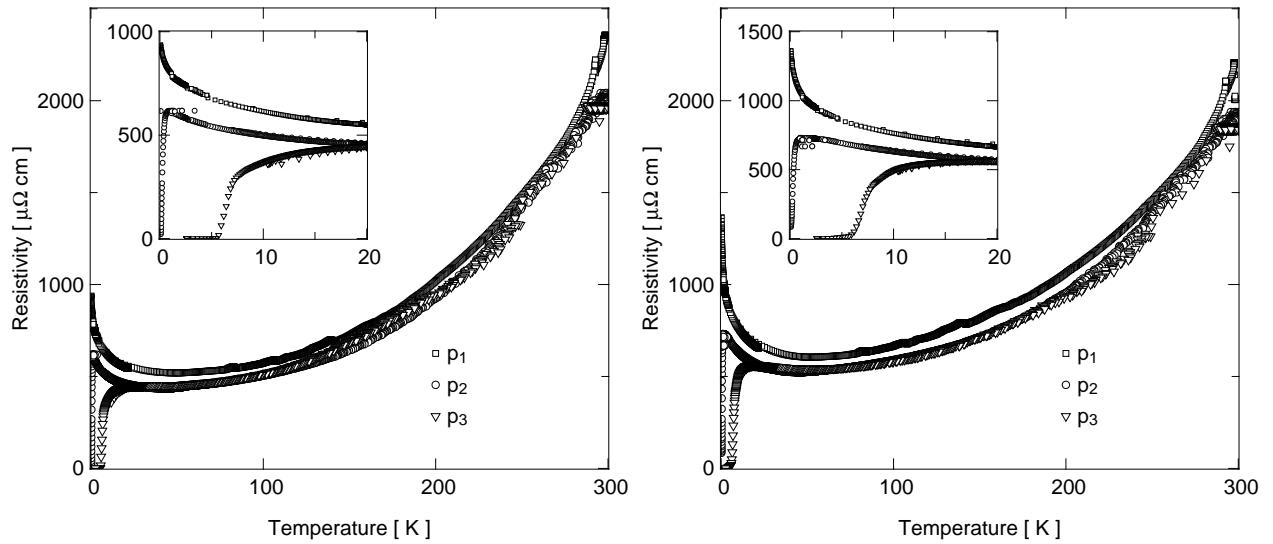
Figure 11.1: **Left** : Resistivity in 0 Tesla for $YBCO_{6.33}$ sample J, as a function of annealing. The states p_1, p_2 and p_3 are the estimated planar hole concentrations define in the text. The inset shows a zoom on the low temperature data, clearly showing the evolution from a non superconducting state at p_1 to a superconductor at p_3 as a function of annealing. **Right** : The same plot for sample L.

these investigations, and contrast the findings with the conclusion drawn from the LSCO systems.

11.2 Charge transport in the normal state of $YBaCuO_{6.33}$

We measured the charge transport of six samples of low doped YBCO prepared so that y $\sim$ 6.33-6.35, near the onset of the superconducting transition. Each of these samples was of the highest possible purity and quality, grown in $BaZrO_3$ crucibles by the UBC group[2]. Four of these samples showed partial resistive transitions near 50 K, consistent with the existence of a small concentration of ortho-II ordered domains. Although this does not affect the bulk measurements of thermal conductivity discussed in the next chapter, we are limited in the information we may extract from measurements of charge conductivity. Fortunately, two of these (samples J and L) did not posses such inhomogeneity, and we confine our discussion to them.

Figure 11.1 shows the resistivity of these two samples measured using the equipment and methods discussed in chapter 4. Each sample was delivered to Sherbrooke on dry

---

[2]Further information on the preparation and characterization of these crystals is described in detail in chapter 6.

ice, having been quenched immediately after growth to lock in oxygen disorder. We then measured the crystals as soon as was possible - approximately 5 hours elapsed between removing samples from their container and cooling them down in the fridge. We repeated the measurement on two additional occasions, after $\sim$ 48 hours and after 3 weeks spent at 300 K. The effects of annealing are quite dramatic, the samples smoothly evolve from a non-superconducting to superconducting state while remaining fixed on the mount.

When the superconducting state was entered, we applied a magnetic field of 10 Tesla to suppress T_c to zero. In this way we may compare the charge conductivity of the two states lying on either side of the quantum critical point at p_{SC}. After the final anneal the samples had a T_c of $\sim$ 5 K, and an 11.5 Tesla field was no longer able to destroy superconductivity down to the lowest temperatures.

Two peculiar facts emerge from the curves in Figure 11.1. First, the curve for the first short anneal (state p_1) is rigidly offset across the entire temperature regime. This could point to the fact that not only is doping being affected by annealing, but the elastic scattering rate (determined by disorder and impurities) is changing as well. In this scenario the enhancement in oxygen coordination reduces the in plane scattering rate by reducing the disorder.

The second observation is the occurrence of paraconductivity in the resistivity curves near the superconducting transition. The gentle roll off of the ρ vs. T curve near T_c indicates the presence of considerable superconducting fluctuations, extending in this case to almost 15K, as observed in sample J. What is curious is that recent low temperature microwave measurements in similarly doped YBCO show no indication of such fluctuations [212].

11.2.1 Metal-to-insulator transition in YBCO vs. LSCO

Early pulsed field work by Boebinger *et.al.* [157] has revealed insulating behaviour in LSCO samples from low doping all the way up to optimal doping at p=0.16. This has been interpreted as evidence of a quantum critical point occurring underneath the peak in the superconducting dome, where the ground state abruptly changes from one that is metallic in nature to one that is insulating. In a similar experiment on $Bi_2Sr_{2-x}La_xCuO_{6+\delta}$ (La doped Bi2201) the same group has reported [213, 214] $d\rho/dT < 0$ to a doping intermediate between the onset of superconductivity at p_{SC} and optimal doping, close to $p = 1/8$. The proposed doping phase diagram of this compound is reproduced from reference [213] in figure 11.2.
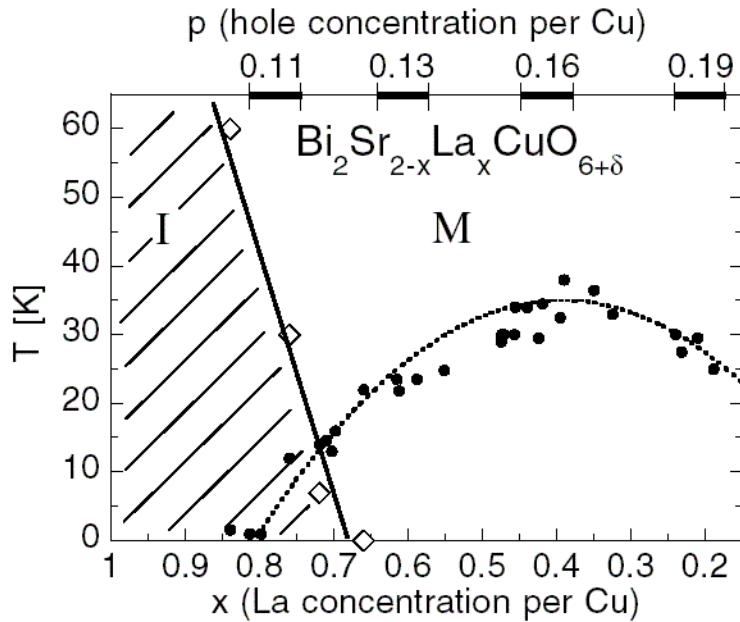
Figure 11.2: The doping phase diagram of La-doped Bi2201 as revealed by pulsed field resistivity measurements (adapted from Ono *et.al.* [213]). A metal-to-insulator transition is proposed to exist near 1/8 doping, arising from localization arising from 1-d stripe order. The solid symbols represent the superconducting T_c while the open symbols represent the minimum in resistivity in the field-induced normal state.

The authors speculate that the insulating behaviour observed in both systems may be accounted for by charge localization due to the presence of stripe order observed with neutron scattering [49]. This observation begs the question as to whether a similar metal-to-insulator transition should be observed in YBCO, which shows no signs of static stripe order [54] and indeed whether the features of normal state transport understood from LSCO and La-doped Bi2201 are universal to cuprates.

Normal state transport, $p < p_{SC}$

We compare our results for transport with doping $p < p_{SC}$ on samples of LSCO with 5 % Sr doping and with a YBCO sample with y=6.37 from the literature. The LSCO crystal was measured and grown in our own lab [62, 7], while the YBCO sample measured by Gantmahker *et.al.* [215] was grown in an alumina crucible [216]. All three samples were non-superconducting in zero field, and their resistivity is shown in figure 11.3. What is immediately apparent is the dramatic difference between the LSCO and YBCO systems. The LSCO 5% grows by a factor of 140 while cooling from 20 to 0.3 K, while our YBCO sample increases by only a modest amount - a factor of 1.5 over the same temperature

range. This dramatic difference could signal two things. First, the level of material disorder in the LSCO compound is much greater than that in YBCO, which leads to stronger insulating behaviour. Alternatively (or additionally), the LSCO ground state may be host to some form of order that is not present in the YBCO system, an order that strongly inhibits charge transport.

It is also apparent that the YBCO sample grown in a comparatively dirty environment posses a sharper upturn at low temperatures. Based on the reasoning in chapter 7 the $BaZrO_3$ grown $YBCO_{6.33}$ is *at least* 10 times more pure than the $YBCO_{6.37}$ sample of Gantmahker *et.al.*, with a correspondingly reduced upturn as $T \rightarrow 0$. This suggests that the localization in the ground state of YBCO is disorder driven, indeed it seems that further increases in crystal purity would serve to remove the insulating behaviour altogether.

A non-superconducting YBCO sample with y=6.22 has been studied by Ando *et.al.* and a sharp upturn in resistivity has been observed [217], consistent with the magnitudes of the upturns in similarly doped LSCO. The authors therefore argue that transport across the lightly doped regime is universal in both systems. The present YBCO data however contradicts this claim, since the magnitude and temperature dependence of the low temperature resistivity is drastically reduced, indicating a much more metallic ground state in the YBCO system, at least at this doping.

Normal state transport, $p > p_{SC}$

We now compare the LSCO and YBCO systems at dopings just above the threshold needed for superconductivity, $p > p_{SC}$. In this regime H_{c2} is sufficiently small that superconductivity may be suppressed by conventional static magnets with fields ~ 13 Tesla applied along the c-axis. In LSCO, we study a sample with Sr = 6 %, which has a T_c of 8 K in zero field. In YBCO we study the same sample as above, sufficiently annealed so that $T_c = 0.1$ K in zero field. We again compare the normal state resistivity to a sample of Gantmahker's with similar T_c to ours [215].

The resistivity of these samples in fields greater than H_{c2} is shown in figure 11.4. The LSCO sample again shows a much larger increase in resistivity at low temperatures, it increases by a factor of 8.4 in cooling from 20 K to 300mK under a field of 15 Tesla[3].

---

[3]Note that the normal state magnetoresistance of cuprates is known to be quite weak, so measurements performed slightly above H_{c2} will give the same temperature dependence as those performed just above H_{c2}.
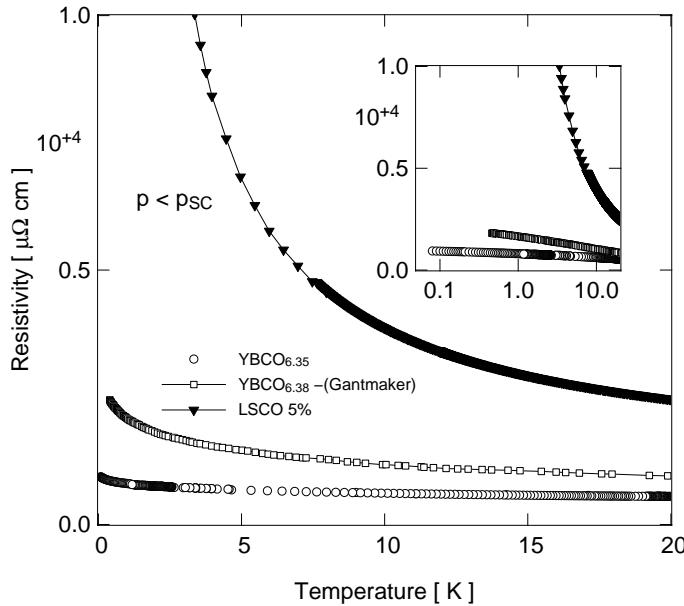
Figure 11.3: **Main** : Zero field resistivity of low doped cuprate samples with $p < p_{SC}$. The LSCO and ultra-pure YBCO$_{6.33}$ sample were measured in our lab, while the YBCO$_{6.37}$ sample was measured by Gantmahker *et.al.* [215]. The degree of insulating behaviour correlates with the estimated disorder levels in the 3 crystals. **Inset** : The low temperature resistivity plotted on a semilog scale.

The BaZrO$_3$ grown YBCO increases only by a factor of 1.4 over the same temperature range, while the alumina grown same of Gantmahker increases by 2.6[4]. In the case of the BaZrO$_3$ the upturn is extremely small, whether one calls this a metal or an insulator is almost relegated to a matter of semantics. This dramatic difference in magnitudes again points to two conclusions - the increased disorder in LSCO increases the degree of charge localization, and the ground state of LSCO may somehow be different than that of YBCO.

Strong evidence for the latter point is found in recent easements of in-field inelastic neutron scattering in underdoped LSCO [55]. Lake *et.al.* have revealed that the application of a 15 Tesla magnetic field in a sample of La$_{1.9}$Sr$_{0.1}$CuO$_4$ greatly enhances the static spin order. This observation is suggestive of an anti-ferromagnetically ordered ground state in the LSCO system. The presence of static spin order could account for the impeded electrical transport evident in our LSCO samples. Indeed, recent ARPES measurements [219] by Shen *et.al.* have detected a small gap around the nodes of lightly doped LSCO, Ca$_{2-x}$Na$_x$CuO$_2$Cl$_2$ and Nd$_{2-x}$Ce$_x$CuO4. The authors speculate that such

---

[4]Similar results were found by Seidler et. al. [218].
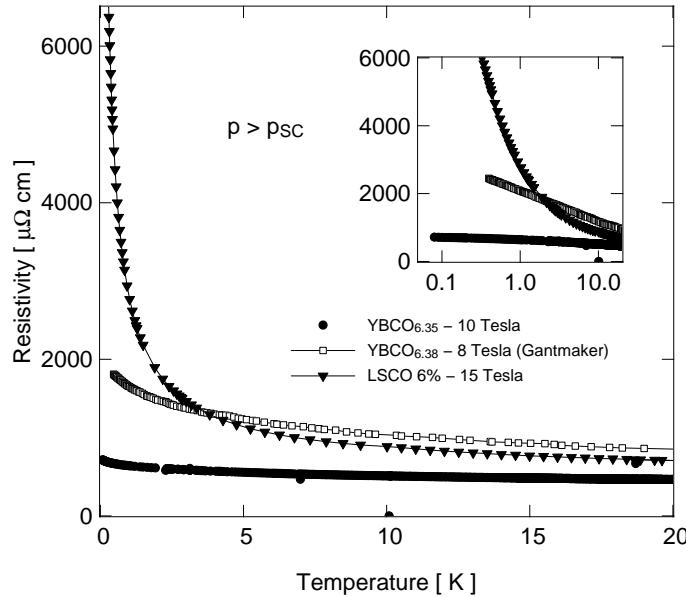
Figure 11.4: **Main** : Resistivity in the field induced normal state of low doped cuprate samples with $p > p_{SC}$ and H ‖c. The LSCO and ultra-pure YBCO$_{6.33}$ sample were measured in our lab, while the YBCO$_{6.37}$ sample was measured by Gantmahker *et.al.* [215]. **Inset** : The low temperature resistivity plotted on a semilog scale.

a gap may arise either from intrinsic disorder and localization within these systems, or the presence of static spin density wave order - similar conclusions to our own.

In this context it is interesting to note that the overall magnitude and temperature dependence of the resistivity does not change significantly in moving from the state with $p < p_{SC}$ to the state with $p > p_{SC}$. This is true in both our ultra-pure samples, and the less pure specimens of Gantmahker *et.al.* This continuity is suggestive that the ground state undergoes no dramatic change in character at $p = p_{SC}$ i.e. a metal-to-insulator transition is not pinned to p_{SC} in YBCO.

Finally, it is commenting on the suppression of the resistivity near T_c in the 0 field curves of the fully annealed samples of YBCO$_{6.33}$, as seen in the inset of figure 11.1. This effect is well-known to occur from fluctuations of the superconducting order parameter [40], which may enhance the electrical conductivity significantly in materials with a low phase stiffness. These fluctuations however are curiously absent in the latest microwave penetration depth measurements on similarly doped samples, where a strictly linear in T dependence of $1/\lambda^2$ is observed right up to T_c [212]. This discrepancy is currently unexplained.

11.2.2 Temperature dependence of the insulating behaviour

The temperature dependence of the divergence in resistivity at low temperatures holds valuable information about the localization mechanism. For LSCO with dopings less than p_{SC} the temperature dependence of the resistivity is seen to be strongly insulating, as T $\rightarrow$ 0. Ando *et.al.* measured resistivity in LSCO samples with dopings from 1 - 5 % Sr, and observe a resistivity which diverges such that $ln\rho \sim T^{-\beta}$ ($\beta = 1/2, 1/3, 1/4$ depending on the dimensionality [220, 217]). This behaviour is expected in the strong localization limit, where transport is achieved by variable-range hopping (VRH), and is observed in our 5 % Sr doped sample seen in Figure 11.3 [62]. In this sample a fit to $\rho = A \times T^{4/3} e^{T_o/T^{\wedge(1/3)}}$ (the 2D limit of VRH) gives A = 0.104 $\pm$ 0.037 mΩ cm K$^{-3/4}$ and $T_o = 286 \pm 17$ K, with a high goodness of fit. Recently, using magneto-resistance measurements Cieplak *et.al.* have argued that this temperature dependence arises from strong spin scattering in very low doped LSCO [221].

For higher dopings, a crossover to a resistivity in which $\rho \sim \log(1/T)$ is seen in LSCO [222]. Suppressing superconductivity with a pulsed field the authors observed a logarithmic divergence of the resistivity which persisted to samples with $p = 0.13$. Similar divergences are observed for our LSCO 6 % sample in 15 Tesla, and in the YBCO sample measured by Gantmahker. To facilitate the comparison, the data for these samples are plotted alongside ours on a logarithmic plot in figure 11.5. For each compound, the state with $p < p_{SC}$ is measured in zero field, and the state with $p > p_{SC}$ is measured with an applied field larger than H_{c2}. A clear $\log(1/T)$ dependence of the resistivity is observed over a large temperatures range only in our sample L prior to annealing (with $p < p_{SC}$). In the other cases the temperature dependence is weaker than $\log(1/T)$, as indicated by the roll-off at low temperatures. This could possibly be explained by the proximity to superconducting order, and the paraconductivity associated with it. There is evidence for the effects of fluctuations of this sort in lightly doped YBCO. In a study of samples of YBCO with dopings $y = 6.2$ - 6.5 Semba et. al. [223] concluded that the doping dependence of $\rho(T_C)$ was driven by quantum phase fluctuations of the order parameter.

Such a temperature dependence is expected in the case of weak-localization, in the limit where corrections to metallic behaviour are small [224], and transport is in the metallic regime $k_F \ell \gg 1$. The electronic mean free path ℓ may be estimated from the resistivity using the fact that [148]:
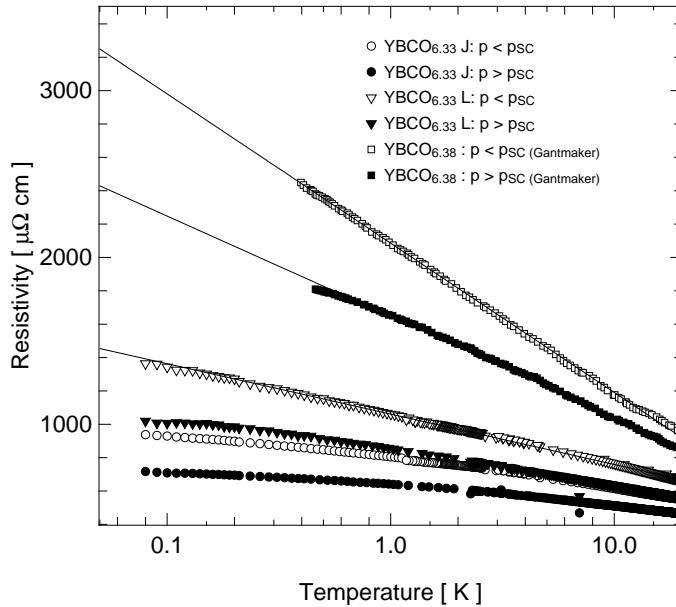
Figure 11.5: Resistivity of YBCO$_{6.33}$ in the normal state for $p < p_{SC}$ and $p > p_{SC}$. The fits are of the form $\rho \sim \log(1/T)$.

$$\ell = hc_0/\rho k_F e^2 \tag{11.1}$$

where c_0 is the c-axis lattice constant. In our samples, ρ is $\sim 600~\mu\Omega$ cm at the minimum of resistivity, and thus $k_F \ell = 5.1$ although it has been noted that this formula underestimates ℓ for nodal quasiparticles [225, 221]. Thus transport is in the metallic regime, although it is clear that the corrections to metallic behaviour are not vanishing small.

In a 2D system the standard expression for weak localization corrections to the conductivity σ is [224]:

$$\sigma(T) = \sigma_0 + \frac{p}{2}\frac{e^2}{\hbar\pi^2} ln \frac{T}{T_0} \tag{11.2}$$

where p is the temperature coefficient of the inelastic scattering, and T_0 is the localization onset temperature[5]. We compare our data to this theory by plotting the conductance on a logarithmic scale, as in figure 11.6.

The basic result is that the observed conductivity in the normal state is not simply due to weak localization. In both the $p < p_{SC}$ and $p > p_{SC}$ cases there is significant curvature to the conductivity, and the fit to equation 11.2 is poor. The peculiar sub logarithmic

---

[5]The same temperature dependence may also arise from strong electron-electron interactions [224]
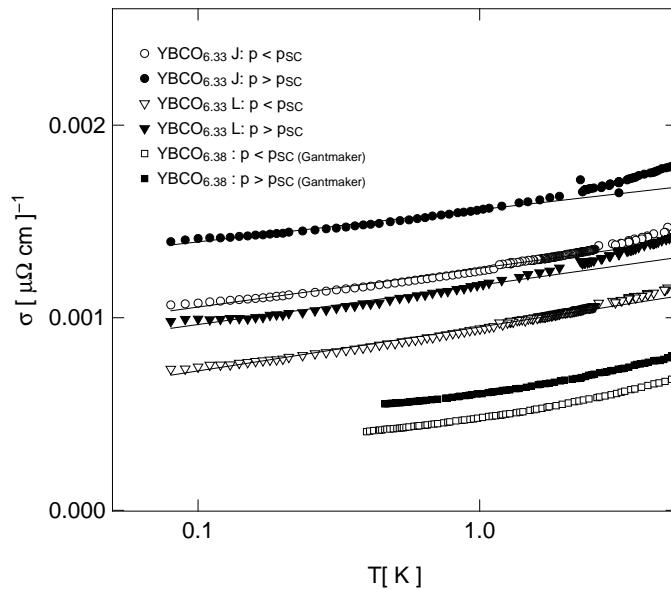
Figure 11.6: Conductivity of YBCO$_{6.33}$ in the normal state for $p < p_{SC}$ and $p > p_{SC}$. The black line is fit to equation 11.2.

temperature dependence of ρ in our samples may thus be significantly influenced by quantum fluctuations, or may emerge to be the hallmark of new physics.

11.3 Charge transport in the normal state of YBaCuO$_{6.50}$

To study the normal state transport in YBCO samples with higher doping, it is necessary to move beyond the limits of static magnetic field technology. Even in a sample with a T_c of 5 K, 11.5 Tesla was insufficient in suppressing superconductivity. To access higher fields we performed resistivity measurements at the Laboratoire National des Champs Magnétiques Pulsés in Toulouse, France in collaboration with Cyril Proust of the CNRS. Using the methods and apparatus discussed in section 4.5 we measured a sample of BaZrO$_3$ grown, ortho-II ordered YBCO$_{6.50}$ in pulsed fields as high as 55 Tesla. The fields were applied such that H $\parallel$ c, and the current was along the a-axis, perpendicular to the chains. The overall disorder of this stoichiometric compound is expected to be very low.

The magnetoresistance of the YBCO$_{6.50}$ crystal is shown for various temperatures in figure 11.7. At the lowest experimentally accessible temperature of 500 mK, the pulsed field is seen to suppress superconductivity entirely, judging by the plateauing of the magnetoresistance data about 50 Tesla. At higher temperatures, the plateau region grows, following the evolution of H$_{c2}$ with temperature. It is immediately clear that there
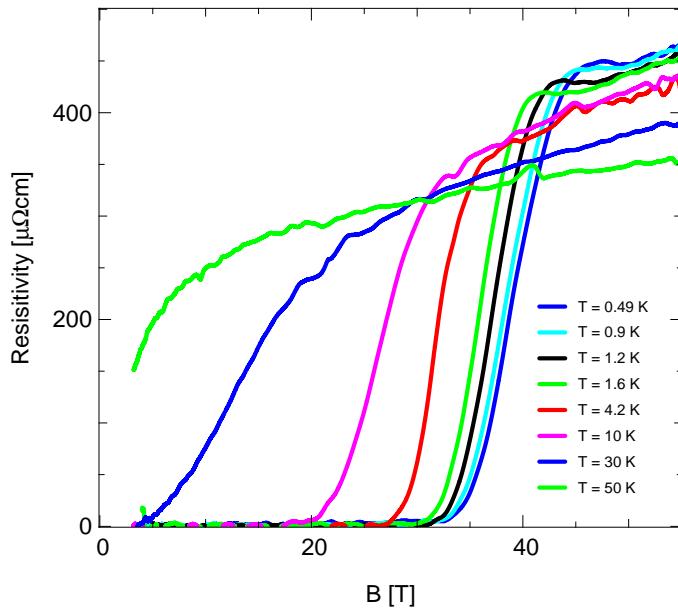
Figure 11.7: Magnetoresistance to 55 Tesla in ortho-II ordered YBCO$_{6.50}$.

is a small upturn in the data at low temperatures, as the higher temperature curves fall slightly below the lower temperature ones[6]. The magnitude of this upturn however is small, and the temperature dependence at very low T is almost masked by the noise in the data, which originates from vibrations of the sample during the field pulse.

To track the temperature dependence of the resistivity in the normal state, we may either take the raw data in 55 T, or try to account for the small, temperature dependent positive magnetoresistance observed in the normal state. In a normal metal we should expect the magnetoresistance to scale as $\sim B^2$, but from the field dependence of the data here it appears to evolve in a linear fashion. Thus, we attempt to extrapolate backwards to zero Tesla using an empirical linear fit to account for magnetoresistance corrections, as is shown in figure 11.8[7]. This fit is likely an overestimate of the actual correction, but it serves to show that the magnitude of the upturn may be accounted for by a small amount of magnetoresistance. The metallic behaviour of underdoped YBCO is most apparent when compared to other cuprates at similar dopings. With a T_c of 55K the

---

[6]It should be noted that the data taken in the higher temperature probe was scaled downwards by 7 % in order to match more closely with the zero field curve. Such small discrepancies are sometimes present in pulsed field measurements due to vibrations of the contacts and sample during the pulsed field sweep. I have included the error caused by this scaling in the error bars estimated for the normal state resistivity points.

[7]The raw data has been smoothed by using a sliding average of 200 data points in order to better accommodate the fitting routine.
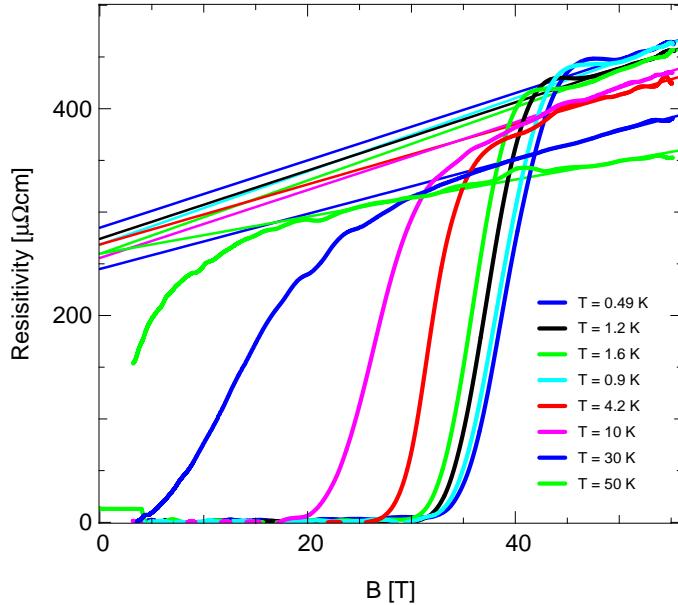
Figure 11.8: Linear extrapolation of the magneto-resistance in YBCO$_{6.50}$ to H=0. The data was fit above H$_{c2}$, determined to be where the slope of the magneto-resistance deviates from a linear fit. Note that the data has been smoothed slightly compared to the raw data in figure 11.7 by performing a sliding average over a window in field to remove some of the noise.

use of equation 6.1 yields an estimate of $p \sim 0.09$. We may thus directly compare with an LSCO sample with a Sr doping of 9%, which we have also measured in pulsed fields at Toulouse [62]. Similarly, a sample of Bi$_2$Sr$_{2-x}$La$_x$CuO$_{6+\delta}$ (BSLCO) with x=0.84 and is estimated to have a doping $p = 0.1 \pm 0.01$ [226]. We plot our data for YBCO and LSCO alongside the data for the La-doped Bi2201 crystal measured by Ono *et.al.* [227] in Figure 11.9.

The difference in the low T limiting behaviour is quite dramatic. In both the LSCO and BSLCO systems the resistivity has a strong upturn as $T \rightarrow 0$, while in the clean YBCO system the upturn is modest, only a factor of 1.5 in cooling from 50 K to 0.5 K. Using the naive correction for normal state magnetoresistance discussed above yields data that essentially produces little or no upturn at low temperatures altogether. From these observations we conclude that the ground state of a clean, underdoped sample of YBCO$_{6.50}$ is essentially a metal. As at lower dopings, this suggests that either a localization mechanism present in the LSCO is absent in YBCO (eg. spin density wave order), or the ultra low disorder in the stoichiometric YBCO wipes out any vestiges of the metal-to-insulator transition at this doping.
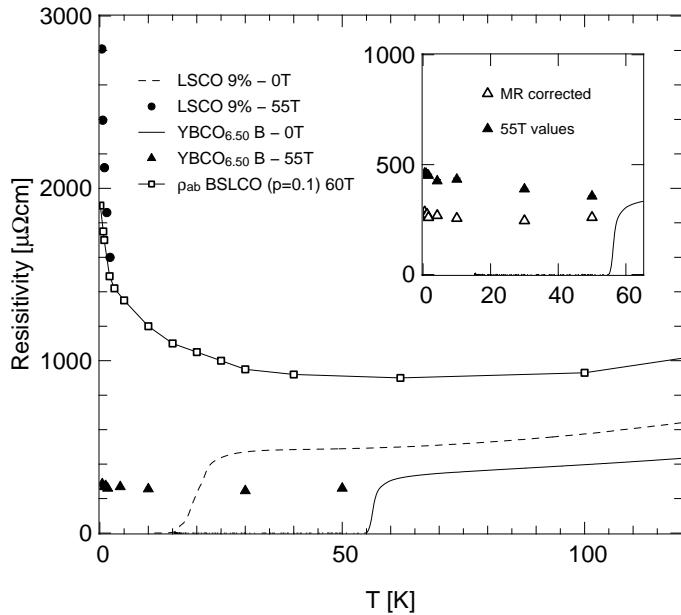
Figure 11.9: **Main** : Temperature dependence of the normal state resistivity at 55 Tesla in YBCO$_{6.50}$. The 0 field data is also plotted (solid line). For comparison, normal state data for cuprates with similar doping ($p \sim 0.09$) is plotted. The LSCO data is on a sample with 9% Sr, from our own lab, and the BSLCO data is from reference [227]. **Inset** : The 0 field and pulsed field data for the YBCO sample using both the raw 55 Tesla data points and the magneto-resistance correction scheme discussed in the text.

11.4   Chapter summary

In this chapter we have studied the normal state electrical transport of ultra-pure YBCO samples via two routes: through underdoping such that $p < p_{SC}$, and suppressing super-conductivity with a large static, or pulsed magnetic field. In very low doped samples of YBCO$_{6.33}$ and moderately underdoped sample of YBCO$_{6.50}$ the conclusions are similar - the ground state is revealed to be essentially metallic, with relatively tiny traces of an upturn at low temperatures possibly due to weak localization. In both samples we compare the results to those obtained using similar techniques in the more disordered LSCO system. We find little evidence for the dramatic metal-to-insulator transition observed in LSCO at moderate dopings, emphasizing that lessons learned from the phase diagram of LSCO are not necessarily generic to the cuprates.

WF law violation in ultra-pure YBCO

12.1 Chapter Overview

Electrons in cuprates adopt a remarkable sequence of ground states as one varies the density of charge carriers. The undoped parent compound is a Mott insulator, where strong Coulomb interactions prevent electrons from being mobile. In the overdoped regime, the cuprates posses metallic conductivity, and the basic properties of Fermi liquid [58]. At intermediate density, it is a superconductor with d-wave symmetry, but the nature of the underdoped phase that lies between the insulator and the superconductor is one of the central puzzles of the field. It is known to be characterised by a pseudogap, and is thought by several authors to be an exotic state of matter [228, 45, 47, 229].

One of the most fundamental tests of this enigmatic phase is to study the conduction of heat and charge in the limit T $\rightarrow$ 0. The ratio of the two has been found to obey $\kappa/\sigma T = L_0$, where L_0 is the Lorenz number in virtually all known materials, a basic property of a Fermi liquid. Measurements of low temperature thermal transport were used to investigate the ground state of high purity single crystals of the lightly doped cuprate $YBa_2Cu_3O_{6.33}$. Samples were investigated on either side of the superconducting phase boundary, in both zero and applied magnetic field. Here I report the observation of delocalized fermionic excitations at zero energy in the non-superconducting state, which reveals that the ground state of clean underdoped cuprates is metallic, in contrast to the insulating ground state observed in underdoped $La_{2-x}Sr_xCuO_4$. The ratio of heat to charge transport in this newly uncovered metallic state was found to violate the Wiedemann-Franz law, the first observation of its kind in an underdoped cuprate.

12.2 Heat transport in low-doped cuprates

In this chapter I present a comparative study of heat transport in two cuprate materials $YBa_2Cu_3O_y$ (YBCO) and $La_{2-x}Sr_xCuO_4$ (LSCO), with the former being prepared with
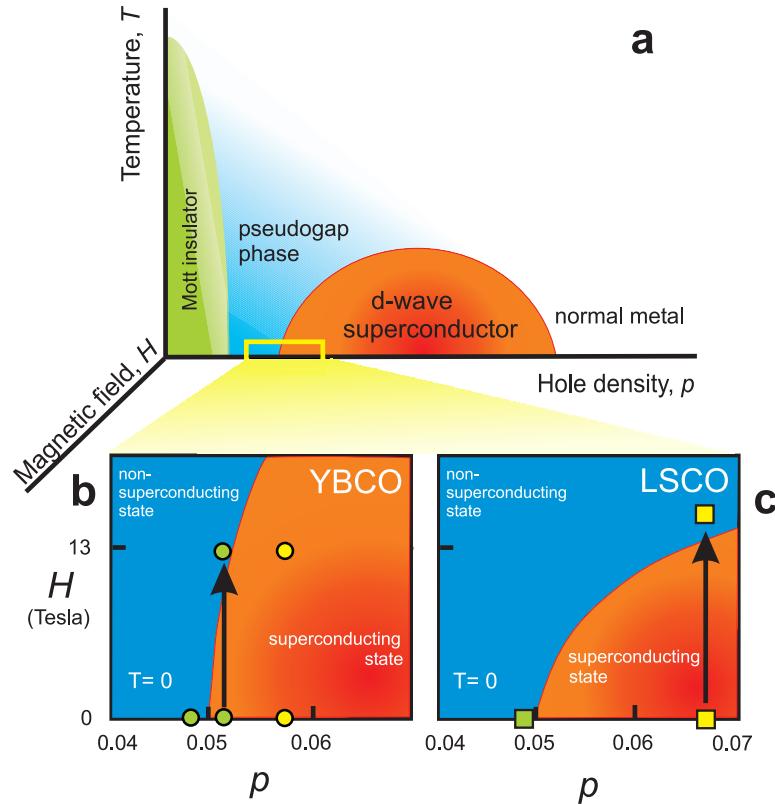
Figure 12.1: **A** : Temperature-doping phase diagram of the cuprates. We focus on low doped samples with $p \sim 0.05$, near p_{SC}. **Bt** : Magnetic field - doping phase diagram of YBCO. We measure samples that are non-superconducting in zero field, $(p < p_{SC})$ and samples that have sufficiently low H_{c2} such that the normal state may be reached by applying 10 Tesla perpendicular to the c-axis. We also measure samples at higher dopings. **C** : Magnetic field - doping phase diagram for our LSCO samples used for comparison.

a much lower level of intrinsic disorder, as discussed in chapter 6. The effect of doping on the electron system is investigated by comparing samples with doping on either side of the critical doping for the onset of superconductivity p_{SC}, for each material. Combining these studies of κ with the results from charge transport studies presented in the previous chapter, we address two fundamental questions in the cuprates: does the onset of superconductivity coincide with the onset of hole mobility, and does the T=0 ground state that gives rise to superconductivity play host to novel physics?

Our basic approach is outlined in Figure 12.1. We first study thermal conductivity in both LSCO and YBCO samples prepared such that $p < p_{SC}$, which are not superconducting in zero field. By allowing the YBCO sample to anneal at room temperature, as discussed in chapter 5, p increases above the threshold for superconductivity p_{SC} and

the samples eventually become bulk superconductors with $T_c \sim 5$ K. We move across the phase boundary in LSCO by preparing samples with a slightly higher concentration of Sr.

In both systems we may suppress superconductivity for $p > p_{SC}$ by the application of a strong magnetic field applied such that $H \parallel c$, shown schematically in the bottom panels of Figure 12.1.

Single crystal samples of YBCO of the highest available purity were used for this study, grown in the $BaZrO_3$ crucibles discussed in chapter 6. As noted previously, in these materials there is ample evidence of extremely long electronic mean free paths [118] estimated to be approximately two orders of magnitude longer [1] than in the best LSCO crystals. In total 6 samples [1]were measured with oxygen content y=6.33-6.35. Of these samples J and L were the most revealing, possessing no downturns in their resistivity and allowing for a direct comparison of heat and charge. The other 4 samples however yielded good quality thermal conductivity data, and we begin our discussion by tracking the value of the linear term in zero field, as a function of p. The hole concentration for each YBCO sample was estimated using the empirical relation between T_c and p, Equation 6.1, where T_c is taken to be the temperature at which ρ=0. For LSCO, two samples are used: one non-superconducting ($T_c = 0$) with x=0.05 ($p < p_{SC}$) and one superconducting ($T_c = 5$ K) with x=0.06 ($p > p_{SC}$), where we simply use $p = x$, the Sr concentration.

12.2.1   Comparison of κ in YBCO and LSCO $p < p_{SC}$

The main panel of Figure 12.2 shows the thermal conductivity of the 5 % sample of LSCO and the unannealed YBCO sample L, both of which are non superconducting in zero field, and have $p \sim 0.05$. The data was fit to the powerlaw form of Equation 2.15, and is plotted as κ/T vs. $T^{\alpha-1}$ to provide a straightforward way of extrapolating to $T = 0$, and obtain the residual linear term κ_0/T [1]. The absence of a residual linear term ($\kappa_0/T = 0$) indicates the absence of fermionic carriers as in an insulator or a fully gapped (s-wave) superconductor. A finite (non-zero) value can be attributed unambiguously to delocalized fermionic excitations. In either case, the slope of the curves is a measure of the phonon conductivity [1].

It can be seen that the value of the residual linear term in the $YBCO_{6.33}$ sample is

---

[1]These are denoted samples B,F,H,J,K,L and detailed characterization information for each is presented in chapter 6.
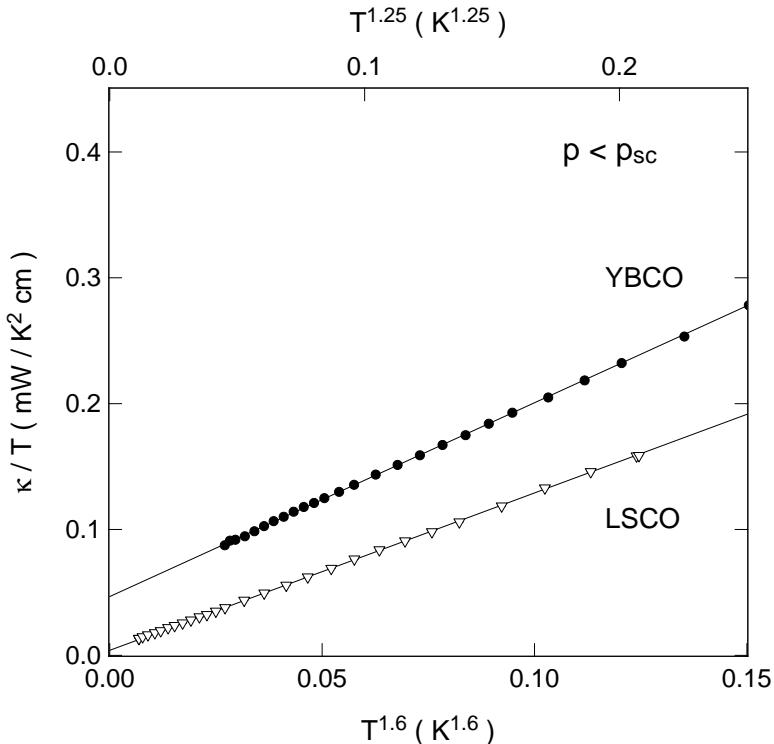
Figure 12.2: Thermal conductivity of underdoped cuprates in the non-superconducting state. Both samples of YBCO and LSCO have a hole concentration p close to, but less than p_{SC}, the critical concentration for the onset of superconductivity. The YBCO sample shows a sizable residual linear term κ_0/T, indicating the presence of delocalized fermionic carriers of heat. By contrast, the LSCO sample shows a vanishing small value of κ_0/T, consistent with an insulating state.

significantly smaller than that of an optimally doped sample ($\kappa_0/T \sim 0.14$ mW/K^{2}cm for YBCO$_{6.95}$), but is still sizable: $\kappa_0/T = 47 \pm 8$ μW K^{-2} cm^{-1}. Special care was taken to establish accurate error bars for these fits by varying the fit range, as summarized in Appendix 3. This result is much larger than that obtained for an undoped crystal [1] (y=0.0) where $\kappa_0/T = 0 \pm 1$ μW K^{-2} cm^{-1}. By contrast, the LSCO sample yields a vanishing small linear term of $\kappa_0/T = 3 \pm 1$ μW K^{-2} cm^{-1}, just as in the undoped ($x = 0.0$) material [7], indicating a ground state devoid of delocalized carriers for all $p < p_{SC}$ (i.e. $x < 0.05$). This observation points to a fundamental difference between the two systems. As one adds carriers to the parent insulator in clean samples of YBCO, the ground state becomes metallic before the emergence of superconductivity, while in LSCO the ground state is an insulator right up to p_{SC}. This is a fundamentally new result - a study of 2D organic conductors as a function of pressure (rather than doping) has found that the electron system goes directly from insulator to superconductor, with
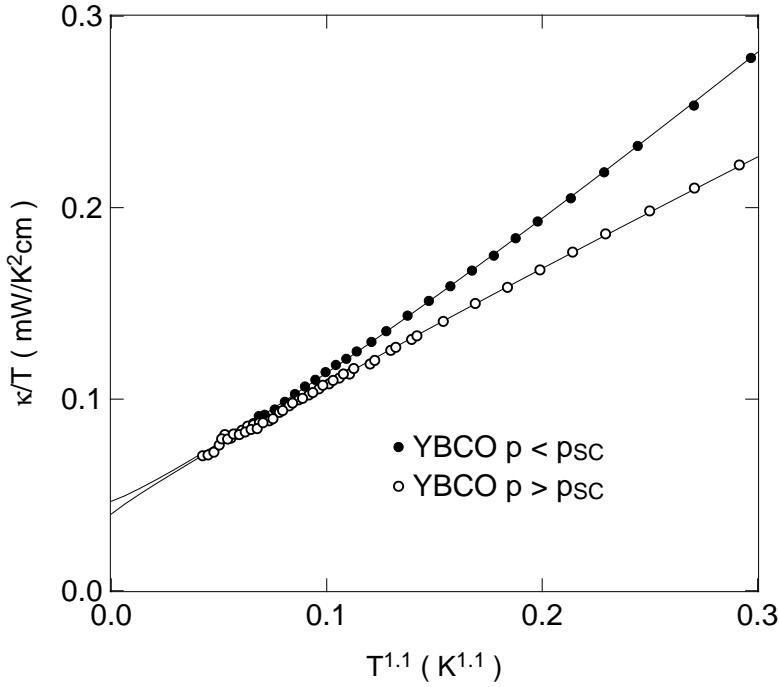
Figure 12.3: Thermal conductivity data for $YBCO_{6.33}$ sample L, in the non superconducting state ($p < p_{SC}$) and in the superconducting state ($p > p_{SC}$ with $T_c = 5K$). The superconducting state is accessed by annealing the sample at room temperature for 3 weeks. The value of the linear term is identical to within the errors in the extrapolated fit.

no intermediate phase [230]. The same has recently been found in V_2O_3 [231].

Having uncovered a metallic phase in a lightly-doped cuprate with no long-range superconducting order, we explore some of the basic properties of its low-lying excitations. Specifically, we ask 1) whether the entropy-carrying fermions also carry charge, 2) how they compare to the well-understood d-wave nodal quasiparticles of the superconducting state (at $p > p_{SC}$), and 3) how they respond to a magnetic field.

12.2.2   Comparison of κ in YBCO and LSCO $p > p_{SC}$

We investigate the superconducting state of both cuprates by annealing the YBCO samples such that $p > p_{SC}$ and measuring an LSCO sample with higher Sr content. Figure 12.3 shows the result for sample L, where the non superconducting state κ data is plotted with the data taken when the sample was a bulk superconductor with a T_c of 5 K. A change is slope is noted between the two curves, but the fundamental result is that the extrapolated value of the linear term *does not change* when moving across the superconducting phase boundary at p_{SC}. The slight difference between the two samples is
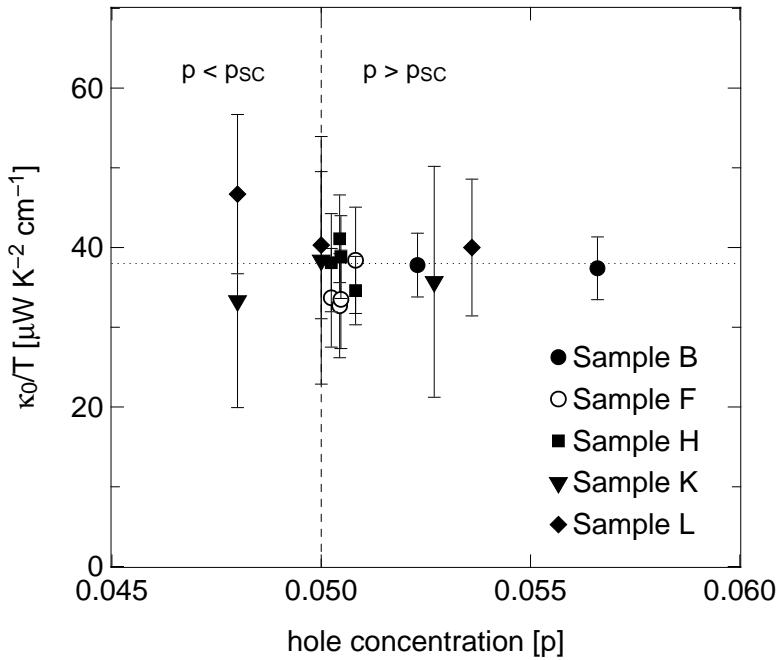
Figure 12.4: The residual linear term versus doping for all samples, all anneals in 0 T. p is estimated from 6.1 where T_c from where $\rho = 0$. The error bars are taken as the sum of the 3 errors discussed in text.

well within the error of the fits. Further evidence for this is found by combining data for all samples, for each anneal as in Figure 12.4[2]. The value of the linear term, within error, remains at an essentially constant value of $\sim 40~\mu$W K^{-2} cm^{-1} in this region of the cuprate doping diagram.

What conclusions can we draw from this apparent insensitivity to the superconducting phase transition? In a d-wave superconductor, nodal quasiparticles are low-lying fermionic excitations that give rise to a finite κ_0/T, the magnitude of which is governed entirely by their Dirac energy spectrum. In the universal limit, where the residual linear term is independent of impurity concentration, the value of κ_0/T only depends on the ratio v_F/v_2, where v_F and v_2 are the quasiparticle velocities perpendicular and parallel to the Fermi surface, respectively [59], as in Equation 3.14.

It is straightforward to use such measurements to extract an estimate of the superconducting gap maximum, assuming a simple d-wave gap of the form $\Delta = \Delta_0 \cos 2\phi$, so that $2\Delta_0 = \hbar k_F v_2$ as in chapter 8. For the highly-underdoped YBCO samples measured here, the linear term of approximately 40 μW K^{-2} cm^{-1} implies a gap maximum of 160

---

[2]Fits to all samples and a discussion of error is presented in Appendix 3

meV, which suggests that the in-plane exchange coupling energy J of the Mott insulator, estimated to be 125 meV [232], sets the magnitude of Δ_0. Note that this type of analysis is only valid in the universal limit (i.e. when the scattering rate is small compared to Δ_0), a condition which was indeed verified in YBCO at $y = 6.9$ and 6.5 [1].

Two important points emerge from Figure 12.4. First, given that the residual linear term is solidly understood as arising from nodal quasiparticles in the superconducting state, its seamless evolution into the non-superconducting state below p_{SC} suggests that a nodal spectrum is also a characteristic of that metallic phase. Strictly speaking, the ultimate test of such a spectrum is the demonstration of universality with respect to variations in impurity concentration. It is likely that in the 6 samples grown in various batches there is some variation in impurity concentration, as well as difference in scattering rate arising from oxygen inhomogeneity. It is however difficult at this point to quantify this variation, and we leave the verification of universality in low doped cuprates for future work. Of particular interest in that respect is the ortho-III inverse arrangement of oxygen (one full chain followed by two empty chains.) Such a compound is superconducting in 0 T and stoichiometric, which would reduce the in plane scattering rate associated with the oxygen chain atoms. A comparison of an ordered and disordered sample of this compound would be very revealing.

The second important conclusion one may draw is that YBCO appears to be qualitatively different from LSCO. While in the former the quantum phase transition at p_{SC} has no impact on the conductivity of the electron system, in the latter it corresponds to a (thermal) metal-insulator transition. Indeed in LSCO, κ_0/T goes to zero precisely where superconductivity disappears. The very same situation was observed to occur as a function of applied magnetic field, for $p > p_{SC}$: the transition from thermal metal (d-wave superconductor) to insulator was found to be simultaneous with the suppression of superconductivity, occurring right at the resistive upper critical field H_{c2}, for a LSCO sample with $x = 0.06$ [7]. The difference between YBCO and LSCO may lie in the greater amount of disorder found in LSCO, which would cause the non-superconducting state of LSCO near $p = p_{SC}$ to be an insulator (thermally and electrically). However, if LSCO were merely a disordered version of YBCO, it is hard to see why the metal-to-insulator transition would be pinned to the onset of superconductivity (at p_{SC}). The latter fact points instead to another explanation, namely a scenario of competing phases where the other phase (e.g. with SDW order) is insulating, for example as a result of having a small gap at the nodes [219]. Along these lines, recent neutron scattering studies [55, 233] of

underdoped LSCO in a magnetic field have revealed a field-induced increase in static SDW order. This happens in parallel with the field-induced decrease in conductivity [7]. The induced magnetic order may well serve to either gap out or localize the fermionic excitations responsible for heat transport as $T \to 0$.

12.2.3 $\kappa(H)$ in low doped YBCO and LSCO

Let us now examine the response of both systems to a magnetic field applied perpendicular to the CuO_2 planes. In a d-wave superconductor, the superfluid flow around each vortex causes a Doppler shift of the quasiparticle energies and thus an increase in the zero-energy density of states. This should lead to an increase in thermal conductivity. In YBCO near optimal doping, an increase in κ_0/T was observed to be on the order of a factor 2 in 10 T or so [61]. In LSCO, a similar increase is seen at optimal doping, but for $p < 0.1$, κ_0/T was found to decrease [7]. This decrease is a signature of the thermal metal-to-insulator transition at $H = H_{c2}$. In YBCO, no such decrease is observed for p close to p_{SC} (or anywhere). In fact, a field of 10 T has very little effect, whether $p < p_{SC}$ or $p > p_{SC}$, as summarized in the tables in Appendix 3. This can be seen in Figure 12.4 where we plot the thermal conductivity of YBCO sample L with a T_c of 0.1 K in zero field. The application of a 10 Tesla field forces the sample into the normal state (ie. no transition is observed in resistivity), however the thermal conductivity data is unaffected - the residual linear term is ~ 41 μW K^{-2} cm^{-1} in both cases. The data for the LSCO 6% crystal is shown for comparison - the application of a 13 Tesla field also suppresses superconductivity entirely, but forces the linear term from a finite value to 0 [7].

The same behaviour is seen in all low doped YBCO samples - even where 13 Tesla is not enough to suppress superconductivity entirely. The data for each crystal is shown in Figure 12.6, where the in-field linear term is divided by the zero-field linear term. In the range of dopings covered in these samples, Figure 12.5 demonstrates that the effects of a magnetic field are negligible. The conclusion is, therefore, that in YBCO near p_{SC} the thermal conductivity does not change across the phase boundary, whether one reaches the non-superconducting state by decreasing p at fixed $H = 0$ or by increasing H at fixed $p > p_{SC}$.

This is reminiscent of previous spectroscopic studies (ARPES [36] and tunnelling [23]) which found the gap in underdoped cuprates to persist largely unchanged as the *temperature* was increased from below to above T_c. The observation of this "pseudogap" above T_c has been interpreted as the persistence of pairing amplitude (gap) once long-
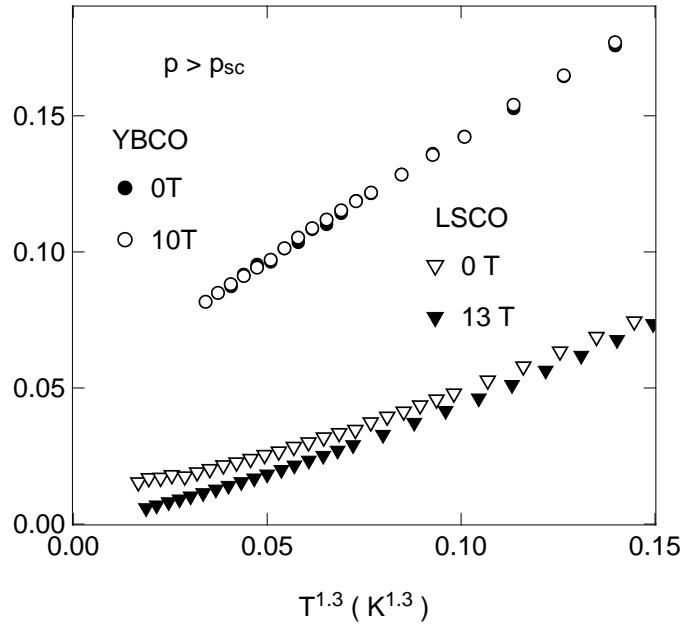
Figure 12.5: Thermal conductivity of underdoped cuprates in the superconducting state (H=0) and the non-superconducting state ($H > H_{c2}$). Both samples of YBCO and LSCO have a hole concentration p close to, but slightly greater than p_{SC}. The application of a field is seen to drive the residual electronic conductivity to zero in LSCO, while in YBCO the conductivity remains unchanged.

range superconducting order has been destroyed by thermal fluctuations of the phase [37]. Within such an interpretation, the fact that our measurements are done essentially at $T = 0$ would imply a quantum (rather than thermal) disordering of the phase with increasing magnetic field or decreasing doping. What our study shows is that this putative phase disordering would leave the system in a metallic ground state. Beyond this particular interpretation, several theoretical models have been proposed for the pseudogap state of underdoped cuprates [47, 234, 39]. It remains to be seen which of the proposed states support both a d-wave-like gap at high energies and fermionic excitations down to zero energy.

12.3 Comparison of heat and charge transport in YBCO

We now turn our attention to a direct comparison of heat and charge conductivity in the normal state of YBCO, beginning with the unannealed sample L with $p < p_{SC}$. This is the first time such a comparison has been reported, and these results on the purest crystals available fill in gaps in our knowledge. Figure 12.7 shows the measured
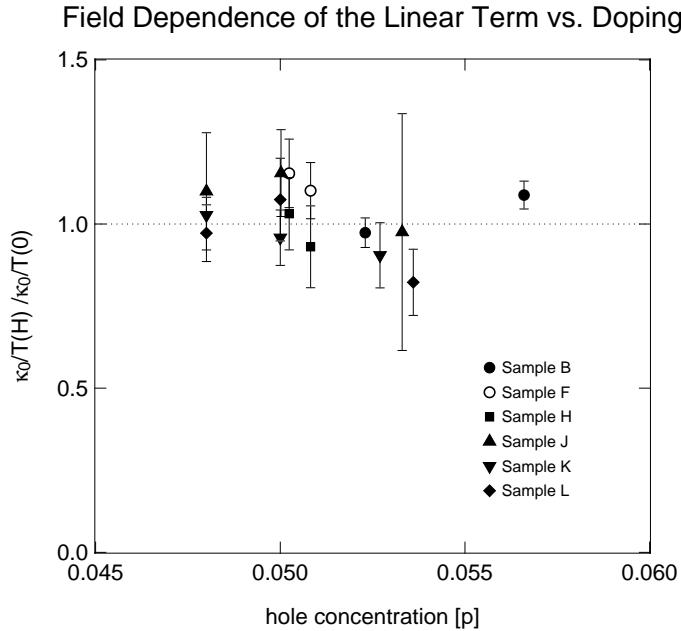
Figure 12.6: The variation of linear term with applied field for all samples. $\kappa_0(H)/T$ is normalized by the corresponding zero field value. The error bars do not include the geometric factor error, just the fit error and range error.

electrical conductivity of the non-superconducting YBCO sample converted into thermal units using the Sommerfeld value of the Lorenz number $L_0 = 2.45 \times 10^{-8} W\Omega/K^2$. On the same scale, the thermal conductivity is also plotted, and it is clear that the two do not meet at T=0. The ratio of heat to charge conduction in this limit yields a non-trivial violation of the Wiedemann-Franz law by a factor of 2.7 $\pm$ 0.2, the first time this has been observed in an underdoped cuprate. We immediately pose the question - is this violation the result of incipient localization, or a fingerprint of fundamental new physics?

It is clear from the temperature dependence of the resistivity presented in chapter 11 that some small amount of localization is present in YBCO. As seen in the inset of 12.7, the resistivity increases by a modest factor of 2 in cooling from 20 K to 100 mK, in dramatic contrast to LSCO where the resistivity diverges strongly as $T \to 0$, growing by a factor of 3000 over the same interval. Whether weak localization of quasiparticles can account for such a large violation in the T=0 limit is at present unknown.

A broader perspective can be achieved by placing these latest results in the context of previous studies of the Wiedemann-Franz law in cuprates. Violations have been observed at optimal doping in the electron doped material PCCO [235], and at optimal doping [236] in $Bi_{2+x}Sr_{2-x}CuO_{6+\delta}$ where a small violation of 1.3 $\pm$ 0.2 was seen when
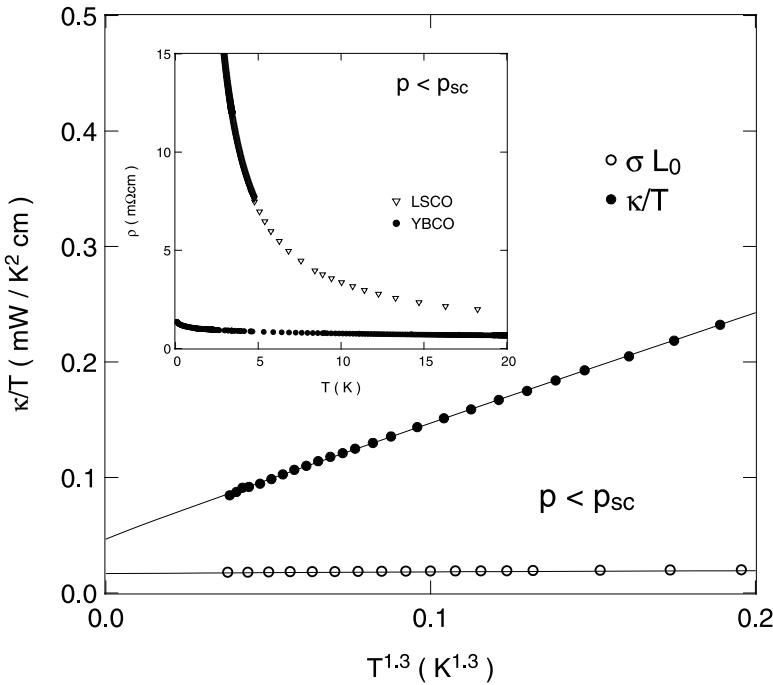
Figure 12.7: Main: The thermal and electrical conductivity of YBCO with $p < p_{SC}$. The electrical conductivity has been converted into thermal units using the Wiedemann-Franz law, and the two conductivities do not meet at $T = 0$. Inset: Resistivity of YBCO and LSCO samples with $p < p_{SC}$, indicating the relatively metallic nature of the much less disordered YBCO system (previously shown in chapter 11).

superconductivity was suppressed with a magnetic field. In a similar experiment in the overdoped material Tl-2201 the Wiedemann-Franz law was recovered [58]. This suggests that the normal ground state evolves from a metallic state at overdoping, to one which increasingly violates the Wiedemann-Franz law as the Mott insulator is approached.

One possible scenario, which is not unexpected in low doped cuprates, is that normal Fermi-liquid quasiparticles observed at higher dopings are no longer the fundamental electronic excitations of the ground state [237, 13, 238]. Instead, the electron itself may fractionalise into a neutral spin-carrying excitation, called a "spinon" and a spinless charge carrying excitation called a "holon" or chargon. Our data would imply that the chargon would localize more readily than the spinon - leading to excess transport of heat and a violation of the Wiedemann-Franz law. Preliminary microwave data from the UBC group [212] supports such an interpretation. They study the evolution of the superfluid density through microwave penetration depth measurements as a function of annealing. They find that the superfluid density becomes anomalously small, and its slope with temperature suggests the effective charge of in-plane quasiparticles falls

Table 12.1: Table summarizing the WF-law violation as a function of doping in high T_c cuprates, using the present work, and data from the literature [236, 58].

Sample	T_c (K)	p - holes/Cu	κ_0/T (μW/cmK^2)	$\rho_0(\mu\Omega$cm)	L/L$_0$
YBCO$_{6.33}$J	-	0.048	52.2 $\pm$ 3.2	972 $\pm$ 50	2.1 $\pm$0.2
YBCO$_{6.33}$J	0.1	0.050	40.6 $\pm$ 2.4	730 $\pm$ 37	1.2 $\pm$ 0.1
YBCO$_{6.33}$L	-	0.048	46.7 $\pm$ 1.9	1460 $\pm$ 73	2.8 $\pm$ 0.2
YBCO$_{6.33}$L	0.1	0.050	40.3 $\pm$ 3.7	1054 $\pm$ 52	1.8 $\pm$ 0.2
YBCO$_{6.33}$B	4	0.053	37.8 $\pm$ 1.3	854 $\pm$ 85	1.3 $\pm$ 0.2
BSCO	10	0.17	320 $\pm$ 30	100	1.3 $\pm$ 0.2
Tl-2201	15	0.26	3950 $\pm$ 40	6.15 $\pm$ 0.03	0.99 $\pm$ 0.01

smoothly to zero with the superconducting transition temperature. In contrast, the charge of electrons tunnelling between the CuO_2 layers is not renormalized, suggestive of spin-charge separation in the 2D CuO_2 planes. Further work will undoubtedly be needed to confirm this interpretation, but the preliminary evidence is compelling.

At higher dopings, after J and L had annealed sufficiently such that bulk superconductivity was achieved, we also find a WF law violation when superconductivity is suppressed by a magnetic field. The extent of the violation is however reduced, with $L/L_0 = 1.8 \pm 0.2$ in sample L. Combined with the previously discussed data in optimal and overdoped cuprates (summarized in Table A.2) the picture that emerges is one where the onset of the WF-law violation is very close to p_{SC}. How this violation evolves as the Mott insulator is approached should be an extremely interesting avenue of investigation. The residual linear term reaches 0 at p=0, but its doping dependence at very low dopings is completely unknown. Our first measurements hint at the existence of a novel and unexplored ground state in the low doped region of clean cuprates, a state in which further measurements and characterization will almost certainly change our understanding of cuprate physics.

The detailed quantitative comparison of heat and charge in low doped YBCO is now underway, and these preliminary results[3] will need close scrutiny. In order to be fully convinced that the observed violation is not related to an unforeseen experimental effect, several tests are underway. The first is performing 6 contact resistivity measurements

---

[3]The experimental work summarized in this chapter was performed during the summer and fall of 2004.

on our samples to complement the 4 wire ones. In such a test there are two sets of voltage pads, on opposing sides of the crystal. The ratio of the resistance of these pairs should be a simple geometric factor, if the current flow is homogenous. If there is any c-axis contribution to the resistance measurement, the temperature dependence of the ratio will pick this up. A comparison to recent measurements of the surface resistance by microwaves from the UBC group will also aid in confirming these findings.

12.4 Chapter summary

In conclusion, we have presented evidence to show that the non-superconducting state of pure cuprates in the underdoped regime of the phase diagram is metallic. The associated low-energy fermionic excitations have a heat conductivity that evolves seamlessly from the superconducting phase, which suggests they have a nodal spectrum akin to that of the d-wave superconductor. In other words, as holes are doped into the Mott insulator, a metallic ground state is first reached before the onset of phase-coherent superconductivity. The ability of these excitations to transport heat and charge is found to be unusual, there is a greater thermal than charge conductivity as $T \to 0$ resulting in a significant violation of the Wiedemann-Franz law. We propose this as the generic scenario of clean cuprates. Note that it is not realized in the case of LSCO, which instead shows insulating behaviour, most likely caused by the presence of static SDW order.

13

SUMMARY AND FUTURE WORK

13.1 Summary and future work

The measurement of thermal conductivity at ultra-low temperatures provides information on materials that is very difficult to obtain by other techniques. By extending our investigations to the $T \to 0$ limit, we reveal information about the quantum mechanical ground state of a material, information which is vital to understanding the physics of any system. In the cuprates, this information is particularly crucial, since as a function of doping these materials reveal a bewildering array of ground states. In the underdoped regime the nature of the ground state is the subject of considerable controversy, and our understanding of this regime thus far is derived mainly from systems with high levels of disorder.

Our study is the first to track the ground state of the very cleanest of these materials from the overdoped superconductor to the Mott insulator. We provide a wealth of data over a broad range of doping, and focus particularly in the very low doped region of the phase diagram where information derived from high quality, homogenous single crystals does not exist. In doing so we establish for the first time the true nature of the state that lies on the threshold of superconductivity - in essence, the results in this Thesis reveal a new phase in the cuprate phase diagram.

13.2 Doping dependence of Δ_0

Studies of the residual linear term in thermal conductivity from the overdoped to the underdoped regime in clean YBCO have, for the first time, revealed the doping dependence of the zero-energy quasiparticle gap. Assuming a d-wave order parameter, the value of the gap was found to agree precisely with the magnitude of the pseudogap, typically measured at higher temperatures. This remarkable scaling sheds new light on the physics of the underdoped regime. First, we confirm that the pseudogap is indeed d-wave

in nature, as suggested from studies of ARPES at $T > T^*$ but until now unproven in the $T \to 0$ limit. Second, we prove that the pseudogap must have nodes, an observation that precludes any possible transition from a d-wave state to one with a complex component. Thirdly, the excellent agreement between our $T = 0$ data and spectroscopic measurements at high temperature implies that the excitations must have a linear dispersion, in other words the formalism of Durst and Lee works well into the underdoped regime. This suggests that either the pseudogap is intrinsic in origin and is related to superconductivity or it requires that any competing order has an identical dispersion relation to the d-wave superconducting state.

What remains to be reconciled with this picture is the very high value of Δ_0 at low dopings. Although the magnitude agrees favourably with that the antiferromagnetic exchange energy, a clear picture of how the gap evolves in the low doped region of the phase diagram is lacking. A series of samples in the regime $6.33 < y < 6.50$ would be very useful in this regard and would fill in a large void in the literature. At present, information on the gap energy scale in this region is very sparse.

All of this underscores the dichotomy of the underdoped phase. The treatment of quasiparticle excitations in a BCS theory suitably modified to incorporate the nodal structure of the order parameter is remarkably successful. It yields a gap magnitude that agrees with independent techniques, and our measurements of samples of similar doping yet different impurity levels establishes universality. On the other hand, a gap that increases as superfluid density heads to zero is very unusual. Though the search continues for an explanation of these observations, our data provides useful new constraints on the development of theories.

13.3   WF law in lightly doped YBCO

The Wiedemann-Franz law is a fundamental consequence of Fermi-liquid physics. For over a century it has been observed to hold across countless materials - metals, semiconductors, disordered solids. A natural place to observe a violation of this law might be expected to be in the underdoped cuprates, where electron electron interactions are large and the physics is decidedly unconventional. Attempts to study the Wiedemann-Franz law in these materials have thus far failed. In LSCO as $p \to p_{SC}$ a diverging resistivity and residual linear term that approached zero combined to give a Lorenz ratio that was inconclusive.

Our measurements on YBCO presented in this thesis finally provide a possible answer to this question. We observe, for the first time, a finite residual linear term in the normal state of YBCO (whether accessed by the application of field or varying doping) and a corresponding electrical conductivity that obtains a finite value of the T=0 limit. The ratio of the two leads to a Wiedemann-Franz law that is violated in the limit $T \rightarrow 0$ in underdoped high-T_c superconductors. The violation appears to onset at, or very near the critical doping p_{SC}. The implications of this observation are far-reaching, and raise numerous questions. Does the violation occur because of the proximity to the Mott insulating phase? Can the fundamental excitations of this phase contribute to Fermionic heat transport in the zero temperature limit? Or is the violation perhaps the result of a novel quantum phase of matter, previously unobserved in 2 dimensional materials, where the electron splinters into charge and spin carrying constituents? Either picture would entail a revisal of our understanding of the cuprates.

The very observation of a finite residual linear term in the normal state of YBCO is an important first. It implies that, unlike LSCO where κ_0/T is zero for $p < p_{SC}$, clean cuprate superconductors become metallic before they become superconducting. The observation is exceptionally robust, the same value of linear term is observed six samples of our low doped YBCO crystals. This is an important new piece of the cuprate puzzle, and highlights the fact that our understanding of the role of disorder in the high-T_c's is far from complete.

The course of study from this point is clear. Further work needs to be done to confirm the observed violation of the Wiedemann-Franz law by carefully examining the charge conductivity. A six-contact resistivity measurement on the samples used in this study would be most useful, to ensure that current flow is homogenous and that any c-axis contributions to the resistivity are negligible. The next step is to push further into the underdoped regime towards the Mott insulator. Eventually, one would expect the linear term to reach zero, but the increasing anti-ferromagnetic correlations may serve to enhance the linear term. The doping dependence of κ_0/T all the way to T=0 would be extremely revealing.

13.4   Concluding remarks

The results presented in this Thesis emphasize that the cuprates are the host of intriguing and still unexplained physics. In particular, the studies summarized above challenge

two of the pillars of modern thought in condensed matter. The establishment of a zero temperature superconducting gap Δ_0 that increases while T_c decreases in the underdoped regime of YBCO directly contradicts the much celebrated theory of Bardeen Cooper and Schrieffer. Although the quasiparticle excitations themselves appear to be conventional, the evolution of the gap most certainly is not, a result that underlies the need for a comprehensive theory of the underdoped state.

In the extreme underdoped regime, where samples are non-superconducting, our observation of a metallic state that violates the Wiedemann-Franz law at T=0 has far reaching implications. Such a state violates the basic assumptions of Fermi-liquid theory, that heat and charge are carried by the same entities and their conductivities are related by a constant. Fermi-liquid theory is the basic starting place for thinking about metals, and our observations will require a re-examination of the integrity of the electron in 2 dimensional materials near a Mott transition.

In closing, this Thesis has demonstrated how a convergence of careful experimental work and advances in crystal growth can provide new perspectives on the hidden secrets of high T_c superconductors. The availability of homogenous, high quality YBCO crystals in the most underdoped region of the phase diagram has opened up an entire new chapter in cuprate physics, and it is likely that experiments on these samples will be key to settling many of the current debates in the high T_c community.

Appendix:Sample Catalog

A.1 Physical Dimensions of Samples Used in the Study

A.1.1 $YBa_2Cu_3O_y$

Table A.1: Table summarizing the physical dimensions of the YBCO samples used in this study. ℓ is the average seperation between the voltage pads, with the errors determined by the width of the pads.

Sample Name	ℓ (mm)	Width (mm)	Thickness (μm)	α (cm)
$YBCO_{6.0}$ old deox A	1.12 ± 0.1	0.61 ± 0.03	153 ± 11	$8.3 \pm 1.0e^{-3}$
$YBCO_{6.35}$ B	1.03 ± 0.09	0.056 ± 0.05	83 ± 10	$4.21 \pm 0.70\ e^{-3}$
$YBCO_{6.35}$ F	0.46 ± 0.08	0.56 ± 0.05	78 ± 0.05	$9.62e^{-3}$
$YBCO_{6.35}$ H	0.61 ± 0.075	0.51 ± 0.05	32	$2.66e^{-3}$
$YBCO_{6.35}$ J	0.70 ± 0.7	0.34 ± 0.01	4.6 ± 0.1	$2.21 \pm 0.27e^{-4}$
$YBCO_{6.35}$ K	0.46 ± 0.4	0.28 ± 0.01	5.9 ± 0.1	$3.64 \pm 0.40\ e^{-4}$
$YBCO_{6.35}$ L	0.51 ± 0.4	0.31 ± 0.01	7.4 ± 0.1	$4.44 \pm 0.75\ e^{-4}$
$YBCO_{6.55}$ A 2002	$0.59 \pm$	0.27 ± 0.02	14 ± 2	$6.43\ e^{-3}$
$YBCO_{6.50}$ B	0.59 ± 0.06	0.52 ± 0.05	73 ± 1	$6.29 \pm 0.9e^{-3}$
$YBCO_{6.50}$ C	1.69 ± 0.01	0.66 ± 0.01	25 ± 1	$9.7 \pm 0.9e^{-4}$
$YBCO_{6.6}$ und F detwin	1.15 ± 0.1	0.96 ± 0.05	70 ± 10	$5.84 \pm 1.02\ e^{-3}$
$YBCO_{6.6}$ und K(detwin)	0.65 ± 0.1	0.25 ± 0.05	45 ± 10	$1.73 \pm 0.58\ e^{-3}$
$YBCO_{6.6}$ und O(detwin)	0.39 ± 0.04	0.33 ± 0.02	40 ± 5	$3.38 \pm 0.64\ e^{-3}$
$YBCO_{6.6}$ und S(detwin)	0.68 ± 0.1	0.55 ± 0.05	42 ± 5	$3.39 \pm 0.72\ e^{-3}$
$YBCO_{6.73}$ robert, detwin	0.88 ± 0.15	0.50 ± 0.03	87 ± 6	$4.9 \pm 0.7e^{-3}$
$YBCO_{6.95}$ A, detwin	0.96 ± 0.1	0.89 ± 0.1	60 ± 10	$5.56 \pm 1.26\ e^{-3}$
$YBCO_{6.95}$ C, detwin	0.38 ± 0.04	0.44 ± 0.02	45 ± 5	$5.3 \pm 0.8e^{-3}$
$YBCO_{6.95}$ D, detwin	1.66 ± 0.17	1.40 ± 0.08	80 ± 5	$6.8 \pm 0.9e^{-3}$
$YBCO_{6.95}$ UBC, detwin	0.97 ± 0.09	0.26 ± 0.02	15 ± 5	$4.0 \pm 1.4e^{-4}$
$YBCO_{6.99}$ UBC	0.99 ± 0.19	0.52 ± 0.20	25 ± 1	$1.3 \pm 0.2e^{-3}$

Table A.2: Table summarizing the physical dimensions of the Y-124 samples used in this study. ℓ is the seperation of the voltage pads.

Sample	ℓ (mm)	Width (mm)	Thickness (μm)	α (cm)	$\alpha_{\rho_{300K}}$ (cm)
$Y124$ A	0.42 ± 0.05	0.15 ± 0.012	62 ± 12	$2.28 \pm 0.56e^{-5}$	$3.4e^{-3}$
$Y124$ B	0.44 ± 0.08	0.073 ± 0.008	25 ± 10	$4.2 \pm 1.9e^{-4}$	$8.2e^{-4}$
$Y124$ C	0.36 ± 0.04	0.053 ± 0.015	25 ± 10	$3.7 \pm 2e^{-5}$	-
$Y124$ D	0.32 ± 0.05	0.026 ± 0.004	10 ± 0.4	$8.1 \pm 1.7e^{-5}$	$1.6e^{-4}$

A.1.2 $YBa_2Cu_4O_8$

This table gives the measured geometric factors for the 4 samples of $YBa_2Cu_4O_8$ used in this study. The length and width were measured by optical microscope while the thicknesses were measured with the assistance of Patrick Morales with an SEM. The column α gives the measured value of the geometric factor, while the column $\alpha_{\rho_{300K}}$ gives the calculated value of the geometric factor if one normalzies the resistivity at 300 K to the values that appear in the literature cite [138].

A.2 Summary of Powerlaw fits to the data of Sun, Ando and Segawa

Sample	T_c K	Doping p	κ_0/T lin. extr. mW/K^2cm	κ_0/T pow. law mW/K^2cm	B	α
Ando $y = 6.45$	20	0.063	0.073±0.006	0.039±0.003	6.9	1.58
Ando $y = 6.5$	39	0.076	0.122±0.013	0.067±0.012	12.0	1.64
Ando $y = 6.6$	53	0.088	0.14±0.015	0.032±0.020	6.5	1.30
Ando $y = 6.7$	59	0.093	0.154±0.015	0.109±0.009	6.6	1.49
Ando $y = 7.0$	91	0.17	0.166±0.016	0.120±0.007	5.6	1.48

Above : Table summarizing the results of power law fitting to the recently published data of Sun *et.al.* [3]. The doping is estimated using equation 6.1, and the column labeled κ_0/T lin. extr. are the values of the linear term obtained from a straight line extrapolation to the data on a T^2 plot, as given in the publication. The column labeled κ_0/T pow. law is the linear term extracted from the fits shown in the figure, with B and α giving the temperature coefficient and exponent respectively.
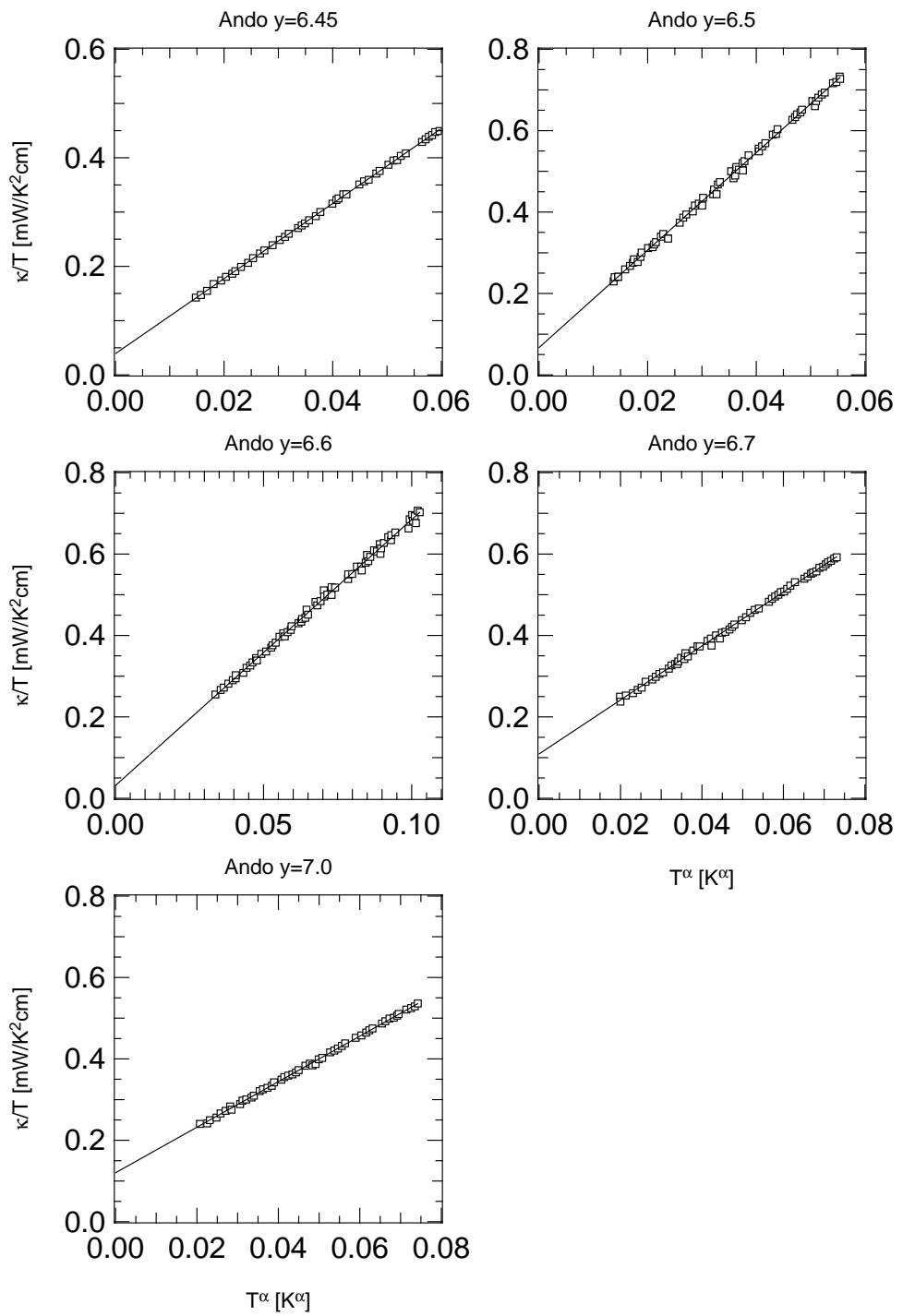
Figure A.1: Powerlaw fits to the data of Sun, Ando and Segawa [3] on the doping dependence of low temperature thermal transport. The data is plotted as κ/T vs. T^α where α is summarized in the table of fit parameters above.

Table A.3: Table summarizing the the powerlaw fits to YBCO$_{6.35}$ crystals.

Sample	κ_0/T $[\mu W K^{-2} cm^{-1}]$	B $\times 10^{-3}$	α	rang err	χ^2
B: 0T, 2002	37.8±0.7	888±4	1.367 ± 0.008	±1.1	6.3
B: 13T, 2002	36.8± 0.8	910±5	1.374 ± 0.009	±0.8	7.3
B: 0T, 2003	37.4±0.7	951±5	1.462±0.009	±1.0	6.5
B: 10 T, 2003	40.7±0.7	1002±6	1.499±0.009	±0.5	7.5
F: 0T, no anneal	33.7±1.5	1383±7	1.239±0.008	±1.8	6.8
F: 13 T, no anneal	38.9±1.4	1456±7	1.277±0.008	±1.6	6.8
F: 0 T, anneal 1	32.7±1.8	1343±8	1.212±0.01	±2.9	13.1
F: 0 T, anneal 3	33.5±1.1	1319±5	1.212±0.006	±2.1	5.4
F: 0 T, anneal 4	38.4±0.8	1269±3	1.217±0.005	±1.1	2.7
F: 12 T, anneal 4	42.3±1.7	1301±8	1.255±0.01	±2.5	10.7
H: 0 T, no anneal	38.1±1.0	938±5	1.212±0.009	±4.0	10.2
H: 13 T, no anneal	39.3±1.0	1003±5	1.255±0.008	±3.5	8.6
H: 0 T, anneal 1	41.1±1.4	965±7	1.243±0.012	±2.0	15.0
H: 0T, anneal 3	38.8±0.7	909±3	1.204±0.006	±2.2	4.9
H: 0 T, anneal 4	34.6±0.7	787±3	1.139±0.006	±0.8	4.4
H: 12T, anneal 4	32.2±1.3	825±5	1.162±0.011	±4	14.1

A.3 Summary of Powerlaw fits to low doped YBCO samples

The fits to the powerlaw form of equation 2.15 for all samples, for each anneal are summarized in Table A.4 at the end of this chapter. Each fit was performed from 0 to 550 mK, with the error originating from three sources. First, there is a direct fit error , governed by random noise in the data and calculated using the least-squares fitting program. Second, there is an error associated with varying the fitting range. The range error is determined by varying the upper range of the power law fit between 300mK and 600mK (the limits of a good fit, as indicated by low χ^2 values.), and noting how much κ_0/T varies in the process. I take the maximum and minimum in this range, and set the fit range error = ± 1/2*[$\kappa_0/T(max)$ -$\kappa_0(min)/T$]. Finally, the geometric factor error for each of the samples is determined by measuring the maximum and minimum distance between the pads, so that $\Delta \alpha_{geo} = ± 1/2$ [max (separation) - min (separation)]. The total error in the residual linear term is thus taken to be the root of the sum of the squares of each independent source of error ie. $\Delta \kappa_0/T = \sqrt{(fit error)^2 + (range error)^2 + (\alpha_{geo} error)^2}$.

Table A.4: Table summarizing the the powerlaw fits to YBCO$_{6.33}$ crystals.

Sample	κ_0/T $[\mu W K^{-2} cm^{-1}]$	B $\times 10^{-3}$	α	rang err	χ^2
J: 0 T, no anneal	52.2±1.3	886±4	1.148±0.009	±2.9	5.6
J: 10 T, no anneal	57.4±2	920±5	1.181±0.013	±5.9	7
J: 0T, anneal 1	40.6±1.2	710±2	0.998±0.007	±2.1	4.0
J: 10T, anneal 1	46.9±1.2	748±2	1.057±0.007	±3.3	3.3
J: 0T, anneal 2	28.5±3.1	523±2	0.824±0.012	±4.0	20.4
J: 11.5T, anneal 2	27.8±3	549±2	0.850±0.015	±8.5	11.7
K: 0 T, no anneal	33.3±0.4	1159±2	1.300±0.003	±1.1	1.7
K: 10 T, no anneal	34.2±0.8	1184±4	1.307±0.006	±1.9	4.1
K: 0T, anneal 1	38.4±0.8	970±4	1.219±0.007	±2.1	5.4
K: 10T, anneal 1	36.8±1.2	1005±4	1.229±0.008	±6.6	6.7
K: 0T, anneal 2	35.7±0.7	747±2	1.104±0.006	±2.3	4.0
K: 11.5T, anneal 2	32.31.6	784±5	1.118±0.012	±6.2	12.5
L: 0 T, no anneal	46.7±0.6	924±2	1.253±0.005	±1.8	2.2
L: 10 T, no anneal	45.4±0.8	957±4	1.260±0.007	±3.5	4.8
L: 0T, anneal 1	40.3±1.1	748±3	1.125±0.009	±3.5	5.4
L: 10T, anneal 1	43.3±1.1	784±4	1.166±0.009	±3	6.8
L: 0T, anneal 2	40.0±0.9	567±3	1.016±0.008	±1.5	11.3
L: 11.5T, anneal 2	32.9±1.1	594±2	1.004±0.008	±3.6	5.5

Bibliography

[1] M. Sutherland, D. G. Hawthorn, R. W. Hill, F. Ronning, S. Wakimoto, H. Zhang, C. Proust, E. Boaknin, C. Lupien, L. Taillefer, R. Liang, W. N. Hardy D. A. Bonn, R. Gagnon, N. E. Hussey, T. Kimura, M. Nohara, and H. Takagi. Thermal conductivity across the phase diagram of cuprates: Low-energy quasiparticles and doping dependence of the superconducting gap. *Phys. Rev. B.*, 67:174520, 2003.

[2] X. F. Sun, Seiki Komiya, J. Takeya, and Yoichi Ando. Magnetic-field-induced localization of quasiparticles in underdoped $La_{2-x}Sr_xCuO_4$ single crystals. *Phys. Rev. Lett.*, 90:117004, 2003.

[3] X.F. Sun, Kouji Segawa, and Yoichi Ando. Metal-to-insulator crossover in $YBa_2Cu_3O_y$ probed by low-temperature quasiparticle heat transport. *Phys. Rev. Lett.*, 93:107001, 2004.

[4] R. W. Hill, Christian Lupien, M. Sutherland, Etienne Boaknin, D. G. Hawthorn, Cyril Proust, F. Ronning, Louis Taillefer, Ruixing Liang, D. A. Bonn, and W. N. Hardy. Transport in ultraclean $YBa_2Cu_3O_7$: Neither unitary nor Born impurity scattering. *Phys. Rev. Lett.*, 92:027001, 2004.

[5] N.E. Hussey, S. Nakamaw, K. Behnia, H. Takagi, C. Urano, S. Adachi, and S. Tajima. Absence of residual quasiparticle conductivity in the underdoped cuprate $YBa_2Cu_4O_8$. *Phys. Rev. Lett.*, 85:4140, 2000.

[6] M. Sutherland, D. G. Hawthorn, R. W. Hill, F. Ronning, H. Zhang, C. Proust, E. Boaknin, C. Lupien, L. Taillefer, R. Liang, W. N. Hardy D. A. Bonn, and R. Gagnon. Doping dependence of superconducting gap in $YBa_2Cu_3O_y$ from universal heat transport. *Physica C*, 408-410:672, 2004.

[7] D. G. Hawthorn, R. W. Hill, C. Proust, F. Ronning, M. Sutherland, E. Boaknin, C. Lupien, S. Wakimoto, H. Zhang, L. Taillefer, N. Hussey, and T. Kimura. Field-induced thermal metal-to-insulator transition in underdoped $La_{2-x}Sr_xCuO_{4+\delta}$. *Phys. Rev. Lett.*, 90:197004, 2003.

[8] J.G. Bednorz and K.A. Müller. Possible high-T_c superconductivity in the la-ba-cu-o system. *Z Phys. B: Condens. Matter*, 64:188, 1986.

[9] J. Orenstein and A. J. Millis. Advances in the physics of high-temperature superconductivity. *Science*, 288:468–474, 2000.

[10] M.R. Norman and C. Pépin. The electronic nature of high temperature superconductors. *Rep. Prog. Phys.*, 2003.

[11] N.E. Hussey. Low-energy quasiparticles in high-T_c cuprates. *Advances in Physics*, 51:1685–1771, 2002.

[12] Robert J. Cava. Oxide superconductors. *J. Am. Ceram. Soc.*, 83:5–28, 2000.

[13] P. W. Anderson. The resonating valence bond state in La_2CuO_4 and superconductivity. *Science*, 235:1196, 1987.

[14] Brian Maple. High temperature superconductivity. *MRS Bulletin XV*, 6:60, 1990.

[15] P. Dai, B.C. Chakoumakos, G.F. Sun, K.W. Wong, D.F. Lu, and Y. Xin. Synthesis and neutron powder diffraction study of the superconductor $HgBa_2Ca_2Cu_3O_{8+\delta}$ by tl substitution. *Physica C*, 243:201, 1994.

[16] R. Joynt and L. Taillefer. The superconducting phases of UPt_3. *Rev. Mod. Phys.*, 74:235, 2002.

[17] A. J. Legget. A theoretical description of the new phases of ^3He. *Rev. Mod. Phys.*, 47:331, 1975.

[18] W.N. Hardy, D.A. Bonn, D.C. Morgan, R.X. Liang, and K. Zhange. Precision measurements of the temperature dependence of lambda in $YBa_2Cu_3O_{6.95}$: Strong evidence for nodes in the gap function. *Phys. Rev. Lett.*, 70:3999, 1993.

[19] C.C. Tsuei et. al. Pairing symmetry and flux quantization in a tricrystal superconducting ring of $YBa_2Cu_3O_{7-\delta}$. *Phys. Rev. Lett.*, 73:593, 1994.

[20] C.C. Tsuei and J.R. Kirtley. Pairing symmetry in cuprate superconductors. *Rev. Mod. Phys.*, 72:969–1016, 2000.

[21] N. D. Mathur, F. M. Groshe, S. R. Julian, I. R. Walker, D. M. Freye, R. K. W. Haselwimmer, and G. G. Lonzarich. Magnetically mediated superconductivity in heavy fermion compounds. *Nature*, 394:39–43, 1998.

[22] A. G. Loeser, Z-X Shen, M. C. Schabel, C. Kim, M. Zhang, A. Kapitulnik, and P. Fournier. Temperature and doping dependence of the Bi-Sr-Ca-Cu-O electronic structure and fluctuation effects. *Phys. Rev. B*, 56:14185, 1996.

[23] C. Renner, B. Revaz, J-Y Genoud, K. Kadowaki, and O. Fisher. Pseudogap precursor of the superconducting gap in under- and overdoped $Bi_2Sr_2CaCu_2O_{8+\delta}$. *Phys. Rev. Lett.*, 80:149, 1998.

[24] Y. DeWilde, N. Miyakawa, P. Guptasarma, M. Iavarone, L. Ozyuzer, J. F. Zasadzinski, P. Romano, D. G. Hinks, C. Kendziora, G. W. Crabtree, and K. E. Gray. Unusual strong-coupling effects in the tunneling spectroscopy of optimally doped and overdoped $Bi_2Sr_2CaCu2O_{8+\delta}$. *Phys. Rev. Lett.*, 80:153, 1998.

[25] Y. J. Uemura, G. M. Luke, B. J. Sternlieb, J. H. Brewer, J. F. Carolan, W. N. Hardy, R. Kadono, J. R. Kempton, R. F. Kiefl, S. R. Kreitzman, P. Mulhern, T. M. Riseman, D. Ll. Williams, B. X. Yang, S. Uchida, H. Takagi, J. Gopalakrishnan, A. W. Sleight, M. A. Subramanian, C. L. Chien, M. Z. Cieplak, Gang Xiao, V. Y. Lee, B. W. Statt, C. E. Stronach, W. J. Kossler, and X. H. Yu9. Universal correlations between T_c and n_s/m^* (carrier density over effective mass) in high-tc cuprate superconductors. *Phys. Rev. Lett.*, 62:2317, 1989.

[26] Andrea Damascelli, Zahid Hussain, and Zhi-Xun Shen. Angle-resolved photoemission studies of the cuprate superconductors. *Rev. Mod. Phys.*, 75:473, 2003.

[27] D.S. Marshall, D. S. Dessau, A. G. Loeser, C.-H. Park, A. Y. Matsuura, J. N. Eckstein, I. Bozovic, P. Fournier, A. Kapitulnik, W. E. Spicer, and Z.-X. Shen. Unconventional electronic structure evolution with hole doping in $Bi_2Sr_2CaCu_2O_{8+\delta}$: Angle-resolved photoemission results. *Phys. Rev. Lett.*, 76:4841, 1996.

[28] M. R. Norman, H. Ding, M. Randeria, J.C. Campuzano, T. Yokoya, T. Takeuchi, T. Takahashi, T. Mochiku, K. Kodwaki, P. Guptasarma, and D.G. Hinks. Destruction of the Fermi surface in underdoped high-T_c superconductors. *Nature*, 392:157, 1998.

[29] X.J. Zhou, T. Yoshida, A. Lanzara, P.V. Bogdanov, S.A. Kellar, K.M. Shen, W.L. Yang, F. Ronning, T. Sasagawa, T. Kakeshita, T. Noda, H. Eisaki, S. Uchida, C.T. Lin, F. Zhou, J.W. Xiong, W.X. Ti, Z.X. Zhao, A. Fujimori, Z. Hussain, and Z.-X. Shen. Universal nodal Fermi velocity in high-temperature superconductors. *Nature*, 423:398, 2003.

[30] Z.-X. Shen and J. R. Schrieffer. Momentum, temperature, and doping dependence of photoemission lineshape and implications for the nature of the pairing potential in high-T_c superconducting materials. *Phys. Rev. Lett.*, 78:1771, 1997.

[31] W. W. Warren Jr, R. E. Walstedt, G. F. Brennert, R. J. Cava, R. Tycko, R. F. Bell, and G. Dabbagh. Cu spin dynamics and superconducting precursor effects in planes above T_c in $YBa_2Cu_3O_{6.7}$. *Phys. Rev. Lett.*, 62:1193, 1989.

[32] Tom Timusk and Bryan Statt. The pseudogap in high-temperature superconductors: an experimental survey. *Rep. Prog. Phys.*, 62:61, 1999.

[33] P. J. White, Z-X Shen, C. Kim, J. M. Harris, A. G. Loeser, P. Fournier, and A. Kapitulnik. Rapid suppression of the superconducting gap in overdoped $Bi_2Sr_2CaCu2O_{8+\delta}$. *Phys. Rev. B*, 54:R15669, 1996.

[34] A. V. Puchkov, D. N. Basov, and T. Timusk. The pseudogap state in high-T_c superconductors: An infrared study. *J. Phys. Condens. Matter*, 8:10049, 1996.

[35] R. Hackl, G. Krug, R. Nemetschcek, M. Opel, and B. Stadlober. Spectroscopic studies of superconductors (proc. SPIE 2696) vol v. page 194, 1996.

[36] J.M. Harris, P. J. White, Z.-X. Shen, H. Ikeda, R. Yoshizaki, H. Eisaki, S. Uchida, W. D. Si, J. W. Xiong, Z.-X. Zhao, and D. S. Dessau. Measurement of an anisotropic energy gap in single plane $Bi_2Sr_{2-x}La_xCuO_{6+\delta}$. *Phys. Rev. Lett.*, 79:143, 1997.

[37] V.J. Emery and S.A. Kivelson. Importance of phase fluctuations in superconductors with small superfluid density. *Nature*, 374:434, 1995.

[38] V.J. Emery and S.A. Kivelson. Superconductivity in bad metals. *Phys. Rev. Lett.*, 74:3253–3256, 1995.

[39] M. Franz and Z. Tesanovic. Algebraic fermi liquid from phase fluctuations: topological fermions, vortex berryons, and QED3 theory of cuprate superconductors. *Phys. Rev. Lett.*, 87:257003, 2001.

[40] E.W. Carson, S.A. Kivelson, V.J. Emery, and E. Manousakis. Classical phase fluctuations in high temperature supersonductors. *Phs. Rev. Lett.*, 83:612, 1999.

[41] Jelena Stajic, Andrew Iyengar, K. Levin, B. R. Boyce, and T. R. Lemberger. Competing order parameters or precursor superconductivity. *Phys. Rev. B*, 68:024520, 2003.

[42] Yayu Wang, Z. A. Xu, T. Kakeshita, S. Uchida, S. Ono, Yoichi Ando, and N. P. Ong. Onset of the vortexlike nernst signal above T_c in $La_{2-x}Sr_xCuO_4$ and $Bi_2Sr_{2-y}La_yCuO_6$. *Phys. Rev. B*, 64:224519, 2001.

[43] Z. A. Xu, N. P. Ong, Y. Wang, T. Kageshita, and S. Uchida. Vortex-like excitations and the onset of superconducting phase fluctuation in underdoped $La_{2-x}Sr_xCuO_4$. *Nature*, 406:486, 2000.

[44] Yayu Wang, N. P. Ong, Z. A. Xu, T. Kakeshita, S. Uchida, D. A. Bonn, R. Liang, and W. N. Hardy. High field phase diagram of cuprates derived from the Nernst effect. *Phys. Rev. Lett.*, 88:257003, 2002.

[45] S. Chakravarty, R. B. Laughlin, D. K. Morr, and C. Nayak. Hidden order in the cuprates. *Phys. Rev. B*, 63:094503, 2001.

[46] C.M. Varma. Pseudogap phase and the quantum-critical point in copper-oxide metals. *Phys. Rev. Lett.*, 83:3528, 1999.

[47] Xiao-Gang Wen and Patrick A. Lee. Theory of underdoped cuprates. *Phys. Rev. Lett.*, 76:503, 1996.

[48] S. A. Kivelson, E. Fradkin, V. Oganesyan, I. P. Bindloss, J. M. Tranquada, A. Kapitulnik, and C. Howald. How to detect fluctuating order in the high-temperature superconductors. *Rev. Mod. Phys.*, 75:1201, 2003.

[49] K. Yamada, C. H. Lee, K. Kurahashi, J. Wada, S. Wakimoto, S. Ueki, H. Kimura, Y. Endoh, S. Hosoya, G. Shirane, R. J. Birgeneau, M. Greven, M. A. Kastner, and

Y. J. Kim. Doping dependence of the spatially modulated dynamical spin correlations and the superconducting-transition temperature in $La_{2-x}Sr_xCuO_4$. *Phys. Rev. B.*, 57:6165, 1998.

[50] J. Tranquada, B. Sternlieb, J. Axe, Y. Nakamura, and S. Uchida. Evidence for stripe correlations of spins and holes in copper oxide superconductors. *Nature*, 375:561, 1995.

[51] J. M. Tranquada, J. D. Axe, N. Ichikawa, A. R. Moodenbaugh, Y. Nakamura, and S. Uchida. Coexistence of, and competition between, superconductivity and charge-stripe order in $La_{1.6-x}Nd_{0.4}Sr_xCuO_4$. *Phys. Rev. Lett.*, 78:338, 1997.

[52] J. Tranquada. Modulated spin and charge densities in cuprate superconductors. *Physica B*, 241:745, 1997.

[53] C. Stock, W. J. L. Buyers, Z. Tun, R. Liang, D. Peets, D. Bonn, W. N. Hardy, and L. Taillefer. Neutron scattering search for static magnetism in oxygen-ordered $YBa_2Cu_3O_{6.5}$. *Phys. Rev. B.*, 66:024505, 2002.

[54] C. Stock, W. J. L. Buyers, Z. Tun, R. Liang, D. Peets, D. Bonn, W. N. Hardy, and L. Taillefer. Dynamic stripes and resonance in the superconducting and normal phases of $YBa_2Cu_3O_{6.5}$ ortho-II superconductor. *Phys. Rev. B.*, 69:024505, 2004.

[55] B. Lake, H. M. Rønnow, N. B. Christensen, G. Aeppli, K. Lefmann, D. F. Mc-Morrow, P. Vorderwisch, P. Smeibidl, N. Mangkorntong, T. Sasagawa, M. Nohara, H. Takagi, and T. E. Mason. Antiferromagnetic order induced by an applied magnetic field in a high-temperature superconductor. *Nature*, 415:299, 2002.

[56] S. Nakamae, K. Behnia, N. Mangkorntong, M. Nohara, H. Takagi, S. J. C. Yates, and N. E. Hussey. Electronic ground state of heavily overdoped nonsuperconducting $La_{2-x}Sr_xCuO_4$. *Phys. Rev. B.*, 68:100502, 2003.

[57] J.L. Tallon and J.W. Loram. The doping dependence of T^* - what is the real high T_c phase diagram? *Physica C*, 349:53–68, 2001.

[58] C. Proust, E. Boaknin, R. W. Hill, L. Taillefer, and A. P. Mackenzie. Heat transport in a strongly overdoped cuprate: Fermi liquid and a pure d-wave BCS superconductor. *Phys. Rev. Lett.*, 89:147003, 2002.

[59] A. C. Durst and P. A. Lee. Impurity-induced quasiparticle transport and universal-limit Wiedemann-Franz violation in d-wave superconductors. *Phys. Rev. B*, 62:1270, 2000.

[60] L. Taillefer, B. Lussier, R. Gagnon, K. Behnia, and H. Aubin. Universal heat conduction in $YBa_2Cu_3O_{6.9}$. *Phys. Rev. Lett.*, 79:483, 1997.

[61] M. Chiao, R.W. Hill, C. Lupien, B. Popic, R. Gagnon, and L. Taillefer. Quasiparticle transport in the vortex state of $YBa_2Cu_3O_{6.9}$. *Phys. Rev. Lett.*, 82:2943, 1999.

[62] D.G. Hawthorn. *Thermal conduction in the high temperature superconductors LSCO and Tl2201: A field and doping dependent study.* PhD thesis, University of Toronto, 2004.

[63] Neil W. Ashcroft and N. David Mermin. *Solid State Physics.* W. B. Saunders Company, 1976.

[64] J.M. Ziman, editor. *Electrons and Phonons.* Clarendon Press, Oxford, UK, 1st edition, 1960.

[65] A. Matthiessen. *Rep. Brit. Ass.*, 32:144, 1862.

[66] G. Wiedemann and R. Franz. Ueber die wärme leitungsfähigkeit der metalle. *Ann. Phys.*, 89:497–532, 1853.

[67] F. Seitz and David Turnbull, editors. *Solid State Physics:Advances in Research and Applications*, volume 7. Academic Press, New York, 1st edition, 1958.

[68] R. Berman. *Thermal Conduction in Solids.* Clarendon Press, Oxford, 1976.

[69] H. B. G. Casimir. *Physica*, 5:495, 1938.

[70] R. O. Pohl and B. Stritzker. Phonon scattering at crystal surfaces. *Phys. Rev. B.*, 25:3608, 1982.

[71] W. S. Hurst and D. R. Frankl. Thermal conductivity of silicon in the boundary scattering regime. *Phys. Rev*, 186:801, 1969.

[72] W. D. Seward. *PhD Thesis.* PhD thesis, Cornell University, 1965.

[73] P. D. Thatcher. Effect of boundaries and isotopes on the thermal conductivity of lif. *Phys. Rev.*, 156:975, 1967.

[74] R. Berman, F. E. Simon, and J. M. Ziman. *Proc. Roy. Soc. (London)*, A220:171, 1953.

[75] Etienne Boaknin, R.W. Hill, Cyril Proust, C. Lupien, Louis Taillefer, and Paul Canfield. Highly anisotropic gap function in borocarbide superconductor $LuNi_2B_2C$. *Phys. Rev. Lett.*, 87:237001, 2001.

[76] M. Sigrsit and K. Ueda. Phenomenological theory of unconventional superconductivity. *Rev. Mod. Phys.*, 63:239, 1991.

[77] E. Puchkaryov and K. Maki. Impurity scattering in d-wave superconductivity. unitarity limit versus Born limit. *European Physical Journal B*, 4:191–194, 1998.

[78] Gianfranco Preosti, Heesang Kim, and Paul Muzikar. Density of states in unconventional superconductors: Impurity-scattering effects. *Phys. Rev. B*, 50:1259–1263, 1994.

[79] M.I. Salkola, A.V. Balatsky, and D.J. Scalapino. Theory of scanning tunneling microscopy probe of impurity states in a d-wave superconductor. *Phys. Rev. Lett*, 77:1841, 1996.

[80] P.J.Hirschfeld and N.Goldenfeld. Effect of strong scattering on the low-temperature penetration depth of a d-wave superconductor. *Phys. Rev. B.*, 48:4219, 1993.

[81] K. Ishida, Y. Kitaoka, T. Yoshitomi, N. Ogata, T. Kamino, and K. Asayama. Gapless superconductivity in Zn-doped $YBa_2Cu_3O_7$ studied by CuNMR and NQR possibility of d-wave superconductivity in high-T_c oxides. *Physica C*, 179:29, 1991.

[82] H. Won, K. Maki, and E. Puchkaryov. *High T_c superconductors and related materials*. Kluwer Academic, 2001.

[83] Heesang Kim, Gianfranco Preosti, and Paul Musikar. Penetration depth and impurity scattering in unconventional superconductors. *Phys. Rev. B*, 49:3544, 1991.

[84] S. Uchida. Zn-impurity effects on high-temperature superconductivity. *Physica C*, 357:25–29, 2001.

[85] P. Arberg, M. Mansor, and J.P. Carbotte. Penetration depth for a 2d d-wave superconductor with impurities. *Sol. Stat. Comm.*, 86:671–673, 1993.

[86] H. Suderow, J.P. Brison, and J. Flouquet. Thermal conductivity and gap structure of the superconducting phases of UPt_3. *J. Low Temp. Phys.*, 108:11–30, 1997.

[87] Patrick Lee. Localized states in a d-wave superconductor. *Phys. Rev. Lett.*, 71:1887, 1993.

[88] M.J.Graf, S-K.Yip, J.A.Sauls, and D.Rainer. Electronic thermal conductivity and the wiedemann-franz law for unconventional superconductors. *Phys. Rev. B.*, 53:15147, 1996.

[89] M. Chiao, R. W. Hill, C. Lupien, L. Taillefer, P. Lambert, R. Gagnon, and P. Fournier. Low-energy quasiparticles in cuprate superconductors: A quantitative analysis. *Phys. Rev. B*, 62:3554, 2000.

[90] J. Mesot, M. R. Norman, H. Ding, M. Randeria, J. C. Campuzano, A. Paramekanti, H. M. Fretwell, A. Kaminski, T. Takeuchi, T. Tokoya, T. Sato, T. Takahashi, T. Mochiku, and K. Kadowaki. Superconducting gap anisotropy and quasiparticle interactions: A doping dependent photoemission study. *Phys. Rev. Lett.*, 83:840, 1999.

[91] Y. Sun and K. Maki. Tranport-properties of d-wave superconductors with impurities. *Europhys. Lett.*, 32:355, 1995.

[92] H. F. Hess, R.B. Robinson, R.C. Dynes, J.M. Valles, and J.V. Waszczak. Scanning-tunneling-microscope observation of the Abrikosov flux lattice and the density of states near and inside a fluxoid. *Phys. Rev. Lett.*, 62:214, 1989.

[93] H.F. Hess, R.B. Robinson, and J.V. Wasczak. Highly anisotropic gap function in borocarbide superconductor LuNi$_2$B$_2$C. *Phys. Rev. Lett.*, 64:2711, 1990.

[94] A. L. Fetter and P.C. Hohenburg. *Superconductivity*. New York, 1969.

[95] J. Lowell and J.B. Sousa. *J. Low Temp. Phys.*, 65:65, 1970.

[96] G.E. Volovik. Superconductivity with lines of gap nodes - density-of-states in the vortex. *JETP Lett.*, 58:469, 1993.

[97] Y. Wang, B. Revaz, A. Erb, and A. Junod. Direct observation and anisotropy of the contribution of gap nodes in the low-temperature specific heat of YBa$_2$Cu$_3$O$_7$. *Phys. Rev. B.*, 63:094508, 2001.

[98] Kathryn A. Moler, D. J. Baar, J. S. Urbach, Ruixing Liang, W. N. Hardy, and A. Kapitulnik. Magnetic field dependence of the density of states of YBa$_2$Cu$_3$O$_{6.95}$ as determined from the specific heat. *Phys. Rev. Lett.*, 73:2744, 1994.

[99] Kathryn A. Moler, David L. Sisson, Jeffrey S. Urbach, Malcolm R. Beasley, Aharon Kapitulnik, David J. Baar, Ruixing Liang, and Walter N. Hardy. Specific heat of YBa$_2$Cu$_3$O$_{7-\delta}$. *Phys. Rev. B.*, 55:3954, 1997.

[100] R.A. Fisher, J.E. Gordon, S.F. Reklis, D.A. Wright, J.P. Emerson, B.F. Woodfield, E.M. McCarron, and N.E. Phillips. Magnetic-field dependence of the low-temperature specific heat of some high-T_c copper-oxide superconductors evidence for an H$^{1/2}$T contribution in the mixed state. *Physica C*, 252:237, 1995.

[101] D.A. Wright, J.P. Emerson, B.F. Woodfield, J.E. Gordon, R.A. Fisher, and N.E. Philips. Low-temperature specific heat of YBa$_2$Cu$_3$O$_{7-\delta}$ evidence for d-wave pairing. *Phys. Rev. Lett.*, 82:1550, 1999.

[102] C.Kübert and P.J.Hirschfeld. Quasiparticle transport properties of *d*-wave superconductors in the vortex state. *Phys. Rev. Lett.*, 80:4963, 1998.

[103] O.V. Lounasmaa, editor. *Experimental Principles and Methods Below 1 K*. Academic Press, New York, 1st edition, 1974.

[104] Etienne Boaknin. *Thermal Conduction in the Vortex State of Unconventional Superconductors*. PhD thesis, University of Toronto, 2003.

[105] D.O. Edwards, D.F. Brewer, P. Seligman, M. Skertic, and M. Yaqub. Solubility of ^3He in liquid ^4He at 0 k. *Phys. Rev. Lett.*, 15:773, 1965.

[106] G.K. White. *Experimental techniques in low temperature physics*. Clarendon Press, Oxford, 1968.

[107] R.F. Corruccini. Gaseous heat conduction at low pressures and temperatures. *Vacuum*, 7-8:19, 1959.

[108] JD Siegwarth R. Radebaugh, NV Frederick. Flexible laminates for thermally grounded terminal strips and shielded electrical leads. *Cryogenics*, 13:41, 1973.

[109] M. Barucci, E. Gottardi, I. Peroni, and G. Ventura. Low temperature thermal conductivity of Kapton and Upilex. *Cryogenics*, 40:145–147, 2000.

[110] Jason Lawrence, A.B. Patel, and J.G. Brisson. The thermal conductivity of kapton HN between 0.5 K and 5 K. *Cryogenics*, 40:203–207, 2000.

[111] B. Baudouy. Kapitza resitance and thermal conductivity of Kapton in superfluid helium. *Cryogenics*, 43:667, 2003.

[112] R.C. Johnson and W.A. Little. Experiments on the kapitza resistance. *Phys. Rev.*, 130:596–604, 1963.

[113] Etienne Boaknin, M.A. Tanatar, Johnpierre Paglione, D. Hawthorn, F. Ronning, R.W. Hill, M. Sutherland, Louis Tailleder, Jeff Sonier, S.M. Hayden, and J.W. Brill. Heat conduction in the vortex state of NbSe$_2$: evidence for multiband superconductivity. *Phys. Rev. Lett.*, 90:117003, 2003.

[114] F. Ronning, M. Sutherland, R.W. Hill, D. Hawthorn, J.P. Paglione, and Makariy Tanatar. Thermal transport in Sr$_3$Ru$_2$O$_7$. to be submitted to Phys. Rev. B.

[115] Johnpierre Paglione. *Thermal Transport in CeCoIn$_5$*. PhD thesis, University of Toronto, 2004.

[116] Ruixing Liang, D.A. Bonn, and W.N. Hardy. Growth of high quality YBCO single crystals using $BaZrO_3$ cruicibles. *Physica C*, 304:105, 1998.

[117] A. Hosseini, R. Harris, S. Kamal, P. Dosanjh, J. Preston, R. Liang, W. N. Hardy, and D. A. Bonn. Microwave spectroscopy of thermally excited quasiparticles in YBa$_2$Cu$_3$O$_{6.99}$. *Phys. Rev. B*, 60:1349, 1999.

[118] P. J. Turner, R. Harris, S. Kamal, M. E. Hayden, D. M. Broun, D. C. Morgan, A. Hosseini, P. Dosanjh, G. Mullins, J. S. Preston, R. Liang, D. A. Bonn, and W. N. Hardy. Observation of weak-limit quasiparticle scattering via broadband microwave spectroscopy of a *d*-wave superconductor. *Phys. Rev. Lett.*, 90:237005, 2003.

[119] R.J. Cava, A.W. Hewat, E.A. Hewat, B.Batlogg, M. Marezio, K.M. Rabe, J.J. Krajewski, F.W. Peck Jr., and L.W. Rupp Jr. Stuctural anomalies, oxygen ordering and superconductivity in oxygen deficient Ba$_2$YCu$_3$O$_x$. *Physica C*, 165:419–433, 1990.

[120] Robert Gagnon, Christian Lupien, and Louis Taillefer. T^2 dependence of the resistivity in the Cu-O chains of YBa$_2$Cu$_3$O$_{6.9}$. *Phys. Rev. B.*, 50:3458–3461, 1994.

[121] M.v.Zimmermann, J.R. Schneider, T. Frello, N.H. Anderson, J. Madsen, M. Käll, H.F. Poulsen, R. Liang, P.Dosanjh, and W.N. Hardy. Oxygen ordered superstructures in underdoped YBa$_2$Cu$_3$O$_{6+x}$ studied by hard x-ray diffraction. *Phys. Rev. B.*, 68:104515, 2003.

[122] B.W. Veal, H. You, A.P. Paulikas, H. Shi, Y. Fang, and J.W. Downey. *Bull. Am. Phys. Soc.*, 35:75, 1990.

[123] J.D. Jorgensen, Shiyou Pei, P. Lightfoot, Hao Shi, A.P. Paulikas, and B.W. Veal. Time-dependent structural phenomena at room temperature in quenched YBa$_2$Cu$_3$O$_{6.41}$. *Physica C*, 167:571, 1990.

[124] B.W. Veal, A.P. Paulikas, Hoydoo You, Hao Shi, Y. Fang, and J.W. Downey. Observation of temperature-dependent site disorder in YBa$_2$Cu$_3$O$_{7-\delta}$, below 150 °c. *Phys. Rev. B*, 42:6305, 1990.

[125] Gennadi Uimin. Order and disorder in the ensemble of cu-o chain fragments in oxygen-deficient planes of $YBa_2Cu_3O_{6+x}$. *Phys. Rev. B*, 50:9531, 1994.

[126] Ruixing Liang, D.A. Bonn, Walter N. Hardy, Janice C. Wynn, K.A. Moler, L. Lu, S. Larochelle, L.Zhou, M. Greven, L. Lurio, and S.G.J. Mochrie. Preparation and characterization of homogenous YBCO single crystals with doping level near the SC-AFM boundary. *Physica C*, 383:1, 2002.

[127] N.H. Andersen, M. von Zimmermann, T. Frello, M. Käll, D. Mönster, P.-A. Lindgärd, J. Madsen, T. Niemöller, H. F. Poulsen, O. Schmidt, J.R. Scheider, Th. Wolf, P. Dosanjh, R. Liang, and W.N. Hardy. Superstructure formation and the structural phase diagram of YBa$_2$Cu$_3$O$_{6+x}$. *Physica C*, 317-318:259, 1999.

[128] P. Monca, S. Sanna, G. Calestani, A. Migliori, S. Lapinskas, and E.E. Tornau. Orthorhombic low-temperature superstructures in YBa$_2$Cu$_3$O$_{6+x}$. *Phys. Rev. B*, 63:134512, 2001.

[129] Masaya Watahiki, Wen-Jye Jang, Setuko Tajima, and Masato Murakami. Magnetic properties of YBa$_2$Cu$_3$O$_y$ crystals with various oxygen annealing conditions. *J. Appl. Phys.*, 83:377–381, 1998.

[130] A.A. Zhukov, H.Küpfer, G. Perkins, L.F. Cohen, A.D. Caplin, S.A. Klestov, H.Claus, V.I. Voronkova, T.Wolf, and H.ühl. Influence of oxygen stoichiometry on the irreversible magnetization and flux creep in $RBa_2Cu_3O_{t-\delta}$ (R =y,tm) single crystals. *Phys. Rev. B*, 51:12704, 1995.

[131] B.W. Veal and A.P. Paulikas. Dependence of hole concentration on oxygen vacancy order in YBa$_2$Cu$_3$O$_{7-\delta}$. *Physica C*, 184:321–331, 1991.

[132] B.W. Veal, H. You, A.P. Paulikas, H. Shi, Y. Fang, and J.W. Downey. Time-dependent superconducting behaviour of oxygen-deficient YBa$_2$Cu$_3$O$_x$: Possible annealing of oxygen vacancies at 300 K. *Phys. Rev. B.*, 42:4770–4773, 1990.

[133] S. Yang, H.Claus, B.W. Veal, R.Wheeler, A.P.Paulikas, and J.W.Downey. New observation of a phase boundary in oxygen deficient $YBa_2Cu_3O_{7-\delta}$. *Physica C*, 193:243–252, 1992.

[134] Sascha Sadewasser, Yong Wang, James S. Schilling, Hong Zheng, Arydas P. Paulikas, and Boyd. W. Veal. Pressure dependent oxygen ordering in strongly underdoped $YBa_2Cu_3O_{7-y}$. *Phy. Rev. B*, 56:14168–14175, 1997.

[135] W.H. Fietz, R. Quenzel, H.A. Ludwig, K.Grube, S.I. Schlachter, F.W. Hornung, T. Wolf, A. Erb, M. Kläser, and G. Müller-Vogt. Giant pressure effect in oxygen deficient $YBa_2Cu_3O_x$. *Physica C*, 270:258–266, 1996.

[136] Vladimir G. Tissen, Yong Wang, Arvydas P. Paulikas, Boyd W. Veal, and James S. Schilling. Pressure dependence of T_c in strongly underdoped $YBa_2Cu_3O_{6.41}$ as a function of pressure-temperature history. *Physica C*, 316:21–26, 1999.

[137] Marsh P, R.M. Fleming, M.L. Mandich, A.M. DeSantolo, J. Kwo, M. Hong, and L.J. Martinez-Miranda. Crystal structure of the 80 K superconductor $YBa_2Cu_4O_8$. *Nature*, 334:141–143, 1988.

[138] N.E. Hussey, K.Nozawa, H.Takagi, S. Adachi, and K. Tanabe. Anisotropic resistivity of $YBa_2Cu_4O_8$: Incoherent-to-metallic crossover in the out-of-plane transport. *Phys. Rev. B*, 56:R11423, 1997.

[139] H. Zimmermann, M. Mali, D. Brinkmann, J. Karpinski, E. Kaldis, and S. Rusiecki. Copper NQR and NMR in the superconductor $YBa_2Cu_4O_{8+x}$. *Physica C*, 159:681, 1989.

[140] H. Zimmermann, M. Mail, I. Mangelschots, J. Roos, L. Pauli, D. Brinkman, J. Karpinski, S. Rusiecki, and E. Kaldis. Spin suceptibility and spin dynamics at Cu sites in $YBa_2Cu_4O_8$. *J, Less-Common Met.*, 164:138, 1990.

[141] B. Bucher, P. Steiner, J.Karpinski, E. Kaldis, and P. Wachter. Influence of the spin gap on the normal state transport in $YBa_2Cu_4O_8$. *Phys. Rev. Lett.*, 70:2012, 1993.

[142] J. L. Tallon, J. R. Cooper, P. S. I. P. N. de Silva, G. V. M. Williams, and J. W. Loram. Thermoelectric power: A simple, instructive probe of high-T_c superconductors. *Phys. Rev. Lett.*, 75:4114, 1995.

[143] A. Erb, E.Walker, and R. Flükiger. $BaZrO_3$: The solution for the crucible corrosion problem during the single crystal growth of high-tc superconductors $REBa_2Cu_3O_{7-d}$; RE = Y, Pr. *Physica C*, 245:245, 1995.

[144] E.Walker A. Erb and R. Flükiger. The use of $BaZrO_3$ crucibles in crystal growth of the high-T_c superconductors. progress in crystal growth as well as in sample quality. *Physica C*, 258:9, 1996.

[145] Ruixing Liang, D.A. Bonn, and Walter N. Hardy. Preparation and x-ray characterization of highly ordered ortho-II phase YBa$_2$Cu$_3$O$_{6.50}$ single crystals. *Physica C*, 2000:57, 336.

[146] P. Schleger, W.N. Hardy, and B.X. Yang. Thermodynamics of oxygen in Y$_1$Ba$_2$Cu$_3$O$_x$ between 450°c and 650°c. *Physica C*, 176:261, 1991.

[147] S. Adachi, K. Nakanishi, K. Tanabe, K. Nozawa, H. Takagi, W. Hu, and Z. Izumi. Preparation of YBa$_2$Cu$_4$O$_8$ single crystals in Y$_2$O$_3$ crucible using O$_2$-HIP apparatus. *Physica C*, 301C:123, 1998.

[148] K Segawa and Y. Ando. Transport properties of untwinned $YBa_2Cu_3O_y$ single crystals and the origin of the 60-K plateau. *JLTP*, 131:821–830, 1993.

[149] T.A. Friedmann, T. A. Friedmann, M. W. Rabin, J. Giapintzakis, J. P. Rice, and D. M. Ginsberg. Direct measurement of the anisotropy of the resistivity in the a-b plane of twin-free, single-crystal, superconducting YBa$_2$Cu$_3$O$_{7-\delta}$. *Phys. Rev. B.*, 42:6217, 1990.

[150] Yoichi Ando, Seiki Komiya, Kouji Segawa, S. Ono, and Y. Kurita. Electronic phase diagram of high-T_c cuprates drawn by resistivity curvature mapping. cond-mat/0403032, 2004.

[151] K. Segawa and Y. Ando. How to know the genuine hall response of the CuO$_2$ planes in a chain-plane-composite system of YBa$_2$Cu$_3$O$_y$. cond-mat/0308201, 2003.

[152] T. Ito, K. Takenaka, and S. Uchida. Systematic deviation from T-linear behavior in the in-plane resistivity of YBa$_2$Cu$_3$O$_{7-y}$: Evidence for dominant spin scattering. *Phys. Rev. Lett.*, 70:3995, 1993.

[153] T. Fujii T. Watanabe and A. Matsuda. Anisotropic resistivities of precisely oxygen controlled single-crystal Bi$_2$Sr$_2$CaCu$_2$O$_{8+\delta}$: Systematic study on 'spin gap' effect. *Phys. Rev. Lett.*, 79:2113, 1997.

[154] J. Takeya, Y. Ando, S. Komiya, and X. F. Sun. Low-temperature electronic heat transport in La$_{2-x}$Sr$_x$CuO$_4$ single crystals: Unusual low-energy physics in the normal and superconducting states. *Phys. Rev. Lett.*, 88:077001, 2002.

[155] M.R. Norman, H. Ding, M. Randeria, J.C. Campuzano, T. Yokoya, T. Takeuchi, T. Takahashi, T. Mochiku, K. Kadowaki, P. Guptasarma, and D.G. Hinks. Destruction of the Fermi surface in underdoped high-t_c superconductors. *Nature*, 392:157, 1998.

[156] Yoichi Ando, Y. Kurita, Seiki Komiya, S. Ono, and Kouji Segawa. Evolution of the hall coefficient and the peculiar electronic structure of cuprate superconductors. cond-mat/0401034, 2004.

[157] G. S. Boebinger, Y. Ando, A. Passner, T. Kimura, M. Okuya, J. Shimoyama, K. Kishio, K. Tamasaku, N. Ichikawa, and S. Uchida. Insulator-to-metal crossover in the normal state of $La_{2-x}Sr_xCuO_4$ near optimum doping. *Phys. Rev. Lett.*, 77:5417, 1996.

[158] M.R. Presland, J.L. Tallon, R.G. Buckley, R.S. Liu, and N.E. Flower. General trends in oxygen stoichiometry effects on T_c in Bi and Tl superconductors. *Physica C*, 176:95–105, 1991.

[159] H. Takagi, T.Ido, S. Ishibashi, M. Uota, S.Uchida, and Y. Tokura. Superconductor-to-nonsuperconductor transition in $(La_{1-x}Sr_x)_2CuO_4$ as investigated by transport and magnetic measurements. *Phys. Rev. B.*, 40:2254, 1989.

[160] J.B. Torrance, A. Bezinge, A.I. Nazzal, T.C. Huang, S.S.P. Parkin, D.T. Keane, S.J. LaPlaca, P.M. Horn, and G.A. Held. Properties that change as superconductivity disappears at high-doping concentrations in $La_{2-x}Sr_xCuO_4$. *Phys. Rev. B.*, 40:8872, 1989.

[161] C.P. Popoviciu and J.L. Cohn. Thermal transport in $YBa_2Cu_3O_{6+x}$: doping dependence across the phase diagram. *Phys. Rev. B*, 55:3155–3162, 1997.

[162] A.V. Inyushkin, A.N. Taldenkov, and T.G. Uvarova. Thermal conductivity of oxygen deficient $YBa_2Cu_3O_{6+x}$. *Phys. Rev. B*, 54:13261–13268, 1996.

[163] S.D. Peacor and et. al. Theoretical analysis of the thermal conductivity of $YBa_2Cu_3O_{7-\delta}$ single crystals. *Phys. Rev. B*, 44:9508, 1991.

[164] D.M. Ginsburg, editor. *Physical Properties of High Temperature Superconductors*, volume 3. World Scientific, Singapore, 1992.

[165] P.J. Hirschfeld and W.O. Putikka. Theory of thermal conductivity in $YBa_2Cu_3O_{7-\delta}$. *Phys. Rev. Lett.*, 77:3909–3912, 1996.

[166] D.A. Bonn and et. al. Microwave determination of the quasiparticle scattering time in $YBa_2Cu_3O_{6.95}$. *Phys. Rev. B*, 47:11314, 1993.

[167] N.P. Ong, K. Krishana, Y. Zhang, and Z.A. Xu. Thermal conductivity as a probe of quasi-particles in the cuprates. cond-mat/9904160, 2000.

[168] Y. Zhang, N.P. Ong, P.W. Anderson, D.A. Bonn, R. Liang, and W.N. Hardy. Giant enhancement of the thermal conductivity κ_{xy} in the superconductor $YBa_2Cu_3O_7$. *Phys. Rev. Lett.*, 86:890, 2001.

[169] K. Takenaka, Y. Fukuzumi, K. Mizuhashi, S. Uchida, H. Asaoka, and H. Takei. In-plane thermal conductivity and Lorenz number in $YBa_2Cu_3O_{7-y}$. *Phys. Rev. B*, 56:5654–5661, 1997.

[170] J.L. Cohn, C.K. Lowe-Ma, and T.A. Vanderah. Anomalous phonon damping and thermal conductivity in insulating cuprates. *Phys. Rev. B.*, 52:R13 134, 1995.

[171] J.L. Cohn, E.F. Skelton, and S.A. Wolf. Thermal conductivity in the ab plane of untwinned YBa$_2$Cu$_3$O$_{7-\delta}$. *Phys. Rev. B.*, 45:13144, 1992.

[172] A.N. Taldenkov, P.Esquinazi, and K. Leicht. Thermal transport in high-T_c crystals: Some aspects on its temperature and magnetic field dependence. *JLTP*, 115:15–44, 1999.

[173] K. Krishana, N.P. Ong, Q. Li, G.D. Gu, and N. Koshizuka. Plateaus observed in the field profile of the thermal conductivity in the superconductor Bi$_2$Sr$_2$CaCu$_2$O$_8$. *Science*, 277:83–85, 1997.

[174] W. N. Hardy, S. Kamal, D. A. Bonn, K. Zhang, R. Liang, E. Klein, D. C. Morgan, and D.J. Baar. Microwave surface impedance of the superconductor YBa$_2$Cu$_3$O$_{6.95}$. *Physica B*, 197:609, 1994.

[175] J.L Kohn and J. Karpinski. Anisotropic in-plane thermal conductivity of single-crystal YBa$_2$Cu$_4$O$_8$. *Phys. Rev. B*, 58:14617–14620, 1998.

[176] P. Hirschfeld, P. Vollhardt, and P. Wölfle. Resonant impurity scattering in heavy-Fermion superconductors. *Solid State Commun.*, 59:111, 1986.

[177] S. Schmitt-Rink, K. Miyake, and C. M. Varma. Transport and thermal properties of heavy-fermion superconductors: A unified picture. *Phys. Rev. Lett.*, 57:2575, 1986.

[178] M. Vojta, Y. Zhang, and S. Sachdev. Quantum phase transitions in d-wave superconductors. *Phys. Rev. Lett.*, 85:4940, 2000.

[179] A. Sharoni, O. Millo, A. Kohen, Y. Dagan, R. Beck, G. Deutscher, and G. Koren. Local and macroscopic tunneling spectroscopy of Y$_{1-x}$Ca$_x$Ba$_2$Cu$_3$O$_{7-\delta}$ films: Evidence for a doping-dependent $i - s$ or $i - d_{xy}$ component in the order parameter. *Phys. Rev. B*, 65:134526, 2002.

[180] Christos Panagopoulos, J.L. Tallon, and Tao Xiang. Effects of the Cu-O chains on the anisotropic penetration depth in YBa$_2$Cu$_4$O$_8$. *Phys. Rev. B.*, 59:R6635, 1999.

[181] J. C. Campuzano, H. Ding, M.R. Norman, H.M. Fretwell, M. Randeria, A. Kaminski, J. Mesot, T. Takeuchi, T. sato, T. Yokoya, T. Takahashi, T. Mochiku, K. Kodwaki, P. Guptasarma, D.G. Hinks, Z. Konstantinovic, Z.Z. Li, and H. Raffy. Electronic spectra and their relation to the (π,π) collective mode in high-T_c superconductors. *Phys. Rev. Lett.*, 83:3709, 1999.

[182] G. Blumberg, M. V. Klein, K. Kadowaki, C. Kendziora, P. Guptasarma, and D. Hinks. Evolution of magnetic and superconducting fluctuations with doping of high-T_c superconductors: An electronic Raman scattering study. *J. Phys. Chem. Solids*, 59:1932, 1998.

[183] E. Fradkin. Critical behavior of disordered degenerate semiconductors. ii. spectrum and transport properties in mean-field theory. *Phys. Rev. B*, 33:3263, 1986.

[184] X. Yang and C. Nayak. Electrical and thermal transport by nodal quasiparticles in the d-density-wave state. *Phys. Rev. B*, 65:064523, 2002.

[185] D.N. Basov, R. Liang, D.A. Bonn, W.N. Hardy, B. Dabrowski, M. Quijada, D.B. Tanner, J.P. Rice, D.M. Ginsberg, and T.Timusk. In-plane anisotropy of the penetration depth in $YBa_2Cu_3O_{7-x}$ and $YBa_2Cu_4O_8$ superconductors. *Phys. Rev. Lett*, 74:598, 1995.

[186] C. Panagopoulos, J.R. Cooper, and T. Xiang. Systematic behavior of the in-plane penetration depth in *d*-wave cuprates. *Phys. Rev. B.*, 57:13422, 1998.

[187] S. Kamal, A. Hosseini, D.A. Bonn, Ruixing Liang, and W.N. Hardy. Magnetic penetration depth and surface resistance in ultrahigh-purity $YBa_2Cu_3O_{7-\delta}$ crystals. *Phys. Rev. B.*, 58:R8933, 1998.

[188] D.A. Bonn, S. Kamal, A. Bonakdarpour, Ruixing Liang, W.N. Hardy, C.C. Homes, D.N. Basov, and T.Timusk. *Czech Journal of Physics*, 46:3195, 1996.

[189] J.E. Sonier et al. Measurement of the fundamental length scales in the vortex state of $YBa_2Cu_3O_{6.60}$. *Phys. Rev. Lett.*, 79:2875, 1997.

[190] T. Pereg-Barnea, P. J. Turner, R. Harris, G. K. Mullins, J. S. Bobowski, M. Raudsepp, Ruixing Liang, D. A. Bonn, and W. N. Hardy. Absolute values of the london penetration depth in $YBa_2Cu_3O_{6+y}$ measured by zero field ESR spectroscopy on Gd doped single crystals. *Phys. Rev. B.*, 69:184513, 2004.

[191] Patrick Turner. Private Communication, 2004.

[192] L. B. Ioffe and A. J. Millis. *d*-wave superconductivity in doped Mott insulators. *J. Phys. Chem. Sol.*, 63:2359, 2002.

[193] C.J.Pethick and D.Pines. Transport processes in heavy-fermion superconductors. *Phys. Rev. Lett.*, 57:118, 1986.

[194] V. Umansky, R. de Picciotto, and M. Heiblum. Extremely high-mobility two dimensional electron gas: Evaluation of scattering mechanisms. *Appl. Phys. Lett.*, 71:683, 1997.

[195] M.Suzuki, M. Suzuki, M. A. Tanatar, N. Kikugawa, Z. Q. Mao, Y. Maeno, and T. Ishiguro. Universal heat transport in Sr_2RuO_4. *Phys. Rev. Lett.*, 88:227004, 2002.

[196] A.J.Berlinsky et al. Microwave conductivity due to impurity scattering in a d-wave superconductor. *Phys. Rev. B.*, 61:9088, 2000.

[197] S. Nakamae, K. Behnia, L. Balicas, F. Rullier-Albenque, H. Berger, and T. Tamegai. Effect of controlled disorder on quasiparticle thermal transport in $Bi_2Sr_2CaCu_2O_8$. *Phys. Rev. B.*, 63:184509, 2001.

[198] M.Franz. Mixed-state quasiparticle transport in high- tc cuprates. *Phys. Rev. Lett.*, 82:1760, 1999.

[199] Ryusuke Ikeda. Fluctuation effects in underdoped cuprate superconductors under a magnetic field. *Phys. Rev. B*, 66:100511, 2002.

[200] H. Aubin, K. Behnia, S. Ooi, T. Tamegai, K. Krishana, N. P. Ong, Q. Li, G. Gu, and N. Koshizuka. Quasiparticles and thermal conductivity. *Science*, 280:11, 1998.

[201] M. Smith, J.P. Paglione, M. Walker, and L. Taillefer. Origin of anomalous low-temperature downturns in the thermal conductivity of cuprates. *Submitted to Phys. Rev. B.*, 2004.

[202] K. Behnia. private communication, 2004.

[203] N.E. Hussey. private communication, 2004.

[204] M. Chiao, Brett Ellman, R. Gagnon, and L. Taillefer. Anisotropy of heat conduction by the residual normal fluid in $YBa_2Cu_3O_{6.9}$. unpublished pre-print, 1998.

[205] S. Massida et al. *Physica C*, 176:159, 1991.

[206] W.C. Wu, D Branch, and J.P. Carbotte. Effect of anisotropy on universal transport in unconventional superconductors. *Phys. Rev. B*, 58:3417–3424, 1998.

[207] A. G. Sun, D. A. Gajewski, M. B. Maple, and R. C. Dynes. Observation of josephson pair tunneling between a high-T_c cuprate ($YBa_2Cu_3O_{7-\delta}$) and a conventional superconductor (Pb). *Phys. Rev. Lett.*, 72:2267, 1994.

[208] A. G. Sun, A. Truscott, A. S. Katzand R. C. Dynes, B. W. Veal, and C. Gu. Direction of tunneling in $Pb/I/YBa_2Cu_3O_{7-x}$ tunnel junctions. *Phys. Rev. B*, 54:6734, 1996.

[209] K. A. Kouznetsov, A. G. Sun, B. Chen, A. S. Katz, S. R. Bahcall1, John Clarke, R. C. Dynes, D. A. Gajewski, S. H. Han, M. B. Maple, J. Giapintzakis, J.-T. Kim, and D. M. Ginsberg. c-axis josephson tunneling between $YBa_2Cu_3O_{7-\delta}$ and Pb: Direct evidence for mixed order parameter symmetry in a high- T_c superconductor. *Phys. Rev. Lett.*, 79:3050, 1997.

[210] W.C. Wu and J.P. Carbotte. Absence of anisotropic universal transport in YBCO. *Phys. Rev. B*, 322:123–128, 1999.

[211] Wu Ting, K. Fossheim, T. Wada, Y. Yaegashi, H. Yamauchi, and S. Tanaka. Ultrasonic measurements on two single-phase polycrystalline $YBa_2Cu_4O_8$ superconducting samples. *Phys. Rev. B*, 47:12197, 1993.

[212] D. M. Broun, P. J. Turner, S.Ozcan, B. Morgan, Ruixing Liang, W. N. Hardy, and D. A. Bonn. The decline of quasiparticle charge in $YBa_2Cu_3O_{6+x}$ on approaching the Mott insulator. Submitted to Science.

[213] S. Ono, Yoichi Ando, T. Murayama, F.F. Balriev, J.B. Betts, and G.S. Boebinger. Metal-to-insulator crossover in the low-temperature normal state of $Bi_2Sr_{2-x}La_xCuO_{6+\delta}$. *Phys. Rev. Lett.*, 85:638, 2000.

[214] Yoichi Ando, S. Ono, X.F. Sun, J. Takeya, F.F. Balkirev, J.B. Betts, and G.S. Boebinger. Quantum phase transition in the cuprate superconductor $Bi_2Sr_{2-x}La_xCuO_{6+\delta}$. *Phys. Rev. Lett.*, 92:247004, 2004.

[215] VF Gantmakher, DA Pushin, DV Shovkun, GE Tsydynzhapov, LP Kozeeva, and AK Lavrov. Low-temperature resistivity of $YBa_2Cu_3O_{6+x}$ single crystals in the normal state. *JETP Letters*, 65:870, 1997.

[216] A.N. Lavrov and L.P. Kozeeva. Study of the antiferromagnetic and superconducting phase boundaries in $RBa_2Cu_3O_{6+x}$ (r= tm,lu). *Physica C*, 248:365, 1995.

[217] Yoichi Ando, Kouji Segawa, A. N. Lavrov, and Seiki Komiya. Charge transport properties of lightly doped cuprates: behaviour of the Hall co-efficient. *JLTP*, 131:793–801, 2003.

[218] G. T. Seidler, T. F. Rosenbaum, and B. W. Veal. Two-dimensional superconductor-insulator transition in bulk single-crystal $YBa_2Cu_3O_{6.38}$. *Phys. Rev. B*, 45:10162, 1992.

[219] K. M. Shen, T. Yoshida, D. H. Lu, F. Ronning, N. P. Armitage, W. S. Lee, X. J. Zhou, A. Damascelli, D. L. Feng, N. J. C. Ingle, H. Eisaki, Y. Kohsaka, H. Takagi, T. Kakeshita, S. Uchida, P. K. Mang, M. Greven, Y. Onose, Y. Taguchi, Y. Tokura, Seiki Komiya, Yoichi Ando, M. Azuma, M. Takano, A. Fujimori, and Z.-X. Shen. Fully gapped single-particle excitations in lightly doped cuprates. *Phys. Rev. B*, 69:054503, 2004.

[220] Yoichi Ando, A. N. Lavrov, Seiki Komiya, Kouji Segawa, and X. F. Sun. Mobility of the doped holes and the antiferromagnetic correlations in underdoped high-T_c cuprates. *Phys. Rev. Lett.*, 87:017001, 2001.

[221] Marta Z. Cieplak, A. Malinowskia, S. Guha, and M.Berkowski. Localization and interaction effects in strongly underdoped $La_{2-x}Sr_xCuO_4$. *Phys. Rev. Lett.*, 92:187003, 2004.

[222] Yoichi Ando, G.S. Boebinger, A. Passner, and T. Kimura nd K. Kishio. Logarithmic divergence of both in-plane and out-of-plane normal-state resistivities of superconducting $La_{2-x}Sr_xCuO_4$ in the zero-temperature limit. *Phys. Rev. Lett.*, 75:4662, 1995.

[223] Kouichi Semba and Azusa Matsuda. Superconductor-to-insulator transition and transport properties of underdoped $YBa_2Cu_3O_y$ crystals. *Phys. Rev. Lett.*, 86:496–499, 2001.

[224] P. A. Lee and T. V. Ramakrishnan. Disordered electronic systems. *Rev. Mod. Phys.*, 57:287, 1985.

[225] T. Yoshida, X. J. Zhou, T. Sasagawa, W. L. Yang, P. V. Bogdanov, A. Lanzara, Z. Hussain, T. Mizokawa, A. Fujimori, H. Eisaki, Z.-X. Shen, T. Kakeshita, and S. Uchida. Metallic behavior of lightly doped $La_{2-x}Sr_xCuO_4$ with a Fermi surface forming an arc. *Phys. Rev. Lett.*, 91:027001, 2003.

[226] Yoichi Ando, Y. Hanaki, S. Ono, T. Murayama, Kouji Segawa, N. Miyamoto, and Seiki Komiya. Carrier concentrations in $Bi_2Sr_{2-x}La_xCuO_{6+\delta}$ single crystals and their relation to the hall coefficient and thermopower. *Phys. Rev. B*, 61:R14956, 2000.

[227] S. Ono, Y. Ando, T. Murayama, F.F. Balakirev, J.B. Betts, and G.S. Boebinger. Low-temperature normal state of BSLCO: Comparison with LSCO. *Physica C*, 357-360:138–141, 2001.

[228] V.J. Emery, S.A. Kivelson, and J.M. Tranquada. Stripe phases in high-temperature superconductors. *Proc. Natl. Acad. Sci.*, 96:8814, 1999.

[229] Subir Sachdev and SC Zhang. Tuning order in cuprate superconductors. *Science*, 295:452, 2002.

[230] S. Lefebvre, P. Wzietek, S. Brown, C. Bourbonnais, M. Fourmig D. Jrom and, C. Mzi and4, and P. Batail. Mott transition, antiferromagnetism, and unconventional superconductivity in layered organic superconductors. *Phys. Rev. Lett.*, 85:5420, 2000.

[231] P. Limelette, A. Georges, D. Jerome, P. Wzietek, P. Metcalf, and J. M. Honig. Universality and critical behanviour at the Mott transition. *Science*, 302:89, 2003.

[232] S.M. Hayden, G. Aeppli, T. G. Perring, H. A. Mook, and F. Dogan. High-frequency spin waves in $YBa_2Cu_3O_{6.15}$. *Phys. Rev. B*, 54:6905, 1996.

[233] B. Khaykovich, R. J. Birgeneau, F. C. Chou, R. W. Erwin, M. A. Kastner, S.-H. Lee, Y. S. Lee, P. Smeibidl, P. Vorderwisch, and S. Wakimoto. Effect of a magnetic field on long-range magnetic order in stage-4 and stage-6 superconducting La_2CuO_{4+y}. *Phys. Rev. B*, 67:054501, 2003.

[234] L. Balents, M.P.A. Fisher, and C. Nayak. Nodal liquid theory of the pseudo-gap phase of high-T_c superconductors. *Int. J. Mod. Phys. B*, 12:1033, 1998.

[235] R.W. Hill, Cyril Proust, Louis Taillefer, P. Fournier, and R.L. Greene. Breakdown of Fermi-liquid theory in a copper-oxide superconductor. *Nature*, 414:711, 2001.

[236] R. Bel, Kamran Behnia, Cyril Proust, Peter van der Linden, Duncan Maude, and Sergey I. Vedeneev. Test of the Wiedemann-Franz law in an optimally doped cuprate. *Phys. Rev. Lett.*, 92:177003, 2004.

[237] Steven A. Kivelson, Daniel S. Rokhsar, and James P. Sethna. Topology of the resonating valence-bond state: Solitons and high-T_c superconductivity. *Phys. Rev. B*, 35:8865, 1987.

[238] T. Senthil and M. P. A. Fisher. Z^2 gauge theory of electron fractionalization in strongly correlated systems. *Phys. Rev. B*, 62:7850, 2000.